Small heat shock protein interactions with *in vivo* partners

Miranda P. Collier

Lady Margaret Hall

University of Oxford



A thesis presented for the degree of

Doctor of Philosophy in Physical and Theoretical Chemistry

10 July 2018

Abstract

Small heat-shock proteins (sHsps) are part of a broad cellular system that functions to maintain a stable proteome under stress. They also perform a variety of regulatory roles at physiological conditions. Despite the multitude of sHsp targets, their interactions with partners are not well understood due to highly dynamical structures. In this thesis, I apply a variety of biophysical and structural approaches to examine distinct interactions made by the abundant human sHsps αB-crystallin and Hsp27. First, I find that αB-crystallin binds a cardiac-specific domain of the muscle sarcomere protein titin. A cardiomyopathy-causative variant of αB-crystallin is shown to disrupt this interaction, with demonstrated implications for tissue biomechanics. Next, I investigate the conformation and unfolding behaviour of another sarcomere-associated protein, filamin C, finding support for the hypothesis that it is mechanosensitive. This leads into an interrogation of the interaction between filamin C and Hsp27, which we find is modulated by phosphorylation of Hsp27. This modulation only manifests during filamin C unfolding, pointing toward a protective chaperoning mode against over-extension during mechanical stress. This finding is bolstered by up-regulation and interaction of both proteins in a mouse model of heart failure. I establish a system for similar studies of a third sHsp, cvHsp, which is muscle-specific and implicated in various myopathies but scantly understood at the molecular level compared to αB-crystallin and Hsp27. Finally, I probe the stoichiometries and kinetics of complexes formed between αB-crystallin and Hsp27 themselves, which co-assemble into a highly polydisperse ensemble. This involved the development of a high-resolution native mass spectrometry method for disentangling heterogeneous systems. Together these findings add to our understanding of the roles and mechanisms of ATP-independent molecular chaperones.

Statement of Originality

This thesis describes research conducted between October 2014 and May 2018. The results are tied to a central theme, with each chapter arising from a distinct project. These projects involved collaboration to varying degrees, but each chapter is an original product of my own writing, and to the extent possible in an inherently collective endeavour, my own thinking. Because I believe in the shared intellectual ownership of the science, I have largely opted for general 'we' pronouns in the text.

Figures can be assumed to contain data or schematics generated by myself, unless otherwise stated in the caption. At the end of each results chapter are acknowledgments specific to the project, further delineating all of the assistance, material and immaterial, that I received.

This work has not been submitted for a degree, diploma, or any other academic certification at any other institution, in whole or in part.

Miranda Page Collier

May 2018

List of Abbreviations

1D	One dimensional
2D	Two dimensional
ABD	Actin-binding domain
ACD	α-crystallin domain
AFM	Atomic force microscopy
ATP	Adenosine triphosphate
ASU	Asymmetric unit
BME	β-Mercaptoethanol
BSA	Bovine serum albumin
CCS	Collision cross-section
CID	Collision-induced dissociation
CIU	Collision-induced unfolding
CPMG	Carr-Purcell-Meiboom-Gill
CTP	C-terminal peptide
DTT	Dithiothreitol
EDTA	Ethylene diamine tetraacetic acid
FFT	Fast Fourier transform
FL	Full-length; comprising the entire amino acid sequence
FLN(A/B/C)	Filamin A/B/C
HCD	High-energy collisional dissociation
HSQC	Heteronuclear single quantum coherence
IDP	Intrinsically disordered protein
IDR	Intrinsically disordered region
Ig	Immunoglobulin
IM	Ion mobility
IPTG	Isopropyl thio galactanoside
IST	In-source trapping
(k)Da	(kilo)Dalton
(k)Hz	(kilo)Hertz
KO	Knock-out (of a gene)
LYM	Linear Young's Modulus
MCP	Micro-channel plate
MD	Molecular dynamics
MLP	Muscle LIM protein

MR	Molecular replacement
MS	Mass spectrometry
MW	Molecular weight
MX	Macromolecular X-ray crystallography
NCS	Non-crystallographic symmetry
nESI	Nano-electrospray ionization
NMR	Nuclear magnetic resonance
NTD	N-terminal domain
OD	Optical density
PAGE	Polyacrylamide gel electrophoresis
PDB	Protein Data Bank
PBS	Phosphate-buffered saline
ppm	Parts per million
PPR	Principle phosphorylation region (of Hsp27)
RMSD	Root mean square deviation
SASA	Solvent-accessible surface area
SDS	Sodium dodecyl sulfate
SEC	Size exclusion chromatography
sHsp	Small heat-shock protein
SL	Sarcomere length
SNP	Single nucleotide polymorphism
SRIG	Stacked ring ion guide
SUMO	Small ubiquitin-like modifier
TEV	Tobacco etch virus
TFZ	Translation function Z-score
TLS	Translation, libration, screw tensors
TOF	Time-of-flight
UHV	Ultra high vacuum
WT	Wild-type; unmodified or not mutated

Acknowledgments

I am grateful to so many people for making my journey to and through this degree such a wonderful experience.

I owe my progress in large part to colleagues who have been generous with their time and expertise. Thanks to Georg Hochberg for his fun and firm guidance at the outset of my DPhil, for showing me the ways of the lab and teaching me how to think about my results, and for dispensing biophysics knowledge and life advice ever since. Thanks to Tim Allison for fielding my many questions about data processing, and for facing the odd hours and the successes and pitfalls of the synchrotron with me. I thank Matteo Degiacomi for all of his help and computational wizardry, and for his general uplifting presence whenever I was plagued by self-critical thoughts. Thanks to Shane Chandler, whom I could always turn to for ideas when stuck on an experiment, for supportive words when I needed them, and for a pub outing whether there was an occasion or not. Thanks to Joe Gault for his help in the lab and for never failing to provide thought-provoking discussion. I have also greatly appreciated advice, assistance, feedback, and laughter from Weston Struwe, Reid Alderson, Lucía Geis Asteggiante, Mike Marty, Jani Bolla, Mike McDonough, Ed Lowe, Max Hantke, Iva Pritišanac, Heidi Gastall, Jason Yen, Idi Liko, Mark Agasid, and Olya Tkachenko.

I have had the good fortune to cross paths with fantastic students. To Ellie Moore, Charlie Silver, India Kelly, Dominik Šaman, and Zihao Wang, thank you for approaching your projects with open minds and good spirits. I have grown and learned from working alongside you all.

My collaborators have shaped my broader understanding of biology and biophysics and fostered my commitment to open communication. Many thanks to Carin de Villiers and Katja Gehmlich, and to everyone else with whom I have tackled these challenges large and small. Thanks also to Carol Robinson for her invaluable perspective and backing when I was making decisions about the future.

To my teachers growing up, I am enormously indebted for instilling in me a strong drive and sense of curiosity. I regret that I cannot name them all, but I know that without their encouragement from a young age, I would not be here. For introduc-

ing me to scientific research as an undergraduate, I thank Stephen Barnes, whose indefatigable sense of wonder toward the natural world is always inspiring.

I owe so much to my parents, who made sure to tear down any boundaries to my ambitions in life from the day I was born – I've seen the proof in their words in home videos filmed when I could barely walk. Through the winding path that led me here, they nurtured every interest and aided every goal.

To friends long-loved and new, I am grateful for repeated willingness to catch up from where we last left things. I especially thank Anna van der Zalm, who has been a source of liveliness and encouragement throughout my time at Oxford; and her family as well, in whom I could always find a haven so far from the home I knew.

An immense thank you to Justin Benesch for his mentorship and support throughout this degree, and for taking a chance on a quiet student from Alabama whom buses befuddled. He has been generous with intellectual freedom over my projects, patient and insightful when I wavered, and thorough in ensuring I had every opportunity to be challenged and to expand what I knew and what I could accomplish. I credit him greatly for the skills I have gained, not only as they apply to our work described here, but across many facets of being a scientist.

And from my heart, I thank Jeremy Pilaar, whose kindness and determination I constantly admire. Our intermittent adventures and countless hours on the phone have nourished my soul. For embarking on three years an ocean apart and yet feeling right by my side the whole time, I am more appreciative than you can know.

Contents

1 Biological context and methods for investigating small heat shock proteins **1**
1.1 Abstract . . . 1
1.2 Protein homeostasis . . . 2
1.3 Small heat-shock proteins . . . 4
1.3.1 Chaperoning: a variable feature . . . 4
1.3.2 Functions and interactors . . . 5
1.3.3 Dynamic structure . . . 7
1.4 Native mass spectrometry in structural biology . . . 12
1.5 Technical overview of native MS . . . 14
1.5.1 Nano-electrospray ionization . . . 15
1.5.2 Macromolecular ion transmission . . . 17
1.5.3 Mass analyzers . . . 18
1.5.4 Interrogating noncovalent complexes . . . 21
1.5.5 Ion mobility . . . 23
1.5.6 Collision-induced unfolding . . . 25
1.6 Macromolecular X-ray crystallography . . . 27
1.6.1 X-ray diffraction and phasing . . . 28
1.6.2 Model building, refinement, and interpretation . . . 29
1.7 Nuclear magnetic resonance spectroscopy . . . 31

References **34**

2 αB-Crystallin modulates the passive stiffness of heart muscle by binding titin **45**
2.1 Abstract . . . 45
2.2 Introduction . . . 46
2.2.1 Titin modulates muscle elasticity . . . 46
2.2.2 αB-crystallin in the heart . . . 47
2.3 Results . . . 48
2.3.1 αB-Crystallin stiffens cardiac muscle fibers . . . 48
2.3.2 αB-Crystallin oligomers bind titin domain I26 . . . 50
2.3.3 Binding to I26 occurs via the αB-crystallin C-terminus . . . 51
2.3.4 Disease variant ^{R157H}αB abrogates C-terminal binding to I26 and the αB ACD . . . 52
2.3.5 Toward an X-ray structure of the I26-αB complex . . . 55
2.3.6 Solution NMR reveals I26 plasticity . . . 59

2.3.7 Atomic force microscopy . . . 61
2.3.8 αB_{Ctp} is sufficient to stiffen muscle fibers and its function is compromised by mutation R157H . . . 63
2.4 Discussion . . . 66
2.5 Methods . . . 70

References **77**

3 Conformational plasticity and extension pathway of the sHsp client filamin C **83**
3.1 Abstract . . . 83
3.2 Introduction . . . 84
3.2.1 Filamin structure, function, and implication in disease . . . 84
3.2.2 Native IM-MS, conformational heterogeneity, and intrinsic disorder . . . 85
3.3 Results and Discussion . . . 88
3.3.1 FLNC adopts compact and extended conformations modulated by the d20 insertion . . . 88
3.3.2 Gas-phase unfolding occurs via discrete biomechanically relevant transitions . . . 92
3.3.3 Cardiomyopathy-associated sequence variants affect FLNC conformational space and stability . . . 96
3.4 Conclusions . . . 100
3.5 Methods . . . 103

References **106**

4 Phosphorylation of Hsp27 regulates its mechanosensitive interaction with native filamin C **111**
4.1 Abstract . . . 111
4.2 Introduction . . . 112
4.3 Results . . . 114
4.3.1 FLNC and Hsp27 are up-regulated and interact in DCM hearts 114
4.3.2 Phosphomimicry reduces Hsp27 oligomer size and modulates N-terminal disorder in a simplified protomer . . . 116
4.3.3 The N-terminal phosphosite-rich region of Hsp27 interacts with a pocket of its ACD . . . 119
4.3.4 Hsp27 residues 80-88 bind multiple domains within FLNC . . . 121
4.3.5 Phosphorylation modifies the force-accessible trajectory of the FLNC-Hsp27 complex . . . 123
4.4 Discussion . . . 126
4.5 Methods . . . 132

References **143**

5 Structural and functional investigations of cvHsp **151**
5.1 Abstract . . . 151
5.2 Introduction . . . 152
5.2.1 cvHsp functions in muscle . . . 152
5.2.2 cvHsp structure and chaperone activity . . . 153
5.3 Results and Discussion . . . 155

5.3.1 cvHsp is small compared to canonical polydisperse sHsps . . . 155
5.3.2 cvHsp assembles via its ACD into dimers . . . 156
5.3.3 Covalent dimerization suggests redox sensitivity and a distinct ACD structure . . . 158
5.3.4 cvHsp does not appear to bind filamin A domains 23 or 24 . . 159
5.3.5 An optical trapping method for *in vitro* measurement of actin network viscosity . . . 161
5.3.6 Free actin can be monitored during real-time assembly in physiological buffer by native MS . . . 163
5.4 Conclusions . . . 165
5.5 Methods . . . 168

References **172**

6 Quantifying polydisperse heteromeric protein assembly **177**
6.1 Abstract . . . 177
6.2 Introduction . . . 178
6.2.1 sHsps co-assemble selectively with implications for function . . 178
6.2.2 Developments enabling native mass spectrometry of a highly heterogeneous system . . . 179
6.3 Results . . . 182
6.3.1 αB-crystallin and Hsp27 share heteromeric affinities at multiple interfaces . . . 182
6.3.2 Optimization of polydisperse sHsp characterization on an Orbitrap Q-Exactive platform . . . 186
6.3.3 αB-crystallin and Hsp27 form large, polydisperse, highly intermixed oligomers . . . 189
6.3.4 Segmented data collection allows broad stoichiometric assignment of heteromer assemblies . . . 192
6.3.5 Monitoring kinetics of co-assembly . . . 198
6.4 Discussion . . . 200
6.5 Methods . . . 204

References **209**

7 Concluding remarks **212**

Chapter 1

Biological context and methods for investigating small heat shock proteins

1.1 Abstract

The cellular processes central to life depend on the coordinated interactions of thousands of proteins. Cells therefore invest significant resources in maintaining a functional protein component. This thesis focuses on the small heat-shock proteins (sHsps), which are found in all kingdoms of life as part of an intricate network responsible for modulating the stability and interactions of the proteome. In this chapter, I provide a concise overview of the role of the sHsps within this broader network, and the current state of the field concerned with sHsp structure and function at the molecular level. This field has uncovered that sHsps are remarkably dynamic, a quality that presents challenges for their detailed characterization by a variety of biophysical approaches. Native mass spectrometry (MS) has yielded valuable insights into sHsp behaviour, and is the primary technique applied in this thesis. Thus, I include an introduction to this method for the non-mass spectrometrist, with a focus on its applicability to sHsp systems. The chapter concludes with brief descriptions of protein X-ray crystallography and NMR spectroscopy, which are also used to derive original results herein.

Biological motivation

1.2 Protein homeostasis

The ability of cells to respond to stress is central to the health and lifespan of organisms (Morimoto and Cuervo, 2014). Various types of stress are particularly damaging to folded proteins, which are only marginally thermodynamically stable in their functioning environments, making them vulnerable to even minor changes to cellular conditions (Kim et al., 2013; Hipp et al., 2014). An increasingly unfolded proteome is functionally impaired and at risk of forming large aggregates or amyloid fibrils. If the cell does not manage to sequester these protein deposits in a controlled manner (Miller et al., 2015; Sontag et al., 2017), they can become pathological (Figure **1.1a**) (Kakkar et al., 2014; Henning and Brundel, 2017; Chiti and Dobson, 2006). To support the integrity of the proteome throughout the protein turnover cycle, from the point of synthesis on the ribosome until degradation, cells across the kingdom of life have developed an intricate network responsible for proteostasis (protein homeostasis, or protein quality control, PQC). Comprising an integral part of this network is a family of proteins known as molecular chaperones (Kim et al., 2013; Bukau et al., 2006).

Chaperones can be broadly grouped into two non-exclusive categories: those that assist in *de novo* folding, and those that sense and mitigate the effects of misfolding at a later stage, performing what has been termed conformational maintenance (Figure **1.1b**) (Kim et al., 2013). Many of the latter are heat-shock proteins (Hsps), discovered upon their up-regulation following thermal stress (Richter et al., 2010; Lindquist, 1986). Although the name points exclusively to stress-related function, most human Hsps are constitutively expressed under basal conditions (Labbadia and Morimoto, 2015). They are classified by approximate subunit molecular masses

into Hsp110, Hsp90, Hsp70, Hsp60, Hsp40, and the small Hsp (sHsp; 16-27 kDa) families. The larger Hsps, often in concert with co-chaperones, consume ATP to perform diverse functions on substrates. These include folding nascent or destabilized polypeptides; aiding the assembly of multi-subunit complexes; disassembling aggregates; and trafficking misfolded species to the autophagic machinery (Kim et al., 2013; Mogk et al., 2018; Bukau et al., 2006; Saibil, 2013).

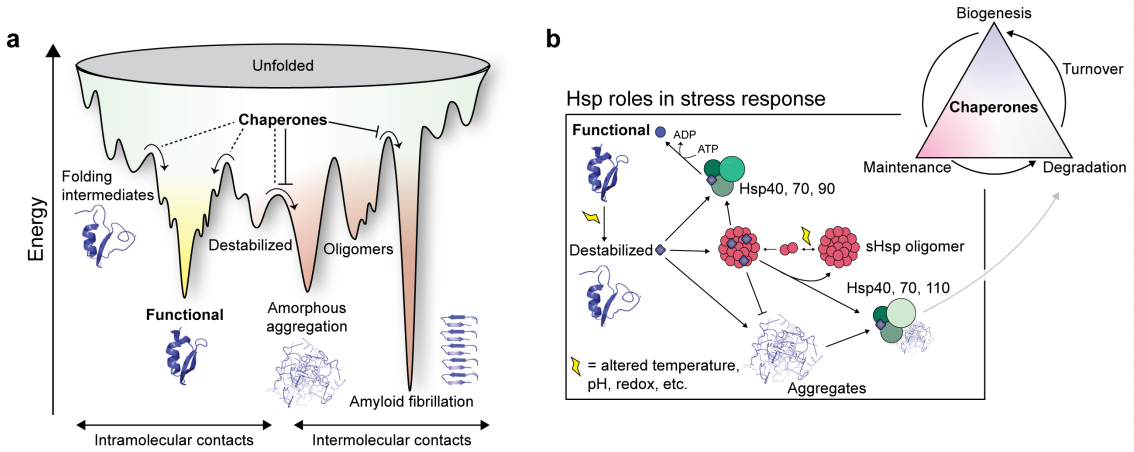


Figure 1.1. Chaperones modulate the stability of the proteome as part of the proteostasis network. a. A protein energy landscape. Unfolded proteins sample conformations to reach a flexible functional or 'native' state. Destabilized proteins can attract intermolecular interactors through exposure of hydrophobic regions, prompting a cascade to aggregation (protective (Sontag et al., 2017) or pathological (Hipp et al., 2014)). Some oligomeric precursors can also form highly thermodynamically stable fibrillar aggregates, which are associated with diseases (Chiti and Dobson, 2006). Chaperones affect various pathways along this energy landscape. **b.** The most prominent roles of mammalian heat-shock proteins during cellular response to stress, as part of the maintenance stage of the protein 'life cycle'. An environmental change causes native protein to misfold. It is then either bound by ATP-dependent Hsp machinery (Hsp40, Hsp70, Hsp90) for refolding, or sequestered by sHsps to prevent aggregation rapidly with less metabolic cost to the cell. sHsps form large oligomers often disrupted by stress conditions (Haslbeck et al., 2016). Additional chaperone complexes (involving Hsp40, Hsp70, and Hsp110) promote aggregate clearance through disassembly or degradation. Hsp60 (not pictured) is a mitochondrial chaperone. Schematics influenced by Kim et al. (2013); Carver et al. (2018); Richter et al. (2010); and Garrido et al. (2012).

In contrast to the others, sHsps are ATP-independent and cannot re-fold substrates. The paradigmatic sHsp populates oligomers hundreds of kDa in size which act as a chaperone reservoir. Upon stress, subunits are released, which then tightly sequester misfolded species in a competent state for downstream refolding or degradation (Figure **1.1b**) (Haslbeck et al., 2005, 2016; Hilton et al., 2013; Garrido et al., 2012). Here, I will dissect this canonical view and provide a more comprehensive introduction to sHsp function and structure.

1.3 Small heat-shock proteins

sHsps are found in archaea, bacteria, and eukarya, meaning they arose before life diverged, at least 3.5 billion years ago. Their evolutionary trajectory since hints at extensive functional diversity (Basha et al., 2012; Waters, 2013). Prokaryotes typically contain very few sHsps, while most eukaryotes have significantly more – the human genome encodes 10; teleost fish, 13; *C. elegans*, 16; and some land plant species have more than 30 (Marvin et al., 2008; Haslbeck et al., 2005; Waters, 2013). The plant sHsps are unique among eukaryotes in that they can be differentiated by their localization in cells, whereas animal sHsps are not targeted to specific organelles (Haslbeck et al., 2016). Plants' immobility in varying temperatures may explain this diversification, necessitating especially responsive and flexible heat-stress mechanisms. Their sHsps therefore constitute a useful system for interrogating the anti-aggregase functional paradigm (Waters, 2013; Jaya et al., 2009; Stengel et al., 2010; Friedrich et al., 2004). In addition to adaptation within plants, phylogenetic analyses have shown that the family has diversified over several different evolutionary timescales and groups (Haslbeck et al., 2005; Basha et al., 2012).

1.3.1 Chaperoning: a variable feature

Vertebrate sHsp expression varies with tissue, stage of development, and level of stress (Klemenz et al., 1993; Lutsch et al., 1997; Doran et al., 2007). They are generally abundant, constituting up to 40% of soluble protein in the eye lens (Horwitz et al., 1999) and up to 3% in non-lenticular tissues in the absence of stress (Klemenz et al., 1993; Kato et al., 1991; Dimauro et al., 2017). Some sHsps serve as a first line of defence when the proteome is compromised by acting as holdases to triage aggregation-prone species (Hilton et al., 2013). Despite the penetrance

of this model of sHsps as generalist chaperones, the description does not faithfully capture the entire protein family (Basha et al., 2012; McHaourab et al., 2009; Vos et al., 2009). Humans express 10 sHsps, categorized based on the presence of a conserved domain (Kappe et al., 2010). Fewer than half of these are up-regulated at the onset of stress (Big, 2015), and fewer than half can suppress the aggregation of a broad range of model substrates *in vitro*, with the rest displaying highly substrate-dependent activity (Table **1.1**) (Mymrikov et al., 2017).

Table 1.1. Features of human sHsps.

Original name[a]	New nomenclature	MW[b] (kDa)	Tissue distribution[c]	Stress-inducible?[d]	Promiscuous chaperone?[e]
Hsp27	HspB1	22.8	Ubiquitous	✓	✓
MKBP	HspB2	20.2	Muscle	×	×
HspL27	HspB3	17.0	Muscle	×	×
αA-crystallin	HspB4	19.9	Eye lens	×	✓
αB-crystallin	HspB5	20.1	Ubiquitous	✓	✓
Hsp20	HspB6	17.1	Muscle, brain	×	×
cvHsp	HspB7	18.6	Muscle	×	×
Hsp22	HspB8	21.6	Muscle, brain	✓*	×
CT51	HspB9	17.5	Testis	×	×
ODF1	HspB10	28.4	Testis	×	×

[a]This thesis will use the most common protein names in the literature, usually the originals.
[b]Molecular weight of the monomer, based on sequences in the UniProt database.
[c]Collated from reviews (The Big Book of Small Heat-Shock Proteins, Chapter 1, 2015 and Garrido et al. 2012) and mRNA levels (Vos et al., 2009).
[d]From The Big Book of Small Heat-Shock Proteins, Chapter 1; * denotes moderate inducibility.
[e]From Mymrikov et al. 2017 (Mymrikov et al., 2017), where ✓ denotes significant ability to suppress aggregation in 6 of 6 model substrates.

1.3.2 Functions and interactors

Evidence suggests that *in vitro* substrate dependence reflects *in vivo* specificity. sHsp interactomes, though difficult to determine comprehensively, clearly contain proteins that are shared between multiple members of the family and others that are distinctly tied to a single sHsp (Mymrikov et al., 2017; Arrigo, 2013). sHsps therefore appear to act within a two-tiered specialist-generalist framework, with a

majority seemingly adopting specialist functions under physiological conditions. It is as yet unclear whether specialists evolved from generalists, or vice versa. However, it is clear that sHsps from both types are implicated in human diseases – alterations to certain genes or expression levels are associated with myopathies, neuropathies, cataract, neurodegenerative disease, and cancer (Kakkar et al., 2014; Bakthisaran et al., 2015; Treweek et al., 2015). sHsp-targeted therapeutics are a potential treatment avenue (Salinthone et al., 2008; Henning and Brundel, 2017), and their development requires in-depth analyses of the interactions underlying these phenotypes. Thus, an improved understanding of the specialist role of the sHsps – and with it, their interactors – is potentially of biomedical as well as purely biological interest.

Terminology has been proposed to distinguish between sHsp interactors that are destabilized under stress and those that are bound physiologically by referring to these as substrates and clients, respectively (Strauch and Haslbeck, 2016). I adhere to this terminology in this thesis when the boundaries are clear, which they are not always. In muscle for example, which expresses the greatest variety of sHsps in humans (Table **1.1**), several sHsps interact with cytoskeletal components and associated proteins (Mounier and Arrigo, 2002; Bennardini et al., 1992; Houck and Clark, 2010; Wu et al., 2017; Tessier et al., 2003). In striated muscle, many also co-localize with the sarcomere, the basic unit of muscle contraction (Mercer et al., 2018; Golenhofen et al., 2004). These interactions have been reported under basal conditions as well as following oxidative, thermal, and mechanical stress (Koh and Escobedo, 2004; Pivovarova et al., 2007; Golenhofen et al., 1999; Shimizu et al., 2016; Ke et al., 2011). They are not yet understood with enough clarity at the molecular level to know whether the sHsps are targeting native-like proteins in a client-based mechanism, or misfolding proteins in a substrate-based mechanism (Seit-Nebi et al., 2013). What is clear, however, is that the interactions play critical roles in the

maintenance of cytoskeletal and muscle structural integrity (Wettstein et al., 2012; Liao et al., 2017; Dreiza et al., 2010), with disruption leading to cardiac and skeletal myopathies (Henning and Brundel, 2017; Inagaki et al., 2006; Kumarapeli et al., 2010; Juo et al., 2016; Unger et al., 2017).

Another prominent class of *in vivo* sHsp interactors is other sHsps themselves. Dynamic oligomerization is a common feature of the protein family (Figure **1.1b**). While most oligomeric proteins related by gene duplication do not co-assemble (Hochberg et al., 2018), hetero-oligomerization is common among human sHsps (Figure **1.2**) (Mymrikov et al., 2012; Arrigo, 2013; Bakthisaran et al., 2015; Fontaine et al., 2005). This implies an evolutionary constraint in the form of shared function, meaning not only do individual sHsps perform specialist roles, but the complexes they form may do so as well. The hypothesis is bolstered by tightly balanced constitutive tissue co-expression profiles (Vos et al., 2009; Sugiyama et al., 2000). Disease-linked mutations have been observed to affect heteromerization (Weeks et al., 2018; Simon et al., 2013; Morelli et al., 2017), but this area remains largely unexplored. Elucidating the purposes and mechanisms of co-assembly is a key aim for the sHsp field.

1.3.3 Dynamic structure

Structural characterization of sHsps has proven challenging due to their high degree of conformational plasticity at all levels of protein organization. At the quaternary level, many sHsps can populate multiple stoichiometries at once (McHaourab et al., 2009; Basha et al., 2012). This is commonly termed polydispersity, as opposed to monodispersity, where a protein adopts a single quaternary organization. Herein, 'more' or 'less' polydisperse will refer to the relative breadth of stoichiometric dis-

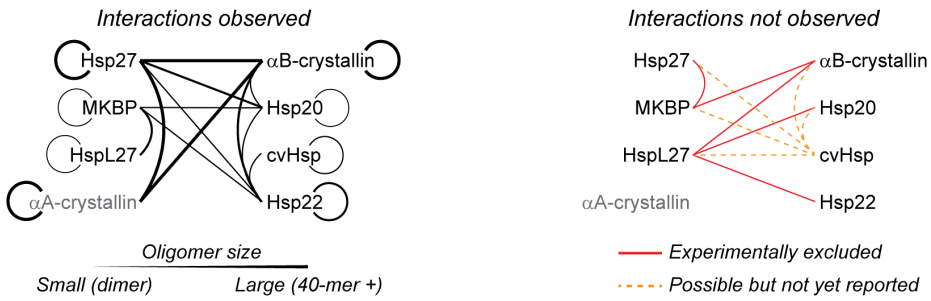


Figure 1.2. Co-assembly of 8 human sHsps. Left, interactions confirmed *in vivo* (Sugiyama et al., 2000; Fontaine et al., 2005; Fu and Liang, 2002; Kato et al., 1994). Circles indicate self-assembly. Line widths indicate approximate sizes of the resulting oligomers, ranging from a dimer to more than 40 subunits. Right, interactions that do not occur, excluded in the same set of studies. At present, published reports have not probed for cvHsp heteromers apart from with Hsp22. Because αA-crystallin is lens-specific, interactions between this protein and sHsps not expressed in the lens are not considered. HspB9 and HspB10 are omitted because they are testis-specific. Note that only the possibility of co-assembly is represented here; we can only infer heteromer prevalence from relative expression levels when preference for self versus other is known. This preference has been reported for three binary possibilities αA·αB (Horwitz et al., 1999); Hsp27-Hsp20 (Heirbaut et al., 2017); and HspB2-HspB3 (den Engelsman et al., 2009).

tributions. sHsp polydispersity is dynamic, involving the continual recycling of subunits (Aquilina et al., 2003; Bova et al., 2000). It is also tuneable: in non-metazoa and plants, they are usually monodisperse under non-stressed conditions and become polydisperse with heat stress (Big, 2015). This has enabled structural characterization of several sHsp oligomers by X-ray crystallography from yeast, wheat, archaea, and bacteria (Strauch and Haslbeck, 2016). These structures reveal polyhedral or stacked-ring arrangements composed of dimeric building blocks (Figure **1.3a**).

Stress-inducible human sHsps are highly polydisperse under basal conditions. αB-crystallin, for example, forms oligomers ranging from 10 to almost 50 subunits (Hochberg and Benesch, 2014). Consequently, these have not yet been fully structurally characterized at high resolution, since their plasticity hampers many biophysical techniques that require homogeneity or report on ensemble averages (Basha et al., 2012). Truncated, and as a result less polydisperse, forms of the proteins have yielded several partial X-ray structures of dimers. To model full-size oligomers, alternative methods have been applied to construct αB-crystallin polyhedra (Figure **1.3b**). Hsp20 is the only human sHsp that has been crystallized in its full-length

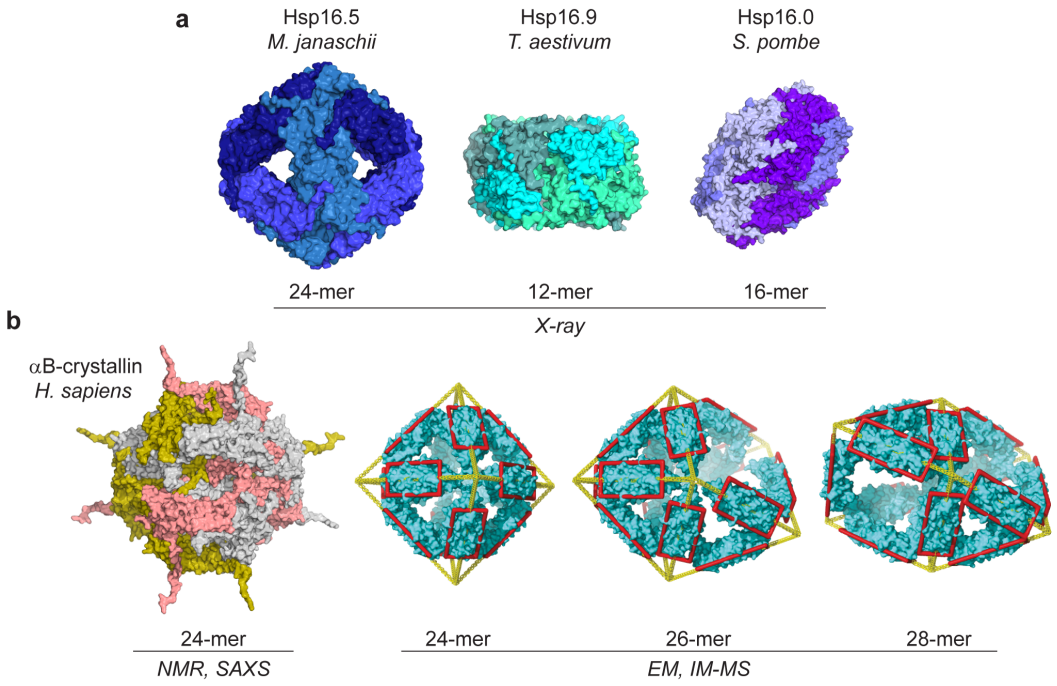


Figure 1.3. sHsp oligomer models. Dimeric building blocks are coloured individually. **a.** X-ray crystal structures of archaeal Hsp16.5 (Kim et al., 1998), wheat Hsp16.9 (van Montfort et al., 2001), and yeast Hsp16.0 (Hanazono et al., 2013) (PDB IDs 1SHS, 1GME, and 3W1Z, respectively). **b.** Human αB-crystallin. Left, a proposed full-length oligomer with 24 subunits based on solid-state nuclear magnetic resonance (NMR) and small angle X-ray scattering (SAXS) data (Jehle et al., 2011). Right, truncated dimer crystal structures (red boxes) are used to construct polyhedral oligomers of varying stoichiometries based on electron microscopy (EM) and ion mobility mass spectrometry (IM-MS) data, adapted from Baldwin et al. (2011a).

form, which is dimeric (Sluchanko et al., 2017). The corresponding structure, in complex with a binding partner, is missing approximately a third of each protein chain due to high flexibility, making it very similar to truncated structures of other members of the family (Sluchanko et al., 2017). The quaternary organization of vertebrate sHsps is susceptible to change not just upon heat stress, but also post-translational modification (PTM), which is very rarely observed in sHsps across plants, bacteria, archaea, or fungi (Garrido et al., 2012). Homeothermic organisms seem to require additional mechanisms of regulating sHsp activity, which is clearly linked to quaternary dynamics, though this link is not fully understood (Big, 2015; McHaourab et al., 2009).

sHsps assemble via a hierarchy of oligomeric interfaces (Figure **1.4**). The α–crystallin domain (ACD), which is highly conserved and defines the family, is lo-

cated in the middle of the primary sequence and adopts a relatively stable β–strand-rich tertiary structure Hilton and Benesch (2012). The sHsp dimer, the basic unit of assembly, forms via β–strand pairing within the ACD. β–strands are conventionally numbered, with non-metazoan sHsps dimerizing via swapping of β6 to pair with β2 of another subunit, and metazoan sHsps dimerizing via a combined and extended β6+7 -strand in an antiparallel (AP) arrangement in all structures observed to date (Figure **1.4b**) (Haslbeck et al., 2016; Treweek et al., 2015). This interface is not especially rigid; in the case of αB-crystallin, the ACD·ACD binding affinity is in the low micromolar range, and several distinct registers have been observed in X-ray structures (AP_I, AP_{II}, AP_{III}) (Figure **1.4c**) (Hochberg et al., 2014).

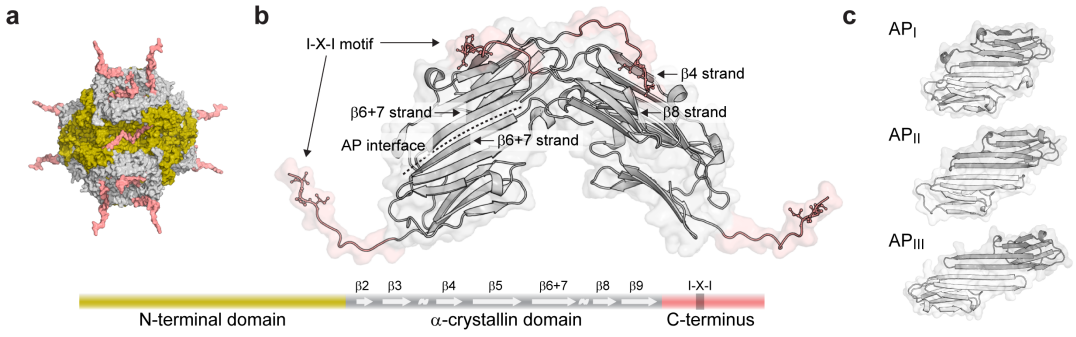


Figure 1.4. Structural regions of sHsps and hierarchy of assembly. The primary sequence encodes three domains: a central β-sheet rich ACD flanked by N- and C-terminal regions. **a.** Model of the αB-crystallin 24-mer as in **1.3**, but coloured by domain. Many C-termini are thought to be exposed on the oligomer periphery (Jehle et al., 2011). **b.** X-ray structure of the αB-crystallin ACD and partial C-terminus, showing 4 monomers (Laganowsky et al., 2010). The ACD dimerizes via an antiparallel (AP) interface between strands β6+7. The C-terminus bridges dimers by docking into a groove between strands β4 and β8 via the I-X-I motif (sticks; in αB-crystallin, X = proline). **c.** The contacts comprising the AP interface may shift under different conditions, evidenced by the observation of three registers of the αB-crystallin dimer by X-ray crystallography (PDB IDs 3L1G, 2WJ7, 4M5S). Multiple registers of the Hsp27 ACD dimer have also been crystallized (H. Gastall, unpublished).

The ACD is flanked by a disordered N-terminal domain (NTD) and a shorter but similarly flexible C-terminal region. The C-terminus is critical for higher order oligomerization. The shortest C-termini are found in the least polydisperse members of the family (Weeks et al., 2014; Boelens et al., 1998); longer C-termini bridge ACD dimers by binding a groove between strands β4 and β8 via a conserved motif, which consists of three residues I-X-I (in some sHsps, valine replaces one or

both isoleucines) (Figure **1.4b**) (Hilton and Benesch, 2012). Excising the region around this motif as a peptide (C-terminal peptide, Ctp) has enabled thermodynamic and kinetic characterization of the ACD·Ctp interface and led to crystallization of ACD·Ctp complexes (Hochberg et al., 2014; Laganowsky et al., 2010). Finally, inter-subunit interactions involving the NTD with another NTD or ACD have been observed (Jehle et al., 2011; McDonald et al., 2012). These are particularly affected by phosphorylation, the predominant PTM affecting sHsps, which seems to occur exclusively within this domain (Garrido et al., 2012; Heirbaut et al., 2017).

Variability across the three regions of human sHsps, but particularly the termini (Kriehuber et al., 2010), is believed to underlie differences in target recognition both directly through sequence motifs, and indirectly through modulation of quaternary structure and dynamics. Although there is still much to learn about their mechanisms of action, a clear portrait has emerged of a sHsp system that is finely tuned to aid in addressing the cellular need to maintain a healthy proteome. Constitutive expression, broad interactomes, and rapid mechanisms of energy-independent responsiveness suggest a range of functions from physiological to pathological conditions. Their complexity of structure and function poses many experimental challenges; thus, disentangling sHsp behaviour necessitates specialized methods that can tolerate heterogeneity.

Technical background

The studies described in this thesis rely on a variety of experimental techniques spanning from the tissue to atomic level, to provide more mechanistic insight into sHsps and their clients than any method could alone. Where data arose from collaboration, I have tried to communicate the importance of the results in the context of the broader story, without delving overly into the underlying theory. A majority of the biophysical findings in this thesis rely on native mass spectrometry (MS) approaches, whereby intact proteins, including protein-ligand or protein-protein complexes, are transferred from solution into gas phase macromolecular ions. These are detected based on their mass-to-charge (m/z) ratio, following optional manipulations to probe their structure, stability, or size. In addition, Chapters 2 and 4 report on original structures derived from protein X-ray crystallography and contain NMR spectroscopy data. Here I give an introduction to native MS and more brief overviews of protein crystallography and NMR spectroscopy, focusing on their applicability to the systems considered in the present work.

1.4 Native mass spectrometry in structural biology

Mass spectrometry (MS) was developed over a century ago for measurement of the elemental compositions of gaseous ions (Yates, 2011). It was originally directed toward small organic molecules before finding biological application in the analysis of peptides, allowing proteins to be identified following enzymatic digestion, and their abundances and modifications characterized from complex mixtures (Aebersold and Mann, 2003). We are now well into the third decade of MS application to the study of intact biomacromolecules and the complexes they form, and with this, its emergence as a tool of structural biologists and biophysicists (Hilton and Benesch,

2012).

Native (or non-denaturing) MS, as it is commonly termed, encompasses a range of gas-phase approaches involving the maintenance of noncovalent interactions and global structure as proteins are ionized and subsequently guided to high resolution mass measurement (Leney and Heck, 2017; Heck, 2008; Boeri Erba and Petosa, 2015; Rajabi et al., 2015; Benesch et al., 2007; Hernandez and Robinson, 2007; Loo, 2000). Pioneering studies have examined a range of biological systems, spanning sizes from small proteins (Chowdhury et al., 1990; Katta and Chait, 1991) to oligomers (Fitzgerald et al., 1996) to ribosomes (Benjamin et al., 1998), and topologies from protein rings (Lorenzen et al., 2008; Ruotolo et al., 2005) to polyhedra (Baldwin et al., 2011b) to membrane-embedded systems (Barrera et al., 2008; Laganowsky et al., 2014). By now the evidence is substantial for retention of solution-representative conformations and interactions in the gas phase, with size- and mass-based confirmation that protein shapes and interactions (hydrophobic, ionic, and hydrogen bonded) persist throughout the timescale of the native MS experiment (Breuker and McLafferty, 2008; Mehmood et al., 2015).

This foundation, combined with a plethora of advancements in instrumentation, has enabled many valuable contributions from native MS to our knowledge of the structures and functions of complex biological systems. Stoichiometries, including complexes that adopt multiple arrangements or populate equilibria with sub-complexes, are readily accessible – even for weak interactions, which emerging evidence suggests dominate the human interactome (Hein et al., 2015). Native MS is well-suited to link such big-data approaches, aiming to map proteome connectivity but lacking structural or dynamical information, with higher resolution approaches such as X-ray crystallography and nuclear magnetic resonance (NMR) spectroscopy, which can provide very detailed structural information but are limited in the flexi-

bility or size they can tolerate (Heck, 2008). While cryo-electron microscopy is not limited in the same ways as other high-resolution methods and is revolutionizing the field of structural biology, it cannot yet resolve small mass differences with the fidelity of native MS (Nogales and Scheres, 2015). Biopharma is increasingly looking to native MS with considerable interest in development of high-throughput assays for drug screening (Eschweiler et al., 2017b; Pedro and Quinn, 2016). And because it is a non-ensemble technique, in essence providing snapshots of solution processes, native MS is very useful for kinetic measurements (Ben-Nissan and Sharon, 2011; Kaltashov and Eyles, 2002).

Given the complexes they are known to form with themselves, other members of the proteostasis network, and their clients, sHsps comprise a highly heterogeneous biological system where multiple masses are virtually guaranteed to be present even in model *in vitro* conditions (Haslbeck et al., 2016; Strauch and Haslbeck, 2016; Hilton and Benesch, 2012). This is also combined with structural fluctuations at the tertiary level and ensembles that can reach hundreds of kDa, hindering methods that are contingent on rigid order and small size. Thus, native MS is at present uniquely suited among modern biophysical techniques to probe sHsp interactions and quaternary organization. In addition, because individual protein complexes are separated from each other on a timescale (milliseconds) shorter than sHsp population-wide interconversion (typically minutes to hours), we can monitor quaternary dynamics (Painter et al., 2008).

1.5 Technical overview of native MS

The MS experiment can be divided into three stages: first the analyte is transferred from solution into the gas phase (ionization), followed by guidance through the instrument with minimal sample loss (transmission), and finally separation of the ions

based on m/z ratio (mass analysis). The adaptation of MS for native biomolecules required technological advancements in each of these stages. This section will discuss in brief the fundamentals of each part of the experiment and the major developments that underlie their application in modern native MS. In addition, I cover strategies that allow us to probe protein assemblies, binding affinities, conformations, and stabilities. Many types of instruments enabling native MS are commercially available. The Synapt G1 QToF (Quadrupole Time-of-Flight) was used for much of the work in this thesis (Figure **1.5**).

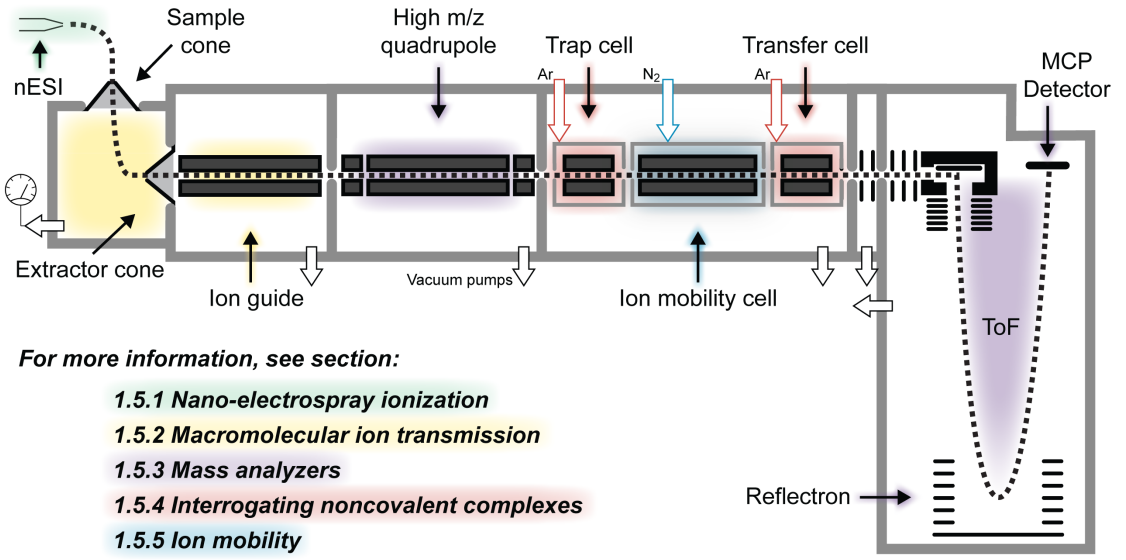


Figure 1.5. Schematic of the Synapt G1 QToF mass spectrometer. Proteins are ionized from solution by nano-electrospray ionization (nESI) and focused by a combination of optics and tunable pressure. The quadrupole acts as a gatekeeper allowing certain ions to be transmitted further, and these species of interest are optionally activated in a collision cell (Trap or Transfer) and separated according to their sizes by ion mobility (IM). The ion beam is then collected and pulsed orthogonally into the time-of-flight (ToF) mass analyser, where the time each takes to reach the detector is converted into m/z. Regions of the instrument discussed in more detail in the chapter are indicated. Figure modified from an original schematic by Heidi Gastall, Frances Kondrat, and Olya Tkachenko.

1.5.1 Nano-electrospray ionization

Electrospray ionization (ESI) involves the generation of ions from charged droplets by applying a high voltage between a conductive capillary and an inlet to the vacuum of the mass spectrometer (Figure **1.6a**) (Fenn et al., 1989). In positive mode, the tip of the capillary becomes enriched in cations and a protrusion known as a

Taylor cone is formed (Kebarle and Verkerk, 2009). As charge builds, Coulombic repulsion exceeds surface tension and small droplets are released, which then accelerate toward the inlet due to gradients of electric potential and pressure. The droplets undergo solvent evaporation, and as their charge-to-size ratio thus increases, multiple asymmetric fission events reduce their size until solvent-stripped analyte ions are produced (Konermann et al., 2013).

Two pathways have been proposed to describe the final generation of a macromolecular ion from a droplet: the Chain Ejection Model (CEM), involving expulsion of the ion from the droplet before complete desolvation, or the Charge Residue Model (CRM), involving exhaustion of the evaporation-fission cycle leaving behind only a molecule containing the charge of the droplet an instant before (Figure **1.6b**) (Konermann et al., 2013). Evidence supports the CRM as the dominant ionization mechanism for folded proteins (de la Mora, 2000; Benesch et al., 2007; Nguyen and Fenn, 2007) and for organic ions generally (Iavarone and Williams, 2003). Proteins that are completely or partially intrinsically disordered appear to ionize via a combination of the CEM and CRM, with unfolded regions attracted to the surface of the droplet where charge accumulates, susceptible to Coulombic repulsion-driven expulsion from the solvated environment (Figure **1.6b**) Konermann et al. (2012); Mehmood et al. (2015). The number of charges an ion carries is variable and largely dependent on the solvent-accessible surface area (Kaltashov and Mohimen, 2005; Li et al., 2016), resulting in a charge state distribution (CSD) for each species along m/z that can be used to determine the mass of the ion (Figure **1.6c**).

Nano-ESI (nESI) is a scaled-down version of conventional ESI, featuring a smaller capillary diameter (1-2 μm as opposed to 25-50 μm) (Juraschek et al., 1999). This reduces sample requirements by lowering the flow rate to nL min^{-1}, and enables

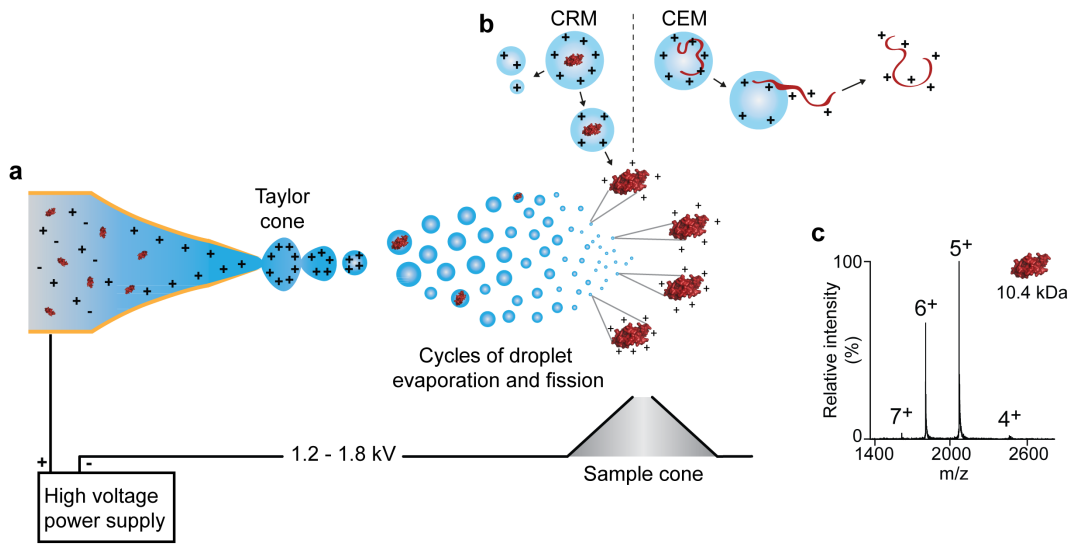


Figure 1.6. Nano-electrospray ionization of proteins. **a.** A potential difference applied to a gold-plated capillary generates a positively charged Taylor cone. Droplets break away and undergo cycles of evaporation and fission as they are guided toward the entrance to the mass spectrometer. In the case of typical aqueous ammonium acetate solvent, positive charges are NH_4^+ as well as many H^+ (Konermann et al., 2013). Note that protein ions are shown entirely desolvated here, but this may not be the case at the point of entry into the vacuum in reality. **b.** The Charged Residue and Chain Ejection Models for ion generation from a charged droplet. The CRM dominates ionization of folded proteins (de la Mora, 2000). The CEM is more salient for intrinsically disordered proteins (Konermann et al., 2012). **c.** The mass spectrum features a series of peaks along a mass-to-charge (m/z) axis, from which mass can be determined.

the use of aqueous as opposed to volatile solvents, critical for maintaining protein structures and interactions. In addition, because smaller droplets undergo fewer evaporation and fission cycles, nESI results in fewer undesirable adducts from residual non-volatile ions such as Na^+ or K^+ (Juraschek et al., 1999; Hilton and Benesch, 2012; Konermann et al., 2013). This gentle ionization technique maintains non-covalent interactions upon transfer to the gas phase, with the majority of droplets entering the inlet containing one or zero protein molecules at low micromolar sample concentrations (Benesch et al., 2007).

1.5.2 Macromolecular ion transmission

Upon entering the initial vacuum stages (the instrument 'source') from atmospheric pressure, the ion plume expands rapidly. Ion guides can be inefficient at focussing large products of nESI, which carry relatively little charge at very high kinetic

energies (Benesch et al., 2007). To focus the ions along the desired trajectory and through various apertures, elevated tuneable pressure in the source was introduced (Figure **1.5**). Collisions with background gas dissipate kinetic energy and help to trap the ions in the potential well created by low radio-frequency (RF) ion guides, a phenomenon termed 'collisional focusing' or 'collisional cooling'. This drastically improves transmission of high-mass ions (above ≈ 50 kDa) and leads to pressure-dependent transmission efficiency in general (Tahallah et al., 2001; Benesch et al., 2007; Chernushevich and Thomson, 2004).

1.5.3 Mass analyzers

Under denaturing conditions, protein ions carry high charges and have m/z below ≈ 3,000, so mass analyzers do not need to be particularly robust in terms of their m/z range. Native MS, however, features lower charges and consequently a much more broad m/z tolerance is required (Ashcroft, 2005). An early analyser of choice for native MS was the quadrupole, which consists of four parallel rods onto which direct current (DC) and RF potentials are applied to create a stable ion trajectory. However, the low RFs necessary to transmit high-mass ions (≈ 300 kHz) decrease quadrupole mass resolution (Collings and Douglas, 1997). Today quadrupoles are commonly employed as an ion filter prior to downstream mass analysis by an analyser with higher resolving power, as in the hybrid QToF (Figure **1.5**) (Sobott et al., 2002). The quadrupole can be configured to transmit effectively all ions, or to allow only a very narrow m/z window to pass through undeflected for selective interrogation in subsequent stages of the instrument (Hilton and Benesch, 2012).

The Time-of-Flight (ToF) mass analyser is popular in native MS because it can in theory report on unlimited m/z, with resolution that is not diminished by low signal intensity and only slightly lessened at high m/z (Lossl et al., 2014). Ions from a

continuous beam are collected and pulsed orthogonally into the ToF analyser (Coles and Guilhaus, 1993). To correct for any differences in kinetic energy ions with the same m/z may have acquired through their trajectories, an ion mirror ('reflectron') at the base of the ToF decelerates the ions before returning them toward the detector (typically a micro-channel plate detector (Fraser, 2002)). An ion with the same m/z as another, but greater kinetic energy, will penetrate the reflectron further, such that the two arrive at the detector closer to the same time. This time t taken to arrive at the detector is used to calculate m/z according to the relationship:

$$\frac{m}{z} = \frac{2eV}{d^2}t^2 \tag{1.1}$$

Where e is the elementary charge, V the electric potential, and d the length of the drift region within the ToF.

The experimentally obtained mass resolution (calculated using the peak full-width at half-maximum intensity, FWHM) depends on a range of factors both external and inherent to the mass spectrometer (Lossl et al., 2014). Externally, sample quality is critical, particularly removal of as much salt as possible from the buffer conditions (for cases where salt is desired or cannot be eliminated, improving the salt tolerance of native MS is an emerging area of study (Susa et al., 2017; Clarke and Campopiano, 2015)). Variables affecting resolution that are inherent to instrumentation include source clean-up and transmission abilities, space-charge effects, and ion dispersion (Lossl et al., 2014). If we assume high sample quality, the resolution of the QToF is sufficient for many native MS applications, allowing clear separation in m/z between peaks of interest. However, protein complexes very close in mass (i.e., unbound and bound states with a small ligand) or highly heterogeneous systems (i.e., heavily glycosylated or polydisperse proteins) may not be fully assignable

in QToF mass spectra due to peak overlap. For such cases, we often turn to the QExactive model (Thermo Fisher Scientific) featuring an Orbitrap mass analyser, which routinely yields peak FWHM up to 4 times smaller than the ToF (Rose et al., 2012; Lossl et al., 2014).

Rather than relying on the time to reach a detector, the Orbitrap confines ions into an orbital trajectory around a spindle electrode, and the ions undergo oscillations parallel to the spindle in addition to their radial motion. The frequency of an ion's oscillation is related to its m/z ratio. Image currents induced by the ions are converted into a mass spectrum using a fast Fourier transform (FFT) (Hu et al., 2005). The outcome is independent of any ion spatial dispersion, part of the reason it can achieve superior mass resolution compared to the ToF. Resolution is limited by the imperfection of the vacuum, since collision with background gas will deflect ions as they oscillate, leading to faster decay of transient signals at higher pressures.

Mass spectrometers with Orbitrap analyzers such as the QExactive have only recently been adapted for the transmission and detection of large macromolecular ions, as discussed and applied in Chapter 6 (Rose et al., 2012; Fort et al., 2017; van de Waterbeemd et al., 2017). While the improvement in mass resolution is an advantage of the QExactive, it has not yet been coupled to size measurement by ion mobility (though relative size measurement by transient signal decay rate is incipient (Sanders et al., 2018)). The QExactive transmits across a broad m/z range with less fidelity than the QToF, and also presents occasional discrepancies in the maintenance of small, noncovalently bound ligands. This is likely because the QExactive is built for more effective desolvation in the source than the QToF, and the balance between desolvation and dissociation is very fine (Liu et al., 2009). The choice among available MS instrumentation for a given biological question therefore depends on a range of considerations in addition to expected resolution.

1.5.4 Interrogating noncovalent complexes

To gain insight into the composition and topology of noncovalent protein complexes, several methods have been developed to activate and disrupt them during the native MS experiment. The most common approach, and the one employed in this work, is collision-induced dissociation (CID) (Sleno and Volmer, 2004; Benesch et al., 2007). Ions are accelerated into a collision cell, gaining kinetic energy which is converted into internal modes (vibrational and rotational) upon collisions with neutral gas, constituting a slow heating. Internal energy is proportional to an ion's charge and to the number of collisions it experiences (typically tens of thousands for a macromolecular complex over the tens to hundreds of microseconds spent in the cell (Benesch et al., 2007; Benesch, 2009)), which can be modulated by changing the acceleration voltage and gas pressure or size (argon is common; SF_6, N_2, Xe are also used). Activation initially prompts small conformational perturbations and is useful for stripping away residual adducts, improving resolution. Further activation causes local unfolding, and charge then migrates to the exposed surface area to minimize Coulombic repulsion. This induces the subunit to continue to unfold until its contacts to the complex are abolished and it dissociates, carrying charge disproportionate to its relative mass (Figure **1.7**) (Benesch, 2009).

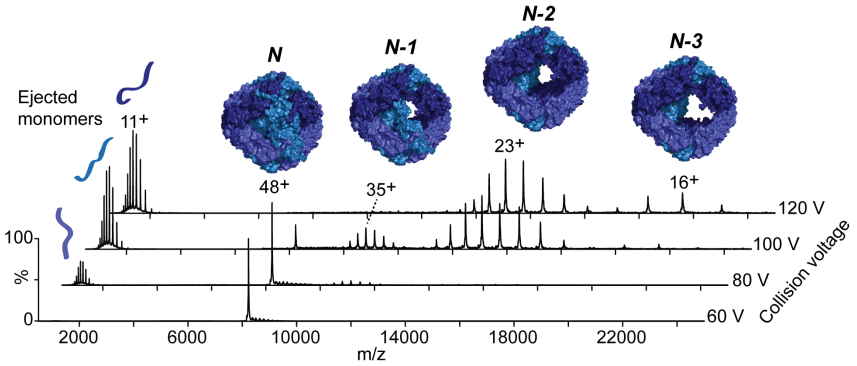


Figure 1.7. Collision-induced dissociation of a protein complex. The 48^+ charge state of *Mj*Hsp16.5 (number of subunits $N = 24$, PDB 1SHS) is selected in the quadrupole. As collision voltage is increased, subunits unfold and eject from the oligomer sequentially, creating stripped oligomers carrying lower average charge, which increases peak separation. Three dissociation events are observed here. Data kindly provided by Shane Chandler.

Depending on a complex's size and the acceleration potentials available in an instrument, several such dissociation events can occur during a single traversing of a collision cell. Each event results in two products in the mass spectrum: an unfolded species at lower m/z, and a subunit-stripped population at higher m/z. Peaks for subunit-stripped populations are further separated than their pre-CID counterparts due to the reduced average charge (Figure **1.7**), facilitating mass assignments (Benesch et al., 2007). CID is useful for identifying subunit composition (Benesch et al., 2006) or assigning stoichiometries in cases where the intact mass spectrum features peak overlap too extensive to be directly interpretable, which is often the case for polydisperse sHsps (Aquilina et al., 2003). The Synapt G1 QToF contains two collision cells, the Trap and the Transfer (Figure **1.5**), enabling greater activation capacity than a single cell and the option of CID before or after ion mobility separation (see section 1.5.5) (Shepherd et al., 2015).

Quantifying binding affinities by native MS

An additional goal of noncovalent complex interrogation by native MS is often the measurement of binding affinities (Daniel et al., 2002; Ayed et al., 1998). This quantitative application requires correlating relative peak intensities in a mass spectrum to relative abundances in solution, and so we must consider, and if necessary correct for, instances where intensities and abundances might deviate. For ions whose masses or conformations differ widely, relative intensities can be distorted by differences in ionization, transmission, and MCP detector efficiencies (Benesch et al., 2007; Fraser, 2002). Much more common, however, is a situation involving similar masses and conformations where one wishes to evaluate binding between a protein and a ligand by titrating the ligand. Binding will be under-reported if the interaction is not maintained until detection, which can result from overly harsh

conditions in the source or in collision cells. Conversely, binding will be overstated if unbound ligands in solution stochastically occupy the same nESI droplet as single protein molecules, creating 'nonspecific' interactions that persist as droplets undergo evaporation and fission. These are indistinguishable in the data from valid binding. Nonspecifics are increasingly likely with climbing ligand concentration, particularly above ≈50 μM (Benesch et al., 2007).

A number of strategies have been devised to address these possibilities and bring native MS binding affinities into good agreement with solution measurements. Firstly, one can take steps to preserve specific interactions and minimize nonspecifics during the experiment. Introducing neutral solvent vapour (i.e. acetonitrile) into the nESI environment reduces average charge states, leading to less disruption of complexes, since activation is a product of potential and charge (Hopper et al., 2012). Introducing additives more volatile than the ligand (i.e. imidazole) into the sample or the source can also preserve noncovalent complexes through a proposed evaporative cooling mechanism (Sun et al., 2007a; Bagal et al., 2009). Enabling post-hoc mathematical correction for nonspecifics can involve: including a reference protein or ligand in the sample (Sun et al., 2007b); confirming the number of specific binding sites by another method (Shimon et al., 2010); performing an analogous titration with a non-binding control (Hilton et al., 2013); or using relative rather than absolute intensities, if two specific ligands are known and introduced in competition (Kozelka, 2011). Corrections in this thesis are noted where relevant, commonly involving both acetonitrile vapour and control titrations.

1.5.5 Ion mobility

Coupling ion mobility spectrometry (IMS, herein IM) to MS introduces orthogonal ion separation on the basis of size rather than mass, which can help elucidate pro-

tein conformations and complex architectures. Several types of IM instruments are commercially available, all based on differential transport through an electric field (Kanu et al., 2008; May and McLean, 2015; Ruotolo et al., 2008). The simplest instrumentation, a linear drift tube, involves constant low electric field strength and a buffer gas. Ion motion through the mobility cell is propelled by the field and interrupted by collisions with the gas, which impede larger species more than smaller ones (May and McLean, 2015). The time an ion requires to traverse the cell (arrival time) is measured and directly related to its collision cross-section (CCS), which can be thought of as being similar to a rotationally averaged projected area (Marklund et al., 2015).

The work in this thesis relies on the traveling-wave drift tube (TWIMS), which consists of a stacked ring ion guide with a roving DC voltage applied between successive ring pairs, creating potential hills that propel ions forward with compensatory impediment by the buffer gas (Figure **1.8**). Through manipulating the wave heights and velocities, TWIMS can be tuned for optimal separation of ions with similar CCSs (Ruotolo et al., 2008; Lanucara et al., 2014; Goth and Pagel, 2017). However, size measurements cannot be directly calculated from arrival times, relying instead on comparison to protein standards with similar mobilities. The CCS values of these standards have been empirically determined using a linear drift tube, and are measured by TWIMS under identical mobility cell conditions to the unknown in order to construct a calibration curve (Michaelevski et al., 2010; Bush et al., 2010).

A variety of uses for IM-MS toward biological macromolecules have been demonstrated. IM data can, for example, be applied in the construction of quaternary models for protein complex topologies (Ruotolo et al., 2008; Marklund et al., 2015; Politis et al., 2010); report on conformational heterogeneity (Maurer et al., 2015) and monitor conformational changes upon ligand binding (Scott et al., 2015); and

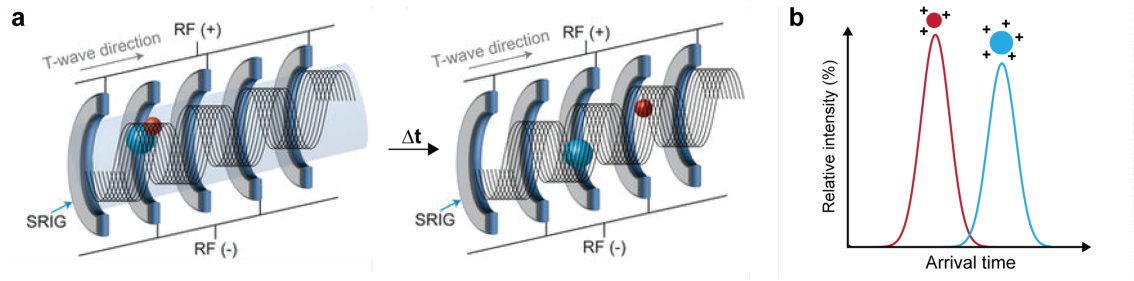


Figure 1.8. Travelling wave ion mobility spectrometry (TWIMS). a. A travelling voltage is applied to a stacked ring ion guide (SRIG), propelling ions through the cell at a speed determined by their size-to-charge ratio. The larger and more highly charged ion (blue) rolls over the waves, increasing its arrival time (**b**) compared to a small ion with lower charge (red). Panel **a** from Lanucara et al., 2014.

facilitate quantitative measurements by allowing relative abundances to be disentangled when different species overlap in m/z (Hilton et al., 2013). CCS should always be interpreted in the context of charge state, because ions are sensitive to charge-dependent structural rearrangement (Jurneczko and Barran, 2011; Mehmood et al., 2015). Low charge states can manifest smaller CCSs than those predicted by crystal structures due to partial collapse of cavities (Jurneczko and Barran, 2011), whereas high charge states may reflect artificially extended conformations due to Coulombic repulsion (Borysik et al., 2015). However, provided care is taken during the IM experiment to minimize activating the ions, evidence suggests that CCSs predominantly reflect functionally relevant positions on the free-energy landscape (Chandler and Benesch, 2017).

1.5.6 Collision-induced unfolding

Using IM to monitor conformational changes in a protein as it is activated is an established method for investigating unfolding pathways and conformational stability (Dixit et al., 2018; Mehmood et al., 2015; Allison et al., 2015; Goth and Pagel, 2017). Collision-induced unfolding (CIU) involves recording IM-MS data along a discrete ramp of acceleration into the Trap collision cell. As regions of a protein begin to unfold, conformational changes are reflected in its arrival time distribution

in the subsequent IM cell, and a plot of activation against size is used to visualize stages of unfolding (Figure **1.9**).

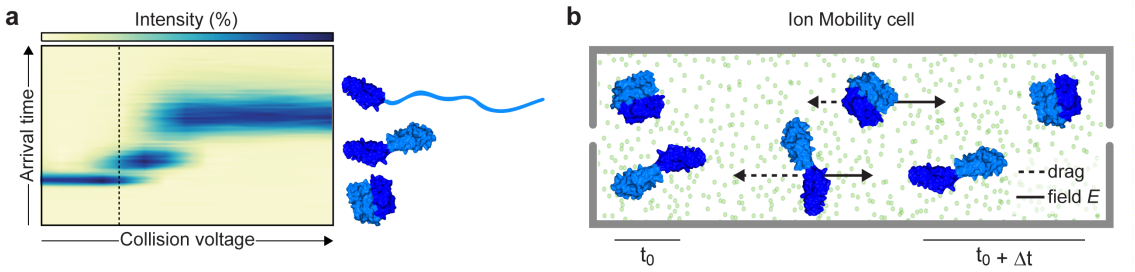


Figure 1.9. Collision-induced unfolding of a protein. a. An unfolding plot for a two-domain protein, where three states of increasing size are observed in the available energy regime, as measured by their arrival time distributions. **b.** Schematic of IM separation at the collision voltage designated by a dotted line in **a**, where the protein exists in two conformations following moderate activation in the Trap. The more compact state traverses the IM cell more quickly.

While the absolute energies required to prompt transitions are likely to be affected by the lack of solvent, functional protein trajectories have been induced by electric fields (Hekstra et al., 2016), and CIU trajectories can be exploited as fingerprints for comparison between analogous starting structures (Clemmer et al., 2017; Goth and Pagel, 2017). For multi-domain proteins, discrete stages along gas-phase unfolding pathways have been shown to correlate with the unfolding trajectories of successive domains in solution (Eschweiler et al., 2017a; Zhong et al., 2014). Primary sequence variation impacts the stabilities of CIU intermediates (Eschweiler et al., 2017a), and differential stabilizing effects of endogenous ligands can also be resolved by this approach (Hopper and Oldham, 2009; Laganowsky et al., 2014; Niu and Ruotolo, 2015). It should be noted that without additional labelling strategies, unfolding regions cannot be assigned from the CIU plot (Figure **1.9** is purely illustrative); and that, as with non-activated CCS data, CIU should be interpreted with respect to charge state, since Coulombic frustration is the primary physical driver of the unfolding process. Thus, the ability to probe the unfolding pathway and stability of multiple charge states of a protein represents the opportunity to access alternative energetic pathways (Chandler and Benesch, 2017). An additional

advantage of the approach is that, with the capabilities of resolving lowly populated species and selecting them in the quadrupole, even weak-affinity complexes can be interrogated individually.

1.6 Macromolecular X-ray crystallography

We can trace the majority of collective knowledge about molecular level protein structure and interface contacts to macromolecular X-ray crystallography (MX). The technique relies on the organization of many identical copies of a protein (or protein complex) into a highly ordered crystal lattice, which then amplifies the regular diffraction of incident X-rays by electrons. This generates a sampling of the Fourier transform of the electron density representing the simplest repeating component in the crystal, the unit cell (Figure **1.10a**). By inverting the Fourier transform, the crystallographer can generate an electron density map and build a model into it, using her knowledge of the components of the crystal.

Homogeneity – a pure sample, a single proteoform, a single stoichiometry – is critical for obtaining a crystal that will diffract well enough to yield a workable dataset, and indeed is the determining factor in whether a protein will crystallize in the first instance (Sherwood and Cooper, 2015). Thus sHsps may not seem an ideal system to tackle crystallographically, since they contain flexible regions and commonly adopt polydisperse quaternary assemblies. However, as discussed in section 1.2.3 on sHsp structure, selective interrogation of highly polydisperse members of the family has led to several models that allow examination of ACD tertiary structure and sHsp interfaces in detail (Laganowsky et al., 2010; Hochberg et al., 2014, 2018; Basha et al., 2012). Strategic X-ray approaches continue to yield valuable insight into human sHsp organization and function (Sluchanko et al., 2017).

1.6.1 X-ray diffraction and phasing

Following identification of a construct and a set of conditions amenable to reproducible crystal growth, the path to a structural model involves several further steps. Data is usually collected under cryogenic conditions to reduce radiation damage (Garman and Nave, 2009), so crystals must be gently isolated and cooled to ≈ 100K, typically in the presence of a vitrifying cryoprotectant such as glycerol (McFerrin and Snell, 2002). Because X-ray wavelengths are comparable to inter-atomic distances, an X-ray beam is focused onto the crystal, usually at a synchrotron light source where brighter beams are available compared to in-house X-ray sources. Opposite the crystal is a detector, which records successive diffraction patterns as the crystal is rotated in the beam.

Mathematically, diffraction of a three-dimensional lattice in real space produces another three-dimensional lattice in Fourier, or reciprocal, space (Sherwood and Cooper, 2015). In practical application to a protein lattice, diffraction of X-rays gives a representation of the macromolecular electron density in reciprocal space. It is not a continuous representation, instead being sampled only at points of constructive interference of the X-rays according to Bragg's law (Figure **1.10b-c**) (Bragg, 1956). The position of each 'Bragg peak' corresponds to an index (*h,k,l*) where *hkl* are sets of parallel planes intersecting the lattice, thereby encoding the coordinates of the unit cell (Figure **1.10a**). The wavelength is set at the X-ray source, and peak intensities relate to diffracted wave amplitudes, which derive from the contributions to diffraction from all atoms in their path. The phases of the waves at each Bragg peak, however, are not recorded in a typical experiment. Solving the phases of a set of reflections from a crystal form is necessary to calculate the electron density (Sherwood and Cooper, 2015). If the target structure is very similar to an available structure, the available structure can often be used as a model to closely estimate

the unknown phases via a process called molecular replacement (MR) (Crowther and Blow, 1967). Alternatively, experimental phasing involves incorporation of one or more heavier atoms into the unit cell, whose signature diffraction patterns can then be used to infer initial phases for the target structure (Hendrickson et al., 1985; Beck et al., 2008).

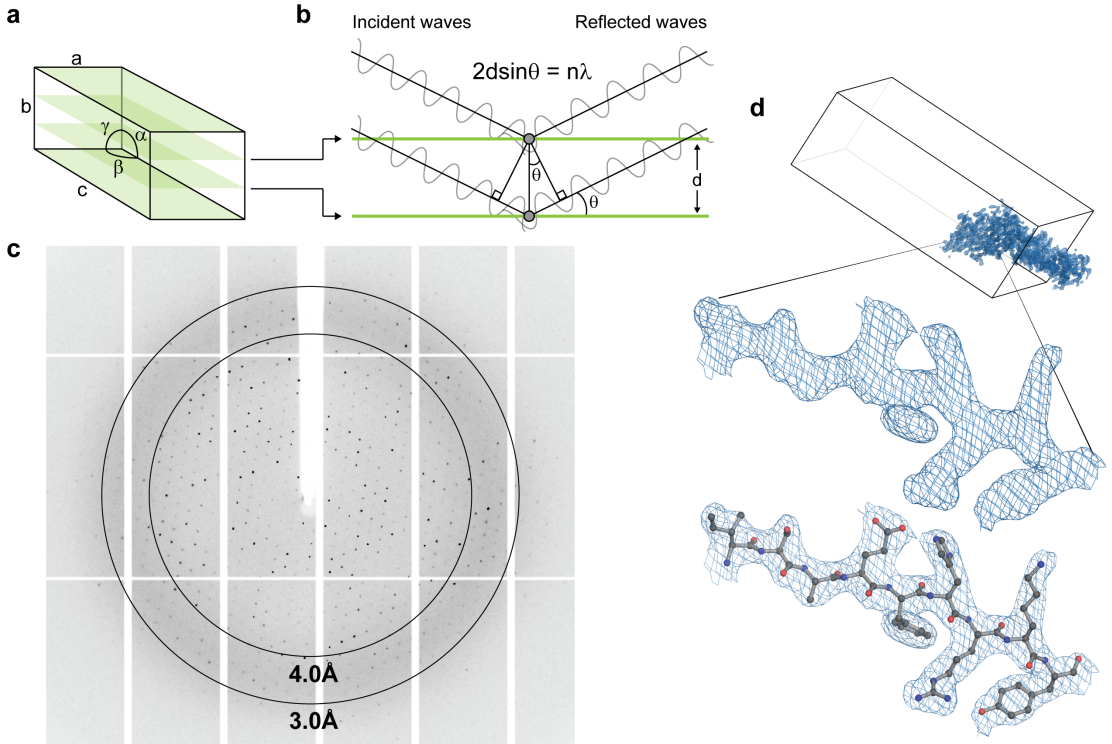


Figure 1.10. X-ray crystallography. **a.** The unit cell is characterized by dimensions *a, b, c* and angles *α, β, γ*, and intersected by planes *h,k,l* (one set of planes represented here). **b.** Bragg's law. Incident X-rays are scattered by electrons on two crystallographic planes. The waves are in phase and produce a diffraction spot (Bragg peak) if the additional length travelled by the second wave ($2d\sin\vartheta$) is an integer multiple of the wavelength (λ). **c.** Diffraction image from a 0.1 degree rotation in the X-ray beam of truncated αB-crystallin variant R116A. Resolution increases the further from the origin useful reflections are recorded. **d.** Electron density map for the simplest repeating component of αB-crystallin R116A (the asymmetric unit, ASU) in the unit cell (hexagonal space group $P6_3$). The ASU is repeated throughout the cell by symmetry operations. An example region of the density (medium resolution) is shown without and with the corresponding model, with clear backbone and side chain orientations. This structure is part of a manuscript in preparation by W. Struwe, B. Girling et al.

1.6.2 Model building, refinement, and interpretation

After assigning the symmetry and geometry of the unit cell; integrating the Bragg peak intensities and combining all observations of the same reflection across the dataset; and solving an initial set of phases, the crystallographer will have a crude

electron density map and usually with modern software algorithms, an incomplete model. The aim from here is to improve both by correctly placing features in the map, using the revised model to calculate new phases, identifying more features, and so on. Phase estimates can also be improved by averaging regions related by symmetry operators (Kleywegt, 1996) and flattening regions containing solvent (30-65% of the unit cell (Matthews, 1968), closer to the 70-80% water content of the crowded cytoplasmic environment than to dilute protein solutions (Fulton, 1982)). Restraints are introduced depending on the balance between observed and assumed knowledge: for example, lower resolution models are more tightly restrained to preferred bond geometries compared to higher resolution models, in which deviations from ideal geometries can be identified with more confidence. In addition to atomic coordinates, atomic occupancies (how often the atom is found in its prescribed location) and temperature factors (the three-dimensional spread of the atom's position) are adjusted (Murshudov et al., 2011). As the model improves, consequent sharpening of the density can enable the incorporation of details such as ligands and co-factors.

A number of validation metrics guide model building and refinement, and the process is halted when the R-factors, measures of the agreement between model and data, no longer decline. The R-factors are calculated as follows:

$$R = \frac{\sum||\mathbf{F_{obs}}| - |\mathbf{F_{calc}}||}{\sum|\mathbf{F_{obs}}|} \tag{1.2}$$

Where $\sum|\mathbf{F}|$ are the reflection amplitudes over all *hkl*. Amplitudes are summed over the observed reflections ($\sum|\mathbf{F_{obs}}|$) and either calculated reflections from the most recent refined model (to derive R_{work}), or a random subset of the data set aside before refinement (to derive R_{free}). With many parameters the data can be overfitted, making R_{work} artificially small; thus, R_{free} is a less biased measure of

the agreement between the model and the data, and acts to guard against such overfitting (Karplus and Diederichs, 2012). An R-factor of 0.0 indicates perfect agreement, and a random model will have R $\approx$ 0.6.

The final model should be evaluated with respect to the way it was constructed, its scoring in the validation tools provided by the Protein Data Bank (PDB), and how the authors' biological conclusions relate to the resolution. Resolution reports on the minimum spacing between *hkl* planes at which diffraction is distinct. At low resolution (>4Å), one can readily observe modes of assembly, interfaces, general folds and locations of α–helices. Approaching approximately 2.7Å resolution, β–sheets can be modelled and some side chain identities and orientations discerned (Figure **1.10d**). Between 2.7-2.0Å, side chain positions are more certain and ordered solvent molecules become visible. Sub-2.0Å resolution is considered high, and at 1.5Å individual atoms start to become distinct, with 'atomic' resolution generally meaning 1.2Å and below (Wlodawer et al., 2008).

Original X-ray crystallography results as well as structures reported in the literature comprise a partial but important component of this thesis. Although proteins are in some ways restricted in their crystallized state, being highly dynamic molecules in solution, the information X-ray structures provide on subunit contacts and domain architectures aids in the interpretation of orthogonal data.

1.7 Nuclear magnetic resonance spectroscopy

Ultimately, we strive toward an integrated approach to draw conclusions about biologically pertinent conformations and behaviours of the proteostasis machinery. To this end, through collaboration, nuclear magnetic resonance (NMR) spectroscopy data form crucial bridges to the narratives in Chapters 2 and 4. A thorough de-

scription of the theory underlying this technique requires substantive quantum mechanics, and is left outside the scope of the present work. However, even without this foundation one can develop an appreciation of the strengths of the method and a basic understanding of its application to biomacromolecules.

NMR spectroscopy relies on magnetization of certain nuclei that have an intrinsic angular momentum known as spin, and detection of their resultant energetic transitions (Wider, 1998). ^{1}H is one such magnetisable isotope; hence any sample can in principle give rise to a one-dimensional ^{1}H-NMR spectrum containing signal from all hydrogen atoms. The intensities of these signals report on dynamics, and they appear at specific chemical shifts which report on atomic environments (Kwan et al., 2011). NMR therefore offers a way of probing protein conformation in solution (an excellent complement to MS and MX, being gas- and pseudo-solid- phase methods).

For richer information, ^{15}N is commonly incorporated into proteins of interest to enable two-dimensional NMR. A typical 2D HSQC (heteronuclear single quantum coherence) spectrum (Figure **1.11**), viewed like a topographical map with ^{1}H and ^{15}N chemical shifts on the x- and y-axes and intensity collapsed into the z-dimension, contains one cross-peak for each ^{1}H-^{15}N bond, creating close to one peak per residue in the protein. The dispersion of these peaks is related to secondary structure content, and their positions and dimensions are sensitive to changes in local environment (Kwan et al., 2011). Thus, NMR can be used to rapidly assess conformational effects of changes such as residue substitution or modification, altered pH or temperature[1], or ligand binding. In order to localize these changes, it is often desirable to assign peaks to specific backbone residues of a protein. This requires triple resonance NMR via incorporation of another magnetisable isotope, ^{13}C. At this stage, if the

[1]Within reasonable bounds; at elevated pH or temperature, signal intensity is compromised by more rapid exchange of labile ^{1}H atoms with the solvent

structure is unknown, NMR-derived constraints can be used to construct a model in the form of a conformational ensemble. Additionally, magnetisation sequences can be crafted to interrogate atomic motions by transferring excitation on selective time scales, from the picosecond through second regimes, making NMR particularly powerful for describing protein motions (Bieri et al., 2011).

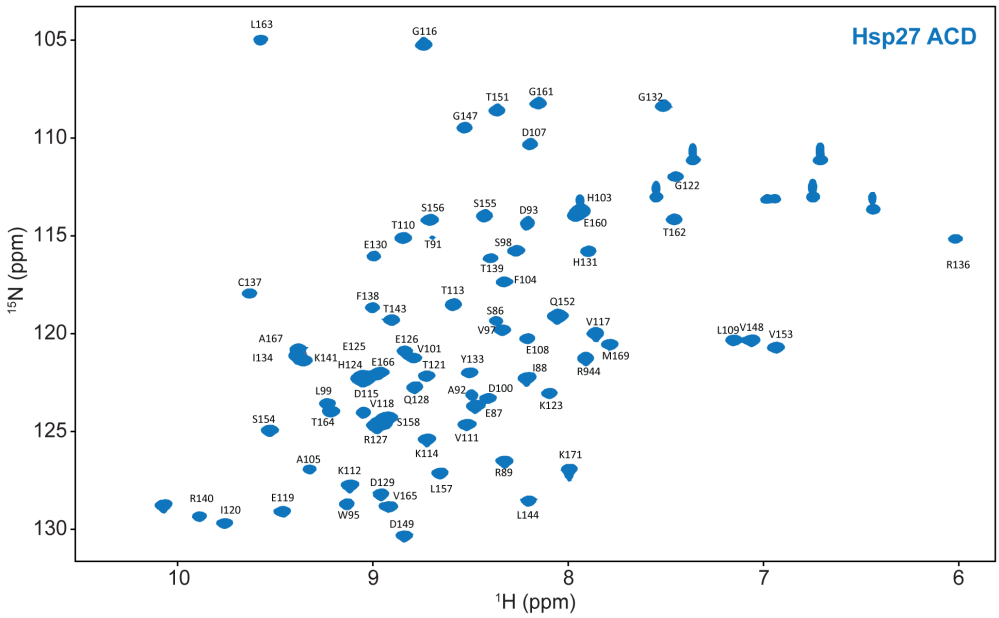


Figure 1.11. A typical NMR spectrum. a. 2D ^{1}H-^{15}N-HSQC spectrum of the isolated α-crystallin domain of Hsp27 (residues 84-171), with cross-peak labels from previously derived triple resonance assignments. Unlabelled peaks correspond to side chain amide bonds. Data kindly provided by Reid Alderson and Daisy Nicholls.

Perhaps the most substantial limitation of traditional NMR is signal deterioration with molecular weight. A protein's rate of tumbling affects the lifetime of its excited state upon interaction with the magnetic field, such that above approximately 25 kDa, structure determination is extremely challenging; and above 50 kDa, signal becomes broadened to a degree that renders it effectively invisible (Kwan et al., 2011). Several clever experimental approaches have been devised to study larger species in some detail (Ikeya et al., 2018); but conventional methods are used in this thesis. These provide insight into conformational flexibility of specific regions and of entire polypeptide chains, and aid in localizing sHsp client and intermolecular interactions.

References

The Big Book on Small Heat Shock Proteins, volume 8 of *Heat Shock Proteins*. Springer, 2015.

R. Aebersold and M. Mann. Mass spectrometry-based proteomics. *Nature*, 422(6928):198–207, 2003.

T. M. Allison, E. Reading, I. Liko, A. J. Baldwin, A. Laganowsky, and C. V. Robinson. Quantifying the stabilizing effects of protein-ligand interactions in the gas phase. *Nat Commun*, 6:8551, 2015.

J. A. Aquilina, J. L. Benesch, O. A. Bateman, C. Slingsby, and C. V. Robinson. Polydispersity of a mammalian chaperone: mass spectrometry reveals the population of oligomers in alphab-crystallin. *Proc Natl Acad Sci U S A*, 100(19):10611–6, 2003.

A. P. Arrigo. Human small heat shock proteins: protein interactomes of homo- and hetero-oligomeric complexes: an update. *FEBS Lett*, 587(13):1959–69, 2013.

A. E. Ashcroft. Recent developments in electrospray ionisation mass spectrometry: noncovalently bound protein complexes. *Nat Prod Rep*, 22(4):452–64, 2005.

A. Ayed, A. N. Krutchinsky, W. Ens, K. G. Standing, and H. W. Duckworth. Quantitative evaluation of protein-protein and ligand-protein equilibria of a large allosteric enzyme by electrospray ionization time-of-flight mass spectrometry. *Rapid Commun Mass Spectrom*, 12(7):339–44, 1998.

D. Bagal, E. N. Kitova, L. Liu, A. El-Hawiet, P. D. Schnier, and J. S. Klassen. Gas phase stabilization of noncovalent protein complexes formed by electrospray ionization. *Anal Chem*, 81(18):7801–6, 2009.

R. Bakthisaran, R. Tangirala, and M. Rao Ch. Small heat shock proteins: Role in cellular functions and pathology. *Biochim Biophys Acta*, 1854(4):291–319, 2015.

A. J. Baldwin, G. R. Hilton, H. Lioe, C. Bagneris, J. L. Benesch, and L. E. Kay. Quaternary dynamics of alphab-crystallin as a direct consequence of localised tertiary fluctuations in the c-terminus. *J Mol Biol*, 413(2):310–20, 2011a.

A. J. Baldwin, H. Lioe, G. R. Hilton, L. A. Baker, J. L. Rubinstein, L. E. Kay, and J. L. Benesch. The polydispersity of alphab-crystallin is rationalized by an interconverting polyhedral architecture. *Structure*, 19(12):1855–63, 2011b.

N. P. Barrera, N. Di Bartolo, P. J. Booth, and C. V. Robinson. Micelles protect membrane complexes from solution to vacuum. *Science*, 321(5886):243–6, 2008.

E. Basha, H. O'Neill, and E. Vierling. Small heat shock proteins and alpha-crystallins: dynamic proteins with flexible functions. *Trends Biochem Sci*, 37(3):106–17, 2012.

T. Beck, A. Krasauskas, T. Gruene, and G. M. Sheldrick. A magic triangle for experimental phasing of macromolecules. *Acta Crystallogr D Biol Crystallogr*, 64(Pt 11):1179–82, 2008.

G. Ben-Nissan and M. Sharon. Capturing protein structural kinetics by mass spectrometry. *Chem Soc Rev*, 40(7):3627–37, 2011.

J. L. Benesch. Collisional activation of protein complexes: picking up the pieces. *J Am Soc Mass Spectrom*, 20(3):341–8, 2009.

J. L. Benesch, J. A. Aquilina, B. T. Ruotolo, F. Sobott, and C. V. Robinson. Tandem mass spectrometry reveals the quaternary organization of macromolecular assemblies. *Chem Biol*, 13 (6):597–605, 2006.

J. L. Benesch, B. T. Ruotolo, D. A. Simmons, and C. V. Robinson. Protein complexes in the gas phase: technology for structural genomics and proteomics. *Chem Rev*, 107(8):3544–67, 2007.

D. R. Benjamin, C. V. Robinson, J. P. Hendrick, F. U. Hartl, and C. M. Dobson. Mass spectrometry of ribosomes and ribosomal subunits. *Proc Natl Acad Sci U S A*, 95(13):7391–5, 1998.

F. Bennardini, A. Wrzosek, and M. Chiesi. Alpha b-crystallin in cardiac tissue. association with actin and desmin filaments. *Circ Res*, 71(2):288–94, 1992.

M. Bieri, A. H. Kwan, M. Mobli, G. F. King, J. P. Mackay, and P. R. Gooley. Macromolecular nmr spectroscopy for the non-spectroscopist: beyond macromolecular solution structure determination. *FEBS J*, 278(5):704–15, 2011.

W. C. Boelens, M. A. M. Van Boekel, and W. W. De Jong. Hspb3, the most deviating of the six known human small heat shock proteins. *Biochimica Et Biophysica Acta-Protein Structure and Molecular Enzymology*, 1388(2):513–516, 1998.

E. Boeri Erba and C. Petosa. The emerging role of native mass spectrometry in characterizing the structure and dynamics of macromolecular complexes. *Protein Sci*, 24(8):1176–92, 2015.

A. J. Borysik, D. Kovacs, M. Guharoy, and P. Tompa. Ensemble methods enable a new definition for the solution to gas-phase transfer of intrinsically disordered proteins. *J Am Chem Soc*, 137 (43):13807–17, 2015.

M. P. Bova, H. S. McHaourab, Y. Han, and B. K. Fung. Subunit exchange of small heat shock proteins. analysis of oligomer formation of alphaa-crystallin and hsp27 by fluorescence resonance energy transfer and site-directed truncations. *J Biol Chem*, 275(2):1035–42, 2000.

L. Bragg. The diffraction of x-rays. *Br J Radiol*, 29(339):121–6, 1956.

K. Breuker and F. W. McLafferty. Stepwise evolution of protein native structure with electrospray into the gas phase, 10(-12) to 10(2) s. *Proc Natl Acad Sci U S A*, 105(47):18145–52, 2008.

B. Bukau, J. Weissman, and A. Horwich. Molecular chaperones and protein quality control. *Cell*, 125(3):443–451, 2006.

M. F. Bush, Z. Hall, K. Giles, J. Hoyes, C. V. Robinson, and B. T. Ruotolo. Collision cross sections of proteins and their complexes: a calibration framework and database for gas-phase structural biology. *Anal Chem*, 82(22):9557–65, 2010.

J. A. Carver, H. Ecroyd, R. J. W. Truscott, D. C. Thorn, and C. Holt. Proteostasis and the regulation of intra- and extracellular protein aggregation by atp-independent molecular chaperones: Lens alpha-crystallins and milk caseins. *Accounts of Chemical Research*, 51(3):745–752, 2018.

S. A. Chandler and J. L. Benesch. Mass spectrometry beyond the native state. *Curr Opin Chem Biol*, 42:130–137, 2017.

I. V. Chernushevich and B. A. Thomson. Collisional cooling of large ions in electrospray mass spectrometry. *Anal Chem*, 76(6):1754–60, 2004.

F. Chiti and C. M. Dobson. Protein misfolding, functional amyloid, and human disease. *Annual Review of Biochemistry*, 75:333–366, 2006.

S. K. Chowdhury, V. Katta, and B. T. Chait. Probing conformational-changes in proteins by mass-spectrometry. *Journal of the American Chemical Society*, 112(24):9012–9013, 1990.

D. J. Clarke and D. J. Campopiano. Desalting large protein complexes during native electrospray mass spectrometry by addition of amino acids to the working solution. *Analyst*, 140(8):2679–86, 2015.

D. E. Clemmer, D. H. Russell, and E. R. Williams. Characterizing the conformationome: Toward a structural understanding of the proteome. *Acc Chem Res*, 50(3):556–560, 2017.

J. Coles and M. Guilhaus. Orthogonal acceleration - a new direction for time-of-flight mass-spectrometry - fast, sensitive mass analysis for continuous ion sources. *Trac-Trends in Analytical Chemistry*, 12(5):203–213, 1993.

B. A. Collings and D. J. Douglas. An extended mass range quadrupole for electrospray mass spectrometry. *International Journal of Mass Spectrometry and Ion Processes*, 162(1-3):121–127, 1997.

R. A. Crowther and D. M. Blow. A method of positioning a known molecule in an unknown crystal structure. *Acta Crystallographica*, 23:544–, 1967.

J. M. Daniel, S. D. Friess, S. Rajagopalan, S. Wendt, and R. Zenobi. Quantitative determination of noncovalent binding interactions using soft ionization mass spectrometry. *International Journal of Mass Spectrometry*, 216(1):1–27, 2002.

J. F. de la Mora. Electrospray ionization of large multiply charged species proceeds via dole's charged residue mechanism. *Analytica Chimica Acta*, 406(1):93–104, 2000.

J. den Engelsman, S. Boros, P. Y. Dankers, B. Kamps, W. T. Vree Egberts, C. S. Bode, L. A. Lane, J. A. Aquilina, J. L. Benesch, C. V. Robinson, W. W. de Jong, and W. C. Boelens. The small heat-shock proteins hspb2 and hspb3 form well-defined heterooligomers in a unique 3 to 1 subunit ratio. *J Mol Biol*, 393(5):1022–32, 2009.

I. Dimauro, A. Antonioni, N. Mercatelli, and D. Caporossi. The role of alphab-crystallin in skeletal and cardiac muscle tissues. *Cell Stress Chaperones*, 2017.

S. M. Dixit, D. A. Polasky, and B. T. Ruotolo. Collision induced unfolding of isolated proteins in the gas phase: past, present, and future. *Curr Opin Chem Biol*, 42:93–100, 2018.

P. Doran, J. Gannon, K. O'Connell, and K. Ohlendieck. Aging skeletal muscle shows a drastic increase in the small heat shock proteins alphab-crystallin/hspb5 and cvhsp/hspb7. *Eur J Cell Biol*, 86(10):629–40, 2007.

C. M. Dreiza, P. Komalavilas, E. J. Furnish, C. R. Flynn, M. R. Sheller, C. C. Smoke, L. B. Lopes, and C. M. Brophy. The small heat shock protein, hspb6, in muscle function and disease. *Cell Stress Chaperones*, 15(1):1–11, 2010.

J. D. Eschweiler, R. Kerr, J. Rabuck-Gibbons, and B. T. Ruotolo. Sizing up protein-ligand complexes: The rise of structural mass spectrometry approaches in the pharmaceutical sciences. *Annu Rev Anal Chem (Palo Alto Calif)*, 10(1):25–44, 2017a.

J. D. Eschweiler, R. M. Martini, and B. T. Ruotolo. Chemical probes and engineered constructs reveal a detailed unfolding mechanism for a solvent-free multidomain protein. *J Am Chem Soc*, 139(1):534–540, 2017b.

J. B. Fenn, M. Mann, C. K. Meng, S. F. Wong, and C. M. Whitehouse. Electrospray ionization for mass spectrometry of large biomolecules. *Science*, 246(4926):64–71, 1989.

M. C. Fitzgerald, I. Chernushevich, K. G. Standing, C. P. Whitman, and S. B. Kent. Probing the oligomeric structure of an enzyme by electrospray ionization time-of-flight mass spectrometry. *Proc Natl Acad Sci U S A*, 93(14):6851–6, 1996.

J. M. Fontaine, X. Sun, R. Benndorf, and M. J. Welsh. Interactions of hsp22 (hspb8) with hsp20, alphab-crystallin, and hspb3. *Biochem Biophys Res Commun*, 337(3):1006–11, 2005.

K. L. Fort, M. van de Waterbeemd, D. Boll, M. Reinhardt-Szyba, M. E. Belov, E. Sasaki, R. Zschoche, D. Hilvert, A. A. Makarov, and A. J. R. Heck. Expanding the structural analysis capabilities on an orbitrap-based mass spectrometer for large macromolecular complexes. *Analyst*, 143(1):100–105, 2017.

G. W. Fraser. The ion detection efficiency of microchannel plates (mcps). *International Journal of Mass Spectrometry*, 215(1-3):13–30, 2002.

K. L. Friedrich, K. C. Giese, N. R. Buan, and E. Vierling. Interactions between small heat shock protein subunits and substrate in small heat shock protein-substrate complexes. *J Biol Chem*, 279(2):1080–9, 2004.

L. Fu and J. J. Liang. Detection of protein-protein interactions among lens crystallins in a mammalian two-hybrid system assay. *J Biol Chem*, 277(6):4255–60, 2002.

A. B. Fulton. How crowded is the cytoplasm. *Cell*, 30(2):345–347, 1982.

E. F. Garman and C. Nave. Radiation damage in protein crystals examined under various conditions by different methods. *Journal of Synchrotron Radiation*, 16:129–132, 2009.

C. Garrido, C. Paul, R. Seigneuric, and H. H. Kampinga. The small heat shock proteins family: the long forgotten chaperones. *Int J Biochem Cell Biol*, 44(10):1588–92, 2012.

N. Golenhofen, P. Htun, W. Ness, R. Koob, W. Schaper, and D. Drenckhahn. Binding of the stress protein alpha b-crystallin to cardiac myofibrils correlates with the degree of myocardial damage during ischemia/reperfusion in vivo. *J Mol Cell Cardiol*, 31(3):569–80, 1999.

N. Golenhofen, M. D. Perng, R. A. Quinlan, and D. Drenckhahn. Comparison of the small heat shock proteins alphab-crystallin, mkbp, hsp25, hsp20, and cvhsp in heart and skeletal muscle. *Histochem Cell Biol*, 122(5):415–25, 2004.

M. Goth and K. Pagel. Ion mobility-mass spectrometry as a tool to investigate protein-ligand interactions. *Anal Bioanal Chem*, 409(18):4305–4310, 2017.

Y. Hanazono, K. Takeda, T. Oka, T. Abe, T. Tomonari, N. Akiyama, Y. Aikawa, M. Yohda, and K. Miki. Nonequivalence observed for the 16-meric structure of a small heat shock protein, sphsp16.0, from schizosaccharomyces pombe. *Structure*, 21(2):220–8, 2013.

M. Haslbeck, T. Franzmann, D. Weinfurtner, and J. Buchner. Some like it hot: the structure and function of small heat-shock proteins. *Nature Structural Molecular Biology*, 12(10):842–846, 2005.

M. Haslbeck, J. Peschek, J. Buchner, and S. Weinkauf. Structure and function of alpha-crystallins: Traversing from in vitro to in vivo. *Biochim Biophys Acta*, 1860(1 Pt B):149–66, 2016.

A. J. Heck. Native mass spectrometry: a bridge between interactomics and structural biology. *Nat Methods*, 5(11):927–33, 2008.

M. Y. Hein, N. C. Hubner, I. Poser, J. Cox, N. Nagaraj, Y. Toyoda, I. A. Gak, I. Weisswange, J. Mansfeld, F. Buchholz, A. A. Hyman, and M. Mann. A human interactome in three quantitative dimensions organized by stoichiometries and abundances. *Cell*, 163(3):712–23, 2015.

M. Heirbaut, F. Lermyte, E. M. Martin, S. Beelen, F. Sobott, S. V. Strelkov, and S. D. Weeks. Specific sequences in the n-terminal domain of human small heat-shock protein hspb6 dictate preferential hetero-oligomerization with the orthologue hspb1. *J Biol Chem*, 292(24):9944–9957, 2017.

D. R. Hekstra, K. I. White, M. A. Socolich, R. W. Henning, V. Srajer, and R. Ranganathan. Electric-field-stimulated protein mechanics. *Nature*, 540(7633):400–405, 2016.

W. A. Hendrickson, J. L. Smith, and S. Sheriff. Direct phase determination based on anomalous scattering. *Methods in Enzymology*, 115:41–55, 1985.

R. H. Henning and Bjjm Brundel. Proteostasis in cardiac health and disease. *Nat Rev Cardiol*, 14 (11):637–653, 2017.

H. Hernandez and C. V. Robinson. Determining the stoichiometry and interactions of macromolecular assemblies from mass spectrometry. *Nat Protoc*, 2(3):715–26, 2007.

G. R. Hilton and J. L. Benesch. Two decades of studying non-covalent biomolecular assemblies by means of electrospray ionization mass spectrometry. *J R Soc Interface*, 9(70):801–16, 2012.

G. R. Hilton, G. K. Hochberg, A. Laganowsky, S. I. McGinnigle, A. J. Baldwin, and J. L. Benesch. C-terminal interactions mediate the quaternary dynamics of alphab-crystallin. *Philos Trans R Soc Lond B Biol Sci*, 368(1617):20110405, 2013.

M. S. Hipp, S. H. Park, and F. U. Hartl. Proteostasis impairment in protein-misfolding and -aggregation diseases. *Trends Cell Biol*, 24(9):506–14, 2014.

G. K. Hochberg and J. L. Benesch. Dynamical structure of alphab-crystallin. *Prog Biophys Mol Biol*, 115(1):11–20, 2014.

G. K. Hochberg, H. Ecroyd, C. Liu, D. Cox, D. Cascio, M. R. Sawaya, M. P. Collier, J. Stroud, J. A. Carver, A. J. Baldwin, C. V. Robinson, D. S. Eisenberg, J. L. Benesch, and A. Laganowsky. The structured core domain of alphab-crystallin can prevent amyloid fibrillation and associated toxicity. *Proc Natl Acad Sci U S A*, 111(16):E1562–70, 2014.

G. K. A. Hochberg, D. A. Shepherd, E. G. Marklund, I. Santhanagoplan, M. T. Degiacomi, A. Laganowsky, T. M. Allison, E. Basha, M. T. Marty, M. R. Galpin, W. B. Struwe, A. J. Baldwin, E. Vierling, and J. L. P. Benesch. Structural principles that enable oligomeric small heat-shock protein paralogs to evolve distinct functions. *Science*, 359(6378):930–935, 2018.

J. T. Hopper, K. Sokratous, and N. J. Oldham. Charge state and adduct reduction in electrospray ionization-mass spectrometry using solvent vapor exposure. *Anal Biochem*, 421(2):788–90, 2012.

J. T. S. Hopper and N. J. Oldham. Collision induced unfolding of protein ions in the gas phase studied by ion mobility-mass spectrometry: The effect of ligand binding on conformational stability. *Journal of the American Society for Mass Spectrometry*, 20(10):1851–1858, 2009.

J. Horwitz, M. P. Bova, L. L. Ding, D. A. Haley, and P. L. Stewart. Lens alpha-crystallin: function and structure. *Eye (Lond)*, 13 (Pt 3b):403–8, 1999.

S. A. Houck and J. I. Clark. Dynamic subunit exchange and the regulation of microtubule assembly by the stress response protein human alphab crystallin. *PLoS One*, 5(7):e11795, 2010.

Q. Hu, R. J. Noll, H. Li, A. Makarov, M. Hardman, and R. Graham Cooks. The orbitrap: a new mass spectrometer. *J Mass Spectrom*, 40(4):430–43, 2005.

A. T. Iavarone and E. R. Williams. Mechanism of charging and supercharging molecules in electrospray ionization. *J Am Chem Soc*, 125(8):2319–27, 2003.

T. Ikeya, D. Ban, D. Lee, Y. Ito, K. Kato, and C. Griesinger. Solution nmr views of dynamical ordering of biomacromolecules. *Biochim Biophys Acta*, 1862(2):287–306, 2018.

N. Inagaki, T. Hayashi, T. Arimura, Y. Koga, M. Takahashi, H. Shibata, K. Teraoka, T. Chikamori, A. Yamashina, and A. Kimura. Alpha b-crystallin mutation in dilated cardiomyopathy. *Biochem Biophys Res Commun*, 342(2):379–86, 2006.

N. Jaya, V. Garcia, and E. Vierling. Substrate binding site flexibility of the small heat shock protein molecular chaperones. *Proc Natl Acad Sci U S A*, 106(37):15604–9, 2009.

S. Jehle, B. S. Vollmar, B. Bardiaux, K. K. Dove, P. Rajagopal, T. Gonen, H. Oschkinat, and R. E. Klevit. N-terminal domain of alphab-crystallin provides a conformational switch for multimerization and structural heterogeneity. *Proc Natl Acad Sci U S A*, 108(16):6409–14, 2011.

L. Y. Juo, W. C. Liao, Y. L. Shih, B. Y. Yang, A. B. Liu, and Y. T. Yan. Hspb7 interacts with dimerized flnc and its absence results in progressive myopathy in skeletal muscles. *J Cell Sci*, 129(8):1661–70, 2016.

R. Juraschek, T. Dulcks, and M. Karas. Nanoelectrospray - more than just a minimized-flow electrospray ionization source. *Journal of the American Society for Mass Spectrometry*, 10(4): 300–308, 1999.

E. Jurneczko and P. E. Barran. How useful is ion mobility mass spectrometry for structural biology? the relationship between protein crystal structures and their collision cross sections in the gas phase. *Analyst*, 136(1):20–8, 2011.

V. Kakkar, M. Meister-Broekema, M. Minoia, S. Carra, and H. H. Kampinga. Barcoding heat shock proteins to human diseases: looking beyond the heat shock response. *Dis Model Mech*, 7 (4):421–34, 2014.

I. A. Kaltashov and S. J. Eyles. Studies of biomolecular conformations and conformational dynamics by mass spectrometry. *Mass Spectrom Rev*, 21(1):37–71, 2002.

I. A. Kaltashov and A. Mohimen. Estimates of protein surface areas in solution by electrospray ionization mass spectrometry. *Anal Chem*, 77(16):5370–9, 2005.

A. B. Kanu, P. Dwivedi, M. Tam, L. Matz, and Jr. Hill, H. H. Ion mobility-mass spectrometry. *J Mass Spectrom*, 43(1):1–22, 2008.

G. Kappe, W. C. Boelens, and W. W. de Jong. Why proteins without an alpha-crystallin domain should not be included in the human small heat shock protein family hspb. *Cell Stress Chaperones*, 15(4):457–61, 2010.

P. A. Karplus and K. Diederichs. Linking crystallographic model and data quality. *Science*, 336 (6084):1030–1033, 2012.

K. Kato, H. Shinohara, N. Kurobe, Y. Inaguma, K. Shimizu, and K. Ohshima. Tissue distribution and developmental profiles of immunoreactive alpha-b-crystallin in the rat determined with a sensitive immunoassay system. *Biochimica Et Biophysica Acta*, 1074(1):201–208, 1991.

K. Kato, S. Goto, Y. Inaguma, K. Hasegawa, R. Morishita, and T. Asano. Purification and characterization of a 20-kda protein that is highly homologous to alpha b crystallin. *J Biol Chem*, 269(21):15302–9, 1994.

V. Katta and B. T. Chait. Observation of the heme globin complex in native myoglobin by electrospray-ionization mass-spectrometry. *Journal of the American Chemical Society*, 113(22): 8534–8535, 1991.

L. Ke, R. A. Meijering, F. Hoogstra-Berends, K. Mackovicova, M. J. Vos, I. C. Van Gelder, R. H. Henning, H. H. Kampinga, and B. J. Brundel. Hspb1, hspb6, hspb7 and hspb8 protect against rhoa gtpase-induced remodeling in tachypaced atrial myocytes. *PLoS One*, 6(6):e20395, 2011.

P. Kebarle and U. H. Verkerk. Electrospray: from ions in solution to ions in the gas phase, what we know now. *Mass Spectrom Rev*, 28(6):898–917, 2009.

K. K. Kim, R. Kim, and S. H. Kim. Crystal structure of a small heat-shock protein. *Nature*, 394 (6693):595–9, 1998.

Y. E. Kim, M. S. Hipp, A. Bracher, M. Hayer-Hartl, and F. U. Hartl. Molecular chaperone functions in protein folding and proteostasis. *Annu Rev Biochem*, 82:323–55, 2013.

R. Klemenz, A. C. Andres, E. Frohli, R. Schafer, and A. Aoyama. Expression of the murine small heat-shock proteins hsp 25 and alpha-b crystallin in the absence of stress. *Journal of Cell Biology*, 120(3):639–645, 1993.

G. J. Kleywegt. Use of non-crystallographic symmetry in protein structure refinement. *Acta Crystallographica Section D-Biological Crystallography*, 52:842–857, 1996.

T. J. Koh and J. Escobedo. Cytoskeletal disruption and small heat shock protein translocation immediately after lengthening contractions. *Am J Physiol Cell Physiol*, 286(3):C713–22, 2004.

L. Konermann, A. D. Rodriguez, and J. Liu. On the formation of highly charged gaseous ions from unfolded proteins by electrospray ionization. *Anal Chem*, 84(15):6798–804, 2012.

L. Konermann, E. Ahadi, A. D. Rodriguez, and S. Vahidi. Unraveling the mechanism of electrospray ionization. *Anal Chem*, 85(1):2–9, 2013.

J. Kozelka. Evaluation of dissociation constants from competition binding experiments based on the relative binding ratio. *Anal Biochem*, 409(1):66–73, 2011.

T. Kriehuber, T. Rattei, T. Weinmaier, A. Bepperling, M. Haslbeck, and J. Buchner. Independent evolution of the core domain and its flanking sequences in small heat shock proteins. *FASEB J*, 24(10):3633–42, 2010.

A. R. Kumarapeli, K. Horak, and X. Wang. Protein quality control in protection against systolic overload cardiomyopathy: the long term role of small heat shock proteins. *Am J Transl Res*, 2 (4):390–401, 2010.

A. H. Kwan, M. Mobli, P. R. Gooley, G. F. King, and J. P. Mackay. Macromolecular nmr spectroscopy for the non-spectroscopist. *FEBS J*, 278(5):687–703, 2011.

J. Labbadia and R. I. Morimoto. The biology of proteostasis in aging and disease. *Annu Rev Biochem*, 84:435–64, 2015.

A. Laganowsky, J. L. Benesch, M. Landau, L. Ding, M. R. Sawaya, D. Cascio, Q. Huang, C. V. Robinson, J. Horwitz, and D. Eisenberg. Crystal structures of truncated alphaa and alphab crystallins reveal structural mechanisms of polydispersity important for eye lens function. *Protein Sci*, 19(5):1031–43, 2010.

A. Laganowsky, E. Reading, T. M. Allison, M. B. Ulmschneider, M. T. Degiacomi, A. J. Baldwin, and C. V. Robinson. Membrane proteins bind lipids selectively to modulate their structure and function. *Nature*, 510(7503):172–175, 2014.

F. Lanucara, S. W. Holman, C. J. Gray, and C. E. Eyers. The power of ion mobility-mass spectrometry for structural characterization and the study of conformational dynamics. *Nat Chem*, 6(4):281–94, 2014.

A. C. Leney and A. J. Heck. Native mass spectrometry: What is in the name? *J Am Soc Mass Spectrom*, 28(1):5–13, 2017.

J. Li, C. Santambrogio, S. Brocca, G. Rossetti, P. Carloni, and R. Grandori. Conformational effects in protein electrospray-ionization mass spectrometry. *Mass Spectrom Rev*, 35(1):111–22, 2016.

W. C. Liao, L. Y. Juo, Y. L. Shih, Y. H. Chen, and Y. T. Yan. Hspb7 prevents cardiac conduction system defect through maintaining intercalated disc integrity. *PLoS Genet*, 13(8):e1006984, 2017.

S. Lindquist. The heat-shock response. *Annu Rev Biochem*, 55:1151–91, 1986.

L. Liu, D. Bagal, E. N. Kitova, P. D. Schnier, and J. S. Klassen. Hydrophobic protein-ligand interactions preserved in the gas phase. *J Am Chem Soc*, 131(44):15980–1, 2009.

J. A. Loo. Electrospray ionization mass spectrometry: a technology for studying noncovalent macromolecular complexes. *International Journal of Mass Spectrometry*, 200(1-3):175–186, 2000.

K. Lorenzen, A. S. Olia, C. Uetrecht, G. Cingolani, and A. J. Heck. Determination of stoichiometry and conformational changes in the first step of the p22 tail assembly. *J Mol Biol*, 379(2):385–96, 2008.

P. Lossl, J. Snijder, and A. J. Heck. Boundaries of mass resolution in native mass spectrometry. *J Am Soc Mass Spectrom*, 25(6):906–17, 2014.

G. Lutsch, R. Vetter, U. Offhauss, M. Wieske, H. J. Grone, R. Klemenz, I. Schimke, J. Stahl, and R. Benndorf. Abundance and location of the small heat shock proteins hsp25 and alphab-crystallin in rat and human heart. *Circulation*, 96(10):3466–76, 1997.

E. G. Marklund, M. T. Degiacomi, C. V. Robinson, A. J. Baldwin, and J. L. Benesch. Collision cross sections for structural proteomics. *Structure*, 23(4):791–9, 2015.

M. Marvin, D. O'Rourke, T. Kurihara, C. E. Juliano, K. L. Harrison, and L. D. Hutson. Developmental expression patterns of the zebrafish small heat shock proteins. *Dev Dyn*, 237(2):454–63, 2008.

B. W. Matthews. Solvent content of protein crystals. *J Mol Biol*, 33(2):491–7, 1968.

M. M. Maurer, G. C. Donohoe, and S. J. Valentine. Advances in ion mobility-mass spectrometry instrumentation and techniques for characterizing structural heterogeneity. *Analyst*, 140(20): 6782–98, 2015.

J. C. May and J. A. McLean. Ion mobility-mass spectrometry: time-dispersive instrumentation. *Anal Chem*, 87(3):1422–36, 2015.

E. T. McDonald, M. Bortolus, H. A. Koteiche, and H. S. McHaourab. Sequence, structure, and dynamic determinants of hsp27 (hspb1) equilibrium dissociation are encoded by the n-terminal domain. *Biochemistry*, 51(6):1257–68, 2012.

M. B. McFerrin and E. H. Snell. The development and application of a method to quantify the quality of cryoprotectant solutions using standard area-detector x-ray images. *Journal of Applied Crystallography*, 35:538–545, 2002.

H. S. McHaourab, J. A. Godar, and P. L. Stewart. Structure and mechanism of protein stability sensors: chaperone activity of small heat shock proteins. *Biochemistry*, 48(18):3828–37, 2009.

S. Mehmood, T. M. Allison, and C. V. Robinson. Mass spectrometry of protein complexes: from origins to applications. *Annu Rev Phys Chem*, 66:453–74, 2015.

E. J. Mercer, Y. F. Lin, L. Cohen-Gould, and T. Evans. Hspb7 is a cardioprotective chaperone facilitating sarcomeric proteostasis. *Dev Biol*, 2018.

I. Michaelevski, N. Kirshenbaum, and M. Sharon. T-wave ion mobility-mass spectrometry: basic experimental procedures for protein complex analysis. *J Vis Exp*, (41), 2010.

S. B. Miller, A. Mogk, and B. Bukau. Spatially organized aggregation of misfolded proteins as cellular stress defense strategy. *J Mol Biol*, 427(7):1564–74, 2015.

A. Mogk, B. Bukau, and H. H. Kampinga. Cellular handling of protein aggregates by disaggregation machines. *Mol Cell*, 69(2):214–226, 2018.

F. F. Morelli, L. Mediani, L. Heldens, J. Bertacchini, I. Bigi, A. D. Carra, J. Vinet, and S. Carra. An interaction study in mammalian cells demonstrates weak binding of hspb2 to bag3, which is regulated by hspb3 and abrogated by hspb8. *Cell Stress Chaperones*, 22(4):531–540, 2017.

R. I. Morimoto and A. M. Cuervo. Proteostasis and the aging proteome in health and disease. *J Gerontol A Biol Sci Med Sci*, 69 Suppl 1:S33–8, 2014.

N. Mounier and A. P. Arrigo. Actin cytoskeleton and small heat shock proteins: how do they interact? *Cell Stress Chaperones*, 7(2):167–76, 2002.

G. N. Murshudov, P. Skubak, A. A. Lebedev, N. S. Pannu, R. A. Steiner, R. A. Nicholls, M. D. Winn, F. Long, and A. A. Vagin. Refmac5 for the refinement of macromolecular crystal structures. *Acta Crystallogr D Biol Crystallogr*, 67(Pt 4):355–67, 2011.

E. V. Mymrikov, A. S. Seit-Nebi, and N. B. Gusev. Heterooligomeric complexes of human small heat shock proteins. *Cell Stress Chaperones*, 17(2):157–69, 2012.

E. V. Mymrikov, M. Daake, B. Richter, M. Haslbeck, and J. Buchner. The chaperone activity and substrate spectrum of human small heat shock proteins. *J Biol Chem*, 292(2):672–684, 2017.

S. Nguyen and J. B. Fenn. Gas-phase ions of solute species from charged droplets of solutions. *Proc Natl Acad Sci U S A*, 104(4):1111–7, 2007.

S. Niu and B. T. Ruotolo. Collisional unfolding of multiprotein complexes reveals cooperative stabilization upon ligand binding. *Protein Sci*, 24(8):1272–81, 2015.

E. Nogales and S. H. Scheres. Cryo-em: A unique tool for the visualization of macromolecular complexity. *Mol Cell*, 58(4):677–89, 2015.

A. J. Painter, N. Jaya, E. Basha, E. Vierling, C. V. Robinson, and J. L. Benesch. Real-time monitoring of protein complexes reveals their quaternary organization and dynamics. *Chem Biol*, 15(3):246–53, 2008.

L. Pedro and R. J. Quinn. Native mass spectrometry in fragment-based drug discovery. *Molecules*, 21(8), 2016.

A. V. Pivovarova, N. A. Chebotareva, I. S. Chernik, N. B. Gusev, and D. I. Levitsky. Small heat shock protein hsp27 prevents heat-induced aggregation of f-actin by forming soluble complexes with denatured actin. *FEBS J*, 274(22):5937–48, 2007.

A. Politis, A. Y. Park, S. J. Hyung, D. Barsky, B. T. Ruotolo, and C. V. Robinson. Integrating ion mobility mass spectrometry with molecular modelling to determine the architecture of multiprotein complexes. *PLoS One*, 5(8):e12080, 2010.

K. Rajabi, A. E. Ashcroft, and S. E. Radford. Mass spectrometric methods to analyze the structural organization of macromolecular complexes. *Methods*, 89:13–21, 2015.

K. Richter, M. Haslbeck, and J. Buchner. The heat shock response: Life on the verge of death. *Molecular Cell*, 40(2):253–266, 2010.

R. J. Rose, E. Damoc, E. Denisov, A. Makarov, and A. J. Heck. High-sensitivity orbitrap mass analysis of intact macromolecular assemblies. *Nat Methods*, 9(11):1084–6, 2012.

B. T. Ruotolo, K. Giles, I. Campuzano, A. M. Sandercock, R. H. Bateman, and C. V. Robinson. Evidence for macromolecular protein rings in the absence of bulk water. *Science*, 310(5754): 1658–61, 2005.

B. T. Ruotolo, J. L. Benesch, A. M. Sandercock, S. J. Hyung, and C. V. Robinson. Ion mobility-mass spectrometry analysis of large protein complexes. *Nat Protoc*, 3(7):1139–52, 2008.

H. Saibil. Chaperone machines for protein folding, unfolding and disaggregation. *Nat Rev Mol Cell Biol*, 14(10):630–42, 2013.

S. Salinthone, M. Tyagi, and W. T. Gerthoffer. Small heat shock proteins in smooth muscle. *Pharmacol Ther*, 119(1):44–54, 2008.

J. D. Sanders, D. Grinfeld, K. Aizikov, A. Makarov, D. D. Holden, and J. S. Brodbelt. Determination of collision cross-sections of protein ions in an orbitrap mass analyzer. *Anal Chem*, 2018.

D. Scott, R. Layfield, and N. J. Oldham. Ion mobility-mass spectrometry reveals conformational flexibility in the deubiquitinating enzyme usp5. *Proteomics*, 15(16):2835–41, 2015.

A. S. Seit-Nebi, P. Datskevich, and N. B. Gusev. Commentary on paper: Small heat shock proteins and the cytoskeleton: An essential interplay for cell integrity? (wettstein et al.). *International Journal of Biochemistry Cell Biology*, 45(2):344–346, 2013.

D. A. Shepherd, M. T. Marty, K. Giles, A. J. Baldwin, and J. L. P. Benesch. Combining tandem mass spectrometry with ion mobility separation to determine the architecture of polydisperse proteins. *International Journal of Mass Spectrometry*, 377:663–671, 2015.

Dennis Sherwood and Jon Cooper. *Crystals, X-rays, and proteins : comprehensive protein crystallography*. Oxford University Press, Oxford, United Kingdom ; New York, NY, paperback edition. edition, 2015.

M. Shimizu, M. Tanaka, and Y. Atomi. Small heat shock protein alphab-crystallin controls shape and adhesion of glioma and myoblast cells in the absence of stress. *PLoS One*, 11(12):e0168136, 2016.

L. Shimon, M. Sharon, and A. Horovitz. A method for removing effects of nonspecific binding on the distribution of binding stoichiometries: application to mass spectroscopy data. *Biophys J*, 99(5):1645–9, 2010.

S. Simon, V. Dimitrova, B. Gibert, S. Virot, N. Mounier, M. Nivon, C. Kretz-Remy, V. Corset, P. Mehlen, and A. P. Arrigo. Analysis of the dominant effects mediated by wild type or r120g mutant of alphab-crystallin (hspb5) towards hsp27 (hspb1). *PLoS One*, 8(8):e70545, 2013.

L. Sleno and D. A. Volmer. Ion activation methods for tandem mass spectrometry. *J Mass Spectrom*, 39(10):1091–112, 2004.

N. N. Sluchanko, S. Beelen, A. A. Kulikova, S. D. Weeks, A. A. Antson, N. B. Gusev, and S. V. Strelkov. Structural basis for the interaction of a human small heat shock protein with the 14-3-3 universal signaling regulator. *Structure*, 25(2):305–316, 2017.

F. Sobott, H. Hernandez, M. G. McCammon, M. A. Tito, and C. V. Robinson. A tandem mass spectrometer for improved transmission and analysis of large macromolecular assemblies. *Anal Chem*, 74(6):1402–7, 2002.

E. M. Sontag, R. S. Samant, and J. Frydman. Mechanisms and functions of spatial protein quality control. *Annu Rev Biochem*, 86:97–122, 2017.

F. Stengel, A. J. Baldwin, A. J. Painter, N. Jaya, E. Basha, L. E. Kay, E. Vierling, C. V. Robinson, and J. L. Benesch. Quaternary dynamics and plasticity underlie small heat shock protein chaperone function. *Proc Natl Acad Sci U S A*, 107(5):2007–12, 2010.

A. Strauch and M. Haslbeck. The function of small heat-shock proteins and their implication in proteostasis. *Proteostasis*, 60(2):163–172, 2016.

Y. Sugiyama, A. Suzuki, M. Kishikawa, R. Akutsu, T. Hirose, M. M. Waye, S. K. Tsui, S. Yoshida, and S. Ohno. Muscle develops a specific form of small heat shock protein complex composed of mkbp/hspb2 and hspb3 during myogenic differentiation. *J Biol Chem*, 275(2):1095–104, 2000.

J. Sun, E. N. Kitova, and J. S. Klassen. Method for stabilizing protein-ligand complexes in nanoelectrospray ionization mass spectrometry. *Anal Chem*, 79(2):416–25, 2007a.

J. Sun, E. N. Kitova, N. Sun, and J. S. Klassen. Method for identifying nonspecific protein-protein interactions in nanoelectrospray ionization mass spectrometry. *Anal Chem*, 79(21):8301–11, 2007b.

A. C. Susa, Z. Xia, and E. R. Williams. Small emitter tips for native mass spectrometry of proteins and protein complexes from nonvolatile buffers that mimic the intracellular environment. *Anal Chem*, 89(5):3116–3122, 2017.

N. Tahallah, M. Pinkse, C. S. Maier, and A. J. Heck. The effect of the source pressure on the abundance of ions of noncovalent protein assemblies in an electrospray ionization orthogonal time-of-flight instrument. *Rapid Commun Mass Spectrom*, 15(8):596–601, 2001.

D. J. Tessier, P. Komalavilas, A. Panitch, L. Joshi, and C. M. Brophy. The small heat shock protein (hsp) 20 is dynamically associated with the actin cross-linking protein actinin. *J Surg Res*, 111(1):152–7, 2003.

T. M. Treweek, S. Meehan, H. Ecroyd, and J. A. Carver. Small heat-shock proteins: important players in regulating cellular proteostasis. *Cell Mol Life Sci*, 72(3):429–451, 2015.

A. Unger, L. Beckendorf, P. Bohme, R. Kley, M. von Frieling-Salewsky, H. Lochmuller, R. Schroder, D. O. Furst, M. Vorgerd, and W. A. Linke. Translocation of molecular chaperones to the titin springs is common in skeletal myopathy patients and affects sarcomere function. *Acta Neuropathol Commun*, 5(1):72, 2017.

M. van de Waterbeemd, K. L. Fort, D. Boll, M. Reinhardt-Szyba, A. Routh, A. Makarov, and A. J. Heck. High-fidelity mass analysis unveils heterogeneity in intact ribosomal particles. *Nat Methods*, 14(3):283–286, 2017.

R. L. van Montfort, E. Basha, K. L. Friedrich, C. Slingsby, and E. Vierling. Crystal structure and assembly of a eukaryotic small heat shock protein. *Nat Struct Biol*, 8(12):1025–30, 2001.

M. J. Vos, B. Kanon, and H. H. Kampinga. Hspb7 is a sc35 speckle resident small heat shock protein. *Biochim Biophys Acta*, 1793(8):1343–53, 2009.

E. R. Waters. The evolution, function, structure, and expression of the plant shsps. *J Exp Bot*, 64 (2):391–403, 2013.

S. D. Weeks, E. V. Baranova, M. Heirbaut, S. Beelen, A. V. Shkumatov, N. B. Gusev, and S. V. Strelkov. Molecular structure and dynamics of the dimeric human small heat shock protein hspb6. *J Struct Biol*, 185(3):342–54, 2014.

S. D. Weeks, L. K. Muranova, M. Heirbaut, S. Beelen, S. V. Strelkov, and N. B. Gusev. Characterization of human small heat shock protein hspb1 alpha-crystallin domain localized mutants associated with hereditary motor neuron diseases. *Sci Rep*, 8(1):688, 2018.

G. Wettstein, P. S. Bellaye, O. Micheau, and P. Bonniaud. Small heat shock proteins and the cytoskeleton: an essential interplay for cell integrity? *Int J Biochem Cell Biol*, 44(10):1680–6, 2012.

G. Wider. Technical aspects of nmr spectroscopy with biological macromolecules and studies of hydration in solution. *Progress in Nuclear Magnetic Resonance Spectroscopy*, 32:193–275, 1998.

A. Wlodawer, W. Minor, Z. Dauter, and M. Jaskolski. Protein crystallography for non-crystallographers, or how to get the best (but not more) from published macromolecular structures. *FEBS J*, 275(1):1–21, 2008.

T. Wu, Y. Mu, J. Bogomolovas, X. Fang, J. Veevers, R. B. Nowak, C. T. Pappas, C. C. Gregorio, S. M. Evans, V. M. Fowler, and J. Chen. Hspb7 is indispensable for heart development by modulating actin filament assembly. *Proc Natl Acad Sci U S A*, 114(45):11956–11961, 2017.

J. R. Yates. A century of mass spectrometry: from atoms to proteomes. *Nature Methods*, 8(8): 633–637, 2011.

Y. Zhong, L. Han, and B. T. Ruotolo. Collisional and coulombic unfolding of gas-phase proteins: high correlation to their domain structures in solution. *Angew Chem Int Ed Engl*, 53(35):9209–12, 2014.

Chapter 2

αB-Crystallin modulates the passive stiffness of heart muscle by binding titin

2.1 Abstract

Regulation of active and passive forces in heart muscle is essential for cardiovascular fitness. Biomechanical dysfunction underlies a range of disorders leading to cardiovascular disease, the number one cause of death globally. Titin, a large protein that extends across half the muscle sarcomere, is the primary regulator of passive stiffness in muscle tissue. In cooperation with a network of accessory proteins, it acts as an elastic molecular spring that generates passive force during muscle relaxation. αB-crystallin prevents aggregation of destabilized titin during stress. Under basal conditions, αB-crystallin also localizes to a region within titin's elastic segment in cardiac but not skeletal muscle, an interaction heretofore unexplored in detail. In this chapter, we show that αB-crystallin stiffens mouse cardiac trabeculae *ex vivo*, and that this is fully recapitulated using only a 9 amino-acid segment from its flexible C-terminal region. We demonstrate that this peptide binds human cardiac-specific titin domain I26 *in vitro*. αB-crystallin variant R157H, which causes a dilated cardiomyopathy (DCM), lowers the affinity of the peptide for domain I26 and reduces its ability to stiffen cardiac muscle fibers. This constitutes a novel description and characterization of a regulatory role for αB-crystallin, bolstering an emerging reconceptualization of the chaperone's functional landscape: in contrast to canonical binding and sequestration of unfolded states, here αB-crystallin recognizes and protects a folded client subject to routine mechanical stress. The chapter includes a summary of ongoing work toward elucidating the structure of the αB-I26 complex and its response to force.

2.2 Introduction

2.2.1 Titin modulates muscle elasticity

Titin, the largest human protein by mass, is one of the major components of the muscle sarcomere, alongside thick filaments (composed of myosin) and thin filaments (actin) (Linke and Hamdani, 2014). During the cardiac contraction cycle, these filaments generate active force (systole) and titin is the compensatory generator and regulator of passive force (diastole) across the physiological sarcomere length range (Granzier and Irving, 1995). 50% of heart failure cases result from diastolic dysfunction (Paulus and Tschope, 2013).

The titin gene consists of 363 exons that encode isoforms ranging from 2.9 to 3.8 MDa in size, adopting a long array of several types of domains. The elastic region of the protein is designated the I-band, named for its preponderance of small ($\approx$ 10 kDa) immunoglobulin (Ig)-fold domains. These are conventionally numbered from the sarcomere Z-disc to the M-line (Figure **2.1**).

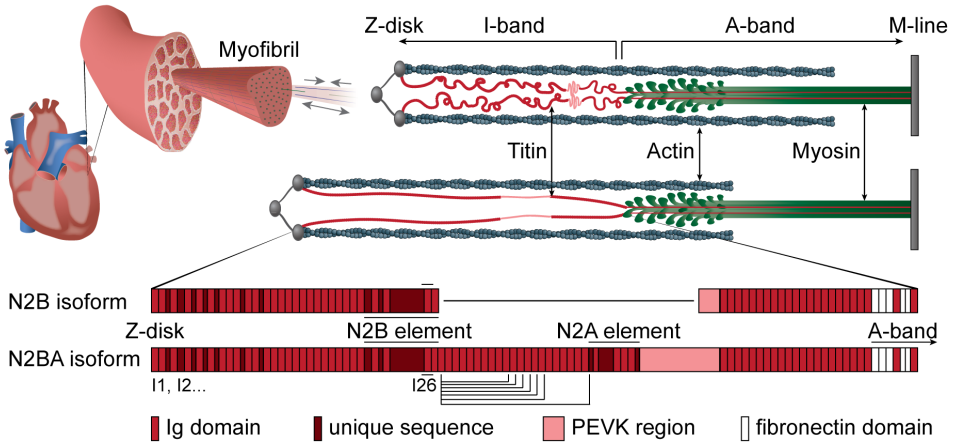


Figure 2.1. Schematic of the sarcomere and titin I-band composition within cardiomyofibrils. Two titin isoforms are expressed in the heart: shorter, stiffer N2B and longer, more extensible N2BA. Unique sequence elements and the PEVK region are primarily intrinsically disordered and highly pliable under strain. Black lines between N2B and N2A elements represent multiple differential splicing possibilities. Figure influenced by Linke and Hamdani (2014) and LeWinter et al. (2007).

A variety of mechanisms interplay to allow titin to regulate passive tension across a range of timescales and conditions, including variability in isoform stiffness due to selective incorporation of Ig domains and unstructured extensible segments (Cazorla et al., 2000; Trombitas et al., 1998); biochemical switches such as redox reactions and post-translational modifications (Grutzner et al., 2009); and many regulatory interactions with binding partners (Linke and Hamdani, 2014), including sHsp αB-crystallin.

2.2.2 αB-crystallin in the heart

αB-crystallin is expressed in cardiac tissue throughout development, comprising up to 3% of all soluble protein in the adult heart under physiological conditions (Dimauro et al., 2017). It localizes to the cardiac cellular support network, including desmin intermediate filaments and myofibrils (Bennardini et al., 1992; Lutsch et al., 1997), with correlation paralleling the degree of ischemic stress (Golenhofen et al., 1999). In particular, an interaction with titin's I-band was observed (distinct from association with desmin, which bisects the I-band at the Z-disc) (Golenhofen et al., 2002). Subsequent force response studies revealed that αB-crystallin alters the mechanical properties of intact cardiomyofibrils under stress conditions (Kotter et al., 2014; Franssen et al., 2017) and of recombinant segments of the I-band consisting of multiple Ig domains (Zhu et al., 2009). Two studies used immunoelectron microscopy to pinpoint the N2B element (Figure **2.1**) as a site within the I-band where αB-crystallin binds without prior external stress, an interaction not observed in skeletal myofibrils (Bullard et al., 2004; Golenhofen et al., 2004).

Given αB-crystallin's known ability to act as a holdase chaperone, authors speculated that these phenomena arise following partial or full structural disruption of

titin. This idea is supported primarily by two indirect observational trends. First, if myofibrils are subjected to conditions promoting titin Ig domain unfolding, the resultant stiffening that is posited to arise from aggregated and thus less elastic titin can be counteracted by αB-crystallin (Kotter et al., 2014; Franssen et al., 2017). Second, αB-crystallin localization along the I-band under stress (ischemia or muscle myopathy) is diffuse, as discovered using correlative immunofluorescence and immunoelectron microscopy (Golenhofen et al., 2002; Unger et al., 2017), suggesting widespread recognition of some structural phenomenon (i.e. misfolding). Thus, mechanistic details of the interaction have remained elusive, including any description of how it may differ between physiological (e.g. routine muscle contraction) and pathological (chronic or acute stress) conditions. This chapter describes our efforts to characterize the effect of αB-crystallin on physiological cardiac passive tension, and to interrogate its underlying interaction with titin at the molecular level.

2.3 Results

2.3.1 αB-Crystallin stiffens cardiac muscle fibers

To examine the effect of αB-crystallin on the force response of cardiac muscle under basal conditions, we first permeabilized murine left-ventricle trabeculae to remove endogenous soluble proteins, leaving only the intact myoarchitecture. This ensured that any observed effect could be attributed to αB-crystallin rather than other accessory proteins to titin. Trabeculae were then incubated in a relaxing solution containing recombinant human αB-crystallin (Figure **2.2a**) and assessed by stretch in the incubation solution. The force response was recorded at 0.1 μm increments (Figure **2.2b**) from a physiological sarcomere length (2.0 μm) to super-physiological (2.6 μm). The passive force peaked sharply at each length (total passive force), and

then decayed over time to a steady-state value as the fiber was held at that length (residual passive force) (Figure **2.2c**).

Muscle fibers incubated with αB-crystallin exhibited increased total and residual passive forces compared to controls at all sarcomere lengths (Figure **2.2d**). As a measure of the tensile strength, or stiffness, of whole fibers, we used the Linear Young's Modulus (LYM) in order to compare across groups. This was calculated by taking the slope of a linear fit to the stress-strain curve. Average LYM of fibers incubated with 1 mg mL^{-1} αB-crystallin was 49.4 ± 7.1 mN mm^{-2} (n = 19), a 2.5-fold increase compared to bovine serum albumin (BSA) as a negative control (18.4 ± 1.9 mN mm^{-2}, n = 20, p <0.001).

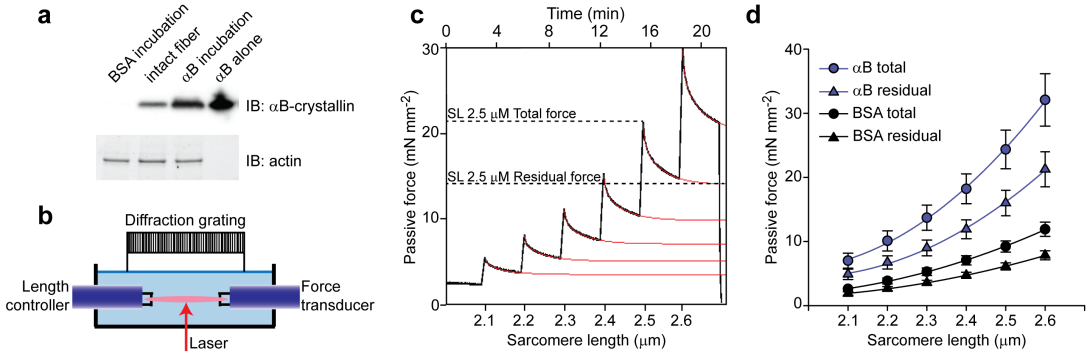


Figure 2.2. αB-Crystallin stiffens cardiac muscle fibers. a. Western blots of murine cardiac trabeculae. The first and third lanes follow extraction of endogenous αB-crystallin; the second lane probes for endogenous αB-crystallin; the fourth is a control with recombinant αB-crystallin and no fiber. **b.** Schematic of the muscle assay experimental apparatus. **c.** At each sarcomere length, passive force exerted by the muscle peaks and then decays to a non-zero value. See Methods for curve fitting parameters. **d.** Fibers incubated with αB-crystallin exhibit increased total and residual passive stiffness at all sarcomere lengths compared to controls. Error bars represent SEM. Data generated by Cameron Turtle.

This stiffening across the range of sarcomere extension suggests that αB-crystallin interacts with one or more domains in resting titin as opposed to solely unfolded domains, which are only likely to appear in overstretched or pre-stretched cardiomyofibrils (Rief et al., 1997; Minajeva et al., 2001). Encompassing the region where αB-crystallin associates, a previous study examined its binding to various recombinant fragments (by Western blot) to identify the site of strongest interaction (Bullard et al., 2004). This excluded domains I24-I25, showed moderate affinity for the exten-

sible N2B-Us and PEVK regions, and narrowed the association most prominently to domains I26-I27. The N2B exon terminates between these domains, resulting in the presence of I27 in all muscle but I26 only in the heart (Freiburg et al., 2000). Given that the interaction is cardiac-specific, we hypothesised that domain I26 (indicated in Figure **2.1**) was a likely candidate as a binding partner.

2.3.2 αB-Crystallin oligomers bind titin domain I26

To interrogate the potential binding of αB-crystallin and I26 *in vitro* we used native mass spectrometry. A mass spectrum of αB-crystallin featured signal between 7,000-13,000 m/z, indicating the co-population of many large oligomeric species that are not immediately resolvable (Figure **2.3a**, upper). A mixture of αB-crystallin and I26 (1:2 monomer molar ratio) produced a similar high m/z interference pattern, with a charge series for the titin monomer at low m/z (Figure **2.3a**, lower). To probe for differences between the complexes, we performed CID, which yielded stripped oligomers with improved charge state resolution (Figure **2.3b**). In the mixture, regions of new signal, a higher baseline, and broadened peaks indicated αB-I26 complexes in addition to αB-crystallin homo-oligomers (Figure **2.3b**, lower). To further confirm that these heteromers were present, we mass selected a 200 m/z wide window around 9,500 m/z in the quadrupole and performed CID to examine only a subset of the distribution of high-mass oligomers (Figure **2.3a**, boxes). In the low m/z region of the resulting mass spectra, where highly charged dissociated subunits appear, we observed both αB-crystallin and I26 peaks (Figure **2.3c**). Thus, the intact oligomers in the selection window were composed of both proteins. We did not observe a sizeable shift in the oligomeric size or distribution, nor a bias toward I26 binding oligomers of any particular stoichiometry. The data therefore reveal weak association between αB-crystallin and native state titin I26.

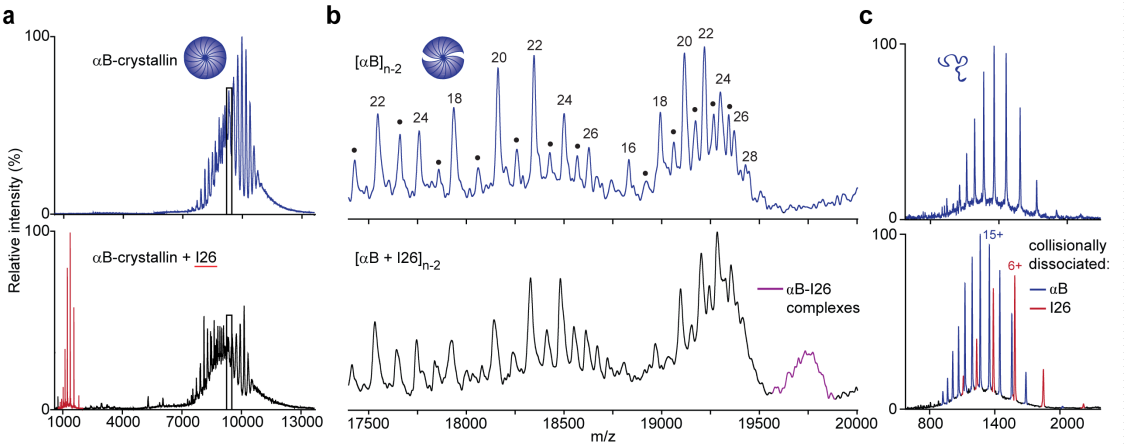


Figure 2.3. αB-Crystallin oligomers bind titin I26. a. Native intact mass spectra of αB-crystallin alone (blue) and following incubation with I26 (red). Coloured peaks indicate signal known to arise from a single protein. I26 is monomeric; αB-crystallin is large and polydisperse, represented by a multi-subunit cartoon. Specific oligomers cannot be resolved. **b.** Native MS with CID of the proteins in **a**, showing a region of the mass spectrum where oligomers have been stripped of two subunits. Species now carry lower charge, which places them at higher m/z and allows peaks to be better separated and assigned to specific αB-crystallin stoichiometries (upper; dots indicate odd stoichiometries). In the mixture, the appearance of new peaks (purple) must arise from complexes with I26. **c.** Unfolded and dissociated subunits following tandem MS and CID of the boxed regions in **a**. In order for I26 peaks to appear here, I26 must be present in the original selected complexes.

2.3.3 Binding to I26 occurs via the αB-crystallin C-terminus

Seeking information regarding the binding site, we used solution NMR spectroscopy and recorded ^{1}H-HSQC spectra of αB-crystallin alone and in the presence of I26 (Figure **2.4a**). Because αB-crystallin oligomers are so large, only residues in the flexible C-terminal region tumble sufficiently rapidly to be observable (Treweek et al., 2010). These peak volumes decreased upon addition of I26, suggesting a reduction in the flexibility of the αB-crystallin C-terminal region. This could result from a larger average oligomer size, inconsistent with native MS results, or a direct interaction between C-terminal αB-crystallin and I26.

To examine the latter possibility, we used a peptide mimicking residues 156-164 from αB-crystallin (ERTIPITRE), which are known to mediate oligomerization by binding a hydrophobic groove on a neighbouring αB-crystallin monomer (Hochberg and Benesch, 2014). Native mass spectra of I26 with this peptide (C-terminal peptide, αB_{Ctp}) displayed peaks corresponding to each of these components alone, as

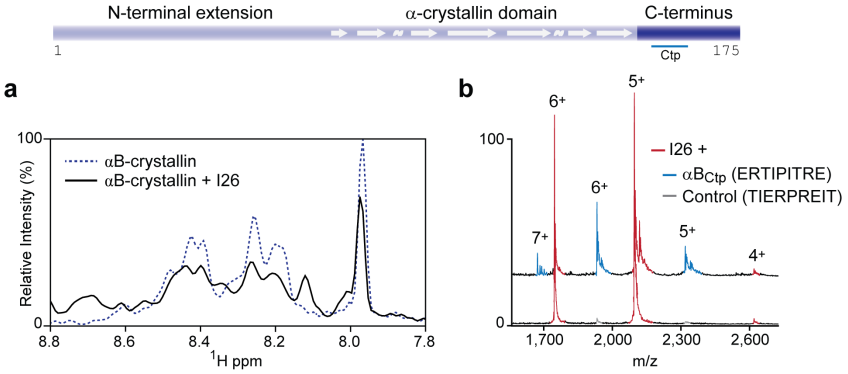


Figure 2.4. Binding titin I26 affects the dynamics of the αB-crystallin C-terminus. Top, schematic of the αB-crystallin monomer primary sequence. Domains are labeled above and secondary structure is indicated in white. The faded portion of the sequence is invisible by NMR. **a.** ^{1}H-HSQC NMR spectra of αB-crystallin alone and following incubation with I26. The reduction in signal of the mixture results from an effect on αB-crystallin C-terminal dynamics. NMR data generated by Henrik Müller. **b.** Native MS of titin I26 with peptide αB_{Ctp} (residues 156-164) indicates specific binding, compared to a scrambled sequence control peptide.

well as a third charge series matching a 1:1 complex (Figure **2.4b**). Consistent with native MS results using full-length αB-crystallin, binding is weak, but clearly distinct from a palindromic peptide of rearranged sequence used to control for nonspecifics formed during nESI (Figure **2.4b**, grey).

2.3.4 Disease variant ^{R157H}αB abrogates C-terminal binding to I26 and the αB ACD

To validate these results in the context of a known functional alteration, we investigated the R157H mutation that lies within the C-terminal region of αB-crystallin and causes an autosomal dominant dilated cardiomyopathy (DCM) (Inagaki et al., 2006). Mass spectra of I26 in the presence of $^{R157H}\alpha B_{Ctp}$ contain peptide-bound peaks that are consistently less intense than in WT experiments yet still distinct from nonspecific binding (Figure **2.5**), evidencing a decreased binding affinity (K_D >1 mM). The interaction between the C-terminal region of αB-crystallin and I26 is thus highly attenuated in the R157H variant at the peptide level.

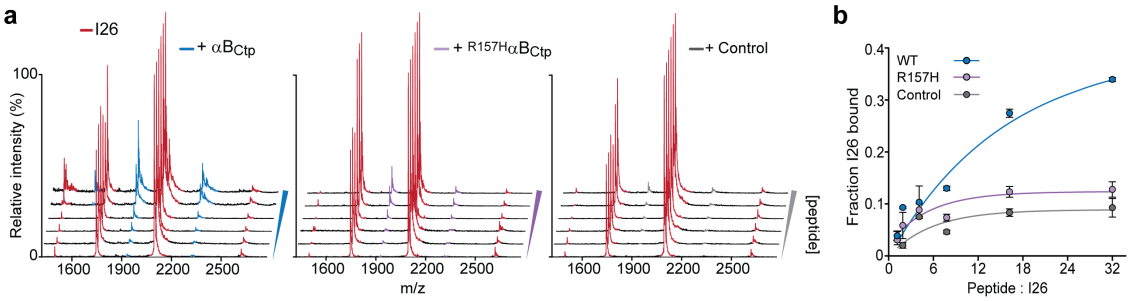


Figure 2.5. αB C-terminal peptide binding to titin I26 is compromised by mutation R157H. a. Representative native mass spectra from titration series of 5 μM I26 with 5, 10, 20, 40, 80, and 160 μM αB peptides (WT, R157H, and scrambled sequence control). **b.** Binding curves extracted from native MS data. Error bars represent SEM.

Given the inter-monomer contacts made by αB_{Ctp} within oligomers (Hochberg and Benesch, 2014), these results imply a competition for binding when αB-crystallin is in the presence of both additional αB-crystallin monomers and I26. We carried out more titration experiments to characterize the thermodynamics of this competition, measuring the K_D of αB_{Ctp} to αB_{ACD} to be 72 ± 3 μM, in good agreement with previous results (Hilton et al., 2013). The mutated peptide $^{R157H}\alpha B_{Ctp}$ exhibited weakened binding to αB_{ACD} (K_D = 226 ± 30 μM), although the mutation did not compromise the ability of full-length protein to assemble into oligomers (Figure **2.6a**).

The free energy of association (ΔG) for both the WT and R157H peptides binding αB_{ACD} or I26 spans -16 to -23 kJ mol^{-1} (Table **2.1**), with a preference for αB_{ACD} over I26 in both cases (Figure **2.6b**). This can be observed directly in the data by comparing the 5^+ and 6^+ charge states of all unbound and peptide-bound monomers (Figure **2.6c**). Interestingly, ΔΔG between binding to αB_{ACD} and I26 is similar whether the αB-crystallin peptide is WT or mutated to R157H (Table 2.1).

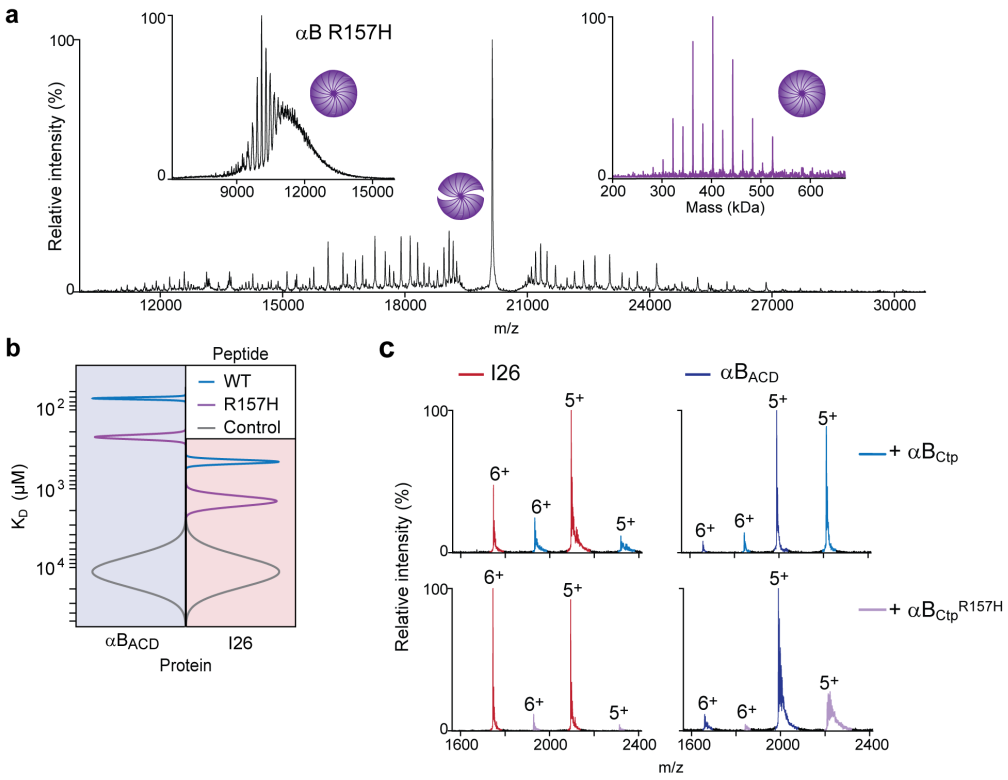


Figure 2.6. Mutation R157H does not inhibit αB-crystallin oligomeric assembly, but weakens binding to both I26 and αB_{ACD}. **a.** Native MS of ^{R157H}αB-crystallin oligomers. Left, intact spectrum; middle, CID; right, reconstructed oligomeric distribution corrected for stripped subunits. (Deriving distributions is described in more detail in Chapter 6.) **b.** K_D measurements for αB_{Ctp} binding to αB_{ACD} and I26. **c.** Representative 5^+ and 6^+ charge states of 5 μM I26 and αB_{ACD} with 80 μM each peptide, for direct comparison of peak intensities underlying the values in **b**.

To examine the molecular determinants of binding, we solved the structure of $^{R157H}\alpha B_{Ctp}$ bound to αB_{ACD} and compared it to the previously reported structure containing WT αB_{Ctp} (Hochberg et al., 2014). The ACD adopts an Ig-like fold comprising six β-strands arranged as two sheets, with the C-terminal peptide binding across a groove between strands β4 and β8 (Figure **2.7a**). The palindrome also enables binding in the opposite direction than shown in the structure (Laganowsky et al., 2010), so mutating either arginine (R157 or R151) will affect contacts made by both. Substitution of histidine for R157 abolished two ionic contacts adjacent to the hydrophobic binding pocket occupied by residues ^{159}IPI^{161} (Figure **2.7b**).

A homology model of I26 adopts the expected fold of a titin Ig domain, with one β-sheet containing strands A, C, F, and G and a second β-sheet comprised of strands B, D, and E by conventional titin nomenclature (Figure **2.7c**) (Mayans

Table 2.1. Thermodynamics of αB_{Ctp} binding αB_{ACD} and I26.

	αB_{Ctp}	$^{R157H}\alpha B_{Ctp}$
K_D (μM)		
I26	382 ± 21	1500 ± 248
αB_{ACD}	73 ± 3	226 ± 30
ΔG (kJ mol^{-1})		
I26	-19.5 ± 0.1	-16.1 ± 0.4
αB_{ACD}	-23.6 ± 0.1	-20.8 ± 0.3
ΔΔG (kJ mol^{-1})		
	4.1 ± 0.2	4.7 ± 0.5

et al., 2001). A groove, analogous to the one between strands β4 and β8 in αB_{ACD}, is present between strands C and D. This intuitively represents a likely site of binding for the αB-crystallin C-terminus.

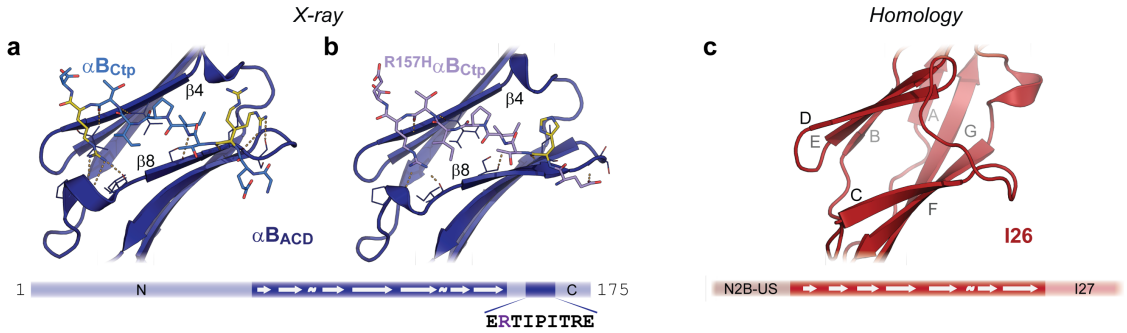


Figure 2.7. Ig-fold binding targets of the αB-crystallin C-terminal palindrome. Crystal structures of αB_{ACD} bound to peptide mimics of residues 156-164, where the peptide is WT **a** or contains mutation R157H **b** (crystallization and data collection by Art Laganowsky; structure refinement by myself and Tim Allison). Schematic of primary sequence below shows which regions of the full-length protein are contained in the X-ray structures. **c.** Homology model of titin I26. This domain sits between the extensible N2B-Unique Sequence and domain I27.

In order to understand the molecular mechanism of titin-based stiffening induced by αB-crystallin binding, we are pursuing a number of strategies toward elucidating the structure of the complex and its behaviour under force. These are summarized in the following sections 2.3.5 - 2.3.7.

2.3.5 Toward an X-ray structure of the I26-αB complex

High resolution structures have been obtained for several domains within the titin I-band, but I26 is not among them. We set out to solve the I26 structure using X-ray crystallography. Crystallization was pursued in both the absence and presence of αB-

crystallin-derived fragments, and in absence and presence of the Ig domain directly adjacent to I26 in cardiac isoforms, I27, connected via their natural linker sequence. A summary of crystallization strategies for constructs that could be successfully over-expressed in *E. coli* is presented in Table 2.2.

Table 2.2. Crystallization strategies in pursuit of the structure of titin I26 alone or in complex with αB-crystallin.

Titin construct	αB-crystallin construct	Reproducible crystal growth
I26	-	×
I26-I27	-	×
I26	156-164	×
I26	68-164	✓
I26-I27	156-164	✓
I26-I27 C45S	156-164	×
$I26_{\Delta 3N}$ [a]	-	×
$I26_{\Delta 6N}$	-	×
$I26_{\Delta 6C}$	-	×
I26-MBP [b]	156-164	×
I26-T4L [c]	-	×
I26-I27-AAAA-I27-I26	-	×

[a] Δ= residues removed from N- or C-terminus compared to base construct. See Methods for base constructs.
[b] Maltose binding protein, employed as a fusion protein to facilitate crystal packing (Laganowsky et al., 2011)
[c] T4-Lysozyme, as above

Reproducible crystals were obtained using two I26-αB combinations. Further details of the appearances, conditions for reproducible growth, and attempted strategies for improvement of these crystals are given in Figure **2.8** and Table 2.3. The needle-like crystals grown from I26 and $\alpha B_{68\text{-}164}$ (Figure **2.8a**) did not diffract as would an ordered protein or salt crystal lattice; most crystals exhibited no visible diffraction, and a few gave a faint pattern resembling what might be expected from an amyloid-like arrangement (data not shown). Possibly, I26 became destabilized and then, rather than interacting with the C-terminal extension, bound the αB-crystallin ACD, which can be sufficient for canonical chaperone activity (Hochberg and Benesch, 2014). Further pursuit of this strategy is not recommended, because it is not likely to capture the active complex.

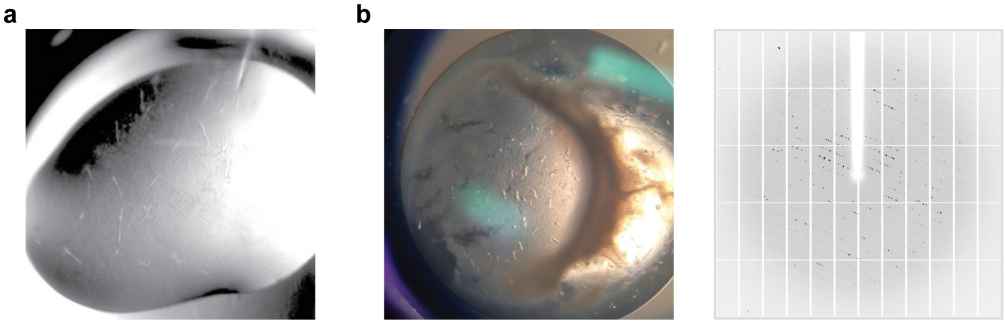


Figure 2.8. I26-αB crystals. **a** I26·$\alpha B_{68\text{-}164}$ needle-like crystals grew readily but did not diffract as a typical protein or salt lattice. **b.** I26-I27·αB_{Ctp} crystals and representative diffraction pattern.

I26 also appeared to become destabilized in the I26-I27-αB_{Ctp} condition, evidenced by dark precipitate characteristic of denatured protein. However, crystals also grew, and with careful harvesting and cryoprotection approximately 1 in 10 of these diffracted beyond 4Å(Figure **2.8b**). Efforts to solve the phases of these data have thus far been unsuccessful despite assistance from experienced crystallogra-

Table 2.3. Conditions and tips for reproducible growth of I26-αB crystals.

a. I26-I27, αB_{Ctp}	**b.** I26, $\alpha B_{68\text{-}164}$
– Concentrations: 20 mg mL^{-1} I26-I27, 7.68 mM αB_{Ctp}	– Concentrations: 3.25 mg mL^{-1} I26, 6.5 mg mL^{-1} $\alpha B_{68\text{-}164}$
– Conditions: 0.22 M $LiSO_4$, 0.1 M Tris pH 8, 24% PEG 3350	– Conditions: 54-60% tacsimate, pH 6.5 or 7.0
– Incubate mixture at ambient temperature 45-60 mins	– $\alpha B_{68\text{-}164}$ is not highly soluble; keep concentration <10 mg mL^{-1}
– Set by hand from precipitated solution	– Set and keep trays at ambient temperature
– Crystals do not grow if EDTA is used in purification	
– A selenomethionine derivative did not yield crystals	
– Dehydration did not improve diffraction	
– Seeding yielded multiple salt crystals	
– Carboxymethylation did not improve diffraction	
– Cryoprotect with 20% glycerol added to growth conditions	

phers. Experimental phasing was pursued using the compound I3C, which contains three iodine atoms for single-wavelength anomalous disperson (SAD) (Beck et al., 2008), but data were insufficiently complete, poorly resolved, and affected by radiation damage. Phasing by molecular replacement was pursued using a variety of search models identified as having the highest homology to I26 or I27 by the HHpred server (Zimmermann et al., 2017). The maximum sequence homology was, however, only 27%. (Interestingly, while inconvenient for crystallographers, consistently low sequence homology in adjacent Ig domains lowers the likelihood of improper refolding and co-aggregation following mechanical strain Wright et al. (2005), making them notoriously difficult MR candidates at low resolution.) For each search model, opportunities for user intervention in MR were exploited along with several platforms for model optimization, including AMPLE (Rigden et al., 2008), MRage (McCoy et al., 2007), Sculptor (Bunkoczi and Read, 2011), Ensembler (McCoy et al., 2007), and Chainsaw (Stein, 2008).

These returned solutions with translation function Z-scores ranging from 3 (false solutions) to 6.4 (ambiguous). For the highest scoring outputs, the goodness of

fit was inspected manually and the density map averaged by non-crystallographic symmetry for additional rounds of MR in efforts to find missing copies of the protein and improve the phases. This approach yielded the highest TFZ score obtained of 11.1, where the initial search model derived from an X-ray structure of titin domains I69-I70 (PDB 3B43). While this score would typically indicate a correct solution, the model was still incomplete, with R_{work}/R_{free} exceeding 0.47-0.55, respectively. These metrics did not improve during attempted rounds of building and refinement.

To advance this structure, three approaches are recommended. First, with optimization toward higher resolution diffraction, the I26-I27·αB_{Ctp} condition may yet yield a tractable solution. Second, while MBP and T4L fusion constructs were screened (Table 2.3), these were not yet mutated to facilitate metal coordination, which has been demonstrated to generate crystal lattice contacts (Laganowsky et al., 2011). Third, screening homologous titin domains from non-human mammals could result in a more ordered system.

2.3.6 Solution NMR reveals I26 plasticity

In collaboration with the group of Andrew Baldwin, University of Oxford

In addition to 1D proton NMR (Figure **2.4**), we explored the I26·αB-crystallin interaction using additional NMR approaches. We collected a $^{15}N^{1}H$-HSQC spectrum of ^{15}N-labelled I26 (Figure **2.9a**). This type of spectrum features a unique signal for each backbone N-H, meaning that for a stable and folded protein, one cross-peak per residue (excluding prolines) is typical. The I26 spectrum features well-dispersed resonances, evidencing a protein with tertiary structure; however, unexpectedly, it contains more peaks than the number of residues present. We prepared ^{13}C,^{15}N-labeled I26 in order to record triple resonance NMR data, assigned the peaks to specific residues, and were able to trace multiple backbones among

split peaks, consistent with multiple structures undergoing slow (> μs) conformational exchange. Chemical shift-based order parameters calculated from these data point toward the expected β-sheet rich structure in general, but some of the backbones contain disordered regions where β-sheets are predicted (Figure **2.9b**). This may explain in part why the domain resists crystallization. We could modulate the prevalence of the different structures by changing pH, adding DTT, or including αB-crystallin oligomers or C-terminal peptide. Further work is ongoing to disentangle the effects of these changes and derive an I26 structural ensemble. It also remains to be determined whether these effects vary with construct boundaries.

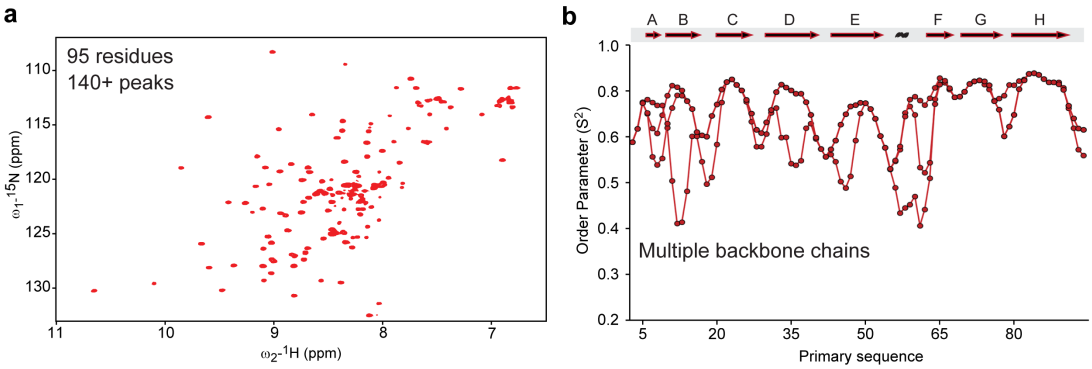


Figure 2.9. Titin I26 populates an ensemble of slowly exchanging structures. a. $^{15}N^1H$-HSQC spectrum of ^{15}N-labelled I26. The spectrum contains many more cross-peaks than residues within the protein, meaning many residues exist within different chemical environments. **b.** Order parameters calculated from triple resonance (HN(CA)CO) NMR data. Tracing through-bond and through-space correlations demonstrates multiple backbone chains with different secondary structural elements. Isotopically labeled protein prepared myself; NMR data generated by Henrik Müller.

In addition to unusual structural multiplicity, we observed redox-dependent behaviour of I26, which contains two cysteines. On a timescale of days, I26 irreversibly unfolds but does not aggregate, evidenced by decay of signal across the ^{1}H-dimension apart from intensification in the 8-8.5 ppm range where random coil nuclei are detected (Figure **2.10a**). As this occurs, native MS shows higher charge states and appearance of a covalent I26 dimer (Figure **2.10b**). This suggests that the dimer is not formed via an existing noncovalent interface on the native structure,

but requires prior denaturation and exposure of one or more cysteines. Inclusion of either reductant or αB-crystallin prevents this irreversible unfolding.

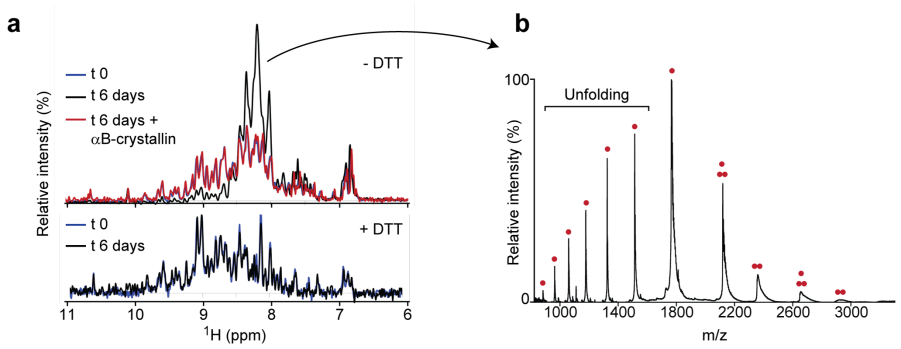


Figure 2.10. Titin I26 is destabilized with concomitant oxidation and can be rescued by reduction or αB-crystallin. a. ^{1}H-NMR spectrum of I26 freshly prepared (blue) and following 3 days at ambient temperature (black). Intensified signal between 8-8.5 ppm reveals substantially increased random coil content. This signal does not appear in the presence of DTT (lower, black) or αB-crystallin (red). NMR data generated by Henrik Müller. **b.** Mass spectrum collected under native nESI conditions of the same I26 used to record the NMR data in **a**. Appearance of highly charged peaks confirms the presence of unfolded monomer, and a new charge series corresponds to oxidized dimer.

Oxidation state and post-translational modification of transiently exposed cysteines affect titin viscoelasticity through modulating the kinetics (Beedle et al., 2016) and efficiency (Alegre-Cebollada et al., 2014; Giganti et al., 2018) of refolding titin Ig domains. Oxidative imbalance, which contributes to a number of cardiovascular pathologies (Gutteridge and Halliwell, 2000), therefore impacts titin function (Beckendorf and Linke, 2015). Future work examining the effect of αB-crystallin on I26 structure and force response under fluctuating oxidative stress conditions may be informative. To interrogate force response, one state of the art approach is atomic force microscopy (AFM).

2.3.7 Atomic force microscopy

In collaboration with the group of Sergi Garcia-Manyes, Kings College London

Single-molecule methods such as optical tweezers, magnetic tweezers, and AFM have come of age for studying the mechanical properties of proteins, leading to advancements in our understanding of titin unfolding and refolding behaviour (Mar-

tonfalvi et al., 2014; Kellermayer et al., 1997; Rivas-Pardo et al., 2016) as well as mechanochemistry (Beedle et al., 2016; Alegre-Cebollada et al., 2014; Giganti et al., 2018). Upon tethering protein termini to a surface and a probe and applying force, these methods can measure the resulting strain and length changes in the piconewton and nanometer regimes, respectively, ideal for many biological experiments. Their application to chaperone binding to single force-bearing substrates is in its infancy, and is an exciting emerging area in single-molecule biophysics. Optical tweezers have been employed to demonstrate binding of ATP-dependent chaperones to model substrates, conferring stabilization against unfolding or refolding depending on binding mode (Mashaghi et al., 2016; Ramirez et al., 2017). However, these experiments required high-affinity binding unlike what we observe for I26 and αB-crystallin (Neuman and Nagy, 2008). Another recent study from the Garcia-Manyes lab using AFM found specificity for unfolded versus partially folded targets by the ATP-dependent DnaKJE system, modulating the folding free-energy landscape and thus elasticity (Perales-Calvo et al., 2018). We collaborated with this lab to investigate αB-crystallin-induced changes in the mechanical stability of I26 by AFM.

We first successfully expressed and purified a polyprotein consisting of 8 consecutive I26 domains and characterized its mechanical fingerprint (Figure **2.11a**). However, we encountered experimental hurdles when introducing αB-crystallin or the C-terminal αB-crystallin peptide. Nonsensical AFM traces were frequently observed in these experiments, possibly due to misfolded protein. Similar to the insolubilization observed in crystallization trials, the high local concentration of I26 within the polyprotein deposited onto a fixed surface seemed to be unstable in the presence of αB-crystallin. Lower concentrations yielded reproducible force-extension curves, but no significant difference in the force required to unfold (F_U) I26. This is shown for addition of 0.1 mM αB_{Ctp} (Figure **2.11b**).

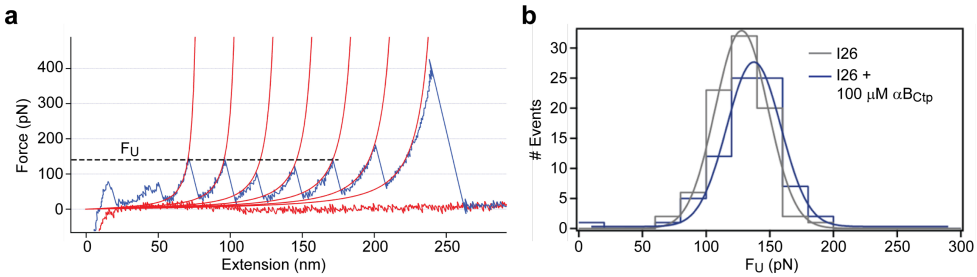


Figure 2.11. Atomic force microscopy. a. Force-extension profile of an $I26_8$ polyprotein. Each peak corresponds to the unfolding of a single domain. Curves were fit using the worm-like chain (WLC) model. **b.** Unfolding force histograms for I26 in absence and presence of 0.l mM αB_{Ctp}. No significant difference in F_U is observed under these conditions. Polyprotein prepared by Palma Rico Lastres; data generated by Amy Beedle.

The only published AFM data probing domain I26 has featured an N2B-inclusive construct (I24-I25-N2BUs-I26(-I27)) rather than a polyprotein (Zhu et al., 2009; Leake et al., 2006). An increase in F_U was observed for Ig domains I24-I26 in the presence of αB-crystallin, attenuated but still significant using R157H-αB-crystallin; however, effects on individual domains could not be deconvolved. This coheres with the *ex vivo* results reported herein. Construct boundaries and interference from neighbouring domains is known to affect single molecule data, as well as the loading rate of applied pulling force; whether force or velocity is held constant; nonspecific interactions with the cantilever tip; and solvent environment (Neuman and Nagy, 2008; Hughes and Dougan, 2016). Hence, we do not rule out the existence of a mechanical effect in αB-I26 binding, and further optimization or alternative methodology may be required in order to achieve comprehensive characterization of the interaction at the single molecule level.

2.3.8 αB_{Ctp} is sufficient to stiffen muscle fibers and its function is compromised by mutation R157H

Having determined that αB-crystallin interacts with I26 via at minimum C-terminal residues 156-164, we repeated cardiac trabeculae assays to investigate whether binding of this region is responsible for stiffening. Following incubation in a solution containing 1 mg mL^{-1} αB_{Ctp}, mouse cardiac trabeculae exhibited a four-fold increase

in LYM (55.9 ± 3.9 mN mm^{-2}, n = 14, p <0.001) compared to controls (LYM = 13.2 ± 1.2 mN mm^{-2}, n = 5) (Figure **2.12**). $^{R157H}\alpha B_{Ctp}$ was a less effective stiffener than αB_{Ctp}, however still displayed some activity (LYM = 26.8 ± 2.1 mN mm^{-2}, n = 11). These results are statistically indistinguishable from those of full-length αB-crystallin (Figure **2.12b**), with the R157H variant also stiffening less effectively (LYM = 33.1 ± 3.3 mN mm^{-2}, n = 18). This mirrors the binding affinity of the different peptides to I26, such that stronger binding appears to confer greater stiffness.

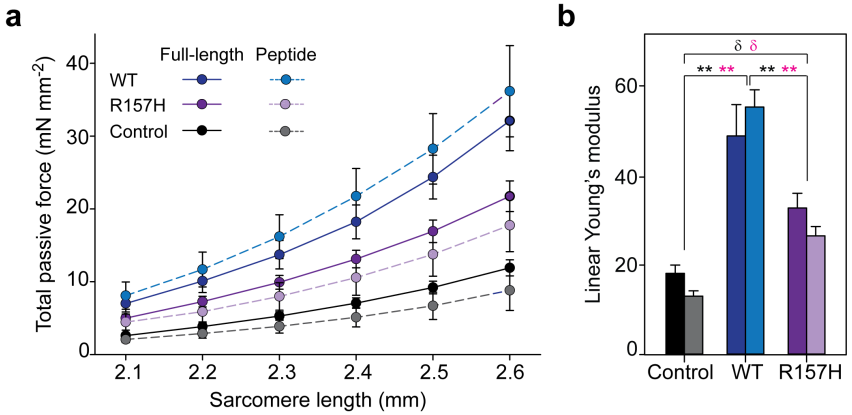


Figure 2.12. The αB-crystallin C-terminal peptide fully recapitulates the stiffening ability of the full-length chaperone. a. Total passive force of murine cardiac muscle fibers stretched in the presence of WT and R157H αB-crystallin and corresponding peptide mimics of residues 156-164. Controls are BSA and a peptide of scrambled sequence. Values of *n* are given in the text, where each is a biological repeat using tissue extracted from a separate heart. **b.** Linear Young's Moduli of whole muscle fibers across groups. Fibers are stiffened by αB-crystallin, less so when it is mutated, with no significant differences between full-length and peptide experiments. ** indicates p < 0.001, δ indicates p < 0.05, black symbols are full-length protein comparisons, pink between peptides. Error bars represent SEM. Data generated by Cameron Turtle.

Variation in fiber stiffness as a function of protein or peptide concentration was also explored, since the inability of peptides to oligomerize would result in different effective concentrations compared to proteins. We incubated fibers in solutions containing 0.1 to 5 mg mL^{-1} protein or peptide, reasoning based on reported values (Klemenz et al., 1993) and Western blot (Figure **2.2b**) that this would encompass sub- to super-physiological concentrations of αB-crystallin. All proteins and peptides displayed significant stiffening activity compared to controls between concentrations ranging from 0.5 to 5 mg mL^{-1}, with the peptides but not full-length proteins also stiffening significantly at 0.1 mg mL^{-1} (Figure **2.13a-d**). Most experiments revealed

an activity plateau, with the exception of WT full-length αB-crystallin, which did not reach a plateau within the range of concentrations tested (Figure **2.13a**). We also asked whether differences could be found in residual, rapid, and slow components of stiffening (see Methods), which may give some mechanistic insight into fiber stiffening. For example, if all of the chaperones increased the rapid component of stiffening compared to controls, we might conclude that we should probe for a kinetically labile mechanism. However, contributions of the components to total stiffness were similar across all groups at both resting and superphysiological sarcomere lengths (Figure **2.13e**). This indicates a shared manner of acting on fibers between proteins and peptides; one which does not alter the fundamental way in which titin is viscoelastic, but merely the magnitude of its force response.

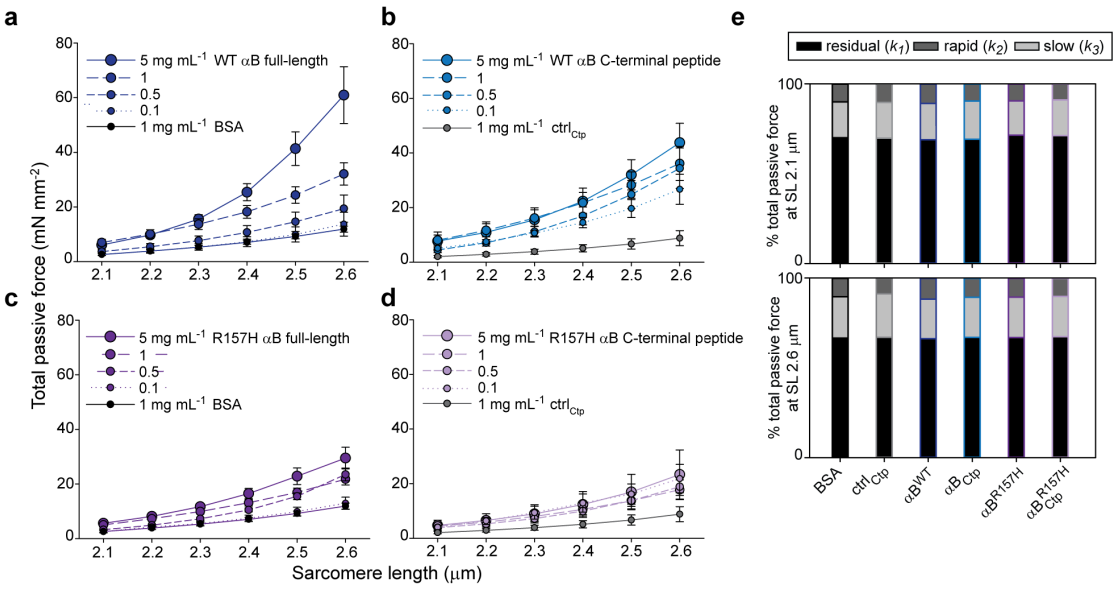


Figure 2.13. αB-crystallin oligomers and peptides stiffen heart muscle fibers via a similar mechanism. a-d. Concentration effects of αB-crystallin variants and derivative peptides on murine cardiac trabeculae stiffening. **e.** Fractions of residual, rapid, and slowly decaying force components between groups at resting (2.1 μM) and superphysiological (2.6 μM) sarcomere lengths. Data generated by Cameron Turtle.

2.4 Discussion

The association of αB-crystallin with titin has long been attributed to its role as a stress-inducible holdase chaperone with affinity for destabilized substrates, and in cases of drastically perturbed titin structure (Kotter et al., 2014; Franssen et al., 2017), the breadth of association indicates that this explanation is likely correct. In contrast, the interaction with titin characterized here represents a departure from canonical sHsp function in several respects. It occurs under basal conditions without prior stress-prompted amplification of chaperone gene expression, and does not require I26 denaturation, revealing native state client binding. Furthermore, it marks a specific role for the flexible C-terminus. High affinity binding to destabilized substrates tends to involve the N-terminus or ACD (Treweek et al., 2015; Hochberg et al., 2014), and the C-terminus is implicated in binding to intermediate filaments (Houck et al., 2011). This region may warrant further exploration in sHsp-client interactions, since here it was sufficient to reproduce full-length protein activity.

This sufficiency of the peptide and the magnitude of fiber stiffening it achieves suggests that it makes similar interactions with titin domains in addition to I26. The interplay between these interactions and application of force may have precluded their detection in prior *in vivo* studies. Oligomer multivalency would concentrate exposed C-termini around large complexes, increasing the client encounter rate and conceivably cross-linking titin regions or adjacent sarcomeres. This could underlie the differences we observed in muscle fiber stiffening between protein and peptide at high concentrations (Figure **2.13**).

The position I26-I27 occupies between two load-bearing extensible segments in the N2B cardiac titin isoform (Figure **2.1**) may render these domains uniquely susceptible to mechanical stress. I24-I26 are less mechanically stable than other

distal Ig domains on average (Zhu et al., 2009), and I26 lacks a motif within other titin inter-Ig-domain linkers that confers structural integrity (von Castelmur et al., 2008). During cardiomyocyte development, αB-crystallin levels increase concomitantly with the replacement of flexible isoforms by the stiffer N2B isoform (Bodi et al., 2017). Thus, the results should be interpreted in the context of titin isoform expression, which is variable across species, heart compartments, and time (Cazorla et al., 2000). Likely due in part to this variability, studies investigating consequences of αB-crystallin knockout in different animal models have yielded differing results: $\alpha B^{-/-}$ zebrafish hearts display normal morphology but low heart rate and marginally reduced contraction dynamics (Mishra et al., 2018), whereas rats lacking αB-crystallin (and HspB2) develop restrictive cardiomyopathy (Kumarapeli et al., 2010). Both, however, experience heart failure following stress, highlighting the distinction between αB-crystallin subtle physiological versus broad pathological roles.

We found that DCM-linked mutation R157H compromised the ability of the chaperone to stiffen cardiac trabeculae and to bind I26 at the peptide level, adding to prior descriptions of this mutant's impaired binding to titin (Inagaki et al., 2006; Zhu et al., 2009). It also weakened the C-terminal oligomeric interface to αB_{ACD}, with changes in free energy implying that while each affinity is reduced, the degree of binding competition is maintained. *In vivo*, heterozygosity and higher expression of the more flexible titin isoform in human compared to mouse cardiac muscle (Cazorla et al., 2000) may contribute to this variant's late-onset human phenotype.

Collectively, these data support specific αB-crystallin function in the heart as it undergoes routine cycles of mechanical activity in addition to the chaperone's promiscuous interactions with destabilized sarcomeric proteins in cardiomyocytes under chronic or acute stress (Golenhofen et al., 1999, 2002; Kotter et al., 2014;

Franssen et al., 2017; Kumarapeli et al., 2008). This involvement of a single sHsp in both physiologic and pathologic functioning of a target advances our understanding of the protein family's functional plasticity. The findings offer a novel interaction for exploration in the pursuit of therapeutic intervention prior to accumulation of damaged titin via small-molecule modulation of cardiac muscle passive stiffness.

Acknowledgments

Many thanks to Georg Hochberg and Cameron Turtle for embarking on this project and transferring it when I began my PhD. Georg's setup of the system (titin constructs, purification protocols, etc.) and Cameron's muscle assays were invaluable to the momentum of the work. We are grateful to Katja Gehmlich and Charles Redwood in the Department of Cardiovascular Medicine for helpful guidance and discussion. I thank Tim Allison, Ed Lowe, and Michael McDonough for all of their advice and assistance with titin crystallography, and Art Laganowsky for the αB-crystallin mutant diffraction dataset. Thanks to Henrik Müller and Andrew Baldwin for extensive NMR collaboration, only a small portion of which was shown here. Thanks to Amy Beedle, Palma Rico Lastres, and Sergi Garcia-Manyes for the AFM work and allowing me to spend an interesting afternoon observing these experiments in their lab at Kings College London.

2.5 Methods

Protein expression and purification

Human full-length αB-crystallin was expressed and purified as described previously (Horwitz et al., 1999). Briefly, cells were lysed following overnight expression at 20°C and protein purified by anion exchange chromatography followed by SEC using a Superdex 200 column. The R157H mutation was introduced using a site-directed mutagenesis kit (Agilent), and ^{R157H}αB-crystallin was expressed and purified in the same manner as wild type. Proteins were stored in PBS at -80°C until use. Concentrations were determined by absorbance at 280 nm using an extinction coefficient of 13980 M^{-1} cm^{-1}.

Gene inserts for titin domain I26 or I26-I27 codon optimized for *E. coli* were ordered from Integrated DNA Technologies and cloned into a pET28b(+) vector (Novagen) modified to include an N-terminal His-tag cleavable by tobacco etch virus (TEV) protease. (Sequences correspond to residues 4290-4381 and 4290-4473 in the UniProtKB accession number Q8WZ42 – this is labeled Ig-like 23 and 24, but these are the two domains following the N2B-Unique sequence.) Protein was over-expressed in BL21(DE3) cells (Novagen) in LB media at 20°C overnight following induction by 0.5 mM IPTG. Cells were lysed in 300 mM NaCl, 50 mM Tris, 20 mM imidazole, 5 mM β-mercaptoethanol (BME) at pH 7.4 with EDTA-free protease inhibitor cocktail (Roche). The lysate was filtered and passed over a HisTrap HP column in the lysis buffer, and eluted using the same buffer containing 500 mM imidazole. The eluent was dialyzed into the loading buffer at room temperature with TEV protease for 16-20 hours to remove the N-terminal His-tag. The sample was then passed over a HisTrap HP column again and then exchanged into 50 mM Tris buffer at pH 9 containing 5 mM BME using a desalting column in preparation for

anion exchange. The sample was loaded onto 4 5-mL HiTrap Q columns connected in tandem. Protein eluted in a gradient of 500-900 mM NaCl in the loading buffer. Finally, I26 was exchanged into storage buffer (100 mM NaCl, 20 mM Tris, 1 mM DTT, pH 8) by SEC using a Superdex 75 column. Concentration was determined by absorbance at 280 nm using an extinction coefficient of 9970 M^{-1} cm^{-1} (I26) or 21430 M^{-1} cm^{-1} (I26-I27). Aliquots were flash-frozen and stored at -80°C.

For NMR experiments, isotopically labeled I26 prepared via expression in M9 media containing ^{15}N-ammonium chloride as the only nitrogen source and, for triple resonance data, ^{13}C-labeled D-glucose as the only carbon source. This was purified as described.

Peptides – αB_{Ctp} (ERTIPITRE), $^{R157H}\alpha B_{Ctp}$ (EHTIPITRE), and scrambled control (TIERPREIT) – were purchased from Biomatik at >99% purity, dissolved in ddH2O to 50 mM, and diluted in 200 mM ammonium acetate pH 6.9 for MS experiments.

Muscle fiber passive force measurements

Solution compositions for force-Ca^{2+} sensitivity measurements were determined using an iterative computer program (Fabiato, 1988) that uses published affinity constants to calculate the equilibrium concentrations of ligands and ions. Solutions contained (in mmol L^{-1}): 80 MOPS, 15 EGTA, 1 Mg^{2+}, 5 MgATP, 135 (Na^+ + K^+), 15 creatine phosphate and 20 units mL^{-1} creatine phosphokinase, pH 7.0 (at 15°C). Ca^{2+} concentration was varied using $CaCl_2$. Total ionic strength was 170 mmol L^{-1}.

Mice were dispatched via cervical dislocation in accordance with Schedule 1 of A(SP)A 1986. Hearts were rapidly excised and dissected in oxygenated physiological salt solution. Left ventricular trabeculae (width: 80-250 μm, length: 1.0-3.0 mm)

were cut and washed overnight at 4°C in relaxing solution containing 1% Triton X-100. Because αB-crystallin is predominantly located in the cytosol (van de Klundert et al., 1998), treatment with detergent to permeabilize the cells and skin the fibers removed endogenous αB-crystallin. After skinning, fibers were stored in 50% glycerol relaxing solution at -20°C for experiments within 1 week. Fibers were incubated in a relaxing solution containing the protein or peptide of interest, ranging from 0.1 to 5 mg mL^{-1}, for 1 hour and subsequently mechanically assessed in the same solution. Western blotting using an anti-αB antibody confirmed that demembranated fibers had little to no αB-crystallin remaining, and that incubated fibers had taken up the recombinant αB-crystallin. Stress-relaxation measurements were conducted at 15°C using an Aurora Scientific Permeabilized Fiber Test System. Skinned trabeculae were connected via aluminium T-clips to pin hooks on a force transducer and motor and sequentially stretched from SL 2.0 μm to 2.6 μm in 0.1 μm increments (measured via laser diffraction) following preconditioning.

Further details of muscle fiber experiments are available from Cameron Turtle.

Muscle fiber passive force quantification

Upon application of the strain and hold procedure, corresponding stresses induced in the fibers decreased over time. The stress decay was fit with a second-order exponential equation:

$$\sigma(t) = k_1 + k_2 e^{\frac{-t}{\tau^2}} + k_3 e^{\frac{-t}{\tau^3}}$$

Where k_1 is residual stiffness; k_2 is rapidly decaying stiffness; k_3 is slowly decaying stiffness; and τ_2 and τ_3 are the rates of rapid and slow stiffness decay, respectively. Selection of a small τ_2 and large τ_3 in the initial fit conditions differentiates the second

and third terms. This model accurately fits cardiac muscle fiber stress relaxation data, allowing quantification of the viscoelastic parameters of relaxation at multiple lengths and permitting comparisons within individual fibers as well as across groups. All instances in the text of total passive stiffness correspond to k where $k = k_1 + k_2 + k_3$. As an estimate of the stiffness of entire fibers, we calculated LYM using the slope of the linear fit to the total stiffness versus strain relationship.

Mass spectrometry

αB-Crystallin concentration was 20 μM and its ratio to I26 was varied from 0.2 to 1, with representative spectra herein collected at a ratio of 0.5. Proteins were mixed in phosphate-buffered saline (PBS) and incubated at 37°C for 1 hour in order to equilibrate the system, based on the complete equilibration of αB-crystallin subunits requiring approximately 40 minutes at this temperature (Hilton et al., 2013). Mixtures were then buffer exchanged into 200 mM ammonium acetate at pH 6.9 via biospin (BioRad columns) prior to nESI experiments. MS experiments were conducted on a Q-ToF mass spectrometer (Waters) with parameters as follows: capillary 1.8kV; sample cone 200V; extractor cone 50V; RF lens 5.0 V; pusher cycle 255 μs; backing pressure 6 mbar; collision cell voltage 10V (non-activating) or 200V (CID). LM and HM resolution were 4.0 and 5.0 V respectively for quadrupole selected acquisitions. Data were visualized using MassLynx 4.1 (Waters).

MS analyses of peptide binding to I26 or αB_{ACD} were performed on a Synapt G2 mass spectrometer modified for the transmission of intact noncovalent protein complexes (Waters) with parameters as follows: capillary 1.38kV; sample cone 10V; extractor cone 4V; backing pressure 4.4 mbar; trap gas (argon) 2-4 mL min^{-1}; trap cell voltage 5V; transfer cell voltage 4V. I26 concentration was held constant at 5 μM and peptide concentration was varied from 5 to 160 μM. For αB_{ACD} titration

series, protein concentration was held constant at 7 μM (a minor fraction of which was dimeric) and peptide concentration was varied from 10 to 80 μM. Peptides and protein were mixed in 200 mM ammonium acetate pH 6.9 immediately prior to data collection. A minimum of three acquisitions were collected at each ratio. nESI was performed in the presence of acetonitrile vapour in order to promote charge reduction and maintenance of noncovalent contacts (Hopper et al., 2012). Data were processed using UniDec (Marty et al., 2015): following deconvolution, relative intensities of each species were used to fit bootstrapped dissociation constants (500 repetitions with replacement). To correct for nonspecific adducts, a control peptide of scrambled sequence TIERPREIT was analysed in the same manner as the WT and mutant peptides and its apparent association constant used to correct the binding of the others as described previously (Hilton et al., 2013).

NMR spectroscopy

Details of NMR experiments can be obtained from Professor Andrew J. Baldwin at the University of Oxford.

Crystallization and structure solution

Screens were set from a mixture containing αB-crystallin residues 68-153 and synthetic peptide GEHTIPITRE. Crystals grew in condition PEG ion condition 7 (Hampton Research) consisting of 0.1 M sodium acetate trihydrate pH 4.0 and 15% PEG 400. Details of concentrations and cryoprotection are available from Arthur Laganowsky, Texas A&M University. X-ray diffraction data were collected in-house at the University of California, Los Angeles, with reflections extending beyond 1.6Å. Data were integrated using XDS (Kabsch, 2010) and scaled and merged in point group I222 using Aimless in the PHENIX program suite (Adams et al.,

2002). Molecular replacement in Phaser (McCoy et al., 2007) using PDB 4M5S (wild-type αB-crystallin, with bound peptide removed) as a search model yielded a single solution. An initial model was constructed using PHENIX Autobuild which built 68 residues in two fragments. The model was finalized (Table 2.4) through cycles of manual building and editing in Coot (Emsley et al., 2010) and refinement using PHENIX.refine. It had final R_{work}/R_{free} values of 17%/19%. It will be deposited in the PDB prior to publication (manuscript in preparation).

Table 2.4. Statistics of X-ray data collection and refinement for the structure of $\alpha B_{68\text{-}153}$ bound to $^{R157H}\alpha B_{156\text{-}164}$.

	αB_{ACD}.^{R157H}Ctp
Crystal parameters	
Space group	I222
Cell dimensions	
a, b, c (Å)	35.57, 47.2, 124.35
α, β, γ(°)	90, 90, 90
Molecules in ASU	1
Data collection	
Beamline	UCLA in-house
Wavelength (Å)	1.5418
Resolution (Å)	19.42-1.60 (1.64-1.60)
Reflections observed/unique	139,684/14,025
Redundancy	10.0 (8.1)
Completeness (%)	98.5 (93.6)
R_{meas}	0.029 (0.195)
I/σI	45.61 (10.86)
Wilson B-value	28.3
CC1/2	1.00 (0.986)
Refinement	
Resolution (Å)	19.42-1.60 (1.72-1.60)
Reflections	14,025
R_{work}	0.1753
R_{free}	0.1928
No. of non-H atoms	
Protein	1511
Water	69
Mean B-factors (Å^2)	
Protein	41.23
Water	38.47
RMSD from target values	
Bond length (Å)	0.013
Bond angle (°)	1.418
Ramachandran statistics	
In preferred regions (%)	96.7
In allowed regions (%)	3.3
Outliers (%)	0

R_{free} calculated using 5% of reflections.
Values in parentheses correspond to the highest resolution shell.

References

P. D. Adams, R. W. Grosse-Kunstleve, L. W. Hung, T. R. Ioerger, A. J. McCoy, N. W. Moriarty, R. J. Read, J. C. Sacchettini, N. K. Sauter, and T. C. Terwilliger. Phenix: building new software for automated crystallographic structure determination. *Acta Crystallogr D Biol Crystallogr*, 58 (Pt 11):1948–54, 2002.

J. Alegre-Cebollada, P. Kosuri, D. Giganti, E. Eckels, J. A. Rivas-Pardo, N. Hamdani, C. M. Warren, R. J. Solaro, W. A. Linke, and J. M. Fernandez. S-glutathionylation of cryptic cysteines enhances titin elasticity by blocking protein folding. *Cell*, 156(6):1235–1246, 2014.

T. Beck, A. Krasauskas, T. Gruene, and G. M. Sheldrick. A magic triangle for experimental phasing of macromolecules. *Acta Crystallogr D Biol Crystallogr*, 64(Pt 11):1179–82, 2008.

L. Beckendorf and W. A. Linke. Emerging importance of oxidative stress in regulating striated muscle elasticity. *J Muscle Res Cell Motil*, 36(1):25–36, 2015.

A. E. Beedle, S. Lynham, and S. Garcia-Manyes. Protein s-sulfenylation is a fleeting molecular switch that regulates non-enzymatic oxidative folding. *Nat Commun*, 7:12490, 2016.

F. Bennardini, A. Wrzosek, and M. Chiesi. Alpha b-crystallin in cardiac tissue. association with actin and desmin filaments. *Circ Res*, 71(2):288–94, 1992.

B. Bodi, E. P. Toth, L. Nagy, A. Toth, L. Martha, A. Kovacs, G. Balla, T. Kovacs, and Z. Papp. Titin isoforms are increasingly protected against oxidative modifications in developing rat cardiomyocytes. *Free Radic Biol Med*, 113:224–235, 2017.

B. Bullard, C. Ferguson, A. Minajeva, M. C. Leake, M. Gautel, D. Labeit, L. Ding, S. Labeit, J. Horwitz, K. R. Leonard, and W. A. Linke. Association of the chaperone alphab-crystallin with titin in heart muscle. *J Biol Chem*, 279(9):7917–24, 2004.

G. Bunkoczi and R. J. Read. Improvement of molecular-replacement models with sculptor. *Acta Crystallogr D Biol Crystallogr*, 67(Pt 4):303–12, 2011.

O. Cazorla, A. Freiburg, M. Helmes, T. Centner, M. McNabb, Y. Wu, K. Trombitas, S. Labeit, and H. Granzier. Differential expression of cardiac titin isoforms and modulation of cellular stiffness. *Circ Res*, 86(1):59–67, 2000.

I. Dimauro, A. Antonioni, N. Mercatelli, and D. Caporossi. The role of alphab-crystallin in skeletal and cardiac muscle tissues. *Cell Stress Chaperones*, 2017.

P. Emsley, B. Lohkamp, W. G. Scott, and K. Cowtan. Features and development of coot. *Acta Crystallogr D Biol Crystallogr*, 66(Pt 4):486–501, 2010.

A. Fabiato. Computer programs for calculating total from specified free or free from specified total ionic concentrations in aqueous solutions containing multiple metals and ligands. *Methods Enzymol*, 157:378–417, 1988.

C. Franssen, J. Kole, R. Musters, N. Hamdani, and W. J. Paulus. alpha-b crystallin reverses high diastolic stiffness of failing human cardiomyocytes. *Circ Heart Fail*, 10(3):e003626, 2017.

A. Freiburg, K. Trombitas, W. Hell, O. Cazorla, F. Fougerousse, T. Centner, B. Kolmerer, C. Witt, J. S. Beckmann, C. C. Gregorio, H. Granzier, and S. Labeit. Series of exon-skipping events in the elastic spring region of titin as the structural basis for myofibrillar elastic diversity. *Circ Res*, 86(11):1114–21, 2000.

D. Giganti, K. Yan, C. L. Badilla, J. M. Fernandez, and J. Alegre-Cebollada. Disulfide isomerization reactions in titin immunoglobulin domains enable a mode of protein elasticity. *Nat Commun*, 9 (1):185, 2018.

N. Golenhofen, P. Htun, W. Ness, R. Koob, W. Schaper, and D. Drenckhahn. Binding of the stress protein alpha b-crystallin to cardiac myofibrils correlates with the degree of myocardial damage during ischemia/reperfusion in vivo. *J Mol Cell Cardiol*, 31(3):569–80, 1999.

N. Golenhofen, A. Arbeiter, R. Koob, and D. Drenckhahn. Ischemia-induced association of the stress protein alpha b-crystallin with i-band portion of cardiac titin. *J Mol Cell Cardiol*, 34(3): 309–19, 2002.

N. Golenhofen, M. D. Perng, R. A. Quinlan, and D. Drenckhahn. Comparison of the small heat shock proteins alphab-crystallin, mkbp, hsp25, hsp20, and cvhsp in heart and skeletal muscle. *Histochem Cell Biol*, 122(5):415–25, 2004.

H. L. Granzier and T. C. Irving. Passive tension in cardiac muscle: contribution of collagen, titin, microtubules, and intermediate filaments. *Biophys J*, 68(3):1027–44, 1995.

A. Grutzner, S. Garcia-Manyes, S. Kotter, C. L. Badilla, J. M. Fernandez, and W. A. Linke. Modulation of titin-based stiffness by disulfide bonding in the cardiac titin n2-b unique sequence. *Biophys J*, 97(3):825–34, 2009.

J. M. Gutteridge and B. Halliwell. Free radicals and antioxidants in the year 2000. a historical look to the future. *Ann N Y Acad Sci*, 899:136–47, 2000.

G. R. Hilton, G. K. Hochberg, A. Laganowsky, S. I. McGinnigle, A. J. Baldwin, and J. L. Benesch. C-terminal interactions mediate the quaternary dynamics of alphab-crystallin. *Philos Trans R Soc Lond B Biol Sci*, 368(1617):20110405, 2013.

G. K. Hochberg and J. L. Benesch. Dynamical structure of alphab-crystallin. *Prog Biophys Mol Biol*, 115(1):11–20, 2014.

G. K. Hochberg, H. Ecroyd, C. Liu, D. Cox, D. Cascio, M. R. Sawaya, M. P. Collier, J. Stroud, J. A. Carver, A. J. Baldwin, C. V. Robinson, D. S. Eisenberg, J. L. Benesch, and A. Laganowsky. The structured core domain of alphab-crystallin can prevent amyloid fibrillation and associated toxicity. *Proc Natl Acad Sci U S A*, 111(16):E1562–70, 2014.

J. T. Hopper, K. Sokratous, and N. J. Oldham. Charge state and adduct reduction in electrospray ionization-mass spectrometry using solvent vapor exposure. *Anal Biochem*, 421(2):788–90, 2012.

J. Horwitz, M. P. Bova, L. L. Ding, D. A. Haley, and P. L. Stewart. Lens alpha-crystallin: function and structure. *Eye (Lond)*, 13 (Pt 3b):403–8, 1999.

S. A. Houck, A. Landsbury, J. I. Clark, and R. A. Quinlan. Multiple sites in alpha b-crystallin modulate its interactions with desmin filaments assembled in vitro. *Plos One*, 6(11), 2011.

M. L. Hughes and L. Dougan. The physics of pulling polyproteins: a review of single molecule force spectroscopy using the afm to study protein unfolding. *Rep Prog Phys*, 79(7):076601, 2016.

N. Inagaki, T. Hayashi, T. Arimura, Y. Koga, M. Takahashi, H. Shibata, K. Teraoka, T. Chikamori, A. Yamashina, and A. Kimura. Alpha b-crystallin mutation in dilated cardiomyopathy. *Biochem Biophys Res Commun*, 342(2):379–86, 2006.

W. Kabsch. Xds. *Acta Crystallogr D Biol Crystallogr*, 66(Pt 2):125–32, 2010.

M. S. Kellermayer, S. B. Smith, H. L. Granzier, and C. Bustamante. Folding-unfolding transitions in single titin molecules characterized with laser tweezers. *Science*, 276(5315):1112–6, 1997.

R. Klemenz, A. C. Andres, E. Frohli, R. Schafer, and A. Aoyama. Expression of the murine small heat-shock proteins hsp 25 and alpha-b crystallin in the absence of stress. *Journal of Cell Biology*, 120(3):639–645, 1993.

S. Kotter, A. Unger, N. Hamdani, P. Lang, M. Vorgerd, L. Nagel-Steger, and W. A. Linke. Human myocytes are protected from titin aggregation-induced stiffening by small heat shock proteins. *J Cell Biol*, 204(2):187–202, 2014.

A. R. Kumarapeli, H. Su, W. Huang, M. Tang, H. Zheng, K. M. Horak, M. Li, and X. Wang. Alpha b-crystallin suppresses pressure overload cardiac hypertrophy. *Circ Res*, 103(12):1473–82, 2008.

A. R. Kumarapeli, K. Horak, and X. Wang. Protein quality control in protection against systolic overload cardiomyopathy: the long term role of small heat shock proteins. *Am J Transl Res*, 2 (4):390–401, 2010.

A. Laganowsky, J. L. Benesch, M. Landau, L. Ding, M. R. Sawaya, D. Cascio, Q. Huang, C. V. Robinson, J. Horwitz, and D. Eisenberg. Crystal structures of truncated alphaa and alphab crystallins reveal structural mechanisms of polydispersity important for eye lens function. *Protein Sci*, 19(5):1031–43, 2010.

A. Laganowsky, M. Zhao, A. B. Soriaga, M. R. Sawaya, D. Cascio, and T. O. Yeates. An approach to crystallizing proteins by metal-mediated synthetic symmetrization. *Protein Sci*, 20(11):1876–90, 2011.

M. C. Leake, A. Grutzner, M. Kruger, and W. A. Linke. Mechanical properties of cardiac titin's n2b-region by single-molecule atomic force spectroscopy. *J Struct Biol*, 155(2):263–72, 2006.

M. M. LeWinter, Y. Wu, S. Labeit, and H. Granzier. Cardiac titin: structure, functions and role in disease. *Clin Chim Acta*, 375(1-2):1–9, 2007.

W. A. Linke and N. Hamdani. Gigantic business: titin properties and function through thick and thin. *Circ Res*, 114(6):1052–68, 2014.

G. Lutsch, R. Vetter, U. Offhauss, M. Wieske, H. J. Grone, R. Klemenz, I. Schimke, J. Stahl, and R. Benndorf. Abundance and location of the small heat shock proteins hsp25 and alphab-crystallin in rat and human heart. *Circulation*, 96(10):3466–76, 1997.

Z. Martonfalvi, P. Bianco, M. Linari, M. Caremani, A. Nagy, V. Lombardi, and M. Kellermayer. Low-force transitions in single titin molecules reflect a memory of contractile history. *J Cell Sci*, 127(Pt 4):858–70, 2014.

M. T. Marty, A. J. Baldwin, E. G. Marklund, G. K. Hochberg, J. L. Benesch, and C. V. Robinson. Bayesian deconvolution of mass and ion mobility spectra: from binary interactions to polydisperse ensembles. *Anal Chem*, 87(8):4370–6, 2015.

A. Mashaghi, S. Bezrukavnikov, D. P. Minde, A. S. Wentink, R. Kityk, B. Zachmann-Brand, M. P. Mayer, G. Kramer, B. Bukau, and S. J. Tans. Alternative modes of client binding enable functional plasticity of hsp70. *Nature*, 539(7629):448–451, 2016.

O. Mayans, J. Wuerges, S. Canela, M. Gautel, and M. Wilmanns. Structural evidence for a possible role of reversible disulphide bridge formation in the elasticity of the muscle protein titin. *Structure*, 9(4):331–40, 2001.

A. J. McCoy, R. W. Grosse-Kunstleve, P. D. Adams, M. D. Winn, L. C. Storoni, and R. J. Read. Phaser crystallographic software. *J Appl Crystallogr*, 40(Pt 4):658–674, 2007.

A. Minajeva, M. Kulke, J. M. Fernandez, and W. A. Linke. Unfolding of titin domains explains the viscoelastic behavior of skeletal myofibrils. *Biophys J*, 80(3):1442–51, 2001.

S. Mishra, S. Y. Wu, A. W. Fuller, Z. Wang, K. L. Rose, K. L. Schey, and H. S. McHaourab. Loss of alphab-crystallin function in zebrafish reveals critical roles in the development of the lens and stress resistance of the heart. *J Biol Chem*, 293(2):740–753, 2018.

K. C. Neuman and A. Nagy. Single-molecule force spectroscopy: optical tweezers, magnetic tweezers and atomic force microscopy. *Nat Methods*, 5(6):491–505, 2008.

W. J. Paulus and C. Tschope. A novel paradigm for heart failure with preserved ejection fraction comorbidities drive myocardial dysfunction and remodeling through coronary microvascular endothelial inflammation. *Journal of the American College of Cardiology*, 62(4):263–271, 2013.

Judit Perales-Calvo, David Giganti, Guillaume Stirnemann, and Sergi Garcia-Manyes. The force-dependent mechanism of dnak-mediated mechanical folding. *Science Advances*, 4(2), 2018.

M. P. Ramirez, M. Rivera, D. Quiroga-Roger, A. Bustamante, M. Vega, M. Baez, E. M. Puchner, and C. A. M. Wilson. Single molecule force spectroscopy reveals the effect of bip chaperone on protein folding. *Protein Sci*, 26(7):1404–1412, 2017.

M. Rief, M. Gautel, F. Oesterhelt, J. M. Fernandez, and H. E. Gaub. Reversible unfolding of individual titin immunoglobulin domains by afm. *Science*, 276(5315):1109–12, 1997.

D. J. Rigden, R. M. Keegan, and M. D. Winn. Molecular replacement using ab initio polyalanine models generated with rosetta. *Acta Crystallogr D Biol Crystallogr*, 64(Pt 12):1288–91, 2008.

J. A. Rivas-Pardo, E. C. Eckels, I. Popa, P. Kosuri, W. A. Linke, and J. M. Fernandez. Work done by titin protein folding assists muscle contraction. *Cell Rep*, 14(6):1339–1347, 2016.

N. Stein. Chainsaw: a program for mutating pdb files used as templates in molecular replacement. *Journal of Applied Crystallography*, 41:641–643, 2008.

T. M. Treweek, A. Rekas, M. J. Walker, and J. A. Carver. A quantitative nmr spectroscopic examination of the flexibility of the c-terminal extensions of the molecular chaperones, alphaa- and alphab-crystallin. *Exp Eye Res*, 91(5):691–9, 2010.

T. M. Treweek, S. Meehan, H. Ecroyd, and J. A. Carver. Small heat-shock proteins: important players in regulating cellular proteostasis. *Cell Mol Life Sci*, 72(3):429–451, 2015.

K. Trombitas, M. Greaser, S. Labeit, J. P. Jin, M. Kellermayer, M. Helmes, and H. Granzier. Titin extensibility in situ: Entropic elasticity of permanently folded and permanently unfolded molecular segments. *Journal of Cell Biology*, 140(4):853–859, 1998.

A. Unger, L. Beckendorf, P. Bohme, R. Kley, M. von Frieling-Salewsky, H. Lochmuller, R. Schroder, D. O. Furst, M. Vorgerd, and W. A. Linke. Translocation of molecular chaperones to the titin springs is common in skeletal myopathy patients and affects sarcomere function. *Acta Neuropathol Commun*, 5(1):72, 2017.

F. A. van de Klundert, M. L. Gijsen, IJssel P. R. van den, L. H. Snoeckx, and W. W. de Jong. alpha b-crystallin and hsp25 in neonatal cardiac cells–differences in cellular localization under stress conditions. *Eur J Cell Biol*, 75(1):38–45, 1998.

E. von Castelmur, M. Marino, D. I. Svergun, L. Kreplak, Z. Ucurum-Fotiadis, P. V. Konarev, A. Urzhumtsev, D. Labeit, S. Labeit, and O. Mayans. A regular pattern of ig super-motifs defines segmental flexibility as the elastic mechanism of the titin chain. *Proc Natl Acad Sci U S A*, 105(4):1186–91, 2008.

C. F. Wright, S. A. Teichmann, J. Clarke, and C. M. Dobson. The importance of sequence diversity in the aggregation and evolution of proteins. *Nature*, 438(7069):878–81, 2005.

Y. Zhu, J. Bogomolovas, S. Labeit, and H. Granzier. Single molecule force spectroscopy of the cardiac titin n2b element: effects of the molecular chaperone alphab-crystallin with disease-causing mutations. *J Biol Chem*, 284(20):13914–23, 2009.

L. Zimmermann, A. Stephens, S. Z. Nam, D. Rau, J. Kubler, M. Lozajic, F. Gabler, J. Soding, A. N. Lupas, and V. Alva. A completely reimplemented mpi bioinformatics toolkit with a new hhpred server at its core. *J Mol Biol*, 2017.

Chapter 3

Conformational plasticity and extension pathway of the sHsp client filamin C

3.1 Abstract

The actin-binding protein filamin C (FLNC) performs a variety of functions in striated muscle, many of which point to an ability to sense local force. Describing the structure of FLNC and the molecular basis of its function under force is necessary to understand how its dysfunction can lead to muscle myopathies. Whereas the structure of the mechanosensitive region of its paralog FLNA is known, FLNC contains an 82-residue insertion thus far intractable to structural characterization. In this chapter, I apply native IM-MS and CIU to examine a multi-domain segment of FLNC homologous to the mechanosensing element of FLNA. The results reveal an inherently extensible architecture, in which the insertion populates minor highly solvent-accessible and major compact transiently structured states. I show that collisionally activating FLNC in the gas phase prompts biomechanically relevant unfolding transitions. Finally, the method is applied to a series of single residue FLNC mutations associated with cardiac disease in humans. Effects of the mutations on CIU pathways show a stronger correlation with mutation phenotype than with chemical or spatial similarities. This chapter establishes a foundation for additional work interrogating FLNC-sHsp complexes (Chapter 4), and constitutes the first systematic investigation of CIU as a suitable proxy method for mechanical unfolding of multi-domain functionally elastic proteins.

3.2 Introduction

3.2.1 Filamin structure, function, and implication in disease

Filamins are large modular proteins that play key roles in signalling pathways, cytoskeletal organization, and cellular motility and differentiation. They cross-link actin polymers into a branched three-dimensional gel and are components of cell-cell and cell-matrix adhesion assemblies, withstanding strain as the cytoskeletal network is subjected to cycles of force (Figure **3.1a**). Three paralogs are expressed in adult humans: filamins A, B, and C (Feng and Walsh, 2004; Razinia et al., 2012). Filamins in general, when damaged, can be degraded via a tension-responsive autophagic pathway involving apparent holdase-like binding of Hsp22 (Ulbricht et al., 2013). FLNC in particular (also γ-FLN; ABP-L; FLN2) has been identified as a specific interaction partner of Hsp27 and cvHsp in cardiac and skeletal muscle (Juo et al., 2016; Kley et al., 2013).

FLNC, effectively the only isoform expressed in striated muscle (Ohashi et al., 2005), associates with thin filaments of sarcomeric actin at myofibrillar Z-discs and intercalated discs (Thompson et al., 2000; Xie et al., 1998; van der Ven et al., 2000). Alterations in FLNC genes are linked to distal myopathy (Duff et al., 2011; Furst et al., 2013), myofibrillar myopathy (Kley et al., 2007; Shatunov et al., 2009; Vorgerd et al., 2005), and cardiac-specific pathologies frequently displaying large aggregates (Brodehl et al., 2016; Valdes-Mas et al., 2014; Gomez et al., 2017). In cardiac or skeletal muscle, loss of cvHsp can result in myopathies featuring increased FLNC turnover, sarcomeric and intercalated disc disruption, and FLNC aggregation (Juo et al., 2016; Mercer et al., 2018; Liao et al., 2017). The interaction between FLNC and Hsp27 may also be relevant to disease, having been proposed based on the prevalence of both in protein deposits from patients with myofibrillar myopathy

(Kley et al., 2013).

Human filamins are 280 kDa homodimers in which each N-terminal actin-binding domain is followed by 24 Ig-like domains (d1-d24), the last of which mediates dimerization (Figure **3.1b**) (Sjekloca et al., 2007). The majority of filamin interactors bind within the d16-d24 region (Razinia et al., 2012), which in FLNA can propagate mechanical cues by partially extending under force to reveal cryptic binding sites (Figure **3.1c**) (Ruskamo et al., 2012; Nakamura et al., 2014; Ehrlicher et al., 2011; Lad et al., 2007). Less is known about this region in FLNC, and thus about the molecular basis of many of its functions, partially due to a long insertion of unknown structure in domain 20 (82 amino acids, comparable to the length of an entire additional domain) (Figure **3.1d**). Evidence that FLNC can also sense local force includes functionality that necessitates a degree of plasticity in response to tension (Sutherland-Smith, 2011); high sequence similarity and overlapping roles and binding partners with FLNA (Kesner et al., 2010; Lad et al., 2008); the ability to protect myofibrillar structural integrity during cycles of mechanical stress (Fujita et al., 2012); and in-cell labelling of shielded cysteines with tension (Johnson et al., 2007).

In this chapter, I use IM-MS and CIU to investigate the FLNC mechanosensing region, with the aims of providing a greater understanding of FLNC structure and stability and establishing a base to draw upon in future studies with sHsps.

3.2.2 Native IM-MS, conformational heterogeneity, and intrinsic disorder

$FLNC_{d20}$ contains a large unique insertion that has resisted attempts at crystallization by other groups. Oftentimes, this is an indication of intrinsic disorder (ID), particularly when the remainder of the protein shares such high sequence identity

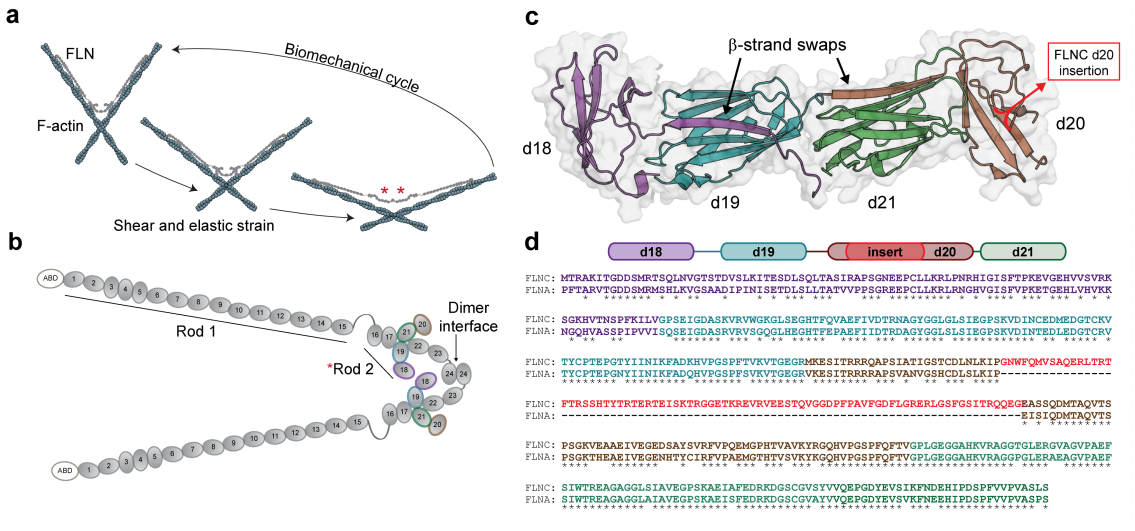


Figure 3.1. Filamins are large mechanosensors which share high homology apart from an insertion in FLNC$_{d20}$. **a.** Schematic of the filamin deformation cycle. Polymeric actin, bound by filamin dimers, is subjected to shear and elastic forces during muscle contraction and cellular motility. Filamin withstands this force via its flexible axis of rotation due to a long structure with a terminal hinge point, and its extensible region (red asterisks). **b.** The filamin dimer comprises an actin-binding domain (ABD) followed by linear (rod 1) and compact (rod 2) Ig domain arrays terminating at d24 which mediates dimerization. **c.** A model of FLNA$_{d18\text{-}21}$, generated by overlay of a solution NMR structure of d18-19 (PDB 2K7Q (Heikkinen et al., 2009)) and an X-ray structure of d19-21 (PDB 2J3S (Lad et al., 2007)), features inter-domain interactions and β-strand swapping, which are disrupted under force. The structure of this region of FLNC, and arrangement of the FLNC d20 insertion, has not been published to date. **d.** Sequence alignment of domains 18-21 of filamins A and C (generated using tcoffee (Notredame et al., 2000)). Asterisks indicate identical residues.

with a well-ordered paralog. Thus, it is worth briefly introducing the application of native IM-MS to IDPs and IDRs (ID proteins and regions).

As discussed in Chapter 1, gentle conditions during nESI ensure that protein structure and noncovalent interactions are maintained upon transfer into the gas phase. This means charge state distributions (CSDs) will reflect solvent-accessible surface area (SASA). Conformational effects dominate the ionization process regardless of protein size and shape (Kaltashov and Mohimen, 2005), with multiple states giving rise to CSDs which can be discrete or multimodal (Li et al., 2016; Testa et al., 2013). An example native mass spectrum of a protein with intrinsically disordered regions is shown in Figure **3.2**.

The relationship between average charge state (z_{av}) and SASA is similar for folded and unfolded proteins acquired under native nESI conditions, diverging slightly at high z_{av} and SASA (Testa et al., 2011), and is largely independent of intrinsic

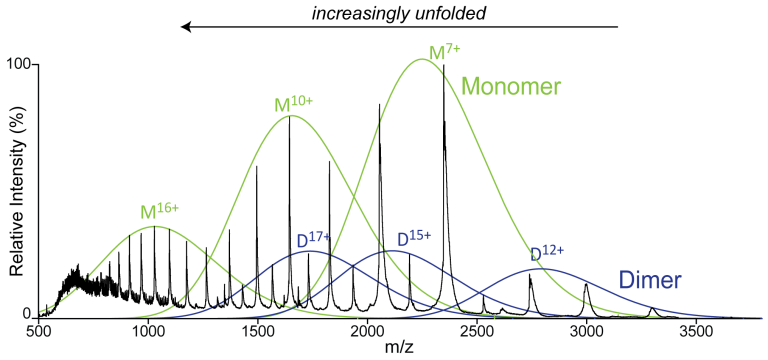


Figure 3.2. Mass spectrum of recombinant human XIRP1, which contains IDRs, acquired under native nESI conditions. Each Gaussian approximates a CSD representing a different conformational state, with breadth dependent on structural dynamics of that state. Monomer and dimer stoichiometries are observed. The construct is XIRP1 isoform A, residues 1686-1812, provided by Carin de Villiers.

basicity (Konermann et al., 2013). These empirically derived relationships have been applied to model partially folded states of IDPs, in good agreement with solvated MD and experimental evidence. In sum, nESI data seems to capture the conformational ensembles of solvated IDPs quite well (Li et al., 2016).

IM is somewhat more controversial. Whereas CSDs acquired at the moment of transfer to the gas phase may reflect solution structural heterogeneity, it does not necessarily follow that throughout the timescale of the experiment, IDP-derived ions retain their original solution dimensions to the same degree that globular proteins do. Studies of p53 and myoglobin found disparities between solution and gas phase structures, which can arise from electrostatically driven expansion in more highly charged species or collapse in lowly charged species (Vahidi et al., 2013; Pagel et al., 2013). Another example of this phenomenon compared the range of sizes of several IDPs by IM-MS and SAXS, finding a wider conformational distribution in the gas phase (Borysik et al., 2015).

Here I harness native IM-MS to examine FLNC domains 18-21, taking these trends into account. I highlight where future MS or complementary experiments would add value. The results shed light on FLNC structure and on the applicability of gas-phase techniques.

3.3 Results and Discussion

3.3.1 FLNC adopts compact and extended conformations modulated by the d20 insertion

To interrogate the conformation of the region of FLNC homologous to mechanosensing FLNA, and the effect of the d20 insertion on its structure, we used native IM-MS to examine several recombinant constructs incorporating d20 (d20-21, d19-21, and d18-21). Each gave rise to two distinct CSDs following nESI, evidencing the presence of two conformations: a dominant low-charge and thus low-SASA state, and a minor more highly charged and relatively extended state (Figure **3.3a**). Quantifying the fraction populating each state revealed that the shorter constructs were somewhat less likely to adopt the extended form than the longest construct (Figure **3.3b**). The z_{avs} of the compact forms closely match the theoretical z_{av} of globular proteins of identical mass (predicted as 10.5^+, 12.8^+, and 14.3^+, respectively) (van de Waterbeemd et al., 2017). This suggests that the constructs adopt architectures that are compact, rather than forming linear arrays of independent domains. To confirm this, we used IM data to calculate CCSs and compared these to theoretical CCSs of linear arrangements of Ig domains with comparable masses (Figure **3.3c**). For each FLNC construct, the CCS of the major state was substantially lower than that predicted for elongated tandem Ig-domain models without inter-domain interactions.

CCSs were not calculated for the extended state, since on a travelling-wave IM instrument the mobility of an elongated ion will differ from that of a compact one, and the globular calibrants used hence do not allow for accurate analysis of this conformer's size from these data (Ruotolo et al., 2008). Nonetheless, we can infer based on the CSD that it has a greater SASA than the compact state but is not fully unfolded. Because the d20 insertion may be an IDR, we hypothesized that

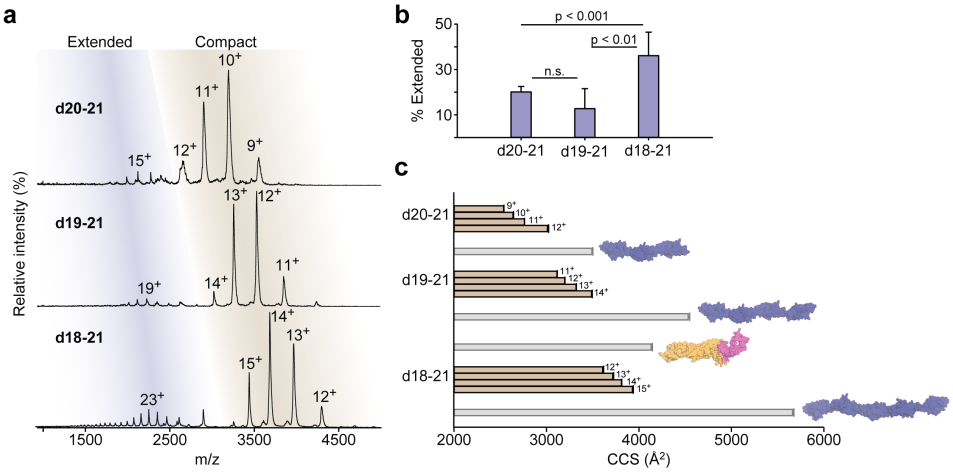


Figure 3.3. FLNC domains adopt two conformations with a dominant compact state. a. Native MS of three FLNC constructs containing d20 at concentration 5 µM. Major and minor CSDs are observed, evidencing conformations with differing SASA. **b.** Fraction of total protein signal arising from extended conformations. Error bars represent one standard deviation; n.s. = not significant by t-test (n = minimum 8). **c.** Experimental collision cross-sections of FLNC conformers; theoretical CCS of models for comparison are faded. Blue structures were derived from PDB 3B43 (titin I65-I70). A homology model of $FLNC_{d19\text{-}21}$ (yellow/pink, from Georg Mlynek, University of Vienna) was constructed using $FLNA_{d19\text{-}21}$ in which the d20 insertion was modelled as a free unstructured region (pink). This model is elongated relative to the compact FLNC structure. CCS error bars represent SD for experimental data (n = minimum 3) and theoretical calculations (n = 5 IMPACT repeats).

this region may be the origin of the ability of all constructs to form an extended conformation. To assess this, we collected native mass spectra of two constructs lacking the insertion (Figure **3.4**). These exhibited unimodal low CSDs, no longer able to adopt extended architectures, implicating the d20 insertion as the source of extension but not the sole source of compaction (an important point, since it rules out artefactual gas-phase collapse of the insertion as the sole reason for compact states). In addition, trace dimer was observed for each. The insertion may therefore shield a FLNC interface that can weakly self-associate.

Thus, the insertion prompts conformational heterogeneity within FLNC as observed by native MS. The key question is whether this behaviour is reflective of solution states, or an artefact of transfer to the gas phase. I posit that it is relevant to the solution structure for several reasons. Firstly, protein structure and disorder prediction algorithms (DisoPred (Jones and Cozzetto, 2015) and Phyre2 (Kelley et al., 2015), which uses PsiPred) return significant β-strand propensity for the d20

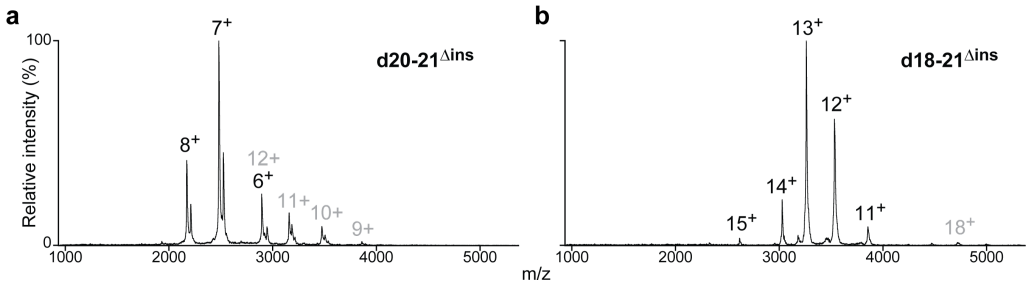


Figure 3.4. Removal of the FLNC d20 insertion yields a single compact conformation that can dimerize. Native MS of 5 μM **a.** d20-21 and **b.** d18-21, each lacking the d20 insertion. Low monomer charge state distributions (black labels) are consistent with compact forms (predicted globular z_{avs} 7.9^{+} and 12.8^{+}, respectively). Small amounts of dimer are detected (grey labels) which persist with addition of DTT (data not shown). d20-21 doublet peaks result from an unidentified adduct. d20-$21^{\Delta ins}$ provided by Georg Mlynek; d18-$21^{\Delta ins}$ provided by Carin de Villiers.

insertion rather than a large random coil. Phyre2 uses template-based modeling to predict secondary structure, whereas DisoPred was trained to identify disordered regions based on high resolution X-ray structures where residues were missing from the density. Predictions (Figure **3.5**) reveal that a region with some secondary structure is not unexpected based on bioinformatical modeling.

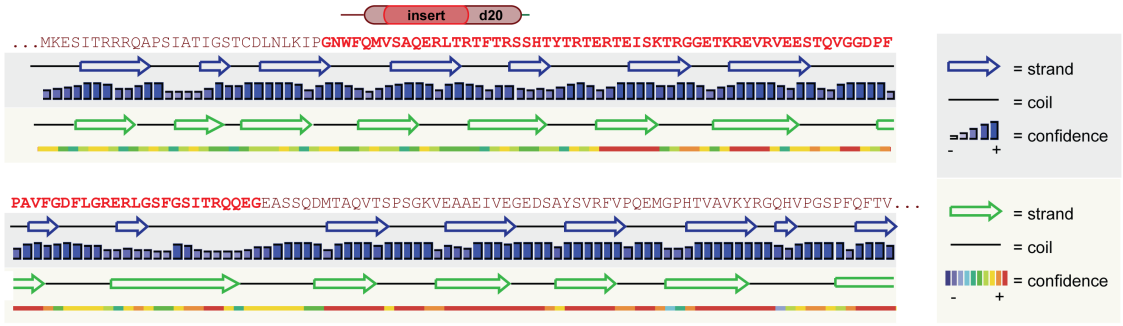


Figure 3.5. Protein structure and disorder prediction algorithms identify β-strand propensity throughout FLNC d20. Sequence of d20 with insertion in bold red and predicted secondary structural elements below according to DisoPred (blue) and Phyre2 (green) (formatted similarly post-hoc). Key indicates each algorithm's scale for confidence in the assignments. Each predicts β-strands within the insertion with intermediate to high confidence.

Second, the approximate density of the compact state does not change upon removal of the insertion (Table 3.1), supporting the hypothesis that the insertion can adopt structure. The nature of this structure is unclear from these data: whether or not it is β-strand rich as predicted based on its sequence, and whether it is

stable at the tertiary level. It could be a native form of molten globule, containing secondary structure with dynamic side chains but no stable tertiary structure, sometimes termed "collapsed disorder" (Xue et al., 2012).

Table 3.1. Densities of FLNC with and without the d20 insertion.

	Mass (Da)	CCS[a] (Å^2)	Density[b] (Da Å^{-3})
d18-21	51,729	3,767	0.30
d18-21 $^{\Delta ins}$	42,474	3,307	0.30

[a]Averaged over compact charge states.
[b]Approximated assuming spherical ions.

Third, the discrepancy between the constructs conformational equilibria (Figure **3.3b**) contrasts what would be expected were the d20 insertion to exist only in a highly solvated state, based on the Chain Ejection Model of ionization (Konermann et al., 2013). As Ig domains are removed, the insertion comprises a greater proportion of the constructs by mass and size. If it were perpetually disordered, the fraction extended should become more, not less, prominent across shrinking constructs. And fourth, analogous nESI-MS behaviour has been observed for other structurally partitioned proteins and experimentally linked to their function. Ataxin-3, 35% IDR by mass, yields a bimodal CSD following nESI, interpreted as an extended state and a metastable state associated with its cytotoxicity (Santambrogio et al., 2012). Similarly, USP5 adopts a bimodal CSD which shifts to the compact form only in the presence of an order-inducing substrate (Scott et al., 2015).

The data suggest that $FLNC_{d18\text{-}21}$ adopts a predominantly compact state, necessitating inter-domain contacts which are likely to be susceptible to breakage under applied force and therefore consistent with mechanosensitive architecture (Sauer et al., 2016).

3.3.2 Gas-phase unfolding occurs via discrete biomechanically relevant transitions

We used collision-induced unfolding (CIU) to investigate the extension pathway and stability of the compact form of FLNC. Because this region undergoes structural rearrangements *in vivo* (Johnson et al., 2007), and filamin domains in general are predicted to be able to fully unfold prior to breakage of the dimer interface at physiologically relevant forces and loading rates (Sutherland-Smith, 2011; Moore et al., 2010), we reasoned that CIU may be useful as a proxy for functionally important mechanical unfolding. The CIU process leads to conformational perturbations and eventual chain extension (Popa et al., 2016; Mehmood et al., 2015). Thus sheared and collisionally activated unfolding share analogous endpoints, with the force-induced pathway dependent largely on the direction and velocity of pulling, and the CIU pathway dependent on Coulombic steering between migrating charges (Popa et al., 2016).

To validate the method as a suitable proxy, we targeted elements of the protein implicated in its ability to sense local force. The first β-strand of d20, which is swapped to associate with d21 in FLNA (Figure **3.1c**) (Lad et al., 2007), is critical for interactions between filamins and binding partners in adhesion assemblies. Both migfilin and β7-integrin displace this β–strand to bind d21 in a mechanism of force-induced cryptic binding (Lad et al., 2008; Kiema et al., 2006). The structure of $FLNA_{d21}$ bound to migfilin-derived peptide is shown in Figure **3.6a**; our collaborators have solved the structure of the migfilin peptide bound to $FLNC_{d21}$ (unpublished), confirming that the binding site is conserved. The insertion in d20 modulates FLNC association with multiple Z-disc proteins (Razinia et al., 2012) and therefore may also be implicated in mechanosensing.

We first carried out CIU of d20-21, focusing on the dominant compact charge

states. As it is collisionally activated, the initial conformation (*A*) transitions through discrete extending forms (*B, C,* etc.). Charge states of a protein can be considered to correspond to various minima on the gas-phase free energy landscape, and may access different unfolding pathways (Chandler and Benesch, 2017) – for example, an additional early transition is observed for 11^+ compared to 10^+ (Figure **3.6b**). Below the WT plots are CIU of d20-21 with the critical β-strand removed (Δd20β). For each charge state (aligned one lower than WT to approximate equivalent surface-charge densities for the most appropriate direct comparison), one of the first unfolding transitions is abolished. This indicates that detachment of the strand is a discrete early step in the gas-phase pathway. CIU after further removal of the d20 insertion from this construct abolishes another unfolding transition (Figure **3.6b** ΔβΔins; one charge state shown because others were confounded by overlapping dimer signal in the mobility dimension). Thus, as elements directly or putatively implicated in mechanosensing are removed, discrete events in the protein's CIU pathway also disappear.

We also assessed these elements' respective contributions to CIU of $FLNC_{d18\text{-}21}$, encompassing more of the mechanosensing region. Two mutations, E2136R and I2138E, were engineered into the critical β-strand to weaken its association with d21. This construct (β-impaired, $^{\beta imp}$d18-21) behaved similarly to ^{WT}d18-21 under no activation, adopting extended and compact states in indistinguishable proportions and sizes (Figure **3.7a**). CIU of $^{\beta imp}$d18-21, however, differed from WT at low charge, with a destabilized 12^+ intermediate (Figure **3.7b**, green boxes).

Next, we unfolded d18-21 lacking the d20 insertion (Δins). Because mass is decreased, Δins ions have fewer degrees of freedom within which they can dissipate activation energy, meaning that if stability is unchanged, the threshold acceleration potential for unfolding should be lower. However, comparing the least Coulombically

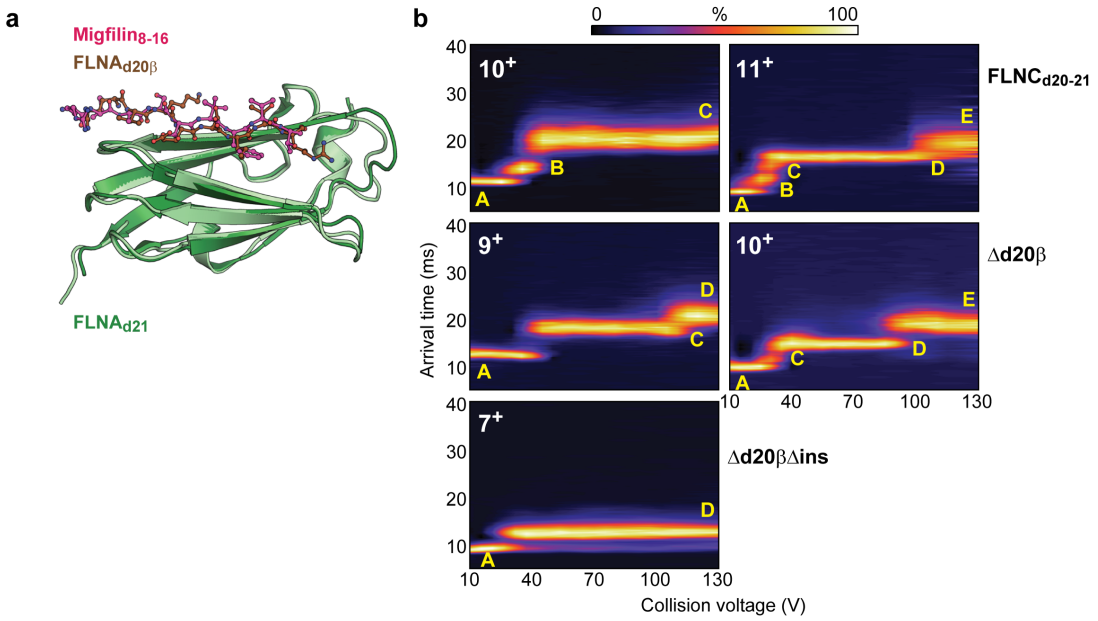


Figure 3.6. The FLNC gas-phase unfolding pathway is mediated by d20 elements and mimics a mechanical unfolding event. a. The first β-strand of $FLNA_{d20}$ (brown) competes with N-terminal residues of migfilin (pink) in binding to $FLNA_{d21}$ (green). Crystal structures, PDB 2J3S and 2W0P. FLNC shares 90% sequence identity with these regions, and binds N-terminal migfilin at the same location. **b.** Removal of the FLNC d20 β-strand and the insertion results in loss of early CIU transitions for d20-21. Letters designate discrete initial and transition states.

frustrated states (12^+ and 10^+, accessed via charge reduction, see Methods), ^{WT}d18-21 required 670 eV to reach the halfway point of the first unfolding transition, whereas $^{\Delta ins}$d18-21 required 800 eV (Figure **3.7b**, white dotted lines; eV_{50} is the product of CV_{50} and charge state). Delayed initial unfolding upon its removal suggests that in the WT segment, the insertion is the first element to unfold.

These results are consistent with a study which found that CIU intermediates accessed by a multi-domain protein depend on tertiary structure, whereas the intermediates' stabilities are sensitive to small changes in primary structure (Eschweiler et al., 2017). The effect of β-strand removal was clear for all d20-21 charge states, but in d18-21, its impairment caused charge state-specific observable change. This can be attributed to the increased complexity of this construct compared to d20-21 introducing more possible unravelling events, such as disruption of inter-domain interactions. These events cause d18-21 CIU intermediates to coalesce in low resolution IM measurements, an effect that becomes more pronounced with increasing

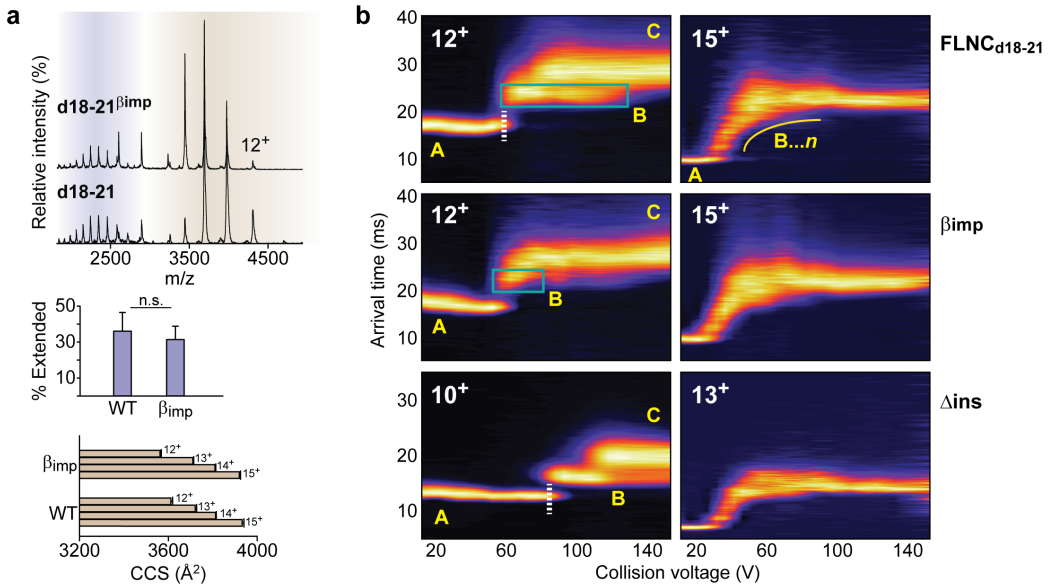


Figure 3.7. FLNC$_{d18\text{-}21}$ exhibits charge-state specific CIU effects upon β-strand impairment and d20 insertion removal. **a.** nESI-MS of β-impaired double mutant E2136R, I2138E compared to WT, and associated extended populations and compact CCSs. The mutations do not significantly change d18-21 resting conformational equilibrium or size. **b.** d18-21 WT and variants CIU: at low Coulombic frustration (left), impairing the β-strand destabilizes an intermediate and removing the d20 insertion prolongs the first transition. At higher charge (right), transitions become less resolved and differences therefore dampened or not present.

charge state (Figure **3.7b**, right). The greater the charge available to migrate to early unfolding elements, the more Coulombic repulsion will drive the process and dampen any differences in stability which, though subtle, may be functionally relevant. This should be considered when designing future experiments, perhaps by deploying the minimal construct necessary to detect CIU effects (provided the construct is still biologically relevant).

From these data, we can begin to construct a mechanism of FLNC unfolding, whereby early events include extension of the d20 insertion; detachment of the first d20 β-strand; and possibly breakage of inter-domain contacts. Next, we further explored the effect of residue-level changes on this pathway.

3.3.3 Cardiomyopathy-associated sequence variants affect FLNC conformational space and stability

Several changes to the *FLNC* gene affecting domain 20 have recently been identified in human patients with cardiomyopathies. Many of these are currently still classified as variants of unknown significance (VUS), requiring further evidence to support disease causality. We used native IM-MS and CIU to probe for effects of a series of seven such variants on FLNC conformation and stability using the d18-21 construct. Sequence alterations are located across d20, lead to varying biochemical and steric changes, and are of interest in relation to dilated cardiomyopathy (DCM), hypertrophic cardiomyopathy (HCM), and/or restrictive cardiomyopathy (RCM), as summarized in Table 3.2. Although *in vivo* aggregation of FLNC upon pathogenic sequence alterations is common (Furst et al., 2013), aggregation has not been observed for any of the variants explored here.

Table 3.2. FLNC variants explored in the present study.

Variant	Location within d20[a]	Phenotype	Source
I2160F	proximal	RCM	Brodehl et al. (2016)
W2164C	insertion	VUS. Complex CM, HCM-like features	WGS500[b]
R2180P	insertion	VUS. DCM	OMGL[c]
R2228W	insertion	VUS. HCM	BRRD[d]
R2293C	distal	VUS. DCM	OMGL
P2298S	distal	HCM	Gomez et al. (2017)
P2301A	distal	VUS. HCM	Gomez et al. (2017)

[a]Proximal and distal refer to d20 segments N- and C-terminally flanking the insertion, respectively.
[b]Next-generation sequencing project involving the Wellcome trust Centre for Human Genetics
[c]Oxford Medical Genetics Laboratories
[d]Bioresource Rare Disease Database

All variants exhibited similar ionization behaviour to WT, with bimodal CSDs indicating compact and extended states (Figure **3.8a**). None caused a shift toward a greater extended population or a more compact state than WT. Four of the mutants displayed significantly less extension (Figure **3.8b**) and three displayed a very small

(approximately 1%) increase in CCS of the compact state, as measured across several charge states (Figure **3.8c**). This may indicate that the compact state is in fact somewhat collapsed at the endpoint of the IM cell, imposing a lower limit on the CCS. Relative amounts of extension as measured by CSDs therefore may be more likely to reflect in-solution differences, though it should be noted that these can vary across repeat recombinant protein preparations of the same construct, and care must be taken to handle all samples to be compared identically. Validation by a solution measurement that can report on conformation, solvent accessibility, and/or degree of disorder – such as circular dichroism spectroscopy, small angle X-ray scattering, or hydrogen-deuterium exchange MS, or NMR spectroscopy, in order of increasing residue-level resolving power – would add confidence, and is recommended to accompany publication of these findings.

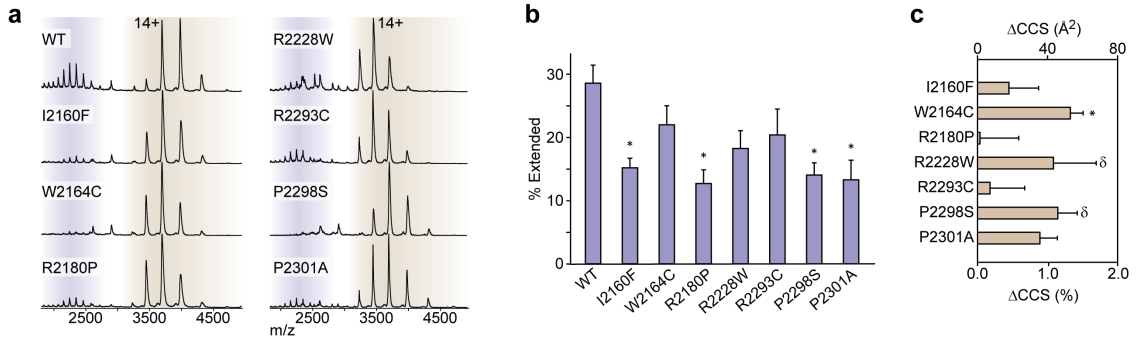


Figure 3.8. Cardiomyopathy-associated sequence mutations within FLNC d20 affect conformational equilibria. a. Representative native MS of each $FLNC_{d18\text{-}21}$ variant. **b.** Fraction of each variant adopting an extended state as opposed to compact (n = minimum 8). **c.** Quantitation of the change in CCS of the compact state of d18-21 for each mutation, using the average of CCSs calculated from charge states 13^+, 14^+, and 15^+ (n = minimum 4). Shifts are very minor and none of the variants became more compact, suggesting a lower limit for CCS of this construct may exist due to some gas-phase collapse. Error bars represent SEM; δ= p <0.05, * = p <0.01 by t-test.

HCM and DCM disorders are complex and arise from a variety of causes, but at the most general level, feature overly stiff and overly compliant ventricular tissue, respectively. They share characteristic impaired cardiac contractility. RCM is more rare and usually accompanied by normal contractility, but abnormal relaxation (Brieler et al., 2017). Since these phenotypes may result from FLNC dysfunction under force, we collected CIU ramps for each $FLNC_{d18\text{-}21}$ variant and subtracted the

resulting plots from that of WT to visualize differences between unfolding pathways (Figure **3.9a**). In agreement with previous CIU results (Figure **3.7**), differences usually manifested as charge state decreased. A dataset of 18 paired repeat CIU experiments was collated to derive a threshold for significant difference from WT based on root mean square deviations across multiple charge states (Figure **3.9b**).

To examine the underlying causes of CIU differences, we considered several possible factors. These included, not mutually exclusively, chemical similarities between residue substitutions, affecting sterics or charge; spatial nature of residue substitutions, hypothesizing that alterations in the same regions of d20 would affect stability similarly; or phenotypic variation, where the outcomes might correlate with associated pathologies. Regarding chemical similaries, all three arginine substitutions (R2180P, R2228W, R2293C) affected CIU. This might be attributed to Coulombic effects in part, but not in full based on the outlying R2180P trend of enhanced differences with decreasing charge state. Two proline removals (P2298S, P2301A) and two cysteine introductions (W2164C, R2293C) produced contrasting and similar effects, respectively. Chemical changes were thus moderately correlated with CIU behaviour. Spatial groupings were also useful predictors in part: sequence alterations within the insertion were more likely than outside the insertion to effect change, but mutation pairs separated by only two (P2298S, P2301A) and three (I2160F, W2164C) residues each yielded different outcomes.

Five of six variants associated with DCM or HCM altered unfolding, with two putative DCM mutations causing the most drastic changes (Figure **3.9b**). The sole RCM-associated variant did not affect FLNC unfolding (though some patients in the cohort expressing W2164C display RCM-like features). Coulombically driven unfolding thus seems to be a promising avenue for investigating the pathway and stability of mechanosensitive protein variants under perturbation. Further study on

these variants, in the clinic and *in vacuo*, would help define the robustness of this correlation.

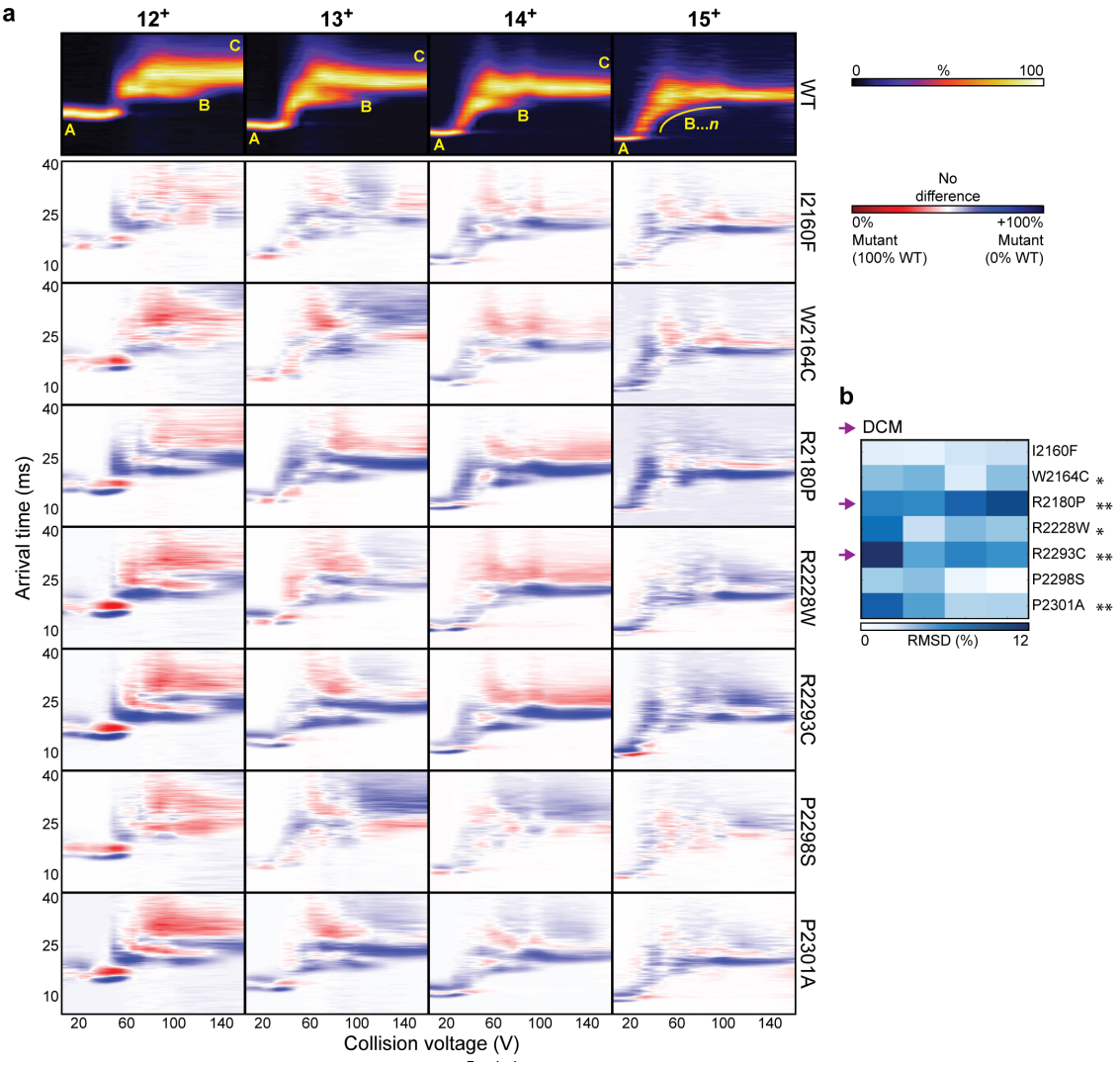


Figure 3.9. Effects of disease-associated FLNC d20 mutations on d18-21 CIU. a. Top row, WT collisional unfolding plots across four compact charge states with initial and transition states labeled where discernable. Below, difference plots between each variant and WT. Initial arrival times were aligned so that any differences reflect changes in the unfolding pathway rather than starting size. **b.** RMSD between each variant and WT plot in **a**. (* = p <0.01, ** = p <0.001 by 1-tailed t-test)

3.4 Conclusions

In this chapter, I have presented novel structural insight into the sHsp client FLNC and demonstrated the utility and limitations of native IM-MS and CIU for its characterization. No structural data has been published on these FLNC domains that lie within its distal region, only homology and evidence of force sensing capability. We show that domains 18-21 assume a compact architecture, in which the 82-residue insertion within d20 can be intrinsically disordered or transiently structured. This coheres with mechanosensitivity, allowing a hierarchy of extension under force.

To probe this hierarchy, we carried out CIU experiments and found that the method is able to resolve the discrete early removal of a single critical β-strand which conceals a cryptic binding site for cell-matrix adhesion partners. Further, mutating this β-strand to weaken its intramolecular association destabilizes a CIU intermediate while leaving the equilibrium architecture of the d18-21 region unaffected. Turning next to a series of cardiomyopathy-linked variants within d20, we found that a selection of these altered conformational equilibria and that 5 of 6 mutations associated with contractile-deficient heart disease altered the CIU behaviour of domains 18-21. Two variants, R2180P and P2301A, significantly affected both conformation and force response. Without quantitatively extrapolating to solution-phase behaviour, our findings align with the prevailing view that CIU trajectories are useful fingerprints for comparison between protein variants (Dixit et al., 2018).

We propose a mechanism (Figure **3.10**) whereby extension of the transiently structured d20 insertion is the first event along the FLNC distal unfolding pathway, similar to the way unstructured extensible segments within titin act as weak links in the chain to confer elasticity to the protein (Chapter 2). This is followed by inter-domain ruptures and removal of the first d20 β-strand, and eventually domain

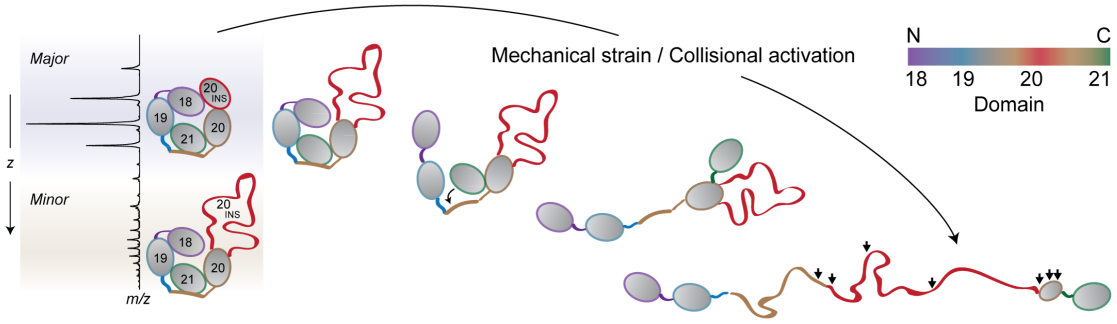


Figure 3.10. Summary: proposed mechanism of FLNC force response. Domains 18-21 adopt a compact form in which the d20 insertion is transiently structured in the major state and unstructured in the minor state. Domain outline colors correspond to the colors used in Figure 3.1 (key, upper right). Schema show examples of possible inter-domain interactions and may not represent the true arrangement. Under perturbation the insertion, if not already disordered, unravels, followed by extension at domain hinges and removal of the first d20 β-strand (curved arrow, middle) to reveal cryptic binding sites for adhesion assembly partners, and finally Ig domain unfolding. Regions of canonical d20 may be among the first to unfold, given the reported impacts on stability caused by cardiac disease-associated mutations (arrows in final state).

unfolding. Notably, the extent of FLNC deformation *in vivo* will depend on detachment kinetics of its peripheral dimer and actin interfaces, since breakage of these would lessen the strain borne by internal domains (Moore et al., 2010). Available evidence suggests that reversible filamin domain unfolding and actin unbinding are energetically similar and each more common than dimer rupture at physiological forces and low loading rates (Sutherland-Smith, 2011; Furuike et al., 2001). The likelihood of deformation is compounded during mechanical stress due to increased force loading rates, the key biophysical determinant by which cells fine-tune mechanotransductive processes (Elosegui-Artola et al., 2018).

Genetic alterations to FLNC or its binding partners could impair its force response by weakening or strengthening certain elements against extension, or modifying the resting conformational equilibrium. This impairment warrants further investigation as an underlying cause of pathologies. Thus, whether FLNC interactions with sHsps are related to its force response will be of interest as well. Importantly, the results support the use of CIU to inform on biomechanically relevant protein behaviour.

Acknowledgments

I am grateful to Carin de Villiers, Giulia Poloni, Katja Gehmlich, and Hugh Watkins for their steering of a much broader FLNC project, for helpful discussions and expertise in filamin biology, and for providing recombinant protein and plasmids. Dieter Fürst and Peter van der Ven first generated the d18-21 and XIRP1 constructs. Thanks to Kristina Djinovic Carugo and Georg Mlynek for designing and providing all of the d20-21 samples and for sharing their work on this system; Timothy Allison for implementing numerous tools in the PULSAR software to assist in processing and comparing the data; and Shane Chandler for helpful discussion throughout and for review of the final chapter.

3.5 Methods

Expression and purification of $FLNC_{d18\text{-}21}$ and variants

Human $FLNC_{d18\text{-}21}$ (WT, Δinsertion, and containing single-residue mutations inserted by site-directed mutagenesis) encoded in pET23-EEF vector with a C-terminal 6xHis tag was transformed into *E. coli* BL21(DE3) pLysS cells (Agilent). Protein was expressed in LB media for 16 hours at 21°C following cell culture growth to OD >0.6 and induction with 0.5 mM IPTG. Typically, an 800 mL expression yielded 30-40 mg sufficiently pure protein. Cells were lysed in 300 mM NaCl, 50 mM Tris, 20 mM imidazole, 5 mM BME at pH 7.7 with EDTA-free protease inhibitor cocktail (Roche) using a microfluidizer. The lysate was clarified by centrifugation at 4°C and 20,000xg for 20 minutes, filtered through a 0.22 μm filter, and loaded onto a 5 mL HisTrap HP column. Protein was eluted using the loading buffer with 500 mM imidazole, concentrated and injected onto a S200 (10/300) column at 4°C. Purity was assessed by SDS-PAGE and protein was stored in 200 mM ammonium acetate pH 6.9 at 4°C and used for MS experiments within 48 hours. Concentration was determined by absorbance at 280 nm. Remaining protein was flash-frozen and stored at -80°C and subjected to SEC and SDS-PAGE quality control again prior to any further experiments, after noticing in initial preparations some propensity for truncation and aggregation over time.

Human $FLNC_{d20\text{-}21}$ and $FLNC_{d19\text{-}21}$ and variants thereof were provided by Georg Mlynek, University of Vienna, in PBS with 2M urea and 250 mM imidazole and stored at -80°C until use. Prior to MS these were buffer exchanged into 200 mM ammonium acetate via SEC.

Native mass spectrometry

Native IM-MS data were recorded on a Synapt G2 mass spectrometer (Waters) modified for the transmission of intact noncovalent protein complexes (Bush et al., 2010) using gold-plated capillaries prepared in-house. Protein concentration was 5 μM. Spectra were recorded with settings as follows: capillary 1.45kV, sample cone 30V; extractor cone 3V; backing pressure 3.8 mbar; trap gas (argon) flow 4 mL min^{-1}; transfer cell voltage 5V; trap cell voltage 5V for all acquisitions used for CCS measurement, and ramped upward in 5V increments until signal was no longer present for all CIU plots. Technical repeats were collected in the presence of acetonitrile vapour in order to promote charge reduction (Hopper et al., 2012). The mobility cell gas flow was 22 mL min^{-1}; wave velocity 300 m s^{-1}; and wave height 5.5V for CCS measurements and 7.0V for CIU experiments.

To derive a threshold for CIU difference, a dataset of 18 repeat unfolding experiments on various FLNC conformers and charge states was used to calculate RMSDs between plots, and each grouping of four charge state RMSDs for each mutant was compared to this dataset by a 1-tailed t-test.

Calculation of experimental and predicted collision cross-sections

To calculate experimental CCS values, mass spectra of β-lactoglobulin and avidin were collected under identical drift cell conditions as all FLNC constructs and used to construct a calibration in PULSAR (Allison et al., 2015) which had R^2 0.9635 using a power law linear fit.

To calculate theoretical CCS values, models from the PDB were first trimmed in PyMol. CCSs were calculated by the projection approximation method using IMPACT (Marklund et al., 2015) accounting for diatomic nitrogen as the collision gas (rProbe set to 1.4; output multiplied by 1.14).

Quantitation of extended and compact conformations

UniDec was used to batch convert raw files containing MS data into text files. These were input into a custom Python script (written by Tim Allison) which takes arguments of mass and a charge range, locates maxima above a set threshold at expected peak values, and normalizes and sums their intensities, dividing each by the following correction for changes in MCP ion detection efficiency with m/z (Fraser, 2002):

$$c = \frac{1}{60}(1 - e^{-1620(\frac{9.1}{m/z})^{1.75}})$$

For each construct, the charge range was split between compact and extended conformations based on observed CSDs such that two sums were generated for each mass spectrum. Data with trap entrance potentials ranging from 5-25V, with and without acetonitrile charge reduction, were combined for a minimum of 8 acquisitions per protein and 100+ scans per acquisition.

References

T. M. Allison, E. Reading, I. Liko, A. J. Baldwin, A. Laganowsky, and C. V. Robinson. Quantifying the stabilizing effects of protein-ligand interactions in the gas phase. *Nat Commun*, 6:8551, 2015.

A. J. Borysik, D. Kovacs, M. Guharoy, and P. Tompa. Ensemble methods enable a new definition for the solution to gas-phase transfer of intrinsically disordered proteins. *J Am Chem Soc*, 137 (43):13807–17, 2015.

J. Brieler, M. A. Breeden, and J. Tucker. Cardiomyopathy: An overview. *Am Fam Physician*, 96 (10):640–646, 2017.

A. Brodehl, R. A. Ferrier, S. J. Hamilton, S. C. Greenway, M. A. Brundler, W. Yu, W. T. Gibson, M. L. McKinnon, B. McGillivray, N. Alvarez, M. Giuffre, J. Schwartzentruber, Forge Canada Consortium, and B. Gerull. Mutations in flnc are associated with familial restrictive cardiomyopathy. *Hum Mutat*, 37(3):269–79, 2016.

M. F. Bush, Z. Hall, K. Giles, J. Hoyes, C. V. Robinson, and B. T. Ruotolo. Collision cross sections of proteins and their complexes: a calibration framework and database for gas-phase structural biology. *Anal Chem*, 82(22):9557–65, 2010.

S. A. Chandler and J. L. Benesch. Mass spectrometry beyond the native state. *Curr Opin Chem Biol*, 42:130–137, 2017.

S. M. Dixit, D. A. Polasky, and B. T. Ruotolo. Collision induced unfolding of isolated proteins in the gas phase: past, present, and future. *Curr Opin Chem Biol*, 42:93–100, 2018.

R. M. Duff, V. Tay, P. Hackman, G. Ravenscroft, C. McLean, P. Kennedy, A. Steinbach, W. Schoffler, P. F. M. van der Ven, D. O. Furst, J. Song, K. Djinovic-Carugo, S. Penttila, O. Raheem, K. Reardon, A. Malandrini, S. Gambelli, M. Villanova, K. J. Nowak, D. R. Williams, J. E. Landers, Jr. Brown, R. H., B. Udd, and N. G. Laing. Mutations in the n-terminal actin-binding domain of filamin c cause a distal myopathy. *Am J Hum Genet*, 88(6):729–740, 2011.

A. J. Ehrlicher, F. Nakamura, J. H. Hartwig, D. A. Weitz, and T. P. Stossel. Mechanical strain in actin networks regulates filgap and integrin binding to filamin a. *Nature*, 478(7368):260–3, 2011.

A. Elosegui-Artola, X. Trepat, and P. Roca-Cusachs. Control of mechanotransduction by molecular clutch dynamics. *Trends Cell Biol*, 2018.

J. D. Eschweiler, R. Kerr, J. Rabuck-Gibbons, and B. T. Ruotolo. Sizing up protein-ligand complexes: The rise of structural mass spectrometry approaches in the pharmaceutical sciences. *Annu Rev Anal Chem (Palo Alto Calif)*, 10(1):25–44, 2017.

Y. Feng and C. A. Walsh. The many faces of filamin: a versatile molecular scaffold for cell motility and signalling. *Nat Cell Biol*, 6(11):1034–8, 2004.

G. W. Fraser. The ion detection efficiency of microchannel plates (mcps). *International Journal of Mass Spectrometry*, 215(1-3):13–30, 2002.

M. Fujita, H. Mitsuhashi, S. Isogai, T. Nakata, A. Kawakami, I. Nonaka, S. Noguchi, Y. K. Hayashi, I. Nishino, and A. Kudo. Filamin c plays an essential role in the maintenance of the structural integrity of cardiac and skeletal muscles, revealed by the medaka mutant zacro. *Dev Biol*, 361 (1):79–89, 2012.

D. O. Furst, L. G. Goldfarb, R. A. Kley, M. Vorgerd, M. Olive, and P. F. van der Ven. Filamin c-related myopathies: pathology and mechanisms. *Acta Neuropathol*, 125(1):33–46, 2013.

S. Furuike, T. Ito, and M. Yamazaki. Mechanical unfolding of single filamin a (abp-280) molecules detected by atomic force microscopy. *FEBS Lett*, 498(1):72–5, 2001.

J. Gomez, R. Lorca, J. R. Reguero, C. Moris, M. Martin, S. Tranche, B. Alonso, S. Iglesias, V. Alvarez, B. Diaz-Molina, P. Avanzas, and E. Coto. Screening of the filamin c gene in a large cohort of hypertrophic cardiomyopathy patients. *Circ Cardiovasc Genet*, 10(2), 2017.

O. K. Heikkinen, S. Ruskamo, P. V. Konarev, D. I. Svergun, T. Iivanainen, S. M. Heikkinen, P. Permi, H. Koskela, I. Kilpelainen, and J. Ylanne. Atomic structures of two novel immunoglobulin-like domain pairs in the actin cross-linking protein filamin. *J Biol Chem*, 284 (37):25450–8, 2009.

J. T. Hopper, K. Sokratous, and N. J. Oldham. Charge state and adduct reduction in electrospray ionization-mass spectrometry using solvent vapor exposure. *Anal Biochem*, 421(2):788–90, 2012.

C. P. Johnson, H. Y. Tang, C. Carag, D. W. Speicher, and D. E. Discher. Forced unfolding of proteins within cells. *Science*, 317(5838):663–6, 2007.

D. T. Jones and D. Cozzetto. Disopred3: precise disordered region predictions with annotated protein-binding activity. *Bioinformatics*, 31(6):857–63, 2015.

L. Y. Juo, W. C. Liao, Y. L. Shih, B. Y. Yang, A. B. Liu, and Y. T. Yan. Hspb7 interacts with dimerized flnc and its absence results in progressive myopathy in skeletal muscles. *J Cell Sci*, 129(8):1661–70, 2016.

I. A. Kaltashov and A. Mohimen. Estimates of protein surface areas in solution by electrospray ionization mass spectrometry. *Anal Chem*, 77(16):5370–9, 2005.

L. A. Kelley, S. Mezulis, C. M. Yates, M. N. Wass, and M. J. Sternberg. The phyre2 web portal for protein modeling, prediction and analysis. *Nat Protoc*, 10(6):845–58, 2015.

B. A. Kesner, S. L. Milgram, B. R. Temple, and N. V. Dokholyan. Isoform divergence of the filamin family of proteins. *Mol Biol Evol*, 27(2):283–95, 2010.

T. Kiema, Y. Lad, P. Jiang, C. L. Oxley, M. Baldassarre, K. L. Wegener, I. D. Campbell, J. Ylanne, and D. A. Calderwood. The molecular basis of filamin binding to integrins and competition with talin. *Mol Cell*, 21(3):337–47, 2006.

R. A. Kley, Y. Hellenbroich, P. F. van der Ven, D. O. Furst, A. Huebner, V. Bruchertseifer, S. A. Peters, C. M. Heyer, J. Kirschner, R. Schroder, D. Fischer, K. Muller, K. Tolksdorf, K. Eger, A. Germing, T. Brodherr, C. Reum, M. C. Walter, H. Lochmuller, U. P. Ketelsen, and M. Vorgerd. Clinical and morphological phenotype of the filamin myopathy: a study of 31 german patients. *Brain*, 130(Pt 12):3250–64, 2007.

R. A. Kley, A. Maerkens, Y. Leber, V. Theis, A. Schreiner, P. F. van der Ven, J. Uszkoreit, C. Stephan, S. Eulitz, N. Euler, J. Kirschner, K. Muller, H. E. Meyer, M. Tegenthoff, D. O. Furst, M. Vorgerd, T. Muller, and K. Marcus. A combined laser microdissection and mass spectrometry approach reveals new disease relevant proteins accumulating in aggregates of filaminopathy patients. *Mol Cell Proteomics*, 12(1):215–27, 2013.

L. Konermann, E. Ahadi, A. D. Rodriguez, and S. Vahidi. Unraveling the mechanism of electrospray ionization. *Anal Chem*, 85(1):2–9, 2013.

Y. Lad, T. Kiema, P. Jiang, O. T. Pentikainen, C. H. Coles, I. D. Campbell, D. A. Calderwood, and J. Ylanne. Structure of three tandem filamin domains reveals auto-inhibition of ligand binding. *EMBO J*, 26(17):3993–4004, 2007.

Y. Lad, P. Jiang, S. Ruskamo, D. S. Harburger, J. Ylanne, I. D. Campbell, and D. A. Calderwood. Structural basis of the migfilin-filamin interaction and competition with integrin beta tails. *J Biol Chem*, 283(50):35154–63, 2008.

J. Li, C. Santambrogio, S. Brocca, G. Rossetti, P. Carloni, and R. Grandori. Conformational effects in protein electrospray-ionization mass spectrometry. *Mass Spectrom Rev*, 35(1):111–22, 2016.

W. C. Liao, L. Y. Juo, Y. L. Shih, Y. H. Chen, and Y. T. Yan. Hspb7 prevents cardiac conduction system defect through maintaining intercalated disc integrity. *PLoS Genet*, 13(8):e1006984, 2017.

E. G. Marklund, M. T. Degiacomi, C. V. Robinson, A. J. Baldwin, and J. L. Benesch. Collision cross sections for structural proteomics. *Structure*, 23(4):791–9, 2015.

S. Mehmood, T. M. Allison, and C. V. Robinson. Mass spectrometry of protein complexes: from origins to applications. *Annu Rev Phys Chem*, 66:453–74, 2015.

E. J. Mercer, Y. F. Lin, L. Cohen-Gould, and T. Evans. Hspb7 is a cardioprotective chaperone facilitating sarcomeric proteostasis. *Dev Biol*, 2018.

S. W. Moore, P. Roca-Cusachs, and M. P. Sheetz. Stretchy proteins on stretchy substrates: the important elements of integrin-mediated rigidity sensing. *Dev Cell*, 19(2):194–206, 2010.

F. Nakamura, M. Song, J. H. Hartwig, and T. P. Stossel. Documentation and localization of force-mediated filamin a domain perturbations in moving cells. *Nat Commun*, 5:4656, 2014.

C. Notredame, D. G. Higgins, and J. Heringa. T-coffee: A novel method for fast and accurate multiple sequence alignment. *J Mol Biol*, 302(1):205–17, 2000.

K. Ohashi, K. Oshima, M. Tachikawa, N. Morikawa, Y. Hashimoto, M. Ito, H. Mori, T. Kuribayashi, and A. G. Terasaki. Chicken gizzard filamin, retina filamin and cgabp260 are respectively, smooth muscle-, non-muscle- and pan-muscle-type isoforms: distribution and localization in muscles. *Cell Motil Cytoskeleton*, 61(4):214–25, 2005.

K. Pagel, E. Natan, Z. Hall, A. R. Fersht, and C. V. Robinson. Intrinsically disordered p53 and its complexes populate compact conformations in the gas phase. *Angew Chem Int Ed Engl*, 52 (1):361–5, 2013.

V. Popa, D. A. Trecroce, R. G. McAllister, and L. Konermann. Collision-induced dissociation of electrosprayed protein complexes: An all-atom molecular dynamics model with mobile protons. *J Phys Chem B*, 120(23):5114–24, 2016.

Z. Razinia, T. Makela, J. Ylanne, and D. A. Calderwood. Filamins in mechanosensing and signaling. *Annu Rev Biophys*, 41:227–46, 2012.

B. T. Ruotolo, J. L. Benesch, A. M. Sandercock, S. J. Hyung, and C. V. Robinson. Ion mobility-mass spectrometry analysis of large protein complexes. *Nat Protoc*, 3(7):1139–52, 2008.

S. Ruskamo, R. Gilbert, G. Hofmann, P. Jiang, I. D. Campbell, J. Ylanne, and U. Pentikainen. The c-terminal rod 2 fragment of filamin a forms a compact structure that can be extended. *Biochem J*, 446(2):261–9, 2012.

C. Santambrogio, A. M. Frana, A. Natalello, E. Papaleo, M. E. Regonesi, S. M. Doglia, P. Tortora, G. Invernizzi, and R. Grandori. The role of the central flexible region on the aggregation and conformational properties of human ataxin-3. *FEBS J*, 279(3):451–63, 2012.

M. M. Sauer, R. P. Jakob, J. Eras, S. Baday, D. Eris, G. Navarra, S. Berneche, B. Ernst, T. Maier, and R. Glockshuber. Catch-bond mechanism of the bacterial adhesin fimh. *Nat Commun*, 7: 10738, 2016.

D. Scott, R. Layfield, and N. J. Oldham. Ion mobility-mass spectrometry reveals conformational flexibility in the deubiquitinating enzyme usp5. *Proteomics*, 15(16):2835–41, 2015.

A. Shatunov, M. Olive, Z. Odgerel, C. Stadelmann-Nessler, K. Irlbacher, F. van Landeghem, M. Bayarsaikhan, H. S. Lee, B. Goudeau, P. F. Chinnery, V. Straub, D. Hilton-Jones, M. S. Damian, A. Kaminska, P. Vicart, K. Bushby, M. C. Dalakas, N. Sambuughin, I. Ferrer, H. H. Goebel, and L. G. Goldfarb. In-frame deletion in the seventh immunoglobulin-like repeat of filamin c in a family with myofibrillar myopathy. *Eur J Hum Genet*, 17(5):656–63, 2009.

L. Sjekloca, R. Pudas, B. Sjoblom, P. Konarev, O. Carugo, V. Rybin, T. R. Kiema, D. Svergun, J. Ylanne, and K. Djinovic Carugo. Crystal structure of human filamin c domain 23 and small angle scattering model for filamin c 23-24 dimer. *J Mol Biol*, 368(4):1011–23, 2007.

A. J. Sutherland-Smith. Filamin structure, function and mechanics: are altered filamin-mediated force responses associated with human disease? *Biophys Rev*, 3(1):15–23, 2011.

L. Testa, S. Brocca, and R. Grandori. Charge-surface correlation in electrospray ionization of folded and unfolded proteins. *Anal Chem*, 83(17):6459–63, 2011.

L. Testa, S. Brocca, C. Santambrogio, A. D'Urzo, J. Habchi, S. Longhi, V. N. Uversky, and R. Grandori. Extracting structural information from charge-state distributions of intrinsically disordered proteins by non-denaturing electrospray-ionization mass spectrometry. *Intrinsically Disord Proteins*, 1(1):e25068, 2013.

T. G. Thompson, Y. M. Chan, A. A. Hack, M. Brosius, M. Rajala, H. G. Lidov, E. M. McNally, S. Watkins, and L. M. Kunkel. Filamin 2 (fln2): A muscle-specific sarcoglycan interacting protein. *J Cell Biol*, 148(1):115–26, 2000.

A. Ulbricht, F. J. Eppler, V. E. Tapia, P. F. van der Ven, N. Hampe, N. Hersch, P. Vakeel, D. Stadel, A. Haas, P. Saftig, C. Behrends, D. O. Furst, R. Volkmer, B. Hoffmann, W. Kolanus, and J. Hohfeld. Cellular mechanotransduction relies on tension-induced and chaperone-assisted autophagy. *Curr Biol*, 23(5):430–5, 2013.

S. Vahidi, B. B. Stocks, and L. Konermann. Partially disordered proteins studied by ion mobility-mass spectrometry: implications for the preservation of solution phase structure in the gas phase. *Anal Chem*, 85(21):10471–8, 2013.

R. Valdes-Mas, A. Gutierrez-Fernandez, J. Gomez, E. Coto, A. Astudillo, D. A. Puente, J. R. Reguero, V. Alvarez, C. Moris, D. Leon, M. Martin, X. S. Puente, and C. Lopez-Otin. Mutations in filamin c cause a new form of familial hypertrophic cardiomyopathy. *Nat Commun*, 5:5326, 2014.

M. van de Waterbeemd, K. L. Fort, D. Boll, M. Reinhardt-Szyba, A. Routh, A. Makarov, and A. J. Heck. High-fidelity mass analysis unveils heterogeneity in intact ribosomal particles. *Nat Methods*, 14(3):283–286, 2017.

P. F. van der Ven, W. M. Obermann, B. Lemke, M. Gautel, K. Weber, and D. O. Furst. Characterization of muscle filamin isoforms suggests a possible role of gamma-filamin/abp-l in sarcomeric z-disc formation. *Cell Motil Cytoskeleton*, 45(2):149–62, 2000.

M. Vorgerd, P. F. van der Ven, V. Bruchertseifer, T. Lowe, R. A. Kley, R. Schroder, H. Lochmuller, M. Himmel, K. Koehler, D. O. Furst, and A. Huebner. A mutation in the dimerization domain of filamin c causes a novel type of autosomal dominant myofibrillar myopathy. *Am J Hum Genet*, 77(2):297–304, 2005.

Z. Xie, W. Xu, E. W. Davie, and D. W. Chung. Molecular cloning of human abpl, an actin-binding protein homologue. *Biochem Biophys Res Commun*, 251(3):914–9, 1998.

B. Xue, A. K. Dunker, and V. N. Uversky. The roles of intrinsic disorder in orchestrating the wnt-pathway. *J Biomol Struct Dyn*, 29(5):843–61, 2012.

Chapter 4

Phosphorylation of Hsp27 regulates its mechanosensitive interaction with native filamin C

4.1 Abstract

Hsp27 is the most widely expressed human sHsp and is prevalent in striated muscle, where the actin cross-linker filamin C (FLNC) is a putative binding partner. Musculoskeletal Hsp27 is phosphorylated in response to a variety of cues, including mechanical stress, which promotes oligomer disassembly and association with myoarchitectural elements. Here, we report the up-regulation and interaction of both proteins in the hearts of a mouse model of heart failure, with Hsp27 phosphorylated and FLNC associated with force-bearing regions of the sarcomere. A combination of structural approaches reveal that phosphorylation of Hsp27 results in increased availability of the residues surrounding the phosphosite, facilitating their interaction with folded FLNC domains equivalent to a force-sensing region in the paralog filamin A. Using native mass spectrometry, we show that phosphorylated Hsp27 stabilises a FLNC intermediate from further unfolding. These findings report on conformations accessible during the cycles of mechanical extension central to filamin function, and are consistent with an interaction between the chaperone and a native target that is strengthened upon the application of force (a catch-bond). This may represent a mode of molecular chaperone activity whereby Hsp27 protects FLNC from overextension during mechanical stress.

4.2 Introduction

Mechanosensitive proteins withstand cycles of force-induced structural changes, and as such it is critical for their function that they maintain a pliable native state (Moore et al., 2010; Luo et al., 2013). Excessive force can lead to loss of function due to unfolding and subsequent formation of deleterious aggregates that overburden the capacity of the protein quality control network, underlying a variety of muscle myopathies (Ferrer and Olive, 2008; Tannous et al., 2008; Willis and Patterson, 2013; Tarone and Brancaccio, 2014). To counter the effects of misfolding in general, cells invest in molecular chaperones, including sHsps. sHsps frequently associate with clients involved in biomechanics, including elements of the cytoskeletal support network (Snoeckx et al., 2001; Mounier and Arrigo, 2002; Robinson et al., 2010; Arrigo, 2013) and muscle contractile machinery (Bitar et al., 1991; Ibitayo et al., 1999; Golenhofen et al., 2004), suggesting that force can play a role in their client-binding.

One potential such interaction is between Hsp27 and filamin C (FLNC). Filamin structure and function was introduced in Chapter 3; in brief, filamins are large modular mechanosensing proteins that cross-link cytoskeletal actin into a branched three-dimensional network, and are adaptor components of cell adhesion assemblies (Feng and Walsh, 2004; Razinia et al., 2012). One of three human paralogs, FLNC is almost exclusively found in striated muscle, where it associates with sarcomeric actin at the myofibrillar Z-discs and intercalated discs (Figure **4.1**) (Xie et al., 1998; Thompson et al., 2000; van der Ven et al., 2000). Alterations in the human *FLNC* gene can lead to severely impaired myoarchitecture and large protein deposits, and were initially linked to skeletal myopathies (designated 'filaminopathies'), with some carriers also displaying cardiac abnormalities (Duff et al., 2011; Furst et al., 2013; Vorgerd et al., 2005; Kley et al., 2007). Hsp27 was found to be prevalent in aggre-

gates from patients with filaminopathy (Kley et al., 2013) and at sarcomeric lesions with FLNC (Chevessier et al., 2015), suggesting a role for their possible association during stress.

Recently, the range of known disease-linked *FLNC* alleles has expanded to include many associated with cardiac pathologies, often without skeletal manifestation. These encode variants implicated in hypertrophic cardiomyopathy (HCM), restrictive cardiomyopathy (RCM), and dilated cardiomyopathy (DCM) (Ortiz-Genga et al., 2016; Brodehl et al., 2016; Valdes-Mas et al., 2014; Jaafar et al., 2016; Gomez et al., 2017; Reinstein et al., 2016; Begay et al., 2016).

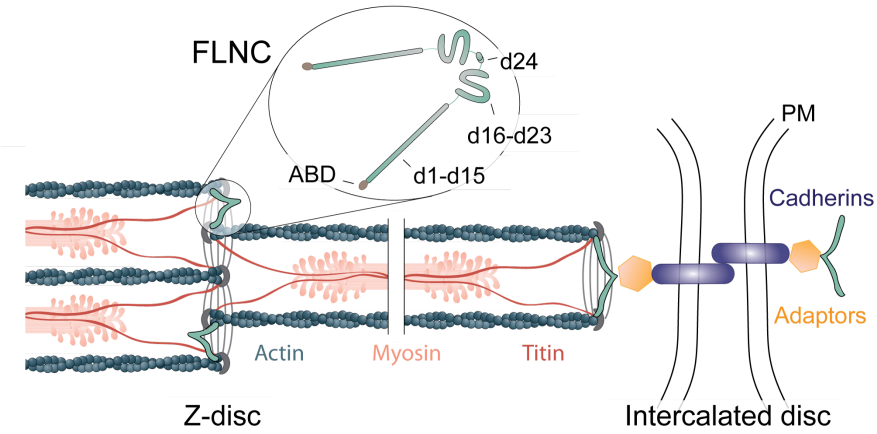


Figure 4.1. Schematic of FLNC composition and localization in striated muscle at the sarcomeric Z-disc and intercalated disc (a type of cell-cell adhesion). Grey lines = multiple Z-disc proteins, including α-actinin, desmin, etc. Adaptors = talin, vinculin, catenins, etc. PM = plasma membrane. Not pictured: possible localization at costameres (cell-matrix adhesions).

Domains 18-21 of FLNC were shown in the previous chapter to adopt a compact and extensible architecture, consistent with predictive and experimental evidence of local force-sensing capabilities (Johnson et al., 2007; Lad et al., 2008; Sutherland-Smith, 2011). The site of its association with Hsp27 likely lies within this region, since the interaction was identified in yeast two-hybrid assays using the segment d19-21 (van der Ven et al., 2006). Each Hsp27 monomer is composed of the canonical conserved core α-crystallin domain (ACD) flanked by the flexible C-terminus and the N-terminal domain (NTD). The NTD confers oligomeric stabilization (Bova

et al., 2000; Lelj-Garolla and Mauk, 2005), with phosphorylation at Ser15, Ser78 or Ser82 causing a shift from a large, polydisperse ensemble to smaller oligomeric species, including dimers (Rogalla et al., 1999; McDonald et al., 2012; Jovcevski et al., 2015). Hsp27 is phosphorylated at Ser82 (the most prevalently modified site (Landry et al., 1992)) in response to mechanical cues, inducing translocation to the sarcomere (Koh and Escobedo, 2004) and sites of increased traction force within the cytoskeleton (Chaudhuri and Smith, 2008; Hoffman et al., 2017), a mechano-accumulation phenomenon similarly observed for filamin (Jackson et al., 2008; Luo et al., 2013). Candidate Hsp27 substrates in these areas also include actin and overstretched titin; however, affinities to these upon phosphorylation are reported as diminished (Benndorf et al., 1994; Lavoie et al., 1995) and unaltered (Frankenberg et al., 2014), respectively, suggesting that phosphorylation may trigger or modulate the interaction between Hsp27 and FLNC in particular.

In this chapter I describe our investigation of the impact of phosphorylation on Hsp27 intra-oligomer contacts and its interaction with FLNC, employing experimental approaches spanning the tissue to atomic levels.

4.3 Results

4.3.1 FLNC and Hsp27 are up-regulated and interact in DCM hearts

We first sought to test the association between Hsp27 and FLNC in cardiac tissue. To examine the effect of impaired cardiac biomechanics on FLNC expression and localization, we used muscle LIM protein (MLP) KO mice. MLP, like FLNC, is specific to striated muscle, and it performs many roles in cardiomyocytes (Buyandelger et al., 2011). The MLP KO mouse phenotype reproduces the morphology of DCM and heart failure in humans (Arber et al., 1997). Frozen sections of ventricu-

lar tissue from WT and MLP KO mice were stained for FLNC, and counter-stained to visualize sarcomeric structure and intercalated discs (Figure **4.2a**). FLNC was located at intercalated discs and Z-discs, with greater intensity in MLP KO hearts and no apparent aggregation. This is consistent with previously reported FLNC localization (van der Ven et al., 2000) and with the role of adhesions as force-bearing sites (Elosegui-Artola et al., 2018). Western blotting, using lysates from WT and MLP KO mouse hearts, revealed that FLNC was up-regulated in the diseased tissue relative to WT (Figure **4.2b**). Hsp25 (mouse Hsp27) was up-regulated in the same samples, including its phosphorylated form (S86, equivalent to S82 in humans; mouse Hsp25 does not contain a phosphosite equivalent to human S78 (Gaestel et al., 1991)) (Figure **4.2b**). A proportion of Hsp27 was co-immunoprecipitated together with FLNC from lysate of MLP KO ventricular tissue, indicating an interaction between these two endogenously expressed proteins (Figure **4.2c**).

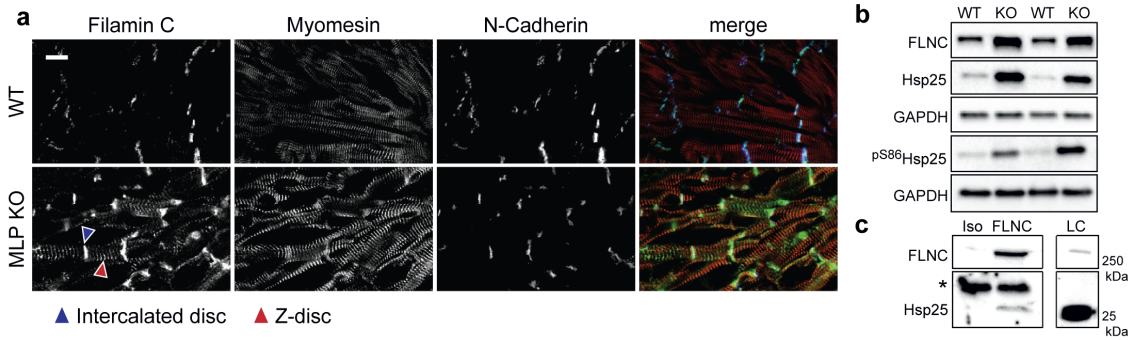


Figure 4.2. FLNC and Hsp27 are up-regulated and interact in MLP KO mouse heart. a. Frozen sections of ventricular tissue from WT mice and MLP KO mice with heart failure. Sections were stained for FLNC and counter-stained to visualize sarcomeres (myomesin) and intercalated discs (N-cadherin). FLNC is primarily localized at intercalated discs and sarcomeric Z-discs and is more abundant in diseased tissue. **b.** Blots for FLNC, Hsp25 (mouse Hsp27), and ^{pS86}Hsp25 in WT and MLP KO mice hearts (and GADPH loading control). Both FLNC and Hsp25 are up-regulated, and a proportion of Hsp25 is phosphorylated at Ser86 (human Ser82). **c.** Immunoprecipitation from MLP KO ventricular tissue lysate using a FLNC-specific antibody or isotype control; and lysate control (LC). Molecular masses from positions of markers; * indicates signal from antibody chains. Hsp25 co-precipitates with FLNC, evidencing an interaction between the endogenous proteins. Data generated by Katja Gehmlich and Carin de Villiers.

Next we expressed EEF-tagged human FLNC domains 18-21, encompassing the Hsp27 binding site (van der Ven et al., 2006), and full length human Hsp27 with a T7 tag. Pulling down the Hsp27 protein with the T7 antibody co-immunoprecipitated

$FLNC_{d18\text{-}21}$ (Figure **4.3a**), confirming a direct interaction between these proteins. To investigate the effect of Hsp27 phosphorylation on the interaction, we expressed WT human Hsp27 and ^{3P}Hsp27, a triple mutant containing phosphomimetic Ser to Asp substitutions at residues 15, 78, and 82, since mechanical insult can correlate with multiple phosphorylation events (Koh and Escobedo, 2004; Hoffman et al., 2017). Upon incubation with $FLNC_{d18\text{-}21}$ *in vitro*, we noticed that mixtures accumulated insoluble protein aggregates while isolated proteins remained soluble. In a 2:1 mixture of the chaperone to the FLNC fragment, both proteins migrated to the pelleted fraction over time, an effect that was substantially increased by phosphomimicry (Figure **4.3b-c**). The results support an interaction between Hsp27 and $FLNC_{d18\text{-}21}$ that can be modulated by phosphorylation of Hsp27.

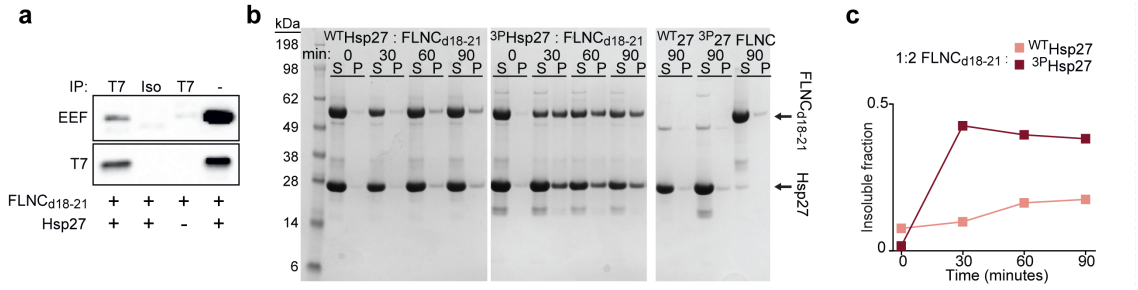


Figure 4.3. FLNC and Hsp27 interact *in vitro* via FLNC domains 18-21 in a manner modulated by phosphorylation of Hsp27. a. Recombinant EEF-tagged $FLNC_{d18\text{-}21}$ mixed with T7-tagged Hsp27 and immunoprecipitated. T7 antibody but not an isotype control pulled down both Hsp27 and $FLNC_{d18\text{-}21}$, indicating binding between the recombinant proteins. Third lane: neither protein is pulled down when Hsp27-T7 is omitted from the sample. Fourth lane: input control. Data generated by Carin de Villiers. **b.** SDS-PAGE showing soluble and pelleted fractions of a 1 to 2 mixture of recombinant WT (left) or ^{3P}Hsp27 (middle) with $FLNC_{d18\text{-}21}$ over 90 minutes at 25°C. Right, individual proteins without mixing remain soluble. **c.** Plot of insoluble fraction from experiment in **b** by densitometry of the gels.

4.3.2 Phosphomimicry reduces Hsp27 oligomer size and modulates N-terminal disorder in a simplified protomer

Full-length Hsp27 assembles into large, dynamic and polydisperse oligomers that compromise its investigation at atomic resolution. To interrogate the regulatory role of phosphorylation, we therefore built on our previous construct of the structured

ACD ($Hsp27_{84\text{-}171}$, Hochberg et al. 2014), which does not assemble beyond a dimer but retains chaperone activity. We incorporated a small part of the N-terminal domain just upstream of the β2 strand, which we term the "principle phosphorylation region" (PPR) as it includes phosphosites Ser78 and Ser82 ($Hsp27_{77\text{-}171}$, Figure **4.4**). We also mutated these sites to mimic phosphorylation events ($^{2P}Hsp27_{77\text{-}171}$).

Two-dimensional NMR spectra of each of the three constructs featured well-dispersed resonances (Figure **4.4a**), evidencing folded structures. The $Hsp27_{84\text{-}171}$ and $Hsp27_{77\text{-}171}$ spectra overlay closely, with additional peaks in the region diagnostic of disorder (7.8-8.6 ppm in the ^{1}H dimension) arising in the longer construct from the additional N-terminal residues. To examine the impact of phosphorylation on the PPR, we compared the NMR spectra of $Hsp27_{77\text{-}171}$ and $^{2P}Hsp27_{77\text{-}171}$. Signal was intensified in the disordered region for the phosphomimic (Figure **4.4a**, arrow), consistent with an increase in flexibility. Chemical shift-based order parameters (Figure **4.4b**) indicated a high degree of backbone flexibility and a low amount of secondary structure for the β2 strand and the PPR.

To visualise the structural fluctuations of β2, we performed a 1 μs molecular dynamics (MD) simulation of $Hsp27_{84\text{-}171}$ starting from a structure (PDB: 4MJH) in which the β2 strand is intra-molecularly hydrogen bonded to β3. Over the course of the simulation, β2 fluctuated considerably, readily losing its secondary structure and detaching from the rest of the ACD (Figure **4.5a**). This corresponds well with our NMR data for this region (Figure **4.4b**) and with the disorder observed by others (Rajagopal et al., 2015). To probe for effects of phosphomimicry on internal dynamics, we recorded ^{15}N spin relaxation measurements and found evidence of conformational exchange on the μs-ms timescale (Figure **4.5b**). We reasoned that this change in dynamics could indicate transient sampling of a lowly populated state involving contact between the PPR and the ACD. The major state would contain

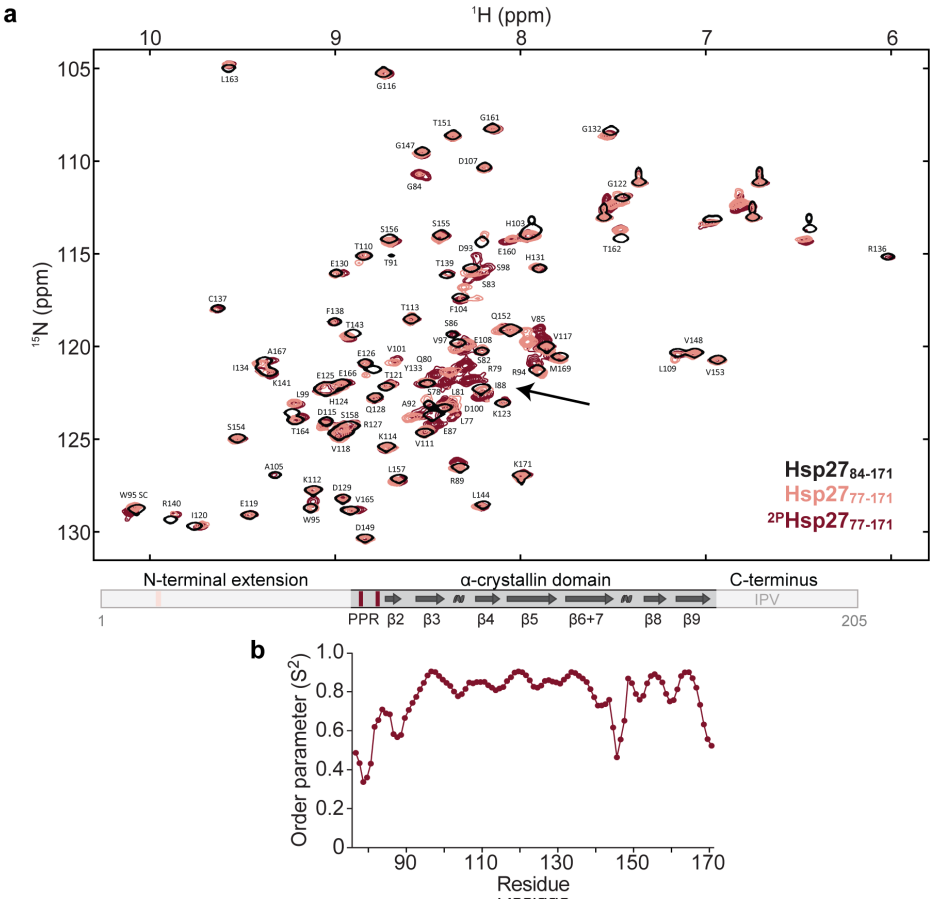


Figure 4.4. The flexibility of the primary phosphorylation region of Hsp27 can be modulated by phosphomimicry. a. Overlay of ^{1}H-^{15}N HSQC spectra of truncated Hsp27 variants. Constructs and phosphosites in the context of the full protein are indicated in the schematic below. Signal intensity between 7.8-8.6 ^{1}H-ppm is increased upon phosphomimicry, likely due in part to greater flexibility and in part to locally diminished solvent exchange caused by the Ser to Asp mutations. **b.** N-H order parameters derived using assigned backbone chemical shifts from ^{2P}Hsp27$_{77-171}$. S^2 closer to 1.0 indicates stable secondary structure. The PPR and β2 are highly dynamic. Data generated by Reid Alderson and Daisy Nicholls.

an unbound PPR, consistent with small chemical shift perturbations, lack of any conformational exchange slow enough to give rise to multiple peaks, and flexibility of the N-terminal residues in solution.

To test whether this transient binding is intra- or inter-molecular, we recorded native mass spectra of Hsp27$_{77-171}$ variants. These data revealed a monomer-dimer equilibrium that is shifted toward the monomer upon incorporation of one and two phosphomimics (Figure **4.5c**). The absence of higher-order oligomers indicates that appreciable intermolecular binding of the PPR is unlikely in the context of this truncated construct. The combined NMR and MS data are therefore consistent

with phosphorylation modulating the disorder of the β2 and PPR and prompting oligomer dissociation via rearrangement of intra-dimer contacts.

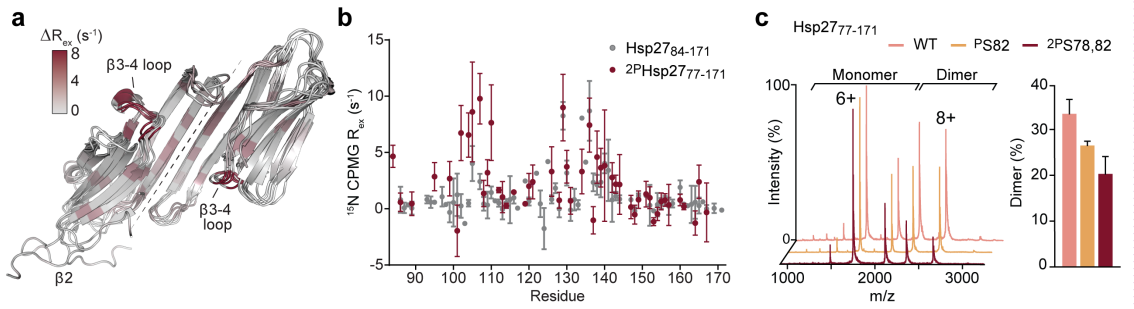


Figure 4.5. Hsp27 undergoes dynamical changes leading to partial dissociation upon phosphomimicry. a. Snapshots from a 1 μs MD simulation of $Hsp27_{84\text{-}171}$ showing the complete dissociation of a β2 strand. Residues are colored according to their changes in R_{ex} (a qualitative metric of μs-ms motions probed by NMR using CPMG relaxation dispersion, values in **b**). The region where these dynamics are most affected is the β3-β4 loop on the side of the ACD. Data generated by Reid Alderson and Matteo Degiacomi. **c.** Native MS and corresponding quantification of $Hsp27_{77\text{-}171}$ WT (pink), P (^{P}Ser82, yellow), and 2P (^{P}Ser78-^{P}Ser82, maroon) stoichiometries. Phosphomimicry shifts the oligomeric equilibrium from dimer to monomer.

4.3.3 The N-terminal phosphosite-rich region of Hsp27 interacts with a pocket of its ACD

We next carried out crystallographic trials, employing a strategy of mixing peptide mimics of the PPR, varying in length and degree of phosphorylation, with a well-ordered ACD construct ($Hsp27_{84\text{-}170}$). This led to a structure of the ACD bound to ALSRQL^{P}SSGVSEI (residues 76-88 phosphorylated at Ser82), solved by molecular replacement in space group $P12_11$, that contains four dimers in the asymmetric unit (Figure **4.6**, Table 4.1, Methods).

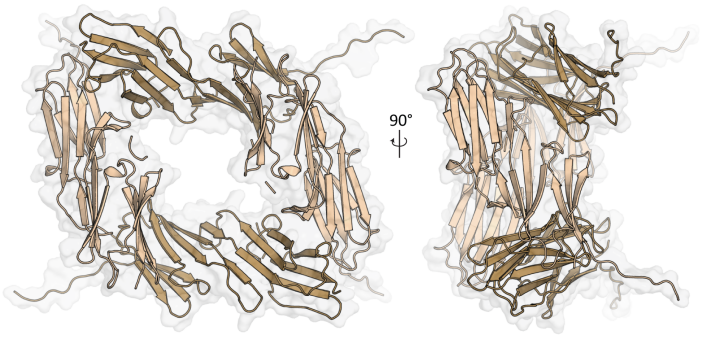


Figure 4.6. Crystal structure of the Hsp27 ACD in complex with a peptide mimic of the N-terminal phosphosite-rich region. The asymmetric unit contains four dimers.

The monomers within each dimer differ at their N-terminal ends: the β2 strand of one is intramolecularly hydrogen bonded to its own β3 strand, whereas in the other, these residues are extended and stabilized by contacts with the β4-β8 groove of a neighbouring subunit within an adjacent dimer (Figure **4.7a-c**). This groove forms the binding pocket for a conserved motif within the C-terminal region (^{181}IPV^{183}), and the position of Val85 in this new structure is analogous to that of Ile181 in our previous structure (Figure **4.7d**) (Hochberg et al., 2014).

Upon refinement of the ACD, the density map displayed a clear unmodelled feature occupying a pocket between the β3-β4 and β8-β9 loops, which lies on the side of the dimer close to the antiparallel interface. This feature was only present adjacent to monomers with intra-molecularly bound β2 strands (Figure **4.7e**), and aligns with the dynamical changes we observed by NMR in the β3-β4 loop (Figure **4.5a**). We were able to build peptides into this density, but only accommodating subsets of the 11 possible residues, with their side chain densities remaining poor in contrast to the ACD. An ensemble of the four peptide-bound ACDs provides the best overview of the interaction available from these data (Figure **4.7f**).

Our results reveal how the β2 strand and PPR assume heterogeneous conformations. Though predominately disordered (Figure **4.4**), this region is also capable of making intra-monomer associations with the β3 strand and stretching to the pocket between β3-β4 and β8-β9 loops (Figure **4.7f**), as well as inter-monomer interactions by occupying a β4-β8 groove in a neighboring dimer (Figure **4.7c**). While it is not clear what the relative populations of these states are in the context of full-length, oligomeric Hsp27, our combined data reveal that this heterogeneity is modulated by phosphorylation, resulting in changes in the stabilities of the interfaces. This acts to shift the equilibrium away from a polydisperse 200-800 kDa assembly and towards smaller oligomers, including monomers and dimers (Jovcevski et al., 2015).

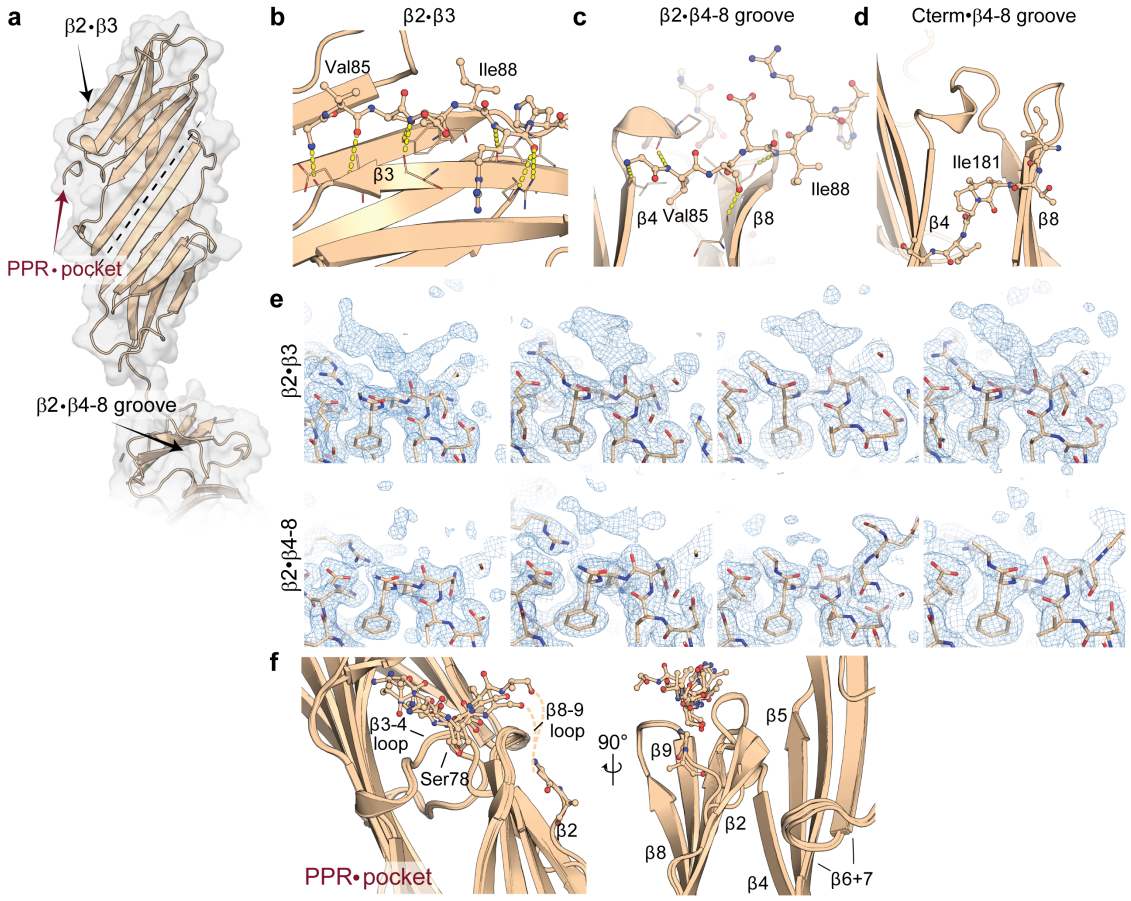


Figure 4.7. The Hsp27 ACD·PPR crystal structure in more detail. a. ACD dimer with PPR peptide bound. Dotted line indicates the AP interface. **b-c.** Areas indicated by black arrows in **a** showing two locations of the β2 strand: bound to β3 or dissociated from the ACD and reaching across the β4-β8 groove of a neighbouring monomer. **d.** Previous crystal structure of the Hsp27 ACD in complex with an Hsp27 C-terminal peptide, where the position of Ile181 is analogous to that of Val85 in the new structure. **e.** 2Fo-Fc electron density map contoured at 0.9σ following building and refinement of the ACD prior to placement of any peptides. Top row: N-terminal peptide binding sites for each of the four monomers in the ASU with intramolecularly bound β2 strands; bottom row: equivalent sites on monomers with extended β2 strands. **f.** PPR binding (red arrow in **a**) shown as an overlay of the four peptide-bound monomers in the ASU. Whereas the ACDs overlay closely, the peptides are more flexible. Rotated view shows β2 strand divergences, sometimes arcing toward the peptide binding site and in one instance partially modelled as continuation of the peptide.

4.3.4 Hsp27 residues 80-88 bind multiple domains within FLNC

We next wished to isolate a stable complex with FLNC and localize the binding. Using native IM-MS, we measured collision cross-sections (CCS) of $FLNC_{d18\text{-}21}$ consistent with compact rather than linear architecture, and observed that this structure extends via biomechanically relevant transitions during collision-induced unfolding (CIU) (Chapter 3). Next, based on the Hsp27 sites whose exposure shifts upon phosphorylation, we mixed $FLNC_{d18\text{-}21}$ with either $Hsp27_{84\text{-}171}$ or peptides mimicking the PPR, since this site was phosphorylated in the heart failure model mice

(Figure **4.2b**). We observed charge state distributions corresponding to complexes between $FLNC_{d18\text{-}21}$ and one or two copies of the peptide $Hsp27_{80\text{-}88}$ (or its phosphorylated counterpart $^{P}Hsp27_{80\text{-}88}$) (Figure **4.8a**). Complexes were not observed in mixtures of $FLNC_{18\text{-}21}$ with negative controls (Figure **4.8a**) or $Hsp27_{84\text{-}171}$ (Figure **4.8b**), revealing a specific interaction with this N-terminal segment of Hsp27. To localise binding of $Hsp27_{80\text{-}88}$ to domains with known Ig-like folds or to the conformationally heterogeneous d20 insertion (Chapter 3), we used the modified FLNC construct lacking the 82 insertion residues ($FLNC_{d18\text{-}21,\Delta Ins}$). This also bound multiple Hsp27 peptides (Figure **4.8c**), indicating that Hsp27 recognizes folded FLNC elements.

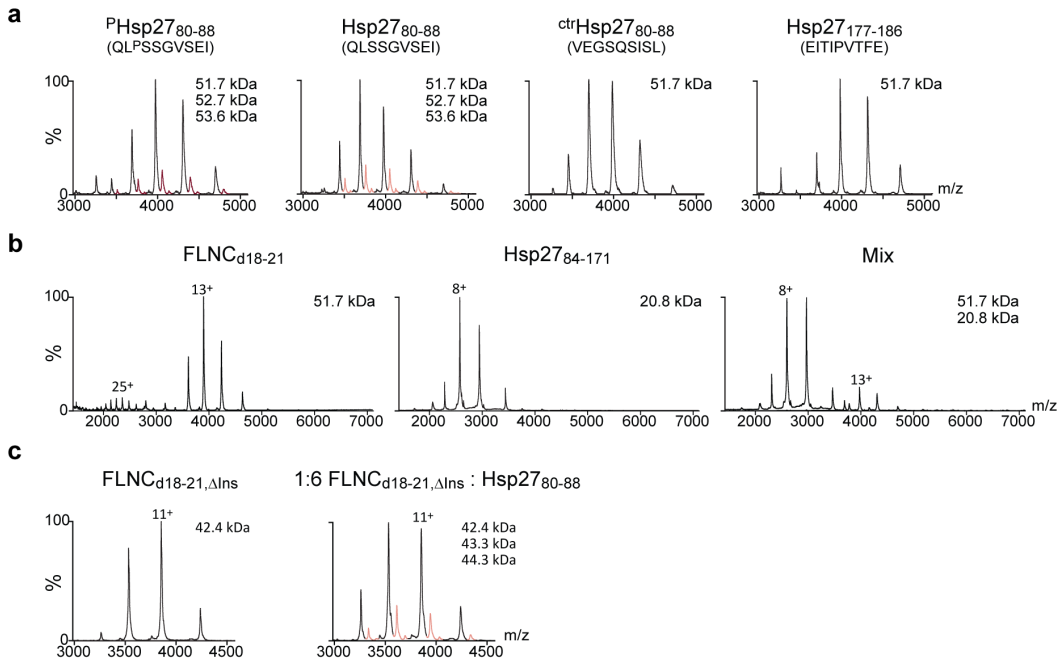


Figure 4.8. $FLNC_{d18\text{-}21}$ binds $Hsp27_{80\text{-}88}$ specifically via its Ig domains. a. Native MS of 5 µM $FLNC_{d18\text{-}21}$ with 30 µM peptides: $^{P}Hsp27_{80\text{-}88}$; $Hsp27_{80\text{-}88}$; $Hsp27_{80\text{-}88}$ with scrambled sequence; Hsp27 C-terminal residues 177-186. No appreciable complex is detected with the C-terminal or scrambled peptides, supporting the specificity of N-terminal binding. Bound peaks in color. **b.** Native MS of $FLNC_{d18\text{-}21}$ and $Hsp27_{84\text{-}171}$ (the ACD) individually, and mixed in a 1:2 ratio. No complex is observed. Labelled charge states are the most intense of two FLNC charge series and of the $Hsp27_{84\text{-}171}$ dimer. The higher FLNC charge series represents a minor conformation, and is left outside the scope of this chapter. **c.** Native MS of 5 µM $FLNC_{d18\text{-}21}$ lacking the d20 insertion (ΔIns) individually and mixed with 30 µM $Hsp27_{80\text{-}88}$. Peptide-bound peaks are observed (pink), evidencing binding to the Ig domains.

To measure the strength of $^{P}Hsp27_{80\text{-}88}$ and $Hsp27_{80\text{-}88}$ association to $FLNC_{d18\text{-}21}$, we recorded mass spectra at increasing peptide concentrations (Figure **4.9a**) and

quantified the relative abundances of $FLNC_{d18\text{-}21}$ alone and peptide-bound. These yielded similar apparent dissociation constants (K_Ds) of 130 ± 17 μM ($Hsp27_{80\text{-}88}$) and 110 ± 10 μM ($^{P}Hsp27_{80\text{-}88}$) (Figure **4.9b**), indicating weak binding that is not affected substantially by phosphorylation. These findings contrast the notable effect of Hsp27 phosphomimicry on the interaction of full-length chaperone with the FLNC fragment (Figure **4.3**). However, they can be rationalised by phosphorylation increasing the effective concentration of the binding region by modulating its conformational state (Figure **4.4**) with respect to different Hsp27 oligomeric ensembles (Figure **4.5c**) (Rogalla et al., 1999; McDonald et al., 2012; Jovcevski et al., 2015).

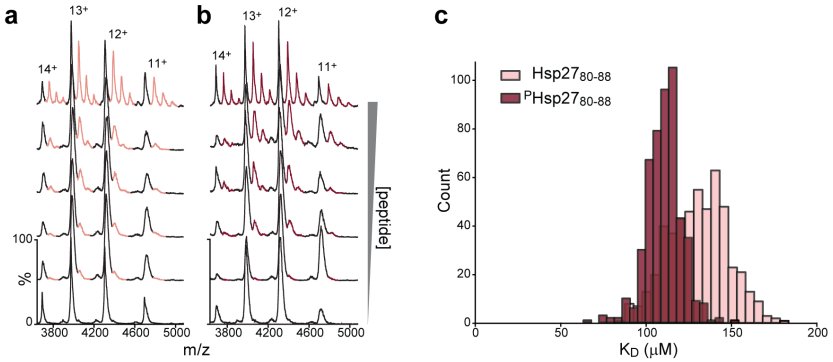


Figure 4.9. $Hsp27_{80\text{-}88}$ unmodified and phosphorylated peptides bind $FLNC_{d18\text{-}21}$ with very similar affinities. Representative native mass spectra from titration series using 5 μM $FLNC_{d18\text{-}21}$ with 5, 10, 20, 40, 80, and 160 μM $Hsp27_{80\text{-}88}$ (**a**) and $^{P}Hsp27_{80\text{-}88}$ (**b**). Bound charge series in color. **c.** Histogram of each dissociation constant (stoichiometries combined) calculated from the full peptide titration datasets (n = minimum 3 per ratio) following 500 bootstraps with replacement. The K_D values are 110 ± 10 μM and 130 ± 17 μM for phosphorylated and unmodified peptides, respectively.

4.3.5 Phosphorylation modifies the force-accessible trajectory of the FLNC-Hsp27 complex

Having found marginal difference in binding affinities between the phosphorylated and unphosphorylated Hsp27 peptides with $FLNC_{d18\text{-}21}$ at equilibrium, we next sought to probe the strength of this interaction under the application of force. The motivation for this stemmed from direct and indirect reports that the FLNC distal region undergoes extension *in vivo* (Johnson et al., 2007; Sutherland-Smith, 2011; Chevessier et al., 2015), and our own work supporting the use of collision-induced

unfolding as a proxy for mechanical stress on FLNC (Chapter 3). An advantage of this approach is that, by capitalising on the sensitivity and capability of ion selection in the mass spectrometer, these low-affinity complexes can be interrogated individually (Dixit et al., 2018).

Upon extending the $Hsp27_{80\text{-}88}$-$FLNC_{d18\text{-}21}$ complex by ramping the activation potential, we observed a gradual reduction in the abundance of peptide-bound $FLNC_{d18\text{-}21}$, indicating dissociation of the peptide. Strikingly, phosphorylation of $Hsp27_{80\text{-}88}$ significantly increased the energy required to remove the peptide from FLNC: at 140 V, all unphosphorylated $Hsp27_{80\text{-}88}$ had dissociated, while $^{P}Hsp27_{80\text{-}88}$-bound FLNC persisted until 180 V (Figure **4.10a**, projections to the right). To quantify this differential dissociation behaviour, while avoiding potential cross-talk between charge states (Rabuck et al., 2013), we selected the 13^{+} ion of $FLNC_{d18\text{-}21}$ bound to a single peptide in the mass spectrometer, and performed analogous activation ramps (Figure **4.10b**). This allowed us to extract the fraction of $FLNC_{d18\text{-}21}$ associated to each peptide as a function of activation. The breakdown curve for the $FLNC_{d18\text{-}21}$:$Hsp27_{80\text{-}88}$ complex (Figure **4.10a**, lower right) revealed two inflection points, at ≈60 V and ≈110 V. This indicates that $Hsp27_{80\text{-}88}$ associates with $FLNC_{d18\text{-}21}$ in (at minimum) two locations, consistent with the observation of multiple peptides binding in our titration experiments. $^{P}Hsp27_{80\text{-}88}$ dissociates less readily from $FLNC_{d18\text{-}21}$, and the breakdown curve features only one inflection point at ≈ 130 V. The results suggest that phosphorylation increases both the selectivity and strength of interaction of Hsp27 with FLNC.

In an attempt to rationalize the phosphorylation-dependent differences under collisional activation but not in its absence, we used IM to examine unfolding trajectories during activation of $FLNC_{d18\text{-}21}$. Over the range of activation potentials that dissociate Hsp27 peptides from $FLNC_{d18\text{-}21}$, the protein extends from an ini-

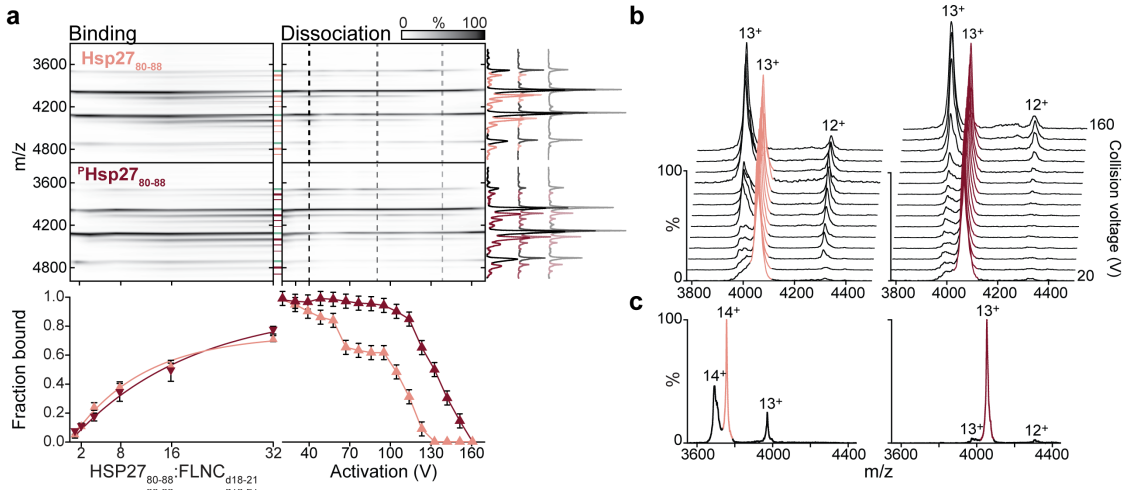


Figure 4.10. Phosphorylation modifies the force-accessible behaviour of the $Hsp27_{80\text{-}88}$-$FLNC_{d18\text{-}21}$ complex. a. Contour plots of representative native mass spectra from titration series (Fig. **4.9**) and from ramps of collisional activation which dissociate the peptides from FLNC. Projected to the right are several mass spectra from the activation ramps. Binding curves overlay, but dissociation curves do not (bottom). **b** Tandem MS collisional activation ramps. The singly bound 13^+ peak was selected in the quadrupole, and loss of neutral and 1^+ peptide gave rise to 13^+ and 12^+ unbound peaks. **c.** Relative peptide bound with activation (plotted in **a**, lower right) is independent of peptide concentration and selected charge state. Left (5 µM $FLNC_{d18\text{-}21}$ with 30 µM $Hsp27_{80\text{-}88}$ at 80V activation) and right (5 µM $FLNC_{d18\text{-}21}$ with 160 µM $^{P}Hsp27_{80\text{-}88}$ at 100V activation) spectra each yielded dissociated fractions within 5% of corresponding activations in **b** which underlie the plot.

tial compact state (A) through transition(s) (B) to reach a final state (C). The same three states were observed for $FLNC_{d18\text{-}21}$ with either peptide bound (Figure **4.11**). In all cases, unfolding commenced at lower potentials than necessary for peptide dissociation. Since domain unfolding typically coincides with ejection of ligand bound to that domain (Eschweiler et al., 2017), this suggests that Hsp27 does not exclusively bind the regions within $FLNC_{d18\text{-}21}$ that extend first. The stability of A, based on activation required to transition to B, was unaffected by either peptide. B, however, required more activation to transition to C when bound to $^{P}Hsp27_{80\text{-}88}$ versus $Hsp27_{80\text{-}88}$. This was consistent across charge states and instrument conditions (Figure **4.11**).

The data point to the formation of interactions when the phosphopeptide-bound FLNC structure is activated, leading to its increased resistance to extension, and dissociation at higher potentials than the unmodified peptide. This suggests a chaperone-target mechanism reliant on the recognition of native-like states but

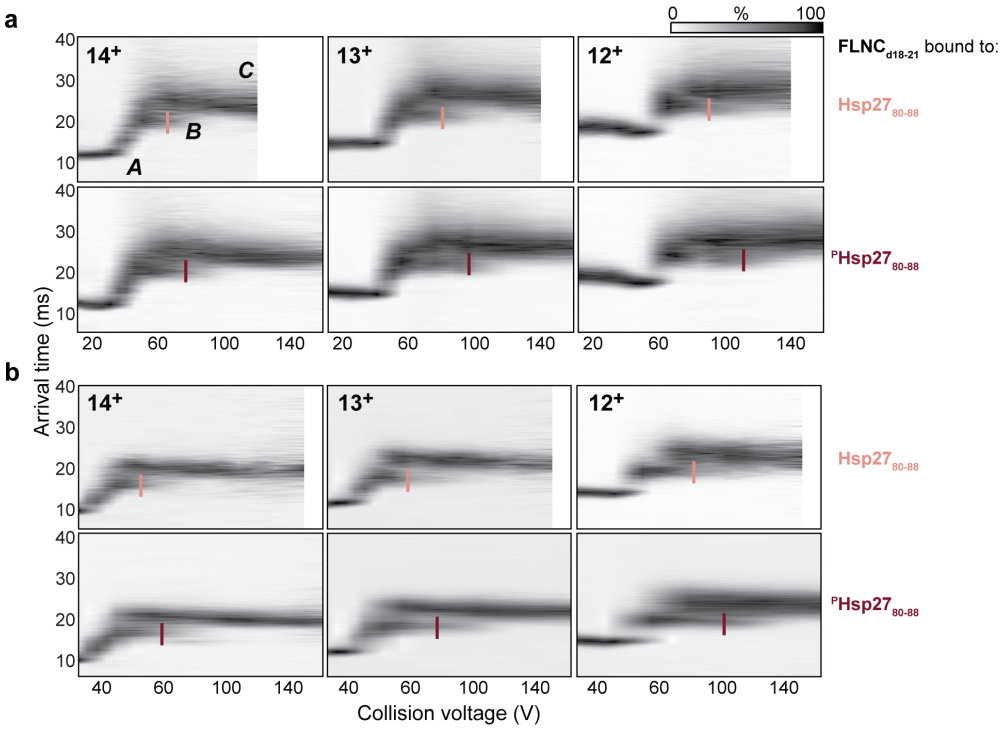


Figure 4.11. Phosphorylated Hsp27$_{80-88}$ stabilizes a FLNC$_{d18-21}$ unfolding intermediate. CIU plots of charge states 14^{+}, 13^{+}, and 12^{+} for FLNC$_{d18-21}$ bound to one Hsp27$_{80-88}$ (top rows) or ^{P}Hsp27$_{80-88}$ (bottom rows). Colored marks designate the activation required to transition half of the intermediate to the final state. Ion mobility drift cell wave heights **a.** 7.0V and **b.** 8.0V.

stabilization of unfolding intermediates, in a manner that is regulated by post-translational modification.

4.4 Discussion

We have investigated how phosphorylation of Hsp27 modulates its interaction with FLNC. Our biophysical and structural studies reveal conformational heterogeneity in the Hsp27 β2 strand and immediately downstream PPR, which encompasses the primary Hsp27 phosphosite. These residues are largely disordered in our construct in solution, but also make intramolecular contacts with β3 and a pocket on the edge of the ACD in a manner that is regulated by phosphorylation. We also observed an additional inter-dimer interaction between the PPR and the β4-β8 groove, the interface for the C-terminal IPV motif (Hochberg et al., 2014), in a crystal structure. This is consistent with alternative modes of occupancy for the β4-β8 groove

observed in other vertebrate sHsps (Weeks et al., 2014; Bagneris et al., 2009), and hints at intra-molecular competition for the binding site in the context of Hsp27 oligomers. The conformational plasticity may be the primary source of the modulation in chaperone activity associated with Hsp27 phosphorylation (Bryantsev et al., 2002; Somara and Bitar, 2004; Abisambra et al., 2010; Jovcevski et al., 2015), exposing binding sites both directly through intramolecular rearrangements and indirectly by prompting oligomeric dissociation (Rogalla et al., 1999; McDonald et al., 2012; Jovcevski et al., 2015).

Similar heterogeneity of N-terminal residues has been observed in other sHsps and shown to regulate assembly (Hochberg et al., 2018), including in αB-crystallin and Hsp20, both of which coassemble with Hsp27 *in vivo* (Sugiyama et al., 2000). The αB-crystallin β2 strand and residues immediately preceding it exist in multiple conformations, including bound to β3 both intra- (Bagneris et al., 2009; Hochberg et al., 2014) and inter-monomer (Jehle et al., 2010). Recent crystal structures of Hsp20 show no resolved density for β2, and support disorder-to-order transitions upon interactions made by the N-terminus (Sluchanko et al., 2017). In both αB-crystallin (Peschek et al., 2013) and Hsp20 (Chernik et al., 2007), these contacts are controlled by phosphorylation. Taken together, these observations indicate a mechanism of tuneable structure and function via phosphorylation-based modulation of local flexibility. Changing the conformational landscape and binding properties of heterogeneous structures in this manner offers a way to balance entropic loss with enthalpic gain (Shammas, 2017), potentially key for the ATP-independent chaperone activity of sHsps.

We observed that Hsp27 associates with FLNC in the heart of MLP KO mice, an established animal model of heart failure, with concomitant up-regulation of both proteins and phosphorylation of the chaperone. We replicated this interaction *in*

vitro, and localised it to $Hsp27_{80\text{-}88}$, encompassing part of the PPR and β2 strand, which binds $FLNC_{d18\text{-}21}$ at multiple locations. While phosphorylation of Hsp27 increases the association by promoting unbinding and flexibility of the PPR, it does not require unfolding of the target. This behaviour may be facilitated by Hsp27 and $FLNC_{d18\text{-}21}$ both containing Ig folds, such that chaperone-target interfaces mimic intramolecular interactions in Hsp27. Such interaction between a sHsp and a target in its native state is one of few directly observed (Pereira et al., 2014; Sluchanko et al., 2017) (Chapter 3 herein), and contrasts the canonical chaperone mode of recognizing unfolded or misfolded substrates (Haslbeck et al., 2016).

We mimicked mechanical strain on FLNC by performing experiments in which we unfolded the protein in the gas phase, along a pathway defined by the Coulombic repulsion between mobile charges (Popa et al., 2016). Orthogonal work on FLNC (Chapter 3) supports the use of the method as a proxy for biomechanical force. Our experiments revealed that $FLNC_{d18\text{-}21}$ adopts a compact state that undergoes a series of unfolding transitions upon extension. Notably, transitions occur without ejection of bound $^{P}Hsp27_{80\text{-}88}$, and involve an unfolding intermediate stabilized by $^{P}Hsp27_{80\text{-}88}$ relative to $Hsp27_{80\text{-}88}$. The results are consistent with a phosphorylation-triggered catch-bond: an interaction with a longer lifetime under the application of force than in its absence (Elosegui-Artola et al., 2018), suggesting that a function of Hsp27 is to regulate the extension of FLNC. More direct structural work focusing on this FLNC region is needed to understand the interaction at the molecular level.

As mentioned previously, the extent of FLNC deformation *in vivo* depends on various interactions, including at its dimer and actin interfaces, since breakage of these would lessen the strain borne by the mechanosensing region (Moore et al., 2010). High loading rates increase interface rupture forces and therefore the likelihood of intra-filamin deformation (Ferrer and Olive, 2008). Since catch-bond

lifetimes are loading rate-dependent (Vogel and Sheetz, 2006), the ^{P}Hsp27-FLNC interaction may be energetically favoured under conditions of stress. This would concur with the increase in expression of both proteins in hearts of MLP KO mice, and implies functional importance in the maintenance of myoarchitectural integrity since these hearts display severe defects in myofibrillar organization (Arber et al., 1997). FLNC may require chaperoning to function properly under stress and avoid adverse disruption of the mechanosensing region. In this role, Hsp27 binding would be preventative rather than a response to damage, lowering the risk of FLNC hyperextension.

Nevertheless, critical force seems to overburden this system, triggering chaperone-assisted selective autophagy (CASA) to clear and degrade filamin in muscle tissue (Arndt et al., 2010; Ulbricht et al., 2013). CASA involves the apparent recognition of compromised filamin by Hsp22 (HspB8), and subsequent scaffolding of HspB8 to Hsp70 via the co-chaperone BAG3. Additional sHsps likely participate in autophagy, since most sHsps that are expressed in muscle can bind BAG3, as demonstrated *in vitro* by isothermal titration calorimetry experiments (Rauch et al., 2017) and *in vivo* by immunoprecipitation (Morelli et al., 2017). Interestingly, although cvHsp was observed not to bind BAG3 (Vos et al., 2010), it can interact with FLNC (Liao et al., 2017). Hsp27, however, is the only sHsp now known to bind native FLNC in addition to BAG3 and readily coassemble with several sHsp paralogs. Whereas phosphorylation disfavors Hsp27 self-association, it may promote association with Hsp22 (Benndorf et al., 2001), the sHsp with highest affinity for BAG3 (Morelli et al., 2017). Co-localization of Hsp27 with FLNC and BAG3 at sarcomeric lesions (Chevessier et al., 2015), and its ability to interact with both compact and extending filamin as demonstrated here, implicate it as a likely key hub in the proteostasis of muscle both during physiological and to pathological conditions (Figure **4.12**).

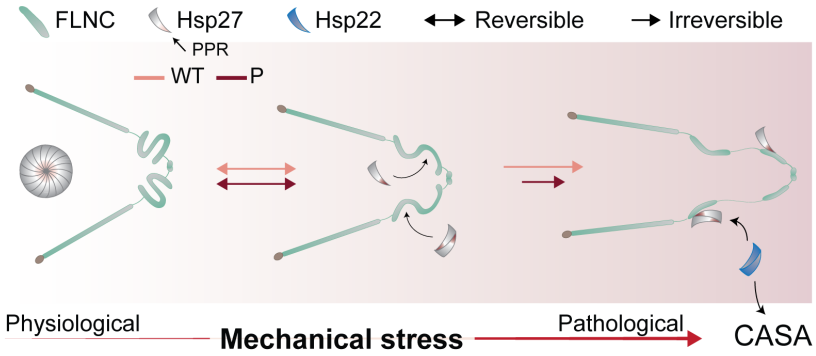


Figure 4.12. Summary of the proposed Hsp27-FLNC interaction during the biomechanical cycle. Schematic of force-induced changes in the structure of FLNC and relation to Hsp27 binding. At low stress, the majority of unmodified Hsp27 self-associates and the FLNC binding site is minimally exposed. At the onset of mechanical stress, Hsp27 is phosphorylated rapidly, whereupon it dissociates to reveal the binding site and recognizes extending FLNC. ^{P}Hsp27 inhibits later stages of unfolding, which may be irreversible. Under extreme stress, CASA is triggered, involving recruitment of Hsp22 and potentially other sHsps.

Our results, in the context of these previous reports, point to a two-tier, sHsp-mediated proteostasis mechanism for maintaining filamin C and the myoarchitecture, active at varying tensions. This is modulated by the cellular response to mechanical stress, via Hsp27 phosphorylation, exposure of its FLNC-binding site, and stabilization of the reputed mechanosensitive region of FLNC. Recent reports have detailed binding of chaperones to model proteins destabilized by the application of force (Mashaghi et al., 2016; Ramirez et al., 2017; Perales-Calvo et al., 2018). These findings suggest a physiological context for such a mechanism, and may provide a new avenue for understanding filaminopathies and FLNC-linked cardiac-specific diseases.

Acknowledgments

I thank Reid Alderson, Daisy Nicholls, and Heidi Gastall for allowing pieces of their own projects to complete this story. Heidi designed the various N-terminal peptides and purified the protein that was crystallized; and Reid contributed the NMR data and provided helpful feedback on the text. Thanks to Carin de Villiers and Katja Gehmlich for the FLNC construct plasmids, the mouse model and immunoprecipitation work, and fruitful discussions. I am grateful to Tim Allison for his advice and time on the crystallography. Thanks to all other co-authors on the manuscript from which this chapter is based for their critical review, including Peter van der Ven, Dieter Fürst, and Kristina Djinovic-Carugo, whose perspectives as experts in FLNC biology and structure were greatly appreciated.

4.5 Methods

Co-immunoprecipitation

1 µg of T7-tagged purified recombinant Hsp27 was added to 10 µg EEF-tagged recombinant $FLNC_{d18\text{-}21}$ in IP buffer (0.05% Triton X-100, 1% BSA, protease inhibitors (Roche mini complete ETDA-free tablets in PBS) and incubated for 1h, shaking, at room temperature. This was followed by another 30 minute incubation, shaking at room temperature after the addition of 0.5 µg anti-T7 (Novagen, 69522) or Mouse Ig2b isotype (Abcam, ab18457) antibody. Next, 25 µl Protein G sepharose resin (Generon, PC-G5) was added to each tube and incubated for a further 1 hour, shaking at room temperature. The beads were then washed 4 times with IP buffer, each time removing the supernatant following centrifugation. Finally the beads were re-suspended in 20 µl 5X SDS sample buffer (312.5 mM Tris HCl pH 6.8, 500 mM DTT, 10% SDS, 30% Glycerol, 0.05% bromophenol blue) and boiled at 95°C for 5 minutes. Immunodetection was performed using the anti-T7 (Novagen, 69522) or anti-EEF/anti-tubulin (YL1/2) (Abcam, ab6160) antibodies.

Analysis of MLP KO mouse hearts

Experimental procedures were performed in accordance with the UK Home office guidelines (project licences 30/2444 and 30/2977) and approved by respective institutional review boards. MLP knockout mice (Arber et al., 1997) were backcrossed with C57BL/6J for >6 generations before generating homozygous MLP knockout mice. WT C57BL/6J were obtained from Harlan. Animals (females, age 3 months) were sacrificed by cervical dislocation, hearts flushed with ice-cold PBS and snap frozen in liquid nitrogen. Immuno-fluorescence from frozen tissue was performed as described (Gehmlich et al., 2007) using FLNC antibody RR90 (van der Ven et al.,

2000), pan-cadherin antibody (Sigma) and myomesin antibody B4 (DSHB, Developmental Studies Hybridoma Bank). Immunoblotting from total protein extracts was performed as described (Gehmlich et al., 2007) using anti-Hsp27 (Cell Signaling, 2442), anti-^{P}Hsp27 (Ser82) (Cell Signaling, 2401) and anti-GAPDH (Merck, ABS16) antibodies and FLNC (R1899) antibody (MRC PPU Reagents and Services, University of Dundee). Immunoprecipitation was performed as described (Gehmlich et al., 2007) using 5 µg of FLNC (R1899) antibody. Blotting for Hsp27 (Cell Signaling, 2442) was performed using "Veriblot" (ab131366) as secondary HRP conjugate.

Protein expression and purification

A pET28d(+) vector encoding human Hsp27 residues 84-171 was transformed into *E. coli* BL21(DE3) cells (Agilent), and expressed and purified as described previously (Hochberg et al., 2014). For crystallography, residue K171 was deleted using a site-directed mutagenesis kit (Agilent) and $Hsp27_{84\text{-}170}$ was expressed and purified as described. $Hsp27_{77\text{-}171}$ and variants thereof were cloned into the same vector and phosphomimetic mutations S78E and S82D were introduced using site-directed mutagenesis. These were expressed in LB media at 37°C for 3 hours and purified as follows: cells were lysed using a cell press with added protease inhibitor cocktail (Roche). Lysate was centrifuged at 20,000×g for 20 minutes and the supernatant filtered and loaded onto a HisTrap column in buffer 20 mM Tris, 150 mm NaCl, 20 mM imidazole, 5 mM BME, pH 8. Protein was eluted with a gradient to 500 mM imidazole, pooled, and dialyzed overnight with TEV protease into the loading buffer at room temperature. The sample was then exchanged into the same buffer with addition of 8 M urea by cycles of centrifugation and dilution using an Amicon concentrator with 3.5 kDa MWCO. The cleaved and unfolded protein was passed over a HisTrap column and flow-through collected and refolded by overnight dialysis

at room temperature into 100 mM NaCl, 20 mM Tris, pH 7.5. Protein was then concentrated and DTT added to a final concentration of 1 mM for storage at -20°C until use. For NMR experiments, Hsp27 variants were expressed in M9 minimal media containing ^{13}C-labeled D-glucose as the only carbon source and ^{15}N-labeled ammonium chloride as the only nitrogen source, and purified as described, with a final SEC (75) step for exchange into the NMR buffer. Concentrations were determined by BCA assay (Thermo Pierce).

Full-length human Hsp27 (WT or 3P, containing mutations S15D, S78D, and S82D) encoded in pETHSUL vector with an N-terminal SUMO and 6xHis-tag was transformed into *E. coli* BL21(DE3) cells. Cells were used to inoculate a 2 mL LB culture and grown for 7 hours at 37°C. Next 500 µl of this culture was transferred to 1 L of ZYP auto-induction media. Cells were left to grow overnight at 24°C and 180 rpm until reaching OD 4, and then another 24 hours at 18°C and 180 rpm. Cells were harvested and lysed using a cell press with added protease inhibitor cocktail, spun down at 20,000xg for 20 minutes, and loaded onto a HisTrap column in 50 mM sodium phosphate, 250 mM NaCl, 12.5 mM imidazole, 5 mM BME, pH 7.5. Protein was eluted with a gradient to 500 mM imidazole. Eluent was pooled, dialyzed overnight with SUMO hydrolase (expressed and purified in-house) at 4°C into the loading buffer, and the sample then passed over a HisTrap column and flow-through collected. This was concentrated and further purified by SEC. Purity was assessed by SDS-PAGE and protein was concentrated, flash-frozen, and stored in PBS with 1 mM DTT at -80°C. Concentration was determined by absorption at 280 nm.

Human FLNC domains 18-21 (WT and Δinsertion) was expressed and purified as described in Chapter 4.

Peptides ($N_{80\text{-}88}$; N_{ctrl}; $^{P}N_{80\text{-}88}$; $N_{76\text{-}88}$; $^{P82}N_{76\text{-}88}$; $^{P78}N_{76\text{-}88}$; $^{P78,82}N_{76\text{-}88}$, where

N refers to the Hsp27 N-terminus) were purchased from Biomatik at 99+% purity with acetylated N-termini when the N-terminal residue was glutamine. Lyophilized peptides were resuspended in ddH2O to a stock concentration of 15 mM, flash-frozen, and stored at -20°C until use.

Hsp27·phosphopeptide crystallization and structure determination

Crystals were obtained following initial screens using 18 mg mL^{-1} $Hsp27_{84\text{-}170}$ with a 4-fold molar excess of one of several peptide mimics of the N-terminal region. Peptides screened varied in their length and degree of phosphorylation. Several peptides yielded reproducible crystals, but most exhibited poor diffraction (7+ Å). Following rounds of optimization using hanging-drop plates (VDX; Hampton Research), we collected a dataset from a crystal grown from 5 mM $^{P82}N_{76\text{-}88}$ and 16 mg mL^{-1} $Hsp27_{84\text{-}170}$ that allowed for structure determination. Drops were set using a protein-peptide mixture in PBS pH 7.0 and equilibrated against 22% PEG 3350; 0.02 M sodium potassium diphosphate; and 0.1 M Bis-Tris propane pH 7.5. The protein was mixed 1:1 with the crystallization solution (0.9 µl each) and drops were left to equilibrate at room temperature. Crystals grew within 2 days and continued growing to maximum size within 6 days. Crystals were cryoprotected by serial transfer from the drop to the crystallization solution containing additional 10% PEG 400 and 5% glycerol, then to the same solution with 10% glycerol, before being flash-frozen in liquid N_2. Diffraction data were collected under cryogenic conditions on beamline I04-1 at Diamond Light Source, Harwell, UK.

Diffraction data were integrated using iMosflm (Battye et al., 2011) and scaled and merged using Aimless in the CCP4 suite with truncation at 2.1Å. Phases were determined by molecular replacement using Phaser (McCoy et al., 2007) with a previous Hsp27 X-ray structure input as a search model (PDB 4MJH, modified by

removal of flexible loops, bound C-terminal peptide, and β2 strands). The four dimers in the asymmetric unit were completed through cycles of manual building in Coot (Emsley et al., 2010) and refinement in Phenix (Adams et al., 2002) imposing NCS restraints. Peptide density was then apparent in the 2Fo-Fc and Fo-Fc maps next to one monomer within each of the four dimers. Peptide fragments were placed through cycles of manual building in Coot and refinement in Phenix, now without NCS restraints and with treatment of TLS parameters (Winn et al., 2001). Most peptide side chains remained irresolvable throughout cycles of refinement in contrast to the well-resolved core. In addition, the peptide density never extended beyond a length accommodating 3 to 6 of 11 residues. Thus, we attempted to deduce the orientation and identity of the residues captured in the density. In light of data suggesting an intramolecular interaction, we treated each peptide as though extending toward the β2 strand of the monomer to which it is bound. The question of which residues occupy the binding pocket was thus restricted to those that could reach from the β2 strand if the chain were continuous, eliminating the latter half of the peptide and leaving, roughly, ALSRQL. The lack of density for the remaining half of peptide is unsurprising, since most of these residues are repeated in the ACD and would compete for contacts with their counterparts which are covalently bound to the core and exist at a much higher local concentration, leaving this portion of the peptide no site to bind and thus too disordered to give rise to electron density. Each peptide region of the map displayed a side chain pointing into a pocket between Phe104 and Gly161 that could not accommodate a bulky residue, but is larger than alanine. Backbone density extends two residues N-terminally from this pocket, excluding Leu77 and implicating Ser78 or Leu81. Modeling each of these caused negligible difference in R_{work} and R_{free}; so based on close examination of the resulting Fo-Fc maps and potential chemical contacts within the pocket, as well as the NMR data supporting dynamic changes in this region of the ACD upon Ser78 mutation, we

placed Ser78 into this location. At each dimer interface, Cys137 density evidenced both disulphide-bonded and reduced conformations, and so we modelled each of these with occupancy 0.5 in all cases, consistent with the labile nature of this bond. The final model with R_{work}/R_{free} 20%/24% is deposited in the RCSB PDB with ID code 6GJH and will be released upon publication. (Statistics, Table 4.1)

NMR Spectroscopy

All NMR spectroscopy experiments were recorded at 298 K on a 14.1 T Varian Inova spectrometer equipped with a 5 mm z-axis gradient triple resonance room temperature probe. Spectra were processed with NMRPipe (Delaglio et al., 1995) and analyzed with NMRFAM-Sparky (Lee et al., 2015). 2D sensitivity-enhanced ^{1}H-^{15}N HSQC spectra were acquired with ^{1}H (^{15}N) 512 (64) complex points, spectral widths of 8012 Hz (1800 Hz), maximum acquisition times of 64 ms (35.6 ms), an inter-scan delay of 1 s, and four scans per FID for a total acquisition time of 19 minutes. ^{13}C,^{15}N-^{2P}Hsp27$_{77\text{-}171}$ was prepared at a final concentration of 0.9 mM in 30 mM sodium phosphate, 2 mM EDTA, pH 7 for resonance assignments, wherein HNCA, HNCO, and HN(CA)CO spectra were recorded. The assigned ^{1}H, ^{15}N, ^{13}CO, and ^{13}Ca chemical shifts were analyzed with TALOS-N (Shen and Bax, 2013) and RCI (Berjanskii and Wishart, 2006) to respectively estimate the secondary structure and N-H order parameters.

Protonated, ^{15}N-labelled proteins were prepared at 0.9 mM (^{2P}Hsp27$_{77\text{-}171}$) or 1 mM (Hsp27$_{84\text{-}171}$) for ^{15}N relaxation studies. Standard pulse sequences to measure transverse relaxation times (T_2), ^{15}N heteronuclear nuclear Overhauser enhancements (hetNOE) (Farrow et al., 1994), and ^{15}N CPMG relaxation dispersion (Loria et al., 1999) were employed. The T_2 experiments contained eight delay times up

Table 4.1. Statistics of X-ray data collection and refinement for the structure of $Hsp27_{84\text{-}170}$ bound to $^{P82}Hsp27_{76\text{-}88}$.

	$Hsp27_{ACD}$·PPR
Crystal parameters	
Space group	$P12_11$
Cell dimensions	
a, b, c (Å)	56.81, 157.67, 57.87
α, β, γ(°)	90.00, 95.45, 90.00
Dimers in ASU	4
Data collection	
Beamline	DLS I02
Wavelength (Å)	0.9282
Resolution (Å)	78.84-2.10 (2.16-2.10)
Reflections observed/unique	165,497/57,271
Redundancy	2.9 (2.9)
Completeness	97.3 (95.8)
R_{meas}	0.144 (0.990)
I/σI	5.1 (1.4)
Wilson B-value	31.6
CC1/2	0.99 (0.528)
Refinement	
Resolution (Å)	57.63-2.10 (2.14-2.10)
Reflections	58,913
R_{work}	0.2108
R_{free}	0.2514
No. of non-H atoms	
Protein	5,622
Water	371
Other	14
Mean B-factors (Å²)	
Protein (ACD)	42.35
Protein (PPR)	84.96
Water	38.23
Other	72.12
RMSD from target values	
Bond length (Å)	0.002
Bond angle (°)	0.524
Ramachandran statistics	
In preferred regions (%)	95.34
In allowed regions (%)	4.51
Outliers (%)	0.15
PDB ID code	6GJH

R_{free} calculated using 5% of reflections.
Values in parentheses correspond to the highest resolution shell.

to 154 ms and an inter-scan delay of 2 s. The intensity changes over time (I/I_0) were fit to an exponential decay, and values are reported as rates (i.e. $1/T_2$) for convenience. hetNOE experiments contained an inter-scan delay of 8 s, with values representing the intensity upon amide proton saturation divided by the intensity in its absence. CPMG relaxation dispersion experiments were recorded with variable delays between 180° pulses in the CPMG pulse train ($\tau_{CPMG} = 4\nu_{CPMG}^{-1}$). A constant relaxation delay of 39 ms for the CPMG period and twenty ν_{CPMG} values ranging from 54 to 950 Hz were employed. Peak shapes were fit with FuDA (Vallurupalli et al., 2008) to extract peak intensities, which were then converted into $R_{2,eff}$ values using the following relation: $R_{2,eff}(\nu CPMG) = -1/T_{relax} \ln(I(\nu_{CPMG})/I(0))$, where $I(\nu_{CPMG})$ is the intensity of a peak at ν_{CPMG}, T_{relax} is the constant relaxation delay of 39 ms that was absent in the reference spectrum, and $I(0)$ is the intensity of a peak in the reference spectrum. Two duplicate νCPMG points were recorded in each dispersion data set for error analysis, and uncertainties in $R_{2,eff}$ were calculated using the standard deviation of peak intensities from such duplicate measurements. From plots of $R_{2,eff}$ as a function of νCPMG, $R_{2,eff}$ was determined by taking the difference of $R_{2,eff}$ (54 Hz) and $R_{2,eff}$ (950 Hz) with error bars representing the propagated errors in $R_{2,eff}$.

Native ion mobility mass spectrometry

Because Hsp27 can form disulphide-linked dimers, experiments involving the ACD were performed in the presence of 10× molar excess DTT. Gold-plated capillaries were prepared in-house. Native MS and IM-MS data were recorded on a Synapt G1 mass spectrometer (Waters) modified for the transmission of intact noncovalent protein complexes (Bush et al., 2010). $Hsp27_{77\text{-}171}$ variants were analyzed at a concentration of 10 μM in 200 mM ammonium acetate pH 6.9. Spectra of $FLNC_{d18\text{-}21}$

and peptide titrations were recorded with settings: capillary 1.4-1.5kV; sample cone 30V; extractor cone 3V; backing pressure 3.8 mbar; trap gas (argon) 4 mL min^{-1}; trap and transfer cell voltages 5V. FLNC concentration was held constant at 5 μM and peptide concentration ($N_{80\text{-}88}$ or $^{P}N_{80\text{-}88}$) was varied from 5 to 160 μM. Peptides and protein were mixed in 200 mM ammonium acetate pH 6.9 immediately prior to data collection. nESI was performed in the presence of acetonitrile vapor in order to promote charge reduction and maintenance of noncovalent contacts and native structure (Hopper et al., 2012). A minimum of three technical repeats were collected at each ratio. Dissociation constants were fit to the data using UniDec software (Marty et al., 2015). Spectra were collected using an excess of peptide with scrambled sequence (N_{ctrl}) to ensure binding was specific. However, the reported dissociation constants were not corrected, and should be considered in comparison to each other rather than as absolute affinities. To control for the possibility of promiscuity in recognition of Ig-domain folds by Hsp27 flexible termini, spectra were also collected using an excess of peptide mimicking Hsp27 C-terminal residues 177-186.

Collision-induced unfolding experiments were performed using the same conditions as described for peptide titrations, with an ion mobility cell gas pressure of 0.533 mbar (N_2) and flow rate 22 mL min^{-1}, at wave velocity 300 m s^{-1} and wave height 7.0V. Collision voltage in the trap cell was varied from 5 to 180V, in 5V increments prior to 100V and 10V increments after 100V. All CIU data shown herein feature FLNC in the presence of 16-fold molar excess of peptide, with the exception of controls in Figure **4.10**. CIU plots are representative of experiments performed with three different protein batch preparations and three peptide to protein ratios. To quantify peptide dissociation with activation, the 13^{+} singly bound peak was selected in the Synapt quadrupole with LM and HM resolution 7.2 and 6.9,

respectively, and trap voltage ramped as described for CIU. Data were smoothed 30×2 in MassLynx and peak intensities recorded, summed as bound or unbound, and converted to percentages. A subtraction was applied to correct for nonspecific adduction at potentials of 30V and below, based on trials with N_{ctrl} which determined this to be approximately the activation required to dissociate a nonspecifically bound ligand.

Aggregation assay

Hsp27 (WT or 3P, with S to D mutations at residues 15, 78, and 82) was mixed with $FLNC_{d18\text{-}21}$ at a 2 to 1 ratio (80 and 40 μM, respectively) in 200 mM ammonium acetate pH 6.9 with 500 μM DTT and incubated at 25°C for 90 minutes. Aliquots were removed periodically and pelleted at 13,000×g at 10°C for 10 minutes. Soluble fractions were diluted by a factor of 3 with 200 mM ammonium acetate for analysis by SDS-PAGE, and pellets were resuspended in the same volume and solubilized upon addition of the SDS-PAGE loading buffer. Gel bands were quantified by densitometry in ImageLab 5.2, using the raw intensities of FLNC and Hsp27 bands to extract relative soluble and insoluble proportions at each time point.

Molecular Dynamics

Two simulations of the Hsp27 dimer were prepared using the ACD crystal structure PDB 4MJH. The systems were immersed into a TIP3P water box and neutralized with 0.15M Na^+ Cl^- ions. Simulations used the Amber99SB force field (Hornak et al., 2006) on NAMD2.9 (Phillips et al., 2005) molecular dynamics engine, with SHAKE algorithm constraining heavy atoms distances, and PME treating the electrostatic interactions in periodic boundary conditions. The systems were first minimized with 2000 conjugate gradient steps, and subsequently simulated using a 2 fs timestep.

Systems were equilibrated in the nPT ensemble for 0.5 ns, with a 10 kcal mol^{-1} constraint on protein alpha carbons. 300K and 1 atm were imposed by Langevin dynamics, using a damping constant of 1 ps^{-1}, a piston period of 200 fs, and a piston decay of 50 fs. Constraints were subsequently removed, and systems were simulated in the nVT ensemble at 300K for 1 ns. Finally, production runs were conducted in the nPT ensemble (300K and 1 Atm) for 1 μs. We extracted the coordinates of each individual monomer every 0.1 ns, yielding 1000 frames per monomer. Figure **4.5a** shows snapshots from between 200 and 400 ns.

References

J. F. Abisambra, L. J. Blair, S. E. Hill, J. R. Jones, C. Kraft, J. Rogers, 3rd Koren, J., U. K. Jinwal, L. Lawson, A. G. Johnson, D. Wilcock, J. C. O'Leary, K. Jansen-West, M. Muschol, T. E. Golde, E. J. Weeber, J. Banko, and C. A. Dickey. Phosphorylation dynamics regulate hsp27-mediated rescue of neuronal plasticity deficits in tau transgenic mice. *J Neurosci*, 30(46): 15374–82, 2010.

P. D. Adams, R. W. Grosse-Kunstleve, L. W. Hung, T. R. Ioerger, A. J. McCoy, N. W. Moriarty, R. J. Read, J. C. Sacchettini, N. K. Sauter, and T. C. Terwilliger. Phenix: building new software for automated crystallographic structure determination. *Acta Crystallogr D Biol Crystallogr*, 58 (Pt 11):1948–54, 2002.

S. Arber, J. J. Hunter, Jr. Ross, J., M. Hongo, G. Sansig, J. Borg, J. C. Perriard, K. R. Chien, and P. Caroni. Mlp-deficient mice exhibit a disruption of cardiac cytoarchitectural organization, dilated cardiomyopathy, and heart failure. *Cell*, 88(3):393–403, 1997.

V. Arndt, N. Dick, R. Tawo, M. Dreiseidler, D. Wenzel, M. Hesse, D. O. Furst, P. Saftig, R. Saint, B. K. Fleischmann, M. Hoch, and J. Hohfeld. Chaperone-assisted selective autophagy is essential for muscle maintenance. *Curr Biol*, 20(2):143–8, 2010.

A. P. Arrigo. Human small heat shock proteins: protein interactomes of homo- and hetero-oligomeric complexes: an update. *FEBS Lett*, 587(13):1959–69, 2013.

C. Bagneris, O. A. Bateman, C. E. Naylor, N. Cronin, W. C. Boelens, N. H. Keep, and C. Slingsby. Crystal structures of alpha-crystallin domain dimers of alphab-crystallin and hsp20. *J Mol Biol*, 392(5):1242–52, 2009.

T. G. Battye, L. Kontogiannis, O. Johnson, H. R. Powell, and A. G. Leslie. imosflm: a new graphical interface for diffraction-image processing with mosflm. *Acta Crystallogr D Biol Crystallogr*, 67 (Pt 4):271–81, 2011.

R. L. Begay, C. A. Tharp, A. Martin, S. L. Graw, G. Sinagra, D. Miani, M. E. Sweet, D. B. Slavov, N. Stafford, M. J. Zeller, R. Alnefaie, T. J. Rowland, F. Brun, K. L. Jones, K. Gowan, L. Mestroni, D. M. Garrity, and M. R. Taylor. Flnc gene splice mutations cause dilated cardiomyopathy. *JACC Basic Transl Sci*, 1(5):344–359, 2016.

R. Benndorf, K. Hayess, S. Ryazantsev, M. Wieske, J. Behlke, and G. Lutsch. Phosphorylation and supramolecular organization of murine small heat shock protein hsp25 abolish its actin polymerization-inhibiting activity. *J Biol Chem*, 269(32):20780–4, 1994.

R. Benndorf, X. Sun, R. R. Gilmont, K. J. Biederman, M. P. Molloy, C. W. Goodmurphy, H. Cheng, P. C. Andrews, and M. J. Welsh. Hsp22, a new member of the small heat shock protein superfamily, interacts with mimic of phosphorylated hsp27 ((3d)hsp27). *J Biol Chem*, 276(29): 26753–61, 2001.

M. Berjanskii and D. S. Wishart. Nmr: prediction of protein flexibility. *Nat Protoc*, 1(2):683–8, 2006.

K. N. Bitar, M. S. Kaminski, N. Hailat, K. B. Cease, and J. R. Strahler. Hsp27 is a mediator of sustained smooth muscle contraction in response to bombesin. *Biochem Biophys Res Commun*, 181(3):1192–200, 1991.

M. P. Bova, H. S. McHaourab, Y. Han, and B. K. Fung. Subunit exchange of small heat shock proteins. analysis of oligomer formation of alphaa-crystallin and hsp27 by fluorescence resonance energy transfer and site-directed truncations. *J Biol Chem*, 275(2):1035–42, 2000.

A. Brodehl, R. A. Ferrier, S. J. Hamilton, S. C. Greenway, M. A. Brundler, W. Yu, W. T. Gibson, M. L. McKinnon, B. McGillivray, N. Alvarez, M. Giuffre, J. Schwartzentruber, Forge Canada Consortium, and B. Gerull. Mutations in flnc are associated with familial restrictive cardiomyopathy. *Hum Mutat*, 37(3):269–79, 2016.

A. L. Bryantsev, S. A. Loktionova, O. P. Ilyinskaya, E. M. Tararak, H. H. Kampinga, and A. E. Kabakov. Distribution, phosphorylation, and activities of hsp25 in heat-stressed h9c2 myoblasts: a functional link to cytoprotection. *Cell Stress Chaperones*, 7(2):146–55, 2002.

M. F. Bush, Z. Hall, K. Giles, J. Hoyes, C. V. Robinson, and B. T. Ruotolo. Collision cross sections of proteins and their complexes: a calibration framework and database for gas-phase structural biology. *Anal Chem*, 82(22):9557–65, 2010.

B. Buyandelger, K. E. Ng, S. Miocic, I. Piotrowska, S. Gunkel, C. H. Ku, and R. Knoll. Mlp (muscle lim protein) as a stress sensor in the heart. *Pflugers Arch*, 462(1):135–42, 2011.

S. Chaudhuri and P. G. Smith. Cyclic strain-induced hsp27 phosphorylation modulates actin filaments in airway smooth muscle cells. *Am J Respir Cell Mol Biol*, 39(3):270–8, 2008.

I. S. Chernik, A. S. Seit-Nebi, S. B. Marston, and N. B. Gusev. Small heat shock protein hsp20 (hspb6) as a partner of 14-3-3gamma. *Mol Cell Biochem*, 295(1-2):9–17, 2007.

F. Chevessier, J. Schuld, Z. Orfanos, A. C. Plank, L. Wolf, A. Maerkens, A. Unger, U. Schlotzer-Schrehardt, R. A. Kley, S. Von Horsten, K. Marcus, W. A. Linke, M. Vorgerd, P. F. van der Ven, D. O. Furst, and R. Schroder. Myofibrillar instability exacerbated by acute exercise in filaminopathy. *Hum Mol Genet*, 24(25):7207–20, 2015.

F. Delaglio, S. Grzesiek, G. W. Vuister, G. Zhu, J. Pfeifer, and A. Bax. Nmrpipe: a multidimensional spectral processing system based on unix pipes. *J Biomol NMR*, 6(3):277–93, 1995.

S. M. Dixit, D. A. Polasky, and B. T. Ruotolo. Collision induced unfolding of isolated proteins in the gas phase: past, present, and future. *Curr Opin Chem Biol*, 42:93–100, 2018.

R. M. Duff, V. Tay, P. Hackman, G. Ravenscroft, C. McLean, P. Kennedy, A. Steinbach, W. Schoffler, P. F. M. van der Ven, D. O. Furst, J. Song, K. Djinovic-Carugo, S. Penttila, O. Raheem, K. Reardon, A. Malandrini, S. Gambelli, M. Villanova, K. J. Nowak, D. R. Williams, J. E. Landers, Jr. Brown, R. H., B. Udd, and N. G. Laing. Mutations in the n-terminal actin-binding domain of filamin c cause a distal myopathy. *Am J Hum Genet*, 88(6):729–740, 2011.

A. Elosegui-Artola, X. Trepat, and P. Roca-Cusachs. Control of mechanotransduction by molecular clutch dynamics. *Trends Cell Biol*, 2018.

P. Emsley, B. Lohkamp, W. G. Scott, and K. Cowtan. Features and development of coot. *Acta Crystallogr D Biol Crystallogr*, 66(Pt 4):486–501, 2010.

J. D. Eschweiler, R. Kerr, J. Rabuck-Gibbons, and B. T. Ruotolo. Sizing up protein-ligand complexes: The rise of structural mass spectrometry approaches in the pharmaceutical sciences. *Annu Rev Anal Chem (Palo Alto Calif)*, 10(1):25–44, 2017.

N. A. Farrow, R. Muhandiram, A. U. Singer, S. M. Pascal, C. M. Kay, G. Gish, S. E. Shoelson, T. Pawson, J. D. Forman-Kay, and L. E. Kay. Backbone dynamics of a free and phosphopeptide-complexed src homology 2 domain studied by 15n nmr relaxation. *Biochemistry*, 33(19):5984–6003, 1994.

Y. Feng and C. A. Walsh. The many faces of filamin: a versatile molecular scaffold for cell motility and signalling. *Nat Cell Biol*, 6(11):1034–8, 2004.

I. Ferrer and M. Olive. Molecular pathology of myofibrillar myopathies. *Expert Rev Mol Med*, 10: e25, 2008.

N. T. Frankenberg, G. D. Lamb, K. Overgaard, R. M. Murphy, and K. Vissing. Small heat shock proteins translocate to the cytoskeleton in human skeletal muscle following eccentric exercise independently of phosphorylation. *J Appl Physiol (1985)*, 116(11):1463–72, 2014.

M. Fuchs, D. J. Poirier, S. J. Seguin, H. Lambert, S. Carra, S. J. Charette, and J. Landry. Identification of the key structural motifs involved in hspb8/hspb6-bag3 interaction. *Biochem J*, 425(1):245–55, 2009.

D. O. Furst, L. G. Goldfarb, R. A. Kley, M. Vorgerd, M. Olive, and P. F. van der Ven. Filamin c-related myopathies: pathology and mechanisms. *Acta Neuropathol*, 125(1):33–46, 2013.

M. Gaestel, W. Schroder, R. Benndorf, C. Lippmann, K. Buchner, F. Hucho, V. A. Erdmann, and H. Bielka. Identification of the phosphorylation sites of the murine small heat shock protein hsp25. *J Biol Chem*, 266(22):14721–4, 1991.

K. Gehmlich, N. Pinotsis, K. Hayess, P. F. van der Ven, H. Milting, A. El Banayosy, R. Korfer, M. Wilmanns, E. Ehler, and D. O. Furst. Paxillin and ponsin interact in nascent costameres of muscle cells. *J Mol Biol*, 369(3):665–82, 2007.

N. Golenhofen, M. D. Perng, R. A. Quinlan, and D. Drenckhahn. Comparison of the small heat shock proteins alphab-crystallin, mkbp, hsp25, hsp20, and cvhsp in heart and skeletal muscle. *Histochem Cell Biol*, 122(5):415–25, 2004.

J. Gomez, R. Lorca, J. R. Reguero, C. Moris, M. Martin, S. Tranche, B. Alonso, S. Iglesias, V. Alvarez, B. Diaz-Molina, P. Avanzas, and E. Coto. Screening of the filamin c gene in a large cohort of hypertrophic cardiomyopathy patients. *Circ Cardiovasc Genet*, 10(2), 2017.

M. Haslbeck, J. Peschek, J. Buchner, and S. Weinkauf. Structure and function of alpha-crystallins: Traversing from in vitro to in vivo. *Biochim Biophys Acta*, 1860(1 Pt B):149–66, 2016.

G. K. Hochberg, H. Ecroyd, C. Liu, D. Cox, D. Cascio, M. R. Sawaya, M. P. Collier, J. Stroud, J. A. Carver, A. J. Baldwin, C. V. Robinson, D. S. Eisenberg, J. L. Benesch, and A. Laganowsky. The structured core domain of alphab-crystallin can prevent amyloid fibrillation and associated toxicity. *Proc Natl Acad Sci U S A*, 111(16):E1562–70, 2014.

G. K. A. Hochberg, D. A. Shepherd, E. G. Marklund, I. Santhanagoplan, M. T. Degiacomi, A. Laganowsky, T. M. Allison, E. Basha, M. T. Marty, M. R. Galpin, W. B. Struwe, A. J. Baldwin, E. Vierling, and J. L. P. Benesch. Structural principles that enable oligomeric small heat-shock protein paralogs to evolve distinct functions. *Science*, 359(6378):930–935, 2018.

L. Hoffman, C. C. Jensen, M. Yoshigi, and M. Beckerle. Mechanical signals activate p38 mapk pathway-dependent reinforcement of actin via mechanosensitive hspb1. *Mol Biol Cell*, 2017.

J. T. Hopper, K. Sokratous, and N. J. Oldham. Charge state and adduct reduction in electrospray ionization-mass spectrometry using solvent vapor exposure. *Anal Biochem*, 421(2):788–90, 2012.

V. Hornak, R. Abel, A. Okur, B. Strockbine, A. Roitberg, and C. Simmerling. Comparison of multiple amber force fields and development of improved protein backbone parameters. *Proteins*, 65(3):712–25, 2006.

A. I. Ibitayo, J. Sladick, S. Tuteja, O. Louis-Jacques, H. Yamada, G. Groblewski, M. Welsh, and K. N. Bitar. Hsp27 in signal transduction and association with contractile proteins in smooth muscle cells. *Am J Physiol*, 277(2 Pt 1):G445–54, 1999.

N. Jaafar, J. Gomez, I. Kammoun, I. Zairi, W. B. Amara, S. Kachboura, S. Kraiem, M. Hammami, S. Iglesias, B. Alonso, and E. Coto. Spectrum of mutations in hypertrophic cardiomyopathy genes among tunisian patients. *Genet Test Mol Biomarkers*, 20(11):674–679, 2016.

W. M. Jackson, M. J. Jaasma, R. Y. Tang, and T. M. Keaveny. Mechanical loading by fluid shear is sufficient to alter the cytoskeletal composition of osteoblastic cells. *Am J Physiol Cell Physiol*, 295(4):C1007–15, 2008.

S. Jehle, P. Rajagopal, B. Bardiaux, S. Markovic, R. Kuhne, J. R. Stout, V. A. Higman, R. E. Klevit, B. J. van Rossum, and H. Oschkinat. Solid-state nmr and saxs studies provide a structural basis for the activation of alphab-crystallin oligomers. *Nat Struct Mol Biol*, 17(9):1037–42, 2010.

C. P. Johnson, H. Y. Tang, C. Carag, D. W. Speicher, and D. E. Discher. Forced unfolding of proteins within cells. *Science*, 317(5838):663–6, 2007.

B. Jovcevski, M. A. Kelly, A. P. Rote, T. Berg, H. Y. Gastall, J. L. Benesch, J. A. Aquilina, and H. Ecroyd. Phosphomimics destabilize hsp27 oligomeric assemblies and enhance chaperone activity. *Chem Biol*, 22(2):186–95, 2015.

R. A. Kley, Y. Hellenbroich, P. F. van der Ven, D. O. Furst, A. Huebner, V. Bruchertseifer, S. A. Peters, C. M. Heyer, J. Kirschner, R. Schroder, D. Fischer, K. Muller, K. Tolksdorf, K. Eger, A. Germing, T. Brodherr, C. Reum, M. C. Walter, H. Lochmuller, U. P. Ketelsen, and M. Vorgerd. Clinical and morphological phenotype of the filamin myopathy: a study of 31 german patients. *Brain*, 130(Pt 12):3250–64, 2007.

R. A. Kley, A. Maerkens, Y. Leber, V. Theis, A. Schreiner, P. F. van der Ven, J. Uszkoreit, C. Stephan, S. Eulitz, N. Euler, J. Kirschner, K. Muller, H. E. Meyer, M. Tegenthoff, D. O. Furst, M. Vorgerd, T. Muller, and K. Marcus. A combined laser microdissection and mass spectrometry approach reveals new disease relevant proteins accumulating in aggregates of filaminopathy patients. *Mol Cell Proteomics*, 12(1):215–27, 2013.

T. J. Koh and J. Escobedo. Cytoskeletal disruption and small heat shock protein translocation immediately after lengthening contractions. *Am J Physiol Cell Physiol*, 286(3):C713–22, 2004.

Y. Lad, P. Jiang, S. Ruskamo, D. S. Harburger, J. Ylanne, I. D. Campbell, and D. A. Calderwood. Structural basis of the migfilin-filamin interaction and competition with integrin beta tails. *J Biol Chem*, 283(50):35154–63, 2008.

J. Landry, H. Lambert, M. Zhou, J. N. Lavoie, E. Hickey, L. A. Weber, and C. W. Anderson. Human hsp27 is phosphorylated at serines 78 and 82 by heat shock and mitogen-activated kinases that recognize the same amino acid motif as s6 kinase ii. *J Biol Chem*, 267(2):794–803, 1992.

J. N. Lavoie, H. Lambert, E. Hickey, L. A. Weber, and J. Landry. Modulation of cellular thermoresistance and actin filament stability accompanies phosphorylation-induced changes in the oligomeric structure of heat shock protein 27. *Mol Cell Biol*, 15(1):505–16, 1995.

W. Lee, M. Tonelli, and J. L. Markley. Nmrfam-sparky: enhanced software for biomolecular nmr spectroscopy. *Bioinformatics*, 31(8):1325–7, 2015.

B. Lelj-Garolla and A. G. Mauk. Self-association of a small heat shock protein. *J Mol Biol*, 345 (3):631–42, 2005.

W. C. Liao, L. Y. Juo, Y. L. Shih, Y. H. Chen, and Y. T. Yan. Hspb7 prevents cardiac conduction system defect through maintaining intercalated disc integrity. *PLoS Genet*, 13(8):e1006984, 2017.

J. P. Loria, M. Rance, and 3rd Palmer, A. G. A trosy cpmg sequence for characterizing chemical exchange in large proteins. *J Biomol NMR*, 15(2):151–5, 1999.

T. Luo, K. Mohan, P. A. Iglesias, and D. N. Robinson. Molecular mechanisms of cellular mechanosensing. *Nat Mater*, 12(11):1064–71, 2013.

M. T. Marty, A. J. Baldwin, E. G. Marklund, G. K. Hochberg, J. L. Benesch, and C. V. Robinson. Bayesian deconvolution of mass and ion mobility spectra: from binary interactions to polydisperse ensembles. *Anal Chem*, 87(8):4370–6, 2015.

A. Mashaghi, S. Bezrukavnikov, D. P. Minde, A. S. Wentink, R. Kityk, B. Zachmann-Brand, M. P. Mayer, G. Kramer, B. Bukau, and S. J. Tans. Alternative modes of client binding enable functional plasticity of hsp70. *Nature*, 539(7629):448–451, 2016.

A. J. McCoy, R. W. Grosse-Kunstleve, P. D. Adams, M. D. Winn, L. C. Storoni, and R. J. Read. Phaser crystallographic software. *J Appl Crystallogr*, 40(Pt 4):658–674, 2007.

E. T. McDonald, M. Bortolus, H. A. Koteiche, and H. S. McHaourab. Sequence, structure, and dynamic determinants of hsp27 (hspb1) equilibrium dissociation are encoded by the n-terminal domain. *Biochemistry*, 51(6):1257–68, 2012.

S. W. Moore, P. Roca-Cusachs, and M. P. Sheetz. Stretchy proteins on stretchy substrates: the important elements of integrin-mediated rigidity sensing. *Dev Cell*, 19(2):194–206, 2010.

F. F. Morelli, L. Mediani, L. Heldens, J. Bertacchini, I. Bigi, A. D. Carra, J. Vinet, and S. Carra. An interaction study in mammalian cells demonstrates weak binding of hspb2 to bag3, which is regulated by hspb3 and abrogated by hspb8. *Cell Stress Chaperones*, 22(4):531–540, 2017.

N. Mounier and A. P. Arrigo. Actin cytoskeleton and small heat shock proteins: how do they interact? *Cell Stress Chaperones*, 7(2):167–76, 2002.

M. F. Ortiz-Genga, S. Cuenca, M. Dal Ferro, E. Zorio, R. Salgado-Aranda, V. Climent, L. Padron-Barthe, I. Duro-Aguado, J. Jimenez-Jaimez, V. M. Hidalgo-Olivares, E. Garcia-Campo, C. Lanzillo, M. P. Suarez-Mier, H. Yonath, S. Marcos-Alonso, J. P. Ochoa, J. L. Santome, D. Garcia-Giustiniani, J. L. Rodriguez-Garrido, F. Dominguez, M. Merlo, J. Palomino, M. L. Pena, J. P. Trujillo, A. Martin-Vila, D. Stolfo, P. Molina, E. Lara-Pezzi, F. E. Calvo-Iglesias, E. Nof, L. Calo, R. Barriales-Villa, J. R. Gimeno-Blanes, M. Arad, P. Garcia-Pavia, and L. Monserrat. Truncating flnc mutations are associated with high-risk dilated and arrhythmogenic cardiomyopathies. *J Am Coll Cardiol*, 68(22):2440–2451, 2016.

Judit Perales-Calvo, David Giganti, Guillaume Stirnemann, and Sergi Garcia-Manyes. The force-dependent mechanism of dnak-mediated mechanical folding. *Science Advances*, 4(2), 2018.

M. B. Pereira, A. M. Santos, D. C. Goncalves, A. C. Cardoso, S. R. Consonni, F. C. Gozzo, P. S. Oliveira, A. H. Pereira, A. R. Figueiredo, A. O. Tiroli-Cepeda, C. H. Ramos, A. A. de Thomaz, C. L. Cesar, and K. G. Franchini. alphab-crystallin interacts with and prevents stress-activated proteolysis of focal adhesion kinase by calpain in cardiomyocytes. *Nat Commun*, 5:5159, 2014.

J. Peschek, N. Braun, J. Rohrberg, K. C. Back, T. Kriehuber, A. Kastenmuller, S. Weinkauf, and J. Buchner. Regulated structural transitions unleash the chaperone activity of alphab-crystallin. *Proc Natl Acad Sci U S A*, 110(40):E3780–9, 2013.

J. C. Phillips, R. Braun, W. Wang, J. Gumbart, E. Tajkhorshid, E. Villa, C. Chipot, R. D. Skeel, L. Kale, and K. Schulten. Scalable molecular dynamics with namd. *J Comput Chem*, 26(16): 1781–802, 2005.

V. Popa, D. A. Trecroce, R. G. McAllister, and L. Konermann. Collision-induced dissociation of electrosprayed protein complexes: An all-atom molecular dynamics model with mobile protons. *J Phys Chem B*, 120(23):5114–24, 2016.

J. N. Rabuck, S. J. Hyung, K. S. Ko, C. C. Fox, M. B. Soellner, and B. T. Ruotolo. Activation state-selective kinase inhibitor assay based on ion mobility-mass spectrometry. *Anal Chem*, 85 (15):6995–7002, 2013.

P. Rajagopal, Y. Liu, L. Shi, A. F. Clouser, and R. E. Klevit. Structure of the alpha-crystallin domain from the redox-sensitive chaperone, hspb1. *J Biomol NMR*, 63(2):223–8, 2015.

M. P. Ramirez, M. Rivera, D. Quiroga-Roger, A. Bustamante, M. Vega, M. Baez, E. M. Puchner, and C. A. M. Wilson. Single molecule force spectroscopy reveals the effect of bip chaperone on protein folding. *Protein Sci*, 26(7):1404–1412, 2017.

J. N. Rauch, E. Tse, R. Freilich, S. A. Mok, L. N. Makley, D. R. Southworth, and J. E. Gestwicki. Bag3 is a modular, scaffolding protein that physically links heat shock protein 70 (hsp70) to the small heat shock proteins. *J Mol Biol*, 429(1):128–141, 2017.

Z. Razinia, T. Makela, J. Ylanne, and D. A. Calderwood. Filamins in mechanosensing and signaling. *Annu Rev Biophys*, 41:227–46, 2012.

E. Reinstein, A. Gutierrez-Fernandez, S. Tzur, C. Bormans, S. Marcu, E. Tayeb-Fligelman, C. Vinkler, A. Raas-Rothschild, D. Irge, M. Landau, M. Shohat, X. S. Puente, D. M. Behar, and C. Lopez-Otin. Congenital dilated cardiomyopathy caused by biallelic mutations in filamin c. *Eur J Hum Genet*, 24(12):1792–1796, 2016.

A. A. Robinson, M. J. Dunn, A. McCormack, C. dos Remedios, and M. L. Rose. Protective effect of phosphorylated hsp27 in coronary arteries through actin stabilization. *J Mol Cell Cardiol*, 49 (3):370–9, 2010.

T. Rogalla, M. Ehrnsperger, X. Preville, A. Kotlyarov, G. Lutsch, C. Ducasse, C. Paul, M. Wieske, A. P. Arrigo, J. Buchner, and M. Gaestel. Regulation of hsp27 oligomerization, chaperone function, and protective activity against oxidative stress/tumor necrosis factor alpha by phosphorylation. *J Biol Chem*, 274(27):18947–56, 1999.

S. L. Shammas. Mechanistic roles of protein disorder within transcription. *Curr Opin Struct Biol*, 42:155–161, 2017.

Y. Shen and A. Bax. Protein backbone and sidechain torsion angles predicted from nmr chemical shifts using artificial neural networks. *J Biomol NMR*, 56(3):227–41, 2013.

N. N. Sluchanko, S. Beelen, A. A. Kulikova, S. D. Weeks, A. A. Antson, N. B. Gusev, and S. V. Strelkov. Structural basis for the interaction of a human small heat shock protein with the 14-3-3 universal signaling regulator. *Structure*, 25(2):305–316, 2017.

L. H. Snoeckx, R. N. Cornelussen, F. A. Van Nieuwenhoven, R. S. Reneman, and G. J. Van Der Vusse. Heat shock proteins and cardiovascular pathophysiology. *Physiol Rev*, 81(4):1461–97, 2001.

S. Somara and K. N. Bitar. Tropomyosin interacts with phosphorylated hsp27 in agonist-induced contraction of smooth muscle. *Am J Physiol Cell Physiol*, 286(6):C1290–301, 2004.

Y. Sugiyama, A. Suzuki, M. Kishikawa, R. Akutsu, T. Hirose, M. M. Waye, S. K. Tsui, S. Yoshida, and S. Ohno. Muscle develops a specific form of small heat shock protein complex composed of mkbp/hspb2 and hspb3 during myogenic differentiation. *J Biol Chem*, 275(2):1095–104, 2000.

A. J. Sutherland-Smith. Filamin structure, function and mechanics: are altered filamin-mediated force responses associated with human disease? *Biophys Rev*, 3(1):15–23, 2011.

P. Tannous, H. Zhu, A. Nemchenko, J. M. Berry, J. L. Johnstone, J. M. Shelton, Jr. Miller, F. J., B. A. Rothermel, and J. A. Hill. Intracellular protein aggregation is a proximal trigger of cardiomyocyte autophagy. *Circulation*, 117(24):3070–8, 2008.

G. Tarone and M. Brancaccio. Keep your heart in shape: molecular chaperone networks for treating heart disease. *Cardiovasc Res*, 102(3):346–61, 2014.

T. G. Thompson, Y. M. Chan, A. A. Hack, M. Brosius, M. Rajala, H. G. Lidov, E. M. McNally, S. Watkins, and L. M. Kunkel. Filamin 2 (fln2): A muscle-specific sarcoglycan interacting protein. *J Cell Biol*, 148(1):115–26, 2000.

A. Ulbricht, F. J. Eppler, V. E. Tapia, P. F. van der Ven, N. Hampe, N. Hersch, P. Vakeel, D. Stadel, A. Haas, P. Saftig, C. Behrends, D. O. Furst, R. Volkmer, B. Hoffmann, W. Kolanus, and J. Hohfeld. Cellular mechanotransduction relies on tension-induced and chaperone-assisted autophagy. *Curr Biol*, 23(5):430–5, 2013.

R. Valdes-Mas, A. Gutierrez-Fernandez, J. Gomez, E. Coto, A. Astudillo, D. A. Puente, J. R. Reguero, V. Alvarez, C. Moris, D. Leon, M. Martin, X. S. Puente, and C. Lopez-Otin. Mutations in filamin c cause a new form of familial hypertrophic cardiomyopathy. *Nat Commun*, 5:5326, 2014.

P. Vallurupalli, D. F. Hansen, and L. E. Kay. Structures of invisible, excited protein states by relaxation dispersion nmr spectroscopy. *Proc Natl Acad Sci U S A*, 105(33):11766–71, 2008.

P. F. van der Ven, W. M. Obermann, B. Lemke, M. Gautel, K. Weber, and D. O. Furst. Characterization of muscle filamin isoforms suggests a possible role of gamma-filamin/abp-l in sarcomeric z-disc formation. *Cell Motil Cytoskeleton*, 45(2):149–62, 2000.

P. F. van der Ven, E. Ehler, P. Vakeel, S. Eulitz, J. A. Schenk, H. Milting, B. Micheel, and D. O. Furst. Unusual splicing events result in distinct xin isoforms that associate differentially with filamin c and mena/vasp. *Exp Cell Res*, 312(11):2154–67, 2006.

V. Vogel and M. Sheetz. Local force and geometry sensing regulate cell functions. *Nat Rev Mol Cell Biol*, 7(4):265–75, 2006.

M. Vorgerd, P. F. van der Ven, V. Bruchertseifer, T. Lowe, R. A. Kley, R. Schroder, H. Lochmuller, M. Himmel, K. Koehler, D. O. Furst, and A. Huebner. A mutation in the dimerization domain of filamin c causes a novel type of autosomal dominant myofibrillar myopathy. *Am J Hum Genet*, 77(2):297–304, 2005.

M. J. Vos, M. P. Zijlstra, B. Kanon, M. A. van Waarde-Verhagen, E. R. Brunt, H. M. Oosterveld-Hut, S. Carra, O. C. Sibon, and H. H. Kampinga. Hspb7 is the most potent polyq aggregation suppressor within the hspb family of molecular chaperones. *Hum Mol Genet*, 19(23):4677–93, 2010.

S. D. Weeks, E. V. Baranova, M. Heirbaut, S. Beelen, A. V. Shkumatov, N. B. Gusev, and S. V. Strelkov. Molecular structure and dynamics of the dimeric human small heat shock protein hspb6. *J Struct Biol*, 185(3):342–54, 2014.

M. S. Willis and C. Patterson. Proteotoxicity and cardiac dysfunction–alzheimer's disease of the heart? *N Engl J Med*, 368(5):455–64, 2013.

M. D. Winn, M. N. Isupov, and G. N. Murshudov. Use of tls parameters to model anisotropic displacements in macromolecular refinement. *Acta Crystallogr D Biol Crystallogr*, 57(Pt 1): 122–33, 2001.

Z. Xie, W. Xu, E. W. Davie, and D. W. Chung. Molecular cloning of human abpl, an actin-binding protein homologue. *Biochem Biophys Res Commun*, 251(3):914–9, 1998.

Chapter 5

Structural and functional investigations of cvHsp

5.1 Abstract

cvHsp (HspB7) is a musculoskeletally expressed sHsp whose dysfunction is implicated in cardiovascular, skeletal, and respiratory diseases. Its structure, from secondary structural elements through quaternary organization, is unknown. cvHsp is involved in maintaining myoarchitectural integrity, and its absence coincides with aggregation of the mechanosensor filamin C, hinting at a role in physiological biomechanical processes. Understanding this role at the molecular level requires a better understanding of cvHsp itself. Here, I apply systems we have used to study other sHsps to cvHsp, and also introduce new approaches tailored to its reputed binding partners and functions. The work is preliminary, with the aims of 1) answering fundamental questions about cvHsp adherence to certain tenets of sHsp assembly, and 2) establishing experimental systems that can be harnessed for more extensive characterization of *in vivo* interactions. I show that while cvHsp contains the canonical ACD with a dimer interface, the structure of this dimer is likely to be distinct from that of other human sHsps; and that the full-length chaperone, unlike many others, does not form large and polydisperse oligomers. The chapter concludes with a description of two methods for measuring the effect of cvHsp (or any protein) on actin network viscoelasticity and potentially assembly.

5.2 Introduction

5.2.1 cvHsp functions in muscle

cvHsp was identified in 1999 and classified as a sHsp based on prediction of an α-crystallin domain due to its homology to other sHsps (Krief et al., 1999). Initially found in the heart (hence 'cv' for cardiovascular), it is now known to also be expressed in skeletal muscle, notably at appreciable levels in the diaphragm, the only muscle besides the heart for which life requires continuous, robust movement (Golenhofen et al., 2004; Doran et al., 2007; Vos et al., 2009). Expression levels increase with age (Doran et al., 2007) and under pathological conditions, including in the diaphragms of patients with Duchenne muscular dystrophy (Doran et al., 2006) and in the hearts of mouse and rat cardiomyopathy models (Krief et al., 1999; Rudebusch et al., 2017). These observations, along with cardioprotective abilities (Ke et al., 2011; Mercer et al., 2018), implicate cvHsp in a stress-related role.

cvHsp also performs physiological functions. Without prior stress, and uniquely among the sHsps, it localizes to speckles in the nucleus involved in storage and assembly of splicing machinery (Vos et al., 2009). Other reported non-aggregating interaction partners include filamins (FLNs) A, B, and C (Krief et al., 1999; Juo et al., 2016; Liao et al., 2017; Mercer et al., 2018), titin (solely observed in zebrafish) (Mercer et al., 2018), and monomeric actin (Wu et al., 2017). cvHsp knockout in mice is fatal, leading to severe myoarchitectural disruption, respiratory failure, and aggregation of FLNC in cardiac and diaphragmatic tissue (Juo et al., 2016; Liao et al., 2017). Knockout in zebrafish, which lack a diaphragm, is tolerated, but causes cardiomyopathic symptoms and predisposes fish to death following exercise stress (Mercer et al., 2018).

Links between cvHsp allelic variants and human disease continue to emerge.

These have been associated with cardiomyopathy and heart failure (Cappola et al., 2010; Stark et al., 2010; Esslinger et al., 2017) and respiratory abnormality with sleep apnea (Wang et al., 2016). Many appear in a database of somatic mutations in cancer (Bindal et al., 2011). The molecular architecture of cvHsp and of its interactions with clients underlying these physiological and pathological functions remain unexplored.

5.2.2 cvHsp structure and chaperone activity

The cvHsp sequence indicates the expected canonical N- and C-terminal regions flanking an α–crystallin domain (ACD) that is more highly conserved than the termini, as seen in an alignment with αB-crystallin and Hsp27 (Figure **5.1**). Three possible cvHsp isoforms are indicated, predicted from low levels of alternative splicing (Kappe et al., 2003; Krief et al., 1999).



Figure 5.1. Sequence alignment of Hsp27, αB-crystallin, and cvHsp. Gray shading indicates residue conservation in 8 or more of the 10 human sHsps; pink shading, conservation in 5 to 7. Cysteines are yellow. Boundaries of ACDs represent constructs used herein. Dotted lines indicate C-terminal peptides (Ctps). cvHsp has three reported isoforms: Iso1 (170 residues), lacking the segment ^{67}AAHPT^{71} according to Kappe et al. (2003) or lacking AHPT according to Krief et al. (1999); Iso2 (174 or 175 residues); and Iso3, terminating at residue 67. Alignment from Kappe et al. (2003).

The oligomerization behaviour of cvHsp has not been determined unambiguously. Polydispersity between a dimer and 12-mer as well as subunit exchange on a similar timescale to αB-crystallin *in vitro* was reported for rat cvHsp (Yang et al., 2011); however, human cvHsp has been measured *in cellulo* and *in vitro* only as small species consistent with monomers and dimers (Vos et al., 2010; Mymrikov

et al., 2017). Structural clues can be drawn from interactions between cvHsp and other proteins: heteromerization with HspB8 involves each protein's C-terminus only (Sun et al., 2004), a departure from ACD·ACD, ACD·C, or NTD·NTD modes of assembly (Basha et al., 2012). Also uniquely, cvHsp is the only sHsp expressed in muscle that does not bind the co-chaperone BAG3 (Vos et al., 2010). BAG3 competes with the C-terminal I-X-I/V motif to bind the β4-β8 groove of sHsp ACDs (Rauch et al., 2017), implying the cvHsp ACD structure may differ from that of the others.

As a canonical chaperone, cvHsp activity varies widely with substrate. It displayed no ability to refold heat-denatured luciferase in nuclear speckles unlike αB-crystallin, αA-crystallin and Hsp27 (Vos et al., 2009), and no ability to suppress heat-induced aggregation in cell lysates unlike seven other sHsps examined (Mymrikov et al., 2017). It is, however, the most potent sHsp suppressor of polyQ aggregation, through a mechanism involving inhibition of aggregate formation and no ability to clear pre-formed aggregates (Vos et al., 2010; Eenjes et al., 2016). PolyQ-containing proteins are unlikely to be endogenous cvHsp targets since these are neurodegenerative hallmarks and cvHsp is muscle-specific, but this mechanism of early chaperoning may apply to other substrates. For example, FLNC aggregates are found in various tissues upon cvHsp knockout (Liao et al., 2017; Mercer et al., 2018), but cvHsp does not appear to be involved in the clearance of damaged FLNC (Ulbricht et al., 2013).

The path toward understanding cvHsp function at the molecular level involves characterizing its own structure and dynamics, and how it binds and affects various clients. In this chapter, I present preliminary data on cvHsp and develop systems and methods toward further pursuit of these goals.

5.3 Results and Discussion

5.3.1 cvHsp is small compared to canonical polydisperse sHsps

First, a protocol was devised to bacterially express and purify human cvHsp. The final purification produced the longest isoform of human cvHsp (174 residues based on Krief et al. (1999)), following unsuccessful attempts with the 170-residue isoform from several species, which may be toxic to bacterial cells and require alternative strategies. Because the protein formed inclusion bodies upon over-expression in *E. coli* (Figure **5.2a**), various conditions for resolubilization and refolding were screened (see Methods). Native mass spectra and ion mobility measurements were recorded for cvHsp refolded from 6M urea by stepwise dialysis (Figure **5.2b**).

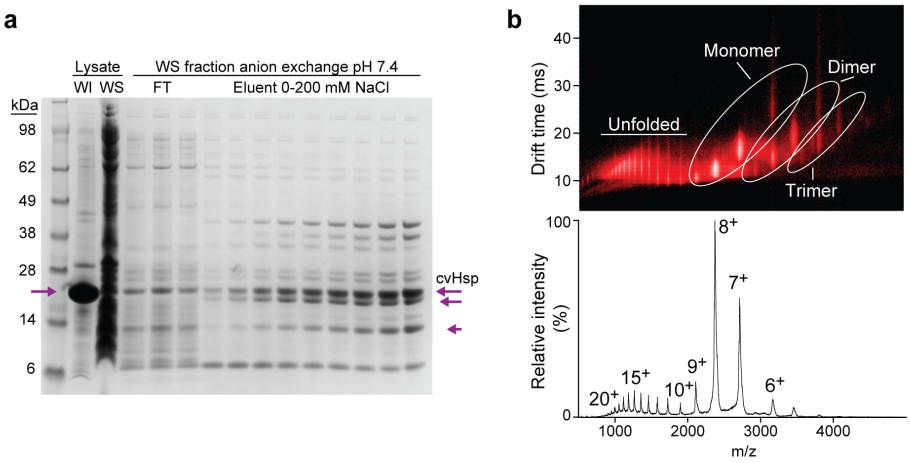


Figure 5.2. cvHsp is purified from inclusion bodies and adopts small stoichiometries. a. SDS-PAGE of soluble and insoluble fractions following cell culture lysis and centrifugation (left) and fractionated anion exchange chromatography elution at pH 7.4 from the WS portion of the lysate (right). cvHsp is highly over-expressed but largely insoluble, and soluble cvHsp is rapidly truncated. Purification of cvHsp from inclusion bodies is described in the Methods. **b.** Native IM-MS of refolded cvHsp. The monomer charge state distribution is bimodal. Visible in the ion mobiligram (intensity on a logarithmic scale) are higher stoichiometries with CSDs evidencing folded structures. Expression plasmid for cvHsp provided by Roy Quinlan, Durham University.

The native mass spectrum shows predominantly monomeric cvHsp with a bimodal charge state distribution. This may indicate that the protein adopts two native conformational states, a phenomenon described seen in Chapter 3; alterna-

tively, it could result from partial instability in the MS buffer or inefficient refolding. Further screening of buffer conditions are underway, and functional assays have demonstrated that the protein is chaperone-active (data generated by Zihao Wang; not shown).

We observe higher stoichiometries at low abundance (Figure **5.2b**). These adopt charge series consistent with folded structures and include dimer and trimer, but no large oligomers like those formed by αB-crystallin and Hsp27. These data are consistent with reports of cvHsp comprising small oligomers (Vos et al., 2010; Mymrikov et al., 2017) and depart from the dodecamer observed for rat cvHsp (Yang et al., 2011). One possible explanation for discrepancies is isoform variability, since it is unclear which isoforms were used in past studies. If the removal of residues in the NTD affects stoichiometry, this would be an interesting finding in compliance with the importance of N-terminal elements for self- and co-assembly of other sHsps (Ghosh and Clark, 2005; Heirbaut et al., 2017).

5.3.2 cvHsp assembles via its ACD into dimers

Having established that cvHsp weakly oligomerizes, we next interrogated whether self-assembly involves similar interfaces to other sHsps. Based on sequence alignment and the boundaries of predicted secondary structural elements, an ACD construct was designed as delineated in Figure **5.1**, and expressed and purified in the same manner as αB-crystallin and Hsp27 ACDs. All three populate a monomer-dimer equilibrium (Figure **5.3**), confirming that cvHsp contains an ACD·ACD interface. The discrepancy between stoichiometries of the truncated and full-length cvHsp could implicate the termini in modulation of intra-subunit interactions.

To examine the possibility of an ACD·C interface within cvHsp, we used a peptide mimicking the 8 most C-terminal residues ($cvHsp_{Ctp}$) because this region

contains the sequence I-K-I, a candidate for the I-X-I/V motif; and because it is far enough upstream of the ACD to be connected via a flexible hinge. In contrast to αB-crystallin and Hsp27, no binding between this peptide and cvHsp$_{ACD}$ was observed at a range of ratios tested, shown here at an 8-fold molar excess for all three systems (Figure **5.3**).

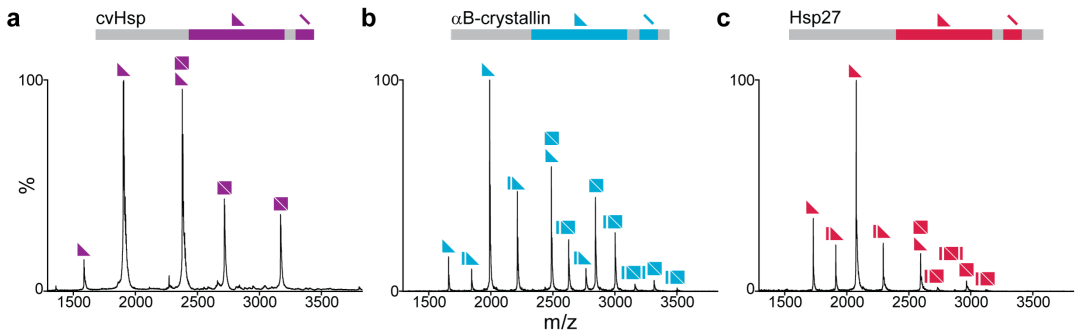


Figure 5.3. cvHsp contains an ACD·ACD interface but may not contain an ACD·C interface. Native MS of 5 μM **a.** cvHsp$_{ACD}$, **b.** αB$_{ACD}$, and **c.** Hsp27$_{ACD}$ with 40 μM each corresponding C-terminal peptide. cvHsp$_{ACD}$ exists as monomer and dimer, like the others, but does not bind cvHsp$_{Ctp}$, whereas αB-crystallin and Hsp27 C-terminal peptides readily bind both monomers and dimers.

We might tentatively conclude from these data that cvHsp does not contain an ACD·C interface, which is conceivable given its deviations from the behaviour of other sHsps. However, caveats apply. First, the constructs should be adjusted to account for possible misappropriation of the C-terminal I-X-I/V motif. While some alignment tools place this in frame with cvHsp's I-K-I (Krief et al., 1999), others place it in frame with residues H-P-H (Kappe et al., 2003). If the HPH region is able to bind the ACD, the binding pocket may differ from the hydrophobic nature of other β4-β8 grooves. Second, the peptide cvHsp$_{Ctp}$ (QTFRTEIKI) displayed evidence by ion mobility of more than one conformation (data not shown). This may indicate an ability to adopt secondary structure or pyroglutamate formation, either of which could have affected its ability to interact with otherwise accessible binding sites.

Following the identification of an oligomeric interface within truncated cvHsp$_{ACD}$, we used this construct in other exploratory studies.

5.3.3 Covalent dimerization suggests redox sensitivity and a distinct ACD structure

During purification of the different cvHsp constructs, some population of covalent dimer was always observed following the final SEC step (Figure **5.4a**). Since the only cysteine is contained within the ACD, we looked at the effect of oxidation on $cvHsp_{ACD}$ dimerization and size. Partially oxidized $cvHsp_{ACD}$ resisted reduction, with the dimer only partially dissociating even at a 300-fold excess of DTT over a short incubation (Figure **5.4b**). This may indicate that the disulphide bond is not labile, and is instead solvent-inaccessible and a determinant of the oxidized dimer structure. Native IM-MS (Figure **5.4c**) was used to calculate the collision cross-sections of reduced and oxidized $cvHsp_{ACD}$ dimers (Figure **5.4d**). CCS distributions overlaid closely, evidencing that the dimer structure does not change appreciably with oxidation state.

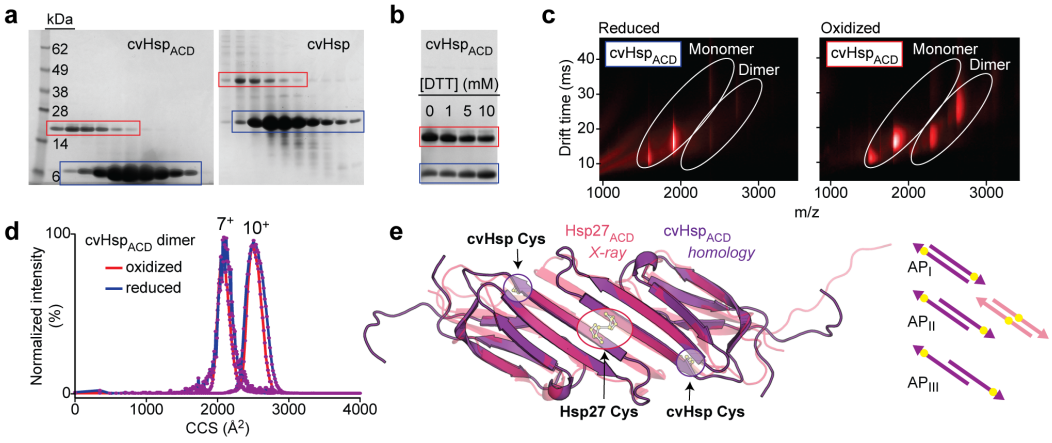


Figure 5.4. cvHsp forms covalent dimers, suggesting a unique ACD structure. **a.** SDS-PAGE of fractionated SEC elutions for $cvHsp_{ACD}$ and full-length cvHsp. Monomers are boxed in blue and covalent dimers (confirmed by MS) are boxed in red. **b.** SDS-PAGE of 30 μM partially oxidized cvHsp alone and following addition of 1, 5, and 10 mM DTT. **c.** Native ion mobiligrams of reduced and partially oxidized $cvHsp_{ACD}$. **d.** Experimental CCS distributions for the 7^+ and 10^+ charge states of reduced and oxidized cvHsp dimers (confirmed by collisional dissociation). **e.** Red, crystal structure of the Hsp27 ACD (Chapter 4) modelled with Cys137 in partial oxidized and reduced occupancies at the centre of an AP_{II} dimer interface. Purple, homology model of the cvHsp ACD. The sole cysteine is predicted to lie on the periphery of the β6+7 strand, incompatible with covalent dimerization via any of the known antiparallel interface register shifts (AP_I, AP_{II}, AP_{III}, right).

Redox-modulated structure and function of a sHsp would not be novel: Hsp27 disulphide and thiol forms have different chaperone potencies (Chalova et al., 2014) and are affected by disease-causative mutation (Kalmar et al., 2017). cvHsp was recently reported to react rapidly with small electrophilic species in cells, functionality lost upon mutating cysteine to serine, suggesting that it can act as a redox regulator through potent cysteine biosensing (Surya et al., 2018). However, our observation of covalent dimerization is surprising in light of the predicted position of the cysteine within the cvHsp ACD. An X-ray structure of the Hsp27 dimer overlaid with a homology model of the cvHsp dimer (Kelley et al., 2015) highlights the different cysteine locations (Figure **5.4e**). If cvHsp does contain an AP interface and cysteine lies on its periphery, in order to align with its counterpart to form a disulphide, it could not adopt any of the previously reported AP registers for metazoan sHsp ACD dimers (**5.4e**). The CCS of the cvHsp dimer (Figure **5.4d**) is larger than that of the αB-crystallin dimer in the AP_{II} register (Hochberg et al., 2014), placing it closer in theory to AP_{III}, which has not been observed before outside of crystal structures. To address the puzzling nature of cvHsp dimerization, we are pursuing X-ray crystallography strategies to solve the ACD structure at high resolution.

5.3.4 cvHsp does not appear to bind filamin A domains 23 or 24

The discovery of cvHsp was reported alongside identification of FLNA as its binding partner (Krief et al., 1999). As described in Chapters 3 and 4, filamins are long, multimodular, actin-binding mechanosensors involved in cellular signalling pathways and cytoskeletal organization. Their N-terminal actin-binding domain is followed by 24 Ig-like domains, the last of which contains the filamin dimer interface (Figure **5.5a**). The two most C-terminal FLNA domains were pinpointed as containing the binding site with cvHsp (Krief et al., 1999). To test the interaction, we successfully

cloned, expressed, and purified the domains linked together ($FLNA_{d23\text{-}24}$) as well as the dimerization domain alone ($FLNA_{d24}$). Both $FLNA_{d23\text{-}24}$ and $FLNA_{d24}$ were predominantly dimeric by native MS, with minor tetrameric populations (Figure **5.5b-c**, lower). When either of these were mixed with cvHsp Isoform 2, $cvHsp_{ACD}$, or $cvHsp_{Ctp}$ at various ratios and analyzed by native MS, no complexes between the proteins were observed. Representative mass spectra with $cvHsp_{ACD}$ are shown here (Figure **5.5b-c**, upper).

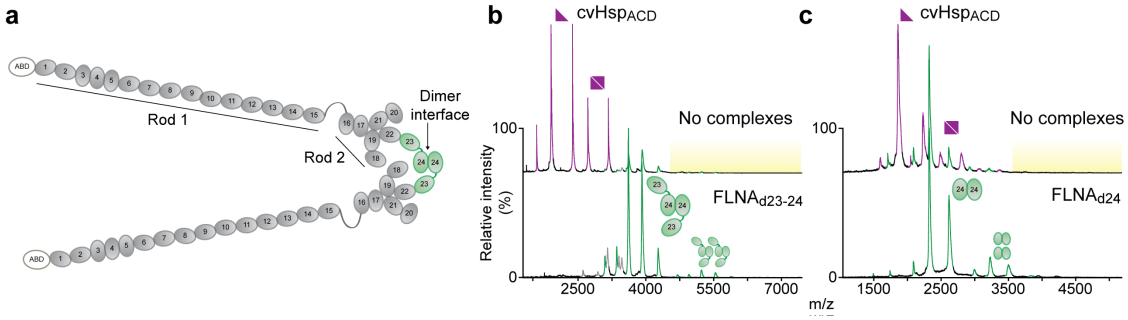


Figure 5.5. No interaction is detected between cvHsp and FLNA C-terminal domains. a. Schematic of full-length human filamin A, as in Chapter 3, Figure 3.1. Domains posited as important for interaction with cvHsp are green. **b-c.** nESI-MS of recombinant $FLNA_{d23\text{-}24}$ and $FLNA_{d24}$ alone and mixed with $cvHsp_{ACD}$. FLNA domains form dimers and, through an unknown interface, tetramers. No peaks corresponding to masses which match FLNA-cvHsp complexes were observed, neither here nor at different ratios or with different cvHsp variants.

Based on these data, we propose that, at least at thermodynamic equilibrium, cvHsp does not bind FLNA domains 23 or 24. While this stands in contrast to a previous study (Krief et al., 1999), it is consistent with reports emerging since the time of these experiments. In recent studies, FLNC is a conclusive binding partner of cvHsp with extensive peptide coverage in LCMS of co-immunoprecipitated proteins (Mercer et al., 2018), and FLNA is sometimes also co-immunoprecipitated with cvHsp (Liao et al., 2017) and sometimes not pulled down at all (Mercer et al., 2018). It is plausible that FLNA is a false positive cvHsp interaction partner, supported by our null results.

5.3.5 An optical trapping method for *in vitro* measurement of actin network viscosity

We found no evidence of interaction between cvHsp and FLNA domains 23 or 24 at equilibrium; however, as implied by the extent of sHsp client function in biomechanics and demonstrated in Chapter 4, application of force can affect these interactions in ways undetectable at rest. Thus, we hypothesized that a function of cvHsp could be to affect the stiffness of a cell or tissue by altering the filamin force response and hence the pliability of the filamin cross-linked actin network. To test this idea, we worked with the Oxford Colloid Group to adapt an existing method for actin network viscosity measurement using microrheology (Lee et al., 2010).

The microrheology experiment is summarized in Figure **5.6a**. We first mix monomeric actin ('G-actin', globular) with recombinant human filamin; if desired, the chaperone; and a dilute suspension of small (3.5 μm diameter) inert plastic colloids. Actin polymerization is initiated by addition of KCl and ATP, and the network (now 'F-actin', filamentous) is transferred to a glass coverslip. Using an optical trapping system with an infrared fiber laser, a colloid is moved by switching two optical traps on and off at a fixed distance several hundred times, at a low frequency exceeding the relaxation time of the network. The colloid movement applies stress to the network which is met by strain, and through precise monitoring of its position over time, viscoelastic properties of the material can be derived (theory and application to actin networks in particular have been described previously (Preece et al., 2011; Broedersz et al., 2010; Lee et al., 2010)).

First, we trapped and manipulated colloids in F-actin without filamin present. These behaved irregularly, some moving freely and some unable to be moved at all, suggesting a patchy network of filaments with dense bundles and sparse areas. Addition of FLNA allowed for much more consistent colloid behaviour throughout

the samples, evidencing a regular microstructure consistent with other reports (Lee et al., 2010; Schmoller et al., 2010). The network became more viscous at higher actin concentrations (Figure **5.6b**). When cvHsp variants were included (Isoform 2 or cvHsp$_{\Delta N}$, a construct lacking only the NTD), no significant changes in network viscoelasticity were observed (Figure **5.6c-d**).

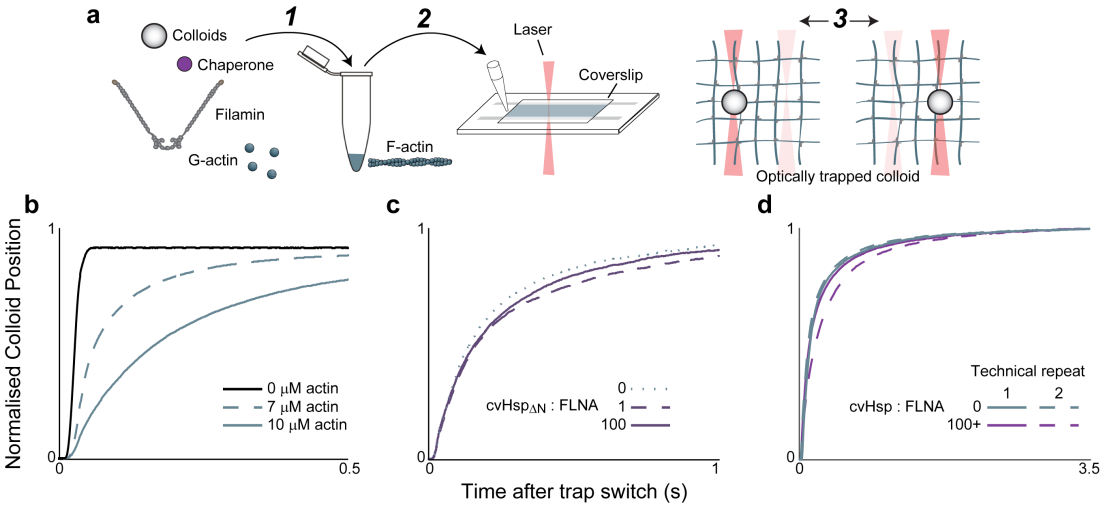


Figure 5.6. Microrheology of FLNA cross-linked actin shows no differences in network viscoelasticity in the presence of cvHsp. a. Schematic of the experiment. Components are mixed and polymerization induced (**1**), the polymerized network is transferred to a coverslip (**2**), and a colloid is moved between two optical traps to perturb the network as its position is monitored (**3**). **b.** Collapsed and averaged colloid position in water and in FLNA-cross-linked actin. The colloid moves more slowly through the network as actin concentration increases, evidencing a more rigid mesh. Filamin to actin ratio is held constant here at 0.005. **c.** Experiments in the presence of cvHsp$_{\Delta N}$, showing two chaperone concentrations, and **d.** full-length cvHsp, showing repeats using two colloids at different areas of the sample. Network viscosity does not change significantly in either case. Note that curves **b-d** should be compared internally and not across plots, as x-axis scales differ. Measurements recorded by Arran Curran. Recombinant FLNA provided by Fumihiko Nakamura.

The lack of an impact of cvHsp on FLNA cross-linked actin network viscoelasticity is consistent with our null binding results between the proteins, and with emerging reports that FLNC rather than FLNA may be the prevalent cvHsp binding partner (Liao et al., 2017; Mercer et al., 2018). Recombinant FLNA requires expression in eukaryotic cells and was kindly provided by the Nakamura lab at Harvard University. More recently, our collaborators at the University of Vienna in the Djinovic-Carugo lab have succeeded in producing recombinant human FLNC. This

will enable rheological experiments using cvHsp and FLNC cross-linked actin, which may be more fruitful based on the emerging relationship between these proteins and myoarchitectural integrity (Liao et al., 2017; Juo et al., 2016). We also note that, with inclusion of dyes in the sample, this method can be accompanied by confocal microscopy using the available instrumentation to visualize network organization and density and possibly chaperone localization.

5.3.6 Free actin can be monitored during real-time assembly in physiological buffer by native MS

In addition to filamins, actin itself is a possible substrate of cvHsp, with binding reported to inhibit G-actin polymerization (Wu et al., 2017). Since the rheology experiment probes F-actin and does not monitor polymerization, our observation that cvHsp does not affect the force response of actin networks (Figure **5.6**) does not necessarily contradict this prior study (Wu et al., 2017), and an alternative approach is needed to examine the putative interaction. Time-resolved native MS can be useful for monitoring protein assembly (Benesch and Ruotolo, 2011) (see also Chapter 6), but in the case of a polymer such as actin rather than an oligomer or complex, this approach presents two immediate challenges. First, the sample may rapidly become too complex for nESI, for example exceeding the capillary tip size, or acquiring too much charge along a lengthy filament to allow for resolution between subtly different species. Second, whereas oligomerization is typically spontaneous and broadly compatible with volatile low-salt buffer conditions, polymerization is usually triggered by nucleotide hydrolysis and studied under carefully controlled counter-ion and salt conditions generally troublesome for native MS.

We wished to determine whether actin assembly could be monitored by native MS from solution conditions more closely mimicking the physiological environment than conventional MS buffers. Ionized from a typical G-actin buffer, with moderate

activation in the mass spectrometer, we were surprisingly able to resolve individual charge states corresponding to the 42 kDa actin monomer (Figure **5.7a**). The charge state distribution (CSD) was initially broad, and high enough to potentially represent non-native or heavily adducted protein; but addition of low concentrations of ammonium acetate shifted the mass spectrum toward a narrower CSD that was also closer to predicted nESI values (theoretical average $z = 12.8$ (van de Waterbeemd et al., 2017)) (Figure **5.7a**).

Next, we initiated polymerization and transferred the sample to the nESI source as quickly as possible to monitor the early stages of assembly. As polymerization proceeded, the signal intensity remained relatively constant for several minutes (Figure **5.7b**), during which time the mass spectrum changed, with charge series corresponding to native-like actin dimers and trimers appearing in addition to the predominant monomer (Figure **5.7c**). This is consistent with recent findings showing the possibility of dimeric and trimeric components to actin filament assembly in solution by Young et al. (2018), with whom we conducted this work as a complementary study.

This approach may allow us to confirm or refute cvHsp binding to G-actin, and if confirmed, characterize its putative effect on filament assembly (Wu et al., 2017). We also could consider application toward other sHsp interactions with cytoskeletal building blocks. Hsp27 is proposed to modulate the G/F-actin equilibrium in a phosphorylation-dependent manner, but it is unclear whether observed effects result from direct Hsp27-native actin binding, or whether the relevant target is instead destabilized actin or even actin-binding proteins (Seit-Nebi et al., 2013) (The Big Book on Small Heat-Shock Proteins, Chapter 18). Similarly, αB-crystallin associates with desmin and tubulin, which comprise intermediate filaments and microtubules (Houck and Clark, 2010; Dimauro et al., 2017). Further optimization of this method, possibly in conjunction with in-solution mass measurements (Young et al., 2018),

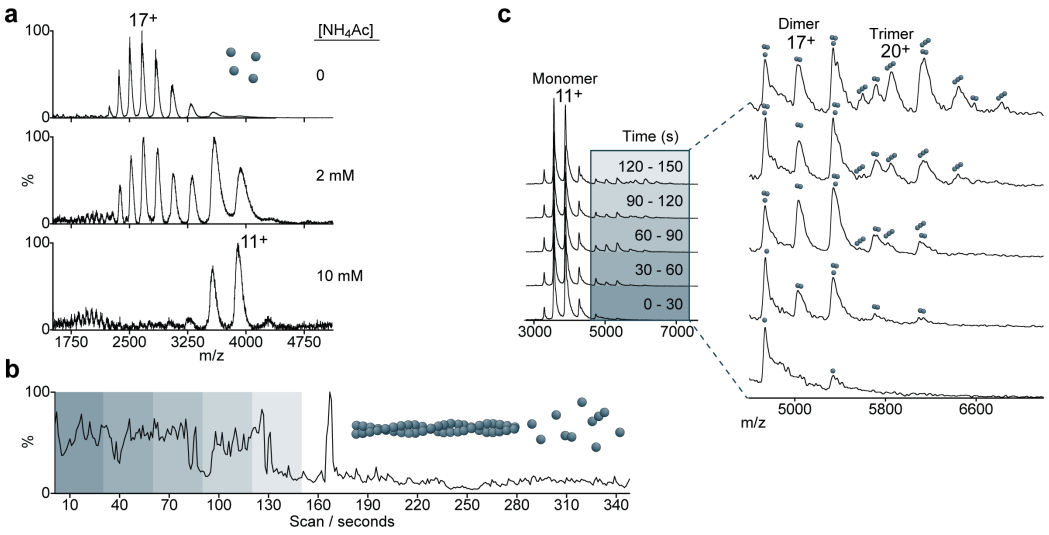


Figure 5.7. Time-resolved native MS of actin. **a.** nESI-MS of 8 µM 42 kDa G-actin in standard buffer conditions (2 mM Tris, 0.2 mM $CaCl_2$, 0.2 mM Mg-ATP, 2 mM DTT, pH 8). Addition of ammonium acetate (pH 8) at low concentrations shifts the CSD to native-like values. **b.** nESI-MS chromatogram for 6 µM actin in the same conditions with 10 mM ammonium acetate pH 7.5, following initiation of polymerization by 2 mM Mg-ATP, 1 mM EGTA, 5 mM KCl at pH 7.5. **c.** Mass spectra of summed scans in groups as colored in **b** reveals formation of small actin oligomers over time. Transmissible species are largely monomers as expected, with dimers and trimers representing intermediates in filament assembly. The stoichiometric distribution reaches equilibrium after 2.5 minutes, and signal drops as free actin is depleted. Samples prepared and experiments conducted in collaboration with Nikolas Hundt.

may illuminate this facet of sHsp function.

5.4 Conclusions

This chapter has described a suite of experimental strategies to probe cvHsp structure and function. We can now produce three cvHsp constructs: a full-length isoform, the ACD only, and a version lacking the NTD. These will enable delineation in future work of which regions of the protein are required for various interactions and functions. The full-length isoform was predominantly monomeric under the conditions employed, but it does contain an ACD·ACD dimer interface. While in other mammalian sHsps this interface is antiparallel (AP), its orientation in cvHsp may differ. Evidence for this comes from its ability to form disulphide-linked dimers, despite the homology-predictive location of its only cysteine on the periphery of

the putative AP interface. To understand these findings, a high-resolution X-ray structure is our next goal.

cvHsp is not up-regulated upon heat-shock, nor is it able to promiscuously suppress aggregation, or clear pre-formed aggregates (Vos et al., 2009; Big, 2015; Mymrikov et al., 2017). This implies specific function in the absence of stress, which may relate to its small stoichiometries. Rather than preferring to bind itself under basal conditions, various regions of the protein may need to be available for its clients.

FLNA does not appear to be among these clients, based on our null results when seeking complex formation between cvHsp and FLNA domains 23 or 24, or cvHsp effects on the viscosity of FLNA-linked actin networks. This interaction (Krief et al., 1999; Liao et al., 2017) is also called into question by other emerging evidence, linking cvHsp much more confidently to FLNC (Juo et al., 2016; Liao et al., 2017; Mercer et al., 2018). This is especially logical in light of the discovery that filamin isoform expression is tissue-specific, with virtually all filamin in cardiac and skeletal muscle being the FLNC isoform (Ohashi et al., 2005). Unlike the interaction between Hsp27 and FLNC explored in Chapter 4, cvHsp appears to associate with dimerized FLNC d24 rather than the segment d18-21, somehow stabilizing the myoarchitecture as a result (Juo et al., 2016). With the ability to mechanically probe FLNC-linked actin networks, the microrheological approach described here may offer more insight into this mechanism.

This chapter has described the foundations for a suite of experimental strategies into cvHsp structure and function. I am hopeful that it can serve as a springboard for a more in-depth investigation of this biomedically interesting chaperone.

Acknowledgments

I gratefully thank Arran Curran in Oxford's Department of Physical and Theoretical Chemistry Colloid Group for his work helping to establish the microrheology assay, and Roel Dullens for willingness to embark on the collaboration; Roy Quinlan and his group at the University of Durham for providing the cvHsp plasmid; Fumihiko Nakamura and Qianjing He from Harvard University for providing recombinant full-length FLNA protein; Nikolas Hundt from Philipp Kukura's group at the University of Oxford for collaborating on the actin experiments; and Reid Alderson for helpful discussion regarding protocols for inclusion body purification.

5.5 Methods

Expression and purification of cvHsp$_{ACD}$ and cvHsp$_{\Delta N}$

Gene inserts encoding human cvHsp$_{ACD}$ (residues 78-162 of Isoform 2) or cvHsp$_{\Delta N}$ (residues 78-175 of Isoform 2) optimized for *E. coli* were purchased from Integrated DNA Technologies and inserted into a pET28a vector linearized with BamHI and XhoI (New England Biolabs) using an In-Fusion HD Cloning Kit (NEB) to generate TEV-cleavable His-tagged constructs. Protein was expressed using BL21(DE3) cells (Agilent) in LB media for 16 hours at 22°C following cell culture growth to OD >0.6 and induction with 0.5 mM IPTG. Cells were lysed in 300 mM NaCl, 50 mM Tris, 20 mM imidazole, 5 mM BME at pH 8 with EDTA-free protease inhibitor cocktail (Roche) using a microfluidizer. The lysate was clarified by centrifugation at 4°C and 20,000×g for 20 minutes, filtered through a 0.22 μm filter, and loaded onto a HisTrap HP column. Protein was eluted using the loading buffer with 500 mM imidazole and dialyzed into the loading buffer at room temperature overnight with TEV protease. The sample was then passed over a HisTrap HP column again and dialyzed overnight at room temperature into 50 mM Tris pH 8.5 with 5 mM BME. It was loaded onto 4 5-mL HiTrap Q anion exchange columns and eluted in a gradient of 500-900 mM NaCl in the loading buffer. Protein was lastly exchanged into the storage buffer (100 mM NaCl, 20 mM Tris, 1 mM DTT, pH 8) using a Superdex S75 column. Concentration was determined by absorbance at 280 nm. Aliquots were flash-frozen and stored at -80°C until use.

Expression and purification of cvHsp Isoform 2

Full-length human cvHsp (Isoform 2 with AHPT, 174 residues) encoded in pET23a was transformed into BL21(DE3) pLysS cells and expressed in LB media (with 0.5%

glucose, 50 μg mL^{-1} ampicillin, and 37 μg mL^{-1} chlorampenicol) for 16 hours at 21°C following cell culture growth to OD >0.6 and induction with 0.5 mM IPTG. Cells were lysed in 20 mM Tris, 1 mM EDTA, 5 mM BME at pH 7.4 with EDTA-free protease inhibitor cocktail using a microfluidizer. Lysate was centrifuged at 4°C and 20,000×g for 20 minutes, which pelleted the desired protein in inclusion bodies. This step was the optimized for purifying the pelleted fraction using two wash steps with the lysis buffer supplemented with 1% triton X-100 and then 1 M urea to remove membrane phase contaminants.

Initial attempts to refold by simply diluting the protein into varying concentrations of NaCl or ammonium sulfate did not solubilize the sample. Dialysis overnight into 6M urea (+10 mM sodium phosphate) at 4°C successfully unfolded the protein and clarified the sample, but attempts to dialyze back into a physiological buffer resulted in immediate visible insolubilization. Refolding was next pursued via two strategies to gradually remove urea: first, refolding on-column via SEC as developed previously (Guan et al., 2005), and second, stepwise dialysis against 100 mM NaCl, 20 mM Tris, 5 mM BME, pH 7.5 with 3M urea, 2M urea, and 1M urea for 2 hours each and then no urea overnight at 4°C. Protein refolded in this manner could be concentrated heavily and freeze-thawed with no insolubilization; however, it was not amenable to biospin.

NB: site-directed mutagenesis was used to prepare a variant of this plasmid encoding ^{Y86W}cvHsp with a tryptophan incorporated to facilitate purification and concentration measurement, which may prove useful for future studies.

Expression and purification of FLNA d24 and d23-24

Gene inserts encoding Ig domains 23 or 23-24 from human FLNA (UniProt ID P21333, residues 2424-2647 and 2552-2646) optimized for *E. coli* were purchased

from Integrated DNA Technologies and inserted into a pET28a vector linearized with BamHI and XhoI (New England Biolabs) using an In-Fusion HD Cloning Kit (NEB) to generate TEV-cleavable His-tagged constructs. Protein was expressed and purified in the same manner as cvHsp truncated constructs, with the exception of the anion exchange step, which was not necessary for FLNA. Concentration was determined by absorbance at 280 nm and protein was stored in PBS pH 7.4 at -80°C until use.

NB: These FLNA constructs exist predominantly as dimers. A mutation was designed (^{L2591D}FLNA) to introduce a negatively charged side chain into a hydrophobic patch of the dimer interface, based on Pudas et al. (2005). We successfully expressed and purified the mutant protein in the same manner as WT and found it to be predominantly monomeric by native MS. This construct may be of use in future studies.

Native mass spectrometry

All mass spectra were collected on a Synapt G2 mass spectrometer modified for the transmission of intact noncovalent protein complexes (Waters). Parameters were adjusted for optimization of the sample under consideration; in general, capillary 1.38-1.5kV; sample cone 10-50V; extractor cone 3-4V; backing pressure 3-4.5 mbar; trap gas (argon) 2-4 mL min^{-1}; transfer cell voltage 5V; trap cell voltage 5-30V. Unless otherwise indicated in the text, spectra were collected in 200 mM ammonium acetate pH 6.9. Concentrations of protein were 5-20 μM with C-terminal peptides in excess up to 40 μM.

Microrheology of cross-linked actin networks

Lyophilized actin (Bioquote) was resuspended in G-buffer (5 mM Tris-HCl, 0.2 mM $CaCl_2$, 0.5 mM DTT, 0.2 mM ATP, pH 8.0) to produce a stock of 20 μM G-actin. Each sample for rheology was prepared to a volume of 20 μl consisting of: 7 μM actin; FLNA at a molar ratio of 0.01 to actin; cvHsp construct of interest ranging from 1 to 100 μM or a control protein (cytochrome C or BSA) exchanged into G-buffer; 1 μl of a dilute suspension of colloids in sterile H_2O. Lastly, 2 μl F-buffer (10X: 50 mM Tris-HCl, 500 mM KCl, 2 mM $MgCl_2$, 2 mM $CaCl_2$, 2 mM DTT, 5 mM ATP, 0.01% (w/v) NaN_3, pH 7.5) was added to induce polymerization. For initial feasibility experiments, no cvHsp was added, only 7 or 10 μM actin and FLNA at ratios of either 0.01 ot 0.05 to actin. Preliminary experiments imaging the networks by confocal microscopy (not shown here) were carried out using samples including phalloidin dye at a ratio of 1 to every 5 actin. Samples were incubated on ice for at least 1 hour to allow polymerization, and then pipetted between two surfaces of a glass coverslip and sealed. Further details of the coverslip and colloid supplies and experimental procedure are available from Arran Curran in the Oxford Colloid Group.

References

The Big Book on Small Heat Shock Proteins, volume 8 of *Heat Shock Proteins*. Springer, 2015.

E. Basha, H. O'Neill, and E. Vierling. Small heat shock proteins and alpha-crystallins: dynamic proteins with flexible functions. *Trends Biochem Sci*, 37(3):106–17, 2012.

J. L. Benesch and B. T. Ruotolo. Mass spectrometry: come of age for structural and dynamical biology. *Curr Opin Struct Biol*, 21(5):641–9, 2011.

N. Bindal, S. A. Forbes, D. Beare, P. Gunasekaran, K. Leung, C. Y. Kok, M. M. Jia, S. Bamford, C. Cole, S. Ward, J. Teague, M. R. Stratton, P. Campbell, and P. A. Futreal. Cosmic: the catalogue of somatic mutations in cancer. *Genome Biology*, 12:5–5, 2011.

C. P. Broedersz, M. Depken, N. Y. Yao, M. R. Pollak, D. A. Weitz, and F. C. MacKintosh. Cross-link-governed dynamics of biopolymer networks. *Phys Rev Lett*, 105(23):238101, 2010.

T. P. Cappola, M. Li, J. He, B. Ky, J. Gilmore, L. Qu, B. Keating, M. Reilly, C. E. Kim, J. Glessner, E. Frackelton, H. Hakonarson, F. Syed, A. Hindes, S. J. Matkovich, S. Cresci, and 2nd Dorn, G. W. Common variants in hspb7 and frmd4b associated with advanced heart failure. *Circ Cardiovasc Genet*, 3(2):147–54, 2010.

A. S. Chalova, M. V. Sudnitsyna, P. I. Semenyuk, V. N. Orlov, and N. B. Gusev. Effect of disulfide crosslinking on thermal transitions and chaperone-like activity of human small heat shock protein hspb1. *Cell Stress Chaperones*, 19(6):963–72, 2014.

I. Dimauro, A. Antonioni, N. Mercatelli, and D. Caporossi. The role of alphab-crystallin in skeletal and cardiac muscle tissues. *Cell Stress Chaperones*, 2017.

P. Doran, G. Martin, P. Dowling, H. Jockusch, and K. Ohlendieck. Proteome analysis of the dystrophin-deficient mdx diaphragm reveals a drastic increase in the heat shock protein cvhsp. *Proteomics*, 6(16):4610–21, 2006.

P. Doran, J. Gannon, K. O'Connell, and K. Ohlendieck. Aging skeletal muscle shows a drastic increase in the small heat shock proteins alphab-crystallin/hspb5 and cvhsp/hspb7. *Eur J Cell Biol*, 86(10):629–40, 2007.

E. Eenjes, J. M. Dragich, H. H. Kampinga, and A. Yamamoto. Distinguishing aggregate formation and aggregate clearance using cell-based assays. *J Cell Sci*, 129(6):1260–70, 2016.

U. Esslinger, S. Garnier, A. Korniat, C. Proust, G. Kararigas, M. Muller-Nurasyid, J. P. Empana, M. P. Morley, C. Perret, K. Stark, A. G. Bick, S. K. Prasad, J. Kriebel, J. Li, L. Tiret, K. Strauch, D. P. O'Regan, K. B. Marguiles, J. G. Seidman, P. Boutouyrie, P. Lacolley, X. Jouven, C. Hengstenberg, M. Komajda, H. Hakonarson, R. Isnard, E. Arbustini, H. Grallert, S. A. Cook, C. E. Seidman, V. Regitz-Zagrosek, T. P. Cappola, P. Charron, F. Cambien, and E. Villard. Exome-wide association study reveals novel susceptibility genes to sporadic dilated cardiomyopathy. *PLoS One*, 12(3):e0172995, 2017.

J. G. Ghosh and J. I. Clark. Insights into the domains required for dimerization and assembly of human alphab crystallin. *Protein Sci*, 14(3):684–95, 2005.

N. Golenhofen, M. D. Perng, R. A. Quinlan, and D. Drenckhahn. Comparison of the small heat shock proteins alphab-crystallin, mkbp, hsp25, hsp20, and cvhsp in heart and skeletal muscle. *Histochem Cell Biol*, 122(5):415–25, 2004.

Y. X. Guan, H. X. Pan, Y. G. Gao, S. J. Yao, and M. G. Cho. Refolding and purification of recombinant human interferon-gamma expressed as inclusion bodies in escherichia coli using size exclusion chromatography. *Biotechnology and Bioprocess Engineering*, 10(2):122–127, 2005.

M. Heirbaut, F. Lermyte, E. M. Martin, S. Beelen, F. Sobott, S. V. Strelkov, and S. D. Weeks. Specific sequences in the n-terminal domain of human small heat-shock protein hspb6 dictate preferential hetero-oligomerization with the orthologue hspb1. *J Biol Chem*, 292(24):9944–9957, 2017.

G. K. Hochberg, H. Ecroyd, C. Liu, D. Cox, D. Cascio, M. R. Sawaya, M. P. Collier, J. Stroud, J. A. Carver, A. J. Baldwin, C. V. Robinson, D. S. Eisenberg, J. L. Benesch, and A. Laganowsky. The structured core domain of alphab-crystallin can prevent amyloid fibrillation and associated toxicity. *Proc Natl Acad Sci U S A*, 111(16):E1562–70, 2014.

S. A. Houck and J. I. Clark. Dynamic subunit exchange and the regulation of microtubule assembly by the stress response protein human alphab crystallin. *PLoS One*, 5(7):e11795, 2010.

L. Y. Juo, W. C. Liao, Y. L. Shih, B. Y. Yang, A. B. Liu, and Y. T. Yan. Hspb7 interacts with dimerized flnc and its absence results in progressive myopathy in skeletal muscles. *J Cell Sci*, 129(8):1661–70, 2016.

B. Kalmar, A. Innes, K. Wanisch, A. K. Kolaszynska, A. Pandraud, G. Kelly, A. Y. Abramov, M. M. Reilly, G. Schiavo, and L. Greensmith. Mitochondrial deficits and abnormal mitochondrial retrograde axonal transport play a role in the pathogenesis of mutant hsp27-induced charcot marie tooth disease. *Hum Mol Genet*, 26(17):3313–3326, 2017.

G. Kappe, E. Franck, P. Verschuure, W. C. Boelens, J. A. Leunissen, and W. W. de Jong. The human genome encodes 10 alpha-crystallin-related small heat shock proteins: Hspb1-10. *Cell Stress Chaperones*, 8(1):53–61, 2003.

L. Ke, R. A. Meijering, F. Hoogstra-Berends, K. Mackovicova, M. J. Vos, I. C. Van Gelder, R. H. Henning, H. H. Kampinga, and B. J. Brundel. Hspb1, hspb6, hspb7 and hspb8 protect against rhoa gtpase-induced remodeling in tachypaced atrial myocytes. *PLoS One*, 6(6):e20395, 2011.

L. A. Kelley, S. Mezulis, C. M. Yates, M. N. Wass, and M. J. Sternberg. The phyre2 web portal for protein modeling, prediction and analysis. *Nat Protoc*, 10(6):845–58, 2015.

S. Krief, J. F. Faivre, P. Robert, B. Le Douarin, N. Brument-Larignon, I. Lefrere, M. M. Bouzyk, K. M. Anderson, L. D. Greller, F. L. Tobin, M. Souchet, and A. Bril. Identification and characterization of cvhsp. a novel human small stress protein selectively expressed in cardiovascular and insulin-sensitive tissues. *J Biol Chem*, 274(51):36592–600, 1999.

H. Lee, J. M. Ferrer, F. Nakamura, M. J. Lang, and R. D. Kamm. Passive and active microrheology for cross-linked f-actin networks in vitro. *Acta Biomater*, 6(4):1207–18, 2010.

W. C. Liao, L. Y. Juo, Y. L. Shih, Y. H. Chen, and Y. T. Yan. Hspb7 prevents cardiac conduction system defect through maintaining intercalated disc integrity. *PLoS Genet*, 13(8):e1006984, 2017.

E. J. Mercer, Y. F. Lin, L. Cohen-Gould, and T. Evans. Hspb7 is a cardioprotective chaperone facilitating sarcomeric proteostasis. *Dev Biol*, 2018.

E. V. Mymrikov, M. Daake, B. Richter, M. Haslbeck, and J. Buchner. The chaperone activity and substrate spectrum of human small heat shock proteins. *J Biol Chem*, 292(2):672–684, 2017.

K. Ohashi, K. Oshima, M. Tachikawa, N. Morikawa, Y. Hashimoto, M. Ito, H. Mori, T. Kuribayashi, and A. G. Terasaki. Chicken gizzard filamin, retina filamin and cgabp260 are respectively, smooth muscle-, non-muscle- and pan-muscle-type isoforms: distribution and localization in muscles. *Cell Motil Cytoskeleton*, 61(4):214–25, 2005.

D. Preece, R. Warren, R. M. L. Evans, G. M. Gibson, M. J. Padgett, J. M. Cooper, and M. Tassieri. Optical tweezers: wideband microrheology. *Journal of Optics*, 13(4), 2011.

R. Pudas, T. R. Kiema, P. J. Butler, M. Stewart, and J. Ylanne. Structural basis for vertebrate filamin dimerization. *Structure*, 13(1):111–9, 2005.

J. N. Rauch, E. Tse, R. Freilich, S. A. Mok, L. N. Makley, D. R. Southworth, and J. E. Gestwicki. Bag3 is a modular, scaffolding protein that physically links heat shock protein 70 (hsp70) to the small heat shock proteins. *J Mol Biol*, 429(1):128–141, 2017.

J. Rudebusch, A. Benkner, A. Poesch, M. Dorr, U. Volker, K. Grube, E. Hammer, and S. B. Felix. Dynamic adaptation of myocardial proteome during heart failure development. *PLoS One*, 12 (10):e0185915, 2017.

K. M. Schmoller, P. Fernandez, R. C. Arevalo, D. L. Blair, and A. R. Bausch. Cyclic hardening in bundled actin networks. *Nat Commun*, 1:134, 2010.

A. S. Seit-Nebi, P. Datskevich, and N. B. Gusev. Commentary on paper: Small heat shock proteins and the cytoskeleton: An essential interplay for cell integrity? (wettstein et al.). *International Journal of Biochemistry Cell Biology*, 45(2):344–346, 2013.

K. Stark, U. B. Esslinger, W. Reinhard, G. Petrov, T. Winkler, M. Komajda, R. Isnard, P. Charron, E. Villard, F. Cambien, L. Tiret, M. C. Aumont, O. Dubourg, J. N. Trochu, L. Fauchier, P. Degroote, A. Richter, B. Maisch, T. Wichter, C. Zollbrecht, M. Grassl, H. Schunkert, P. Linsel-Nitschke, J. Erdmann, J. Baumert, T. Illig, N. Klopp, H. E. Wichmann, C. Meisinger, W. Koenig, P. Lichtner, T. Meitinger, A. Schillert, I. R. Konig, R. Hetzer, I. M. Heid, V. Regitz-Zagrosek, and C. Hengstenberg. Genetic association study identifies hspb7 as a risk gene for idiopathic dilated cardiomyopathy. *PLoS Genet*, 6(10):e1001167, 2010.

X. Sun, J. M. Fontaine, J. S. Rest, E. A. Shelden, M. J. Welsh, and R. Benndorf. Interaction of human hsp22 (hspb8) with other small heat shock proteins. *J Biol Chem*, 279(4):2394–402, 2004.

S. L. Surya, M. J. C. Long, D. A. Urul, Y. Zhao, E. J. Mercer, E. Isaid IM, T. Evans, and Y. Aye. Cardiovascular small heat shock protein hspb7 is a kinetically privileged reactive electrophilic species (res) sensor. *ACS Chem Biol*, 2018.

A. Ulbricht, F. J. Eppler, V. E. Tapia, P. F. van der Ven, N. Hampe, N. Hersch, P. Vakeel, D. Stadel, A. Haas, P. Saftig, C. Behrends, D. O. Furst, R. Volkmer, B. Hoffmann, W. Kolanus, and J. Hohfeld. Cellular mechanotransduction relies on tension-induced and chaperone-assisted autophagy. *Curr Biol*, 23(5):430–5, 2013.

M. van de Waterbeemd, K. L. Fort, D. Boll, M. Reinhardt-Szyba, A. Routh, A. Makarov, and A. J. Heck. High-fidelity mass analysis unveils heterogeneity in intact ribosomal particles. *Nat Methods*, 14(3):283–286, 2017.

M. J. Vos, B. Kanon, and H. H. Kampinga. Hspb7 is a sc35 speckle resident small heat shock protein. *Biochim Biophys Acta*, 1793(8):1343–53, 2009.

M. J. Vos, M. P. Zijlstra, B. Kanon, M. A. van Waarde-Verhagen, E. R. Brunt, H. M. Oosterveld-Hut, S. Carra, O. C. Sibon, and H. H. Kampinga. Hspb7 is the most potent polyq aggregation suppressor within the hspb family of molecular chaperones. *Hum Mol Genet*, 19(23):4677–93, 2010.

M. Wang, H. Ding, J. Kang, K. Hu, W. Lu, X. Zhou, and L. Xu. Association between polymorphisms of the hspb7 gene and cheyne-stokes respiration with central sleep apnea in patients with dilated cardiomyopathy and congestive heart failure. *Int J Cardiol*, 221:926–31, 2016.

T. Wu, Y. Mu, J. Bogomolovas, X. Fang, J. Veevers, R. B. Nowak, C. T. Pappas, C. C. Gregorio, S. M. Evans, V. M. Fowler, and J. Chen. Hspb7 is indispensable for heart development by modulating actin filament assembly. *Proc Natl Acad Sci U S A*, 114(45):11956–11961, 2017.

Z. Yang, Y. Wang, Y. Lu, and X. Zhao. Molecular characterization of rat cvhsp/hspb7 in vitro and its dynamic molecular architecture. *Mol Med Rep*, 4(1):105–11, 2011.

G. Young, N. Hundt, D. Cole, A. Fineberg, J. Andrecka, A. Tyler, A. Olerinyova, A. Ansari, E. G. Marklund, M. P. Collier, S. A. Chandler, O. Tkachenko, J. Allen, M. Crispin, N. Billington, Y. Takagi, J. R. Sellers, C. Eichmann, P. Selenko, L. Frey, R. Riek, M. R. Galpin, W. B. Struwe, J. L. P. Benesch, and P. Kukura. Quantitative mass imaging of single biological macromolecules. *Science*, 360(6387):423–427, 2018.

Chapter 6

Quantifying polydisperse heteromeric protein assembly

6.1 Abstract

Native MS is a well-established method for analyzing the compositions of noncovalent protein assemblies. Extensive signal overlap in m/z will impede mass assignments, creating an inherent limitation in sample complexity. Thus, as with all *in vitro* experiments, the caveat applies that the system under consideration is likely to be more complex *in vivo*. This is especially true for the sHsps, most of which selectively co-assemble with other sHsps in addition to self-assembling into a range of oligomers. The complexes formed between αB-crystallin and Hsp27, the two most abundant and widely expressed human sHsps, are so heterogeneous as to be thus far intransigent to structural techniques, including native MS. Here, we combine advances in MS hardware and software with new insight into the molecular biology of sHsps to achieve detailed characterizations of the distributions and assembly kinetics of αB-crystallin·Hsp27 heteromers. Our method allows identification and relative quantitation of over 120 distinct stoichiometries from a single sample, with mass differences reaching less than 1%; and real-time tracking of specific stoichiometry formation. We confirm that the proteins can interact via at least two inter-subunit interfaces, and that consequently at a range of subunit ratios, neither exists on its own in large oligomers. Co-assembly results in polydisperse complexes, intermixing via unbiased exchange of monomers. We anticipate that this approach could be broadly applicable to other heterogeneous protein systems; and it will enable future studies of sHsp co-assembly in the context of client binding and stress- and disease-related changes, providing a new avenue to explore the assembly-function relationship.

6.2 Introduction

6.2.1 sHsps co-assemble selectively with implications for function

Most proteins related by gene duplication evolve to avoid interacting with each other as they acquire distinct functions (Hochberg et al., 2018). However, in addition to self-assembling into homomers, many human sHsp paralogs can form heteromers. Their selectivity and restrictive tissue co-expression profiles (Sugiyama et al., 2000; Vos et al., 2009) hint at functional importance. Some heteromer assemblies have been amenable to detailed characterization: HspB2·HspB3, for example, adopt up to 6 stoichiometries in a strict 3:1 subunit ratio (den Engelsman et al., 2009). Others, including any co-assembled population involving αB-crystallin, exhibit a degree of polydispersity beyond that of the individual homomeric ensembles. These have eluded high resolution analysis.

In general, we can conceive of several modes of interaction (or lack thereof) between two polydisperse paralogs. First, they do not co-assemble at all (Figure **6.1a**), having strongly self-selective interfaces. Second, they co-assemble via interfaces that are highly hetero-selective, resulting in a limited distribution of obligate heteromers (Figure **6.1b**). The aforementioned 3:1 HspB2·HspB3 is an example of this mode, and it also seems to be the case for Hsp27·Hsp20 complexes, which are comprised exclusively of heterodimers at equimolar ratios (Heirbaut et al., 2017). Third, they co-assemble more or less stochastically, creating a new distribution an order of magnitude more complex than the individual homomers (Figure **6.1c**).

The two most abundant and widely expressed human sHsps, Hsp27 and αB-crystallin, can co-localize in cells (Sugiyama et al., 2000; Simon et al., 2013) and form polydisperse heteromers with average mass between that of the two homomer distributions and with variable molar ratios (Aquilina et al., 2013). Thus, evidence

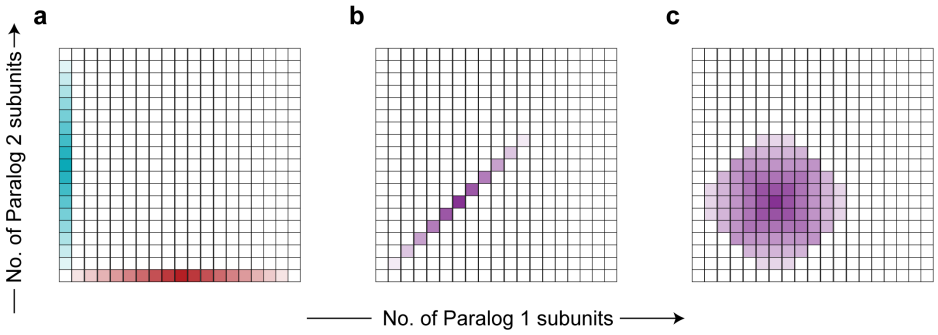


Figure 6.1. Hypothetical assembly of two polydisperse paralogs. a. The proteins only self-assemble. **b.** They co-assemble into a restricted distribution via highly hetero-selective interfaces. **c.** Co-assembly is broadly stochastic, and the resulting distribution is determined by the mixing entropy. All possibilities present challenges to modern structural biology techniques. Only **a** and **b** have been amenable to full characterization by native MS thus far. (Red and blue boxes represent homomers; purple, heteromers. These schema assume that average mass is broadly conserved; were this not the case, distributions would simply shift within the grids.)

points toward the probabilistic mode of interaction (Figure **6.1c**). This degree of heterogeneity has limited descriptions of the complexes' sizes to low resolution, and of their kinetics to ensemble averages (Datskevich et al., 2012; Aquilina et al., 2013). Mixed assemblies can exhibit improved chaperone efficacy compared to Hsp27 alone against a range of substrates *in vitro* (Skouri-Panet et al., 2012; Aquilina et al., 2013), but the functions of these heteromers in cells and *in vivo* remains unknown.

In this chapter, I explore the co-assembly of Hsp27 and αB-crystallin in unprecedented detail. I show that, from just picomoles of sample, stoichiometry-specific assembly kinetics and oligomer distributions are accessible by native MS.

6.2.2 Developments enabling native mass spectrometry of a highly heterogeneous system

In a system seemingly as polydisperse as sHsp heteromers, we knew that several benchmarks needed to be met in order for native MS to be a workable approach.

First, sample quality would be critical: in addition to being pure, protein must be homogeneous, since modifications disperse signal intensity over multiple proteoforms. This is especially a problem for oligomers, because each modified subunit will broaden the MS peaks. Expertise within the group purifying and handling

αB-crystallin lent confidence in this sample; Hsp27, however, initially yielded a mixture of masses where the protein had undergone partial cleavage of the N-terminal methionine. Fusing a tag to the N-terminus offered the most promising way to counteract this problem, but previous sHsp fusion efforts had led to heterogeneity upon tag cleavage. For example, oligomerization can hinder separation of tagged and untagged protein, or imprecise cleavage can leave behind residues that affect assembly. To circumvent these issues, we expressed SUMO-tagged Hsp27 following a strategy developed in the group of Stephen Weeks. Because the SUMO protein is bulky, it appears to disrupt oligomerization, making separation by affinity chromatography straightforward; and because the SUMO protease recognizes the tertiary structure of the tag and leaves no extra residues behind, the desired 205-residue Hsp27 is obtained in pure form. Thus, with pure proteins of defined homogeneous primary structure, we cleared this hurdle.

A second barrier to this type of project in the past lay in the lack of appropriately robust software tools. A system resembling Figure **6.1c**, for example, with 5 charge states per unique mass, would give rise to 350+ peaks – and this precedes collisional dissociation, which generates a new mass and a new set of peaks each time a subunit is removed. It would therefore not be feasible to deconvolve the data manually, and automated processing must allow for accurate assignment of complex peak patterns. The recent release of Bayesian algorithm-based MS deconvolution software UniDec (Marty et al., 2015), and its continual development by our close collaborator, meant that this was achievable.

Lastly, the mass spectrometer must be able to both transmit ions up to approximately 800 kDa and detect them with sufficient intensity and mass resolution to allow for clear distinction between species whose masses differ by less than 1%. All of the native MS in Chapters 2-5 were collected using mass spectrometers with

time-of-flight mass analyzers. As discussed in Chapter 1, the inherent resolution of the Orbitrap mass analyzer exceeds that of the ToF. Until very recently, Orbitrap instruments configured for native protein analysis performed well for small species, but transmission efficiency diminished rapidly at m/z >20,000, and mass resolution also worsened at high m/z due to inhibited transient length acquisitions following poor transmission. Researchers at the University of Utrecht and Thermo Fisher Scientific modified an Orbitrap platform to address these shortcomings (Figure **6.2**) (Fort et al., 2017).

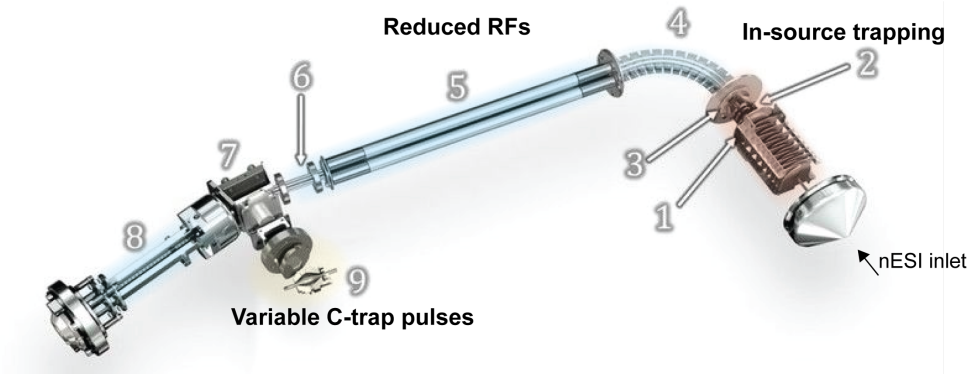


Figure 6.2. Model of the Q-Exactive Plus mass spectrometer highlighting modifications made to facilitate transmission and detection of high mass ions. Modifications can be sorted into 3 major changes. First, in-source trapping (IST) was introduced by enabling lowering of the injection flatapole (**2**) and raising of the inter-flatapole lens (**3**) potentials relative to that of the S-lens (**1**). The source can then act as a trap where ions undergo collisions with background gas. This enhances resolution by aiding in desolvation, and improves transmission by dampening ion momentum following expansion upon entering the vacuum. Second, RF frequencies were reduced on all ion guides including the bent flatapole (**4**), quadrupole (**5**), transport multipole (**6**), C-trap (**7**), and HCD cell (**8**). Third, an option was introduced to extend the time interval for which ions are pulsed into the Orbitrap mass analyzer (**9**) from the C-trap, such that large ions have enough time to enter. Figure adapted from van de Waterbeemd et al. (2017); modifications are described in more detail elsewhere (Fort et al., 2017).

The modifications enabled the analysis of large protein complexes at high resolution (van de Waterbeemd et al., 2017). Following our acquisition of an identically modified instrument, in conjunction with the aforementioned advancements in sample preparation and software, we believed we could expand on the capabilities of the technology by applying it to the highly polydisperse αB-crystallin·Hsp27 assembly. Here I report a method to disentangle the heterogeneous behaviour of these proteins.

6.3 Results

6.3.1 αB-crystallin and Hsp27 share heteromeric affinities at multiple interfaces

We first wished to examine the compatibility of specific oligomeric interfacial regions between Hsp27 and αB-crystallin. Heteromerization at the ACD·ACD and ACD·C interfaces has been reported (Delbecq et al., 2012; Mymrikov et al., 2012), but without quantitation. To gain thermodynamic insight, we used simplified systems as described elsewhere in this thesis and in the literature (Delbecq et al., 2012; Hilton et al., 2013; Hochberg et al., 2014). (We omit NTD·NTD interactions at present, since N-terminal disorder has precluded an analogous reduced system; NTD contributions to sHsp assemblies can be derived from targeted deletion experiments (Heirbaut et al., 2017).)

We recorded native mass spectra of αB_{ACD} and $Hsp27_{ACD}$ alone and mixed at several ratios. Each ACD in isolation populated a monomer-dimer equilibrium as expected (Figure **6.3a**). In mixtures, a new charge series was observed corresponding to heterodimer (Figure **6.3b**). We noticed that the heterodimer intensity was close to that expected if the dimer affinities for self and other were equivalent, such as in native mass spectra of an ACD mixed with a heavier version of itself (Hochberg and Benesch, 2014). If this were the case, we could model the expected heterodimer population *P(x)* by a binomial distribution:

$$P(x) = \frac{n!}{(n-x)!(x)!} p^x q^{n-x} \tag{6.1}$$

Where p and q are the fractional populations of Hsp27 and αB-crystallin and n is the total number of possible outcomes (two: homo- or hetero-dimer). When we

calculated anticipated binomial heterodimer fractions, the results were so close to the experimental heterodimer fractions as to be indistinguishable (Figure **6.3c**).

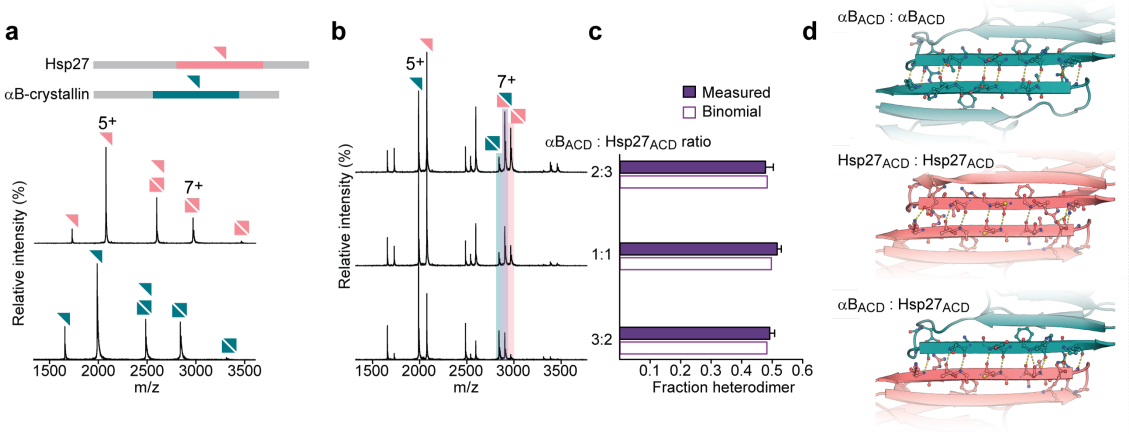


Figure 6.3. The antiparallel inter-dimer interfaces of αB crystallin and Hsp27 exhibit highly similar homo- and heteromeric affinities. a. Native MS of the isolated ACD of each protein (locations within the full sequences as above). Each populates a monomer-dimer equilibrium. **b.** Native MS of αB_{ACD} and $Hsp27_{ACD}$ mixed at three ratios. Two charge series are observed for the monomers and three for the dimers, corresponding to each homodimer and a heterodimer. **c.** Comparison of the experimental heterodimeric fraction with a fraction calculated assuming a binomial distribution. The values are very similar (2.2% different on average), evidencing close to equal affinities between the two interface types. **d.** High resolution structures of αB_{ACD} and $Hsp27_{ACD}$ (PDBs 2WJ7 and 4MJH), and a model of the heterodimeric interface.

Thus, αB_{ACD} and $Hsp27_{ACD}$ antiparallel dimer interface interactions have $\Delta\Delta G \approx 0$ kJ mol^{-1}. This coheres with the similarities between the contacts made at each homomeric interface in the most common registers (AP_{II}) as captured in crystal structures (Figure **6.3d**), and with the high sequence homology between these ACDs (56% identical, 70% similar; alignment in Figure **5.1**).

Next, to interrogate ACD·C interactions, we titrated peptide mimics of the C-terminal interfacial regions (C-terminal peptides: αB_{Ctp}, residues 156-164 ERTIPITRE, and $Hsp27_{Ctp}$, residues 178-186 EITIPVTFE) with ACDs and recorded native mass spectra at each ratio. Each peptide readily bound its hetero-ACD (Figure **6.4a**). We also noted a decrease in the overall abundance of dimeric species within both series. This could result from allostery between the ACD·ACD and ACD·C interfaces, such that binding at one weakens the other, as reported for αB-crystallin (Hochberg and Benesch, 2014). It could also result from a pH change upon

mixing effecting ACD·ACD affinities (Baldwin et al., 2011). To distinguish between these, we collected native mass spectra of each ACD with an excess of scrambled sequence peptides ($Hsp27_{Ctp\text{-}ctrl}$, EIFITEVTP, and $\alpha B_{Ctp\text{-}ctrl}$, TIERPREIT). Since these peptides should not bind the ACDs specifically but should change the pH equivalently to the WT peptides, any reduction in the dimer population observed can be attributed to pH and not allostery.

Addition of control peptide significantly reduced the dimeric population of αB_{ACD}, pointing to a pH effect at least in part, but not of $Hsp27_{ACD}$, pointing to an allosteric effect (Figure **6.4b**). In light of this, we used only the monomeric regions of the titration mass spectra to construct binding curves and approximate ACD·C K_Ds (curves in Figure **6.4c**; fitted thermodynamic values, Table 6.1). The experiment was performed in the same manner using homomeric ACD·Ctp combinations to enable comparison of all competing interactions within heteromers. Affinities span 24 to 151 μM, with αB_{Ctp} exhibiting a higher affinity to both ACDs than $Hsp27_{Ctp}$ to either. Interestingly, the ΔΔG between $Hsp27_{Ctp}$ binding either ACD is ≈ 0 kJ mol^{-1} (Table 6.1).

Table 6.1. Thermodynamic parameters for αB-crystallin and Hsp27 ACD·Ctp oligomer interfaces. These should be considered close approximations since dimers were excluded.

	αB_{ACD}	$Hsp27_{ACD}$
K_D (μM)		
αB_{Ctp}	67 ± 4[a]	140 ± 8
$Hsp27_{Ctp}$	24 ± 1	151 ± 16
ΔG (kJ mol^{-1})		
αB_{Ctp}	-23.8 ± 0.1	-22.0 ± 0.1
$Hsp27_{Ctp}$	-26.4 ± 0.1	-21.8 ± 0.3
ΔΔG (kJ mol^{-1})[b]		
	-2.5 ± 0.3	-0.2 ± 0.4

[a]The only previously reported affinity, which is in good agreement with our measurement (Hilton et al., 2013).
[b]Calculated by subtracting homomeric from heteromeric values.

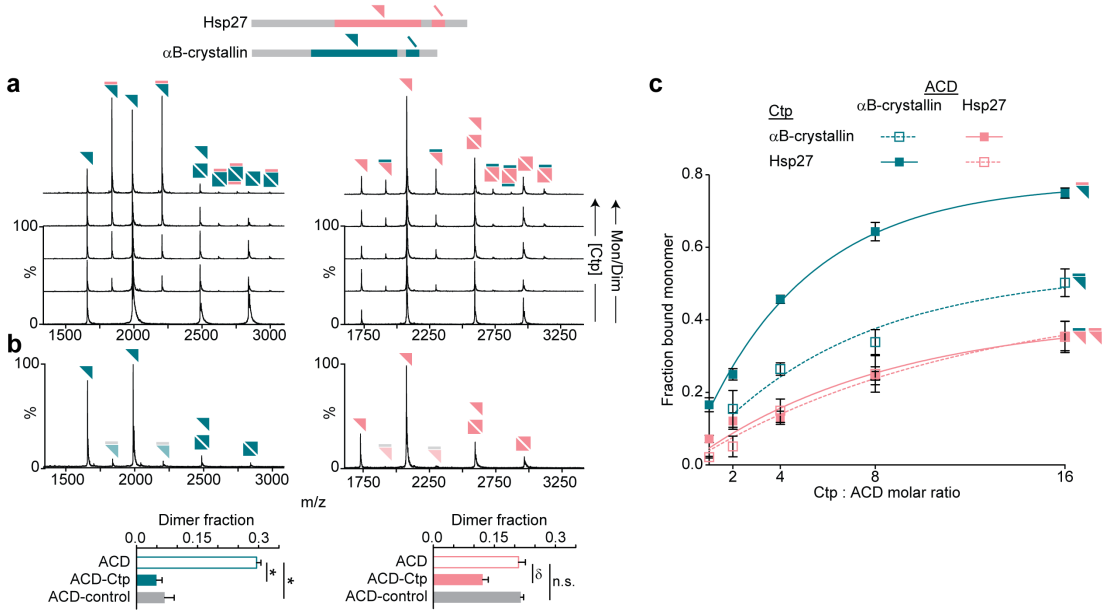


Figure 6.4. The ACD·Ctp interfaces of αB-crystallin and Hsp27 can make homo- and heteromeric contacts. a. Native MS of 5 μM αB_{ACD} (left) or $Hsp27_{ACD}$ (right) with 0, 5, 10, 20, and 40 μM $Hsp27_{Ctp}$ (left) or αB_{Ctp} (right). Both combinations feature charge series corresponding to peptide binding ACD monomer and dimer. Dimer abundance diminished with increasing peptide ratio. **b.** Native MS of 5 μM each ACD with excess scrambled sequence C-terminal peptides $Hsp27_{Ctp,ctrl}$ and $\alpha B_{Ctp,ctrl}$ (50 and 80 μM respectively). Below, quantitation of the fractions of dimeric ACD alone and in presence of hetero- or control peptides, to differentiate between allosteric and artefactual (presumably pH) effects. * indicates p <0.01, δ indicates p <0.05, n.s. = not significant by t-test. Since αB-crystallin dimerization is affected by the control, only monomers were used to calculate binding curves (**c**).

Using these simplified systems allowed quantitative measurements of isolated interactions involved in sHsp co-assembly. We established that two oligomer interfaces known to exist in αB-crystallin and Hsp27 homomers are also compatible in heteromers, with apparent nonselectivity for ACD·ACD and Hsp27 C-terminal interactions, and moderate selectivity for αB-crystallin C-terminal interactions. From this, we predicted that full-length heteromers may be maximally polydisperse, resembling our third hypothetical model of assembly (Figure **6.1c**). We next focused on optimizing the Orbitrap platform for the type of high resolution analysis such a system would require.

6.3.2 Optimization of polydisperse sHsp characterization on an Orbitrap Q-Exactive platform

To design a workflow for optimal sHsp data collection on the modified Orbitrap instrument, we first examined homomeric αB-crystallin and Hsp27. For all remaining experiments, we used a variant of Hsp27 containing mutation C137S, to preclude disulphide bond formation without the need for reductant in the samples. (We confirmed that ^{C137S}Hsp27 oligomerization is identical to that of reduced ^{WT}Hsp27.)

Native mass spectra were recorded for intact αB-crystallin and Hsp27 assemblies (Figure **6.5**). Consistent with prior size measurements, these data showed αB-crystallin existing only as a series of large oligomers (Hochberg and Benesch, 2014), and Hsp27 populating a set of small species in addition to large oligomers (Jovcevski et al., 2015). In-source trapping (IST) potentials were tuned to maximally desolvate the ions without inducing fragmentation, and ion optics and HCD pressure were tuned for high mass transmission (see Methods). Under these conditions, individual charge series could be resolved for intact large oligomers (Figure **6.5a**). This contrasts intact MS of the same proteins on TOF platforms, which features broad irresolvable signal (for example, see Figure **2.3**).

However, the median sizes of the assemblies were smaller than expected. When the modification extending the time interval of pulses into the mass analyzer was enabled, the maximum m/z and baseline intensity of the oligomer signal increased for both proteins (Figure **6.5b**). These results established several important benchmarks going forward. First, it would be necessary to operate the instrument in the mode configured for C-trap release of large ions or otherwise risk excluding larger complexes from detection. Second, since it is challenging to achieve faithful transmission across a broad m/z range, we should exercise caution and not extrapolate from relative intensities of the smallest and largest ion species to relative abundances.

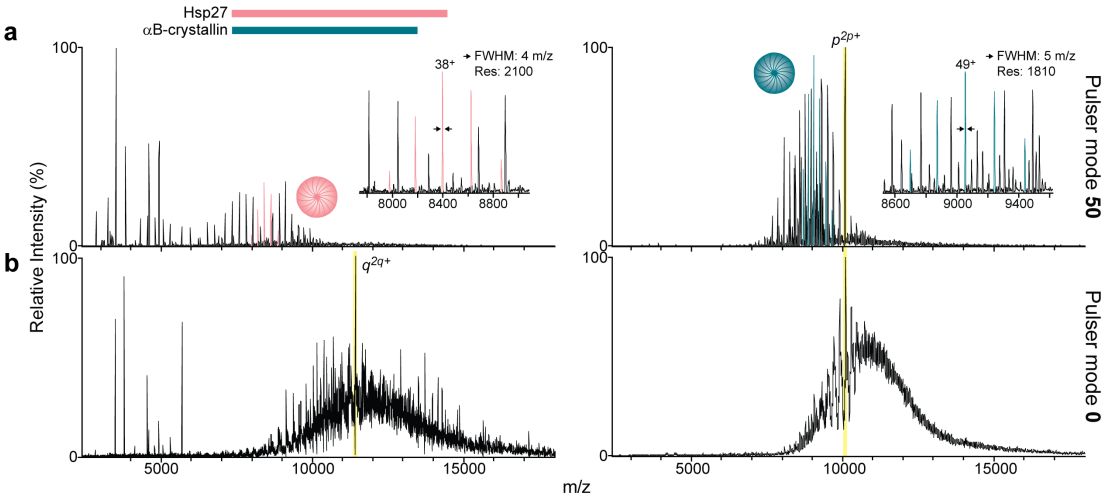


Figure 6.5. Intact native MS of polydisperse full-length αB-crystallin and Hsp27 using the Q-Exactive Orbitrap. With in-source trapping tuned for desolvation and UHV pressure tuned for high mass transmission, individual high mass charge series can be resolved without CID (top row, colored peaks correspond to a 14-mer and 22-mer, respectively). Lengthening the C-trap deflector electrode pulse intervals into the mass analyzer by changing the pulser mode allows more high mass species to be detected (**b**). Peak overlap occurs where all oligomers carry twice as many charges as subunits (yellow). This feature is labelled for Hsp27 with q subunits and αB-crystallin with p subunits.

Conditions facilitating transmission of one size group are employed at the expense of the other. (In addition to pulser mode, HCD pressure is a primary contributor to this bias.) And third, despite the improvement in resolution, charge reduction via CID would still be required to fully assign stoichiometries.

Thus, we performed CID on the Orbitrap platform by increasing the the acceleration potential into the HCD cell (high-energy collisional dissociation cell; analagous to the Synapt QToF Trap or Transfer) to dissociate up to two subunits from the homomers. This increases peak separation by stripping charge from large species, allowing baseline resolution of individual subunit-stripped oligomer charge states (Aquilina et al., 2003). Charge states arising from different assembly stoichiometries overlap to create distinct spectral features, such as when charge equals subunit number (Figure **6.6a**). Plotting the deconvolved mass assignments against charge allows splitting of the data into distinct bands according to how many subunits have been lost (Figure **6.6b**), adhering to the empirical relationship:

$$Z_{Av} = 0.0467m^{0.533} + F \tag{6.2}$$

Where Z_{Av} is the average charge, m is the mass in Da, and F is an offset from the native state. This has been reported previously for αB-crystallin (Marty et al., 2015); here, the processing pipeline was updated to scale intensities with charge state, as required for Orbitrap instruments (Hu et al., 2005). After Gaussian extraction of the charge curves, we add subunit masses to correct for each dissociation step, allowing us to back-calculate best approximations of the solution distributions (Figure **6.6c**). The mean masses for Hsp27 and αB-crystallin under these conditions are between 450 and 500 kDa, with a slightly wider variance for Hsp27, and a less pronounced dimeric substructure for αB-crystallin.

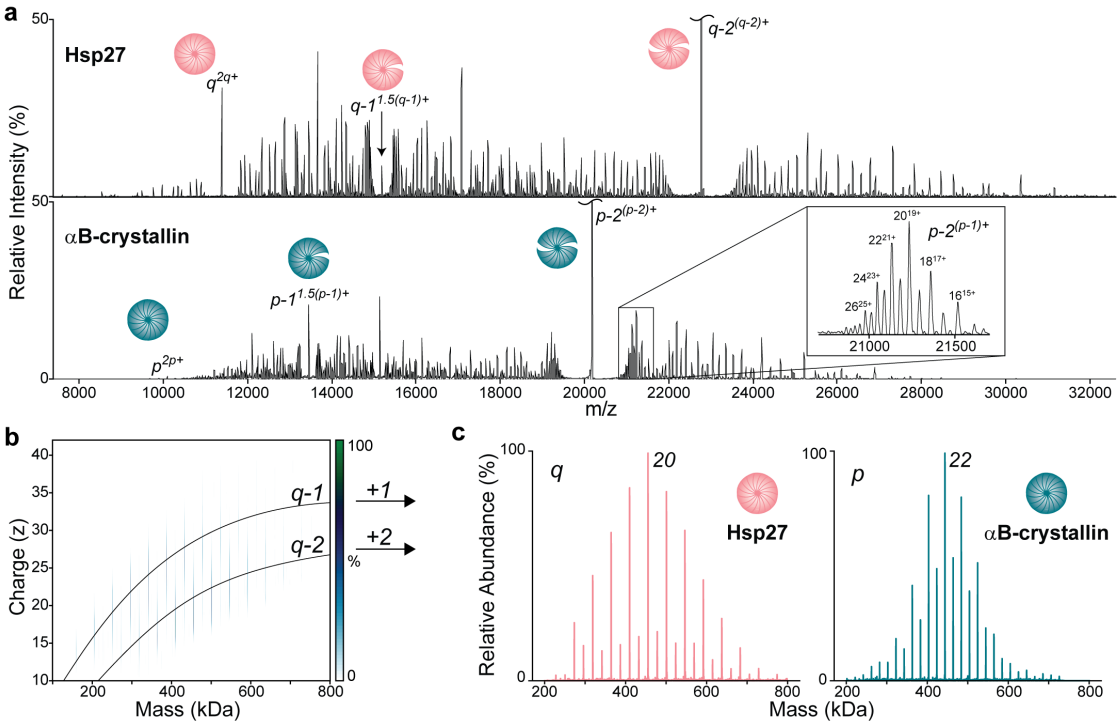


Figure 6.6. Deconvoluting CID MS of polydisperse full-length αB-crystallin and Hsp27. Cartoons represent oligomers which have lost 0, 1, or 2 subunits. Inset shows baseline resolved double-stripped αB-crystallin peaks. **b.** Deconvolved Hsp27 masses plotted against charge. Curves are extracted for oligomers which have lost 1 or 2 subunits, allowing for mass correction. **c.** Reconstructed oligomeric distributions. The most abundant species contain 20 and 22 subunits. Data were collected at HCD energies of 300V (Hsp27) and 200V (αB-crystallin).

Having found conditions on the modified instrument enabling good measurements of polydisperse systems, and adapted the software accordingly, we next looked at mixed assemblies.

6.3.3 αB-crystallin and Hsp27 form large, polydisperse, highly intermixed oligomers

Mixtures of Hsp27 and αB-crystallin at several ratios were incubated at 37°C for 90 minutes to reach equilibrium exchange of subunits (Datskevich et al., 2012; Aquilina et al., 2013), and native mass spectra were collected of both intact and collisionally dissociated assemblies. Intact spectra featured broad, irresolvable oligomer signal; however, upon CID, we obtained well-resolved peaks (Figure **6.7a**). Similar to homomeric CID spectra, these peaks spanned ≈ 10,000-32,000 m/z; however, prominent homomer spectral features were now absent, suggesting that the new assemblies were entirely or almost entirely heteromeric.

Seeking diagnostic features, we looked for the overlap of all ions with equimolar subunits and an identical number of charges ($\alpha B_p Hsp27_q{}^{(p+q)+}$). This feature appeared in all spectra (Figure **6.7a**, green), but it was not the predominant peak, evidencing a variety of additional subunit compositions. We also noted that features were highly variable with protein ratio (for example Figure **6.7a**, yellow).

To interpret these complex data, we considered a general expression for any ion arising from a heteromer of proteins A and B with p and q subunits, respectively:

$$A_p B_q{}^{(p+q+r)+} \tag{6.3}$$

Where r is a variable integer that defines the charge state. Approximating the mass of a proton as 1 Da, the position of the peak for this ion in the mass spectrum is

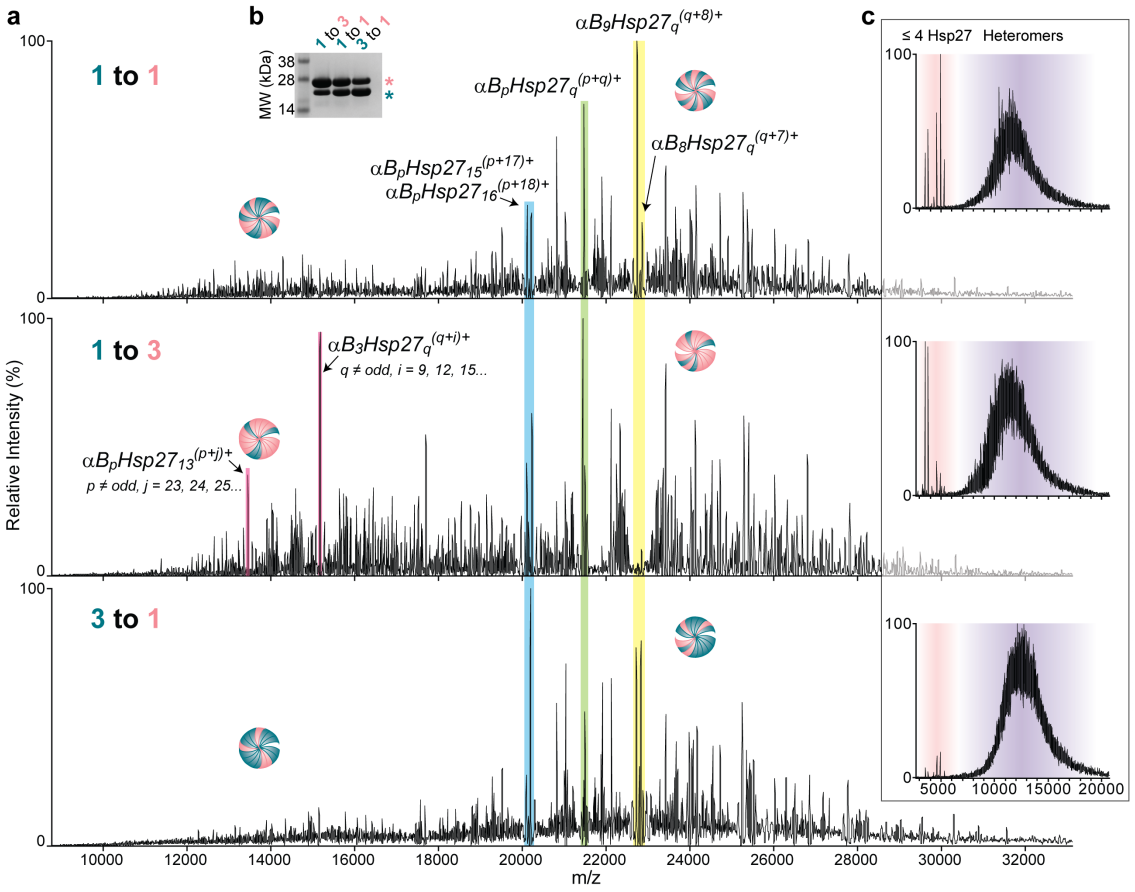


Figure 6.7. Native MS of αB-crystallin·Hsp27 assemblies at equilibrium. a. Collisionally dissociated MS (HCD energy 300V) at ratios of 1 to 1, 1 to 3, and 3 to 1 αB-crystallin to Hsp27 (SDS-PAGE in **b**). Cartoons represent the protein monomer molar ratios and approximate regions of signal where oligomers have lost one and two subunits. Certain features are highlighted and assigned as described in the text. Where p or q are designated, any number of subunits is possible. **c.** Intact MS of corresponding assemblies. Small species are assignable and exclusively comprised of Hsp27. Large species are irresolvable, but known from CID (**a**) to be heteromers.

given by:

$$\frac{m}{z} = \frac{pm_A + qm_B + (p+q+r)}{p+q+r} \tag{6.4}$$

The separation between peaks for two oligomers with the same number of protein A subunits (constant p) and differing numbers of B subunits (q and $q{+}\Delta q$) can be expressed (following simplification):

$$(\Delta\frac{m}{z})_{\Delta q} = (\frac{m}{z})_{p,q+\Delta q} - (\frac{m}{z})_{p,q} = \frac{\Delta q\,(pm_B + rm_B - pm_A)}{(p+q+\Delta q+r)(p+q+r)} \tag{6.5}$$

To identify features arising from intersecting signal, we hone in on the lower limit of peak separation by setting $\Delta m/z = 0$. Disregarding $\Delta q = 0$ since this refers to an identical ion, we solve for p and arrive at an expression for an optimal number of subunits of protein A for yielding overlap, designated p_{opt}:

$$p_{opt} = \frac{r}{\frac{m_A}{m_B} - 1} \tag{6.6}$$

Similarly, if oligomers have identical q and differing p, there exists a q_{opt}:

$$q_{opt} = \frac{r}{\frac{m_B}{m_A} - 1} \tag{6.7}$$

From these expressions, it is clear that features in the mass spectra of a two-component heteromeric assembly will always be highly dependent on the ratio of the masses of the proteins. In the case of A = αB-crystallin and B = Hsp27, the mass ratio is 0.886, which is very close to 8/9 (0.889). Thus, addition of 9 αB-crystallin (181,430 Da) is similar in mass to addition of 8 Hsp27 (182,132 Da). Certain groups of charge states have smaller $\Delta m/z$ than peak widths, creating information-rich spectral features. For example, we identify a p_{opt} feature at 8.73 αB-crystallin subunits when r = -1 (Figure **6.7** yellow, peaks overlap for αB_8 and αB_9 with any number of Hsp27) and a q_{opt} feature at 15.46 Hsp27 subunits when $r = 2$ (Figure **6.7** blue, peaks overlap for $Hsp27_{15}$ and $Hsp27_{16}$ with any number of αB). This rationalizes the spectral dependence on molar ratio: when optimal stoichiometries are lowly populated, features disappear. Thus, from CID experiments on heteromeric assemblies, we can conclude that large oligomers are highly intermixed and that stoichiometric distribution depends on molar ratio, unlike obligate heteromers Hsp27·Hsp20 (Heirbaut et al., 2017) and HspB2·HspB3 (den Engelsman et al., 2009).

Examining the signal from smaller oligomers, we assign only Hsp27 up to tetrameric species (Figure **6.7c**). Because each ACD readily heterodimerizes and binds both C-terminal interfacial regions, the lack of αB-crystallin in small oligomers indicates that NTD interactions are important in allowing free Hsp27 building blocks in solution, and in excluding free αB-crystallin. These small oligomers may perform functions diversified from those of the larger assemblies.

6.3.4 Segmented data collection allows broad stoichiometric assignment of heteromer assemblies

Performing CID on the entire heteromeric distribution allowed us to assess the degree of subunit intermixing by identifying features in the spectra. However, in this experiment many charge states were effectively suppressed due to limitations in the dynamic range of detection. Thus the data could not be fully deconvolved into relative abundances of stoichiometries, since this requires multiple charge states per mass. To allow for mass assignments, we needed to visualize suppressed charge states by compartmentalizing the complexes prior to mass analysis and simplifying the spectra. This could be approached in one of two ways: offline, involving separation of the sample, i.e. via SEC; or online, involving separation of the ions, via quadrupole selection. Because the former introduces the possibility of re-equilibration, we pursued the latter strategy.

To capture some of the most abundant complexes, we isolated the region encompassing all oligomers with charge double their subunit number. This ranged from m/z 10,080 (where $q = 0$) to 11,383 (where $p = 0$), such that any nonzero p,q oligomer with charge 2(p+q)+ was included. Dissociating and detecting only these ions gave rise to a fully assignable mass spectrum (Figure **6.8a**). Standard deviations in mass assignments were on the order of 10-20 Da and mass errors around 50 ppm. The smallest possible heteromer mass difference is ≈ 500 Da, so each species

could be assigned a p,q stoichiometry with confidence.

We next wished to correct for the dissociated subunits. Uniform subunit composition makes this correction straightforward for homomers (Figure **6.6**); however, for heteromers we could not assume that subunits dissociated in the same ratio as they were present in the sample. This is because Hsp27 is 11% larger in mass than αB-crystallin, and therefore requires more collisional energy to unfold and dissociate (Benesch et al., 2007). So, enabling post-hoc subunit correction for heteromers necessitates measurement of how much dissociation arose from the loss of each protein, i.e. measurement of relative abundances of unfolded subunits. These small, highly charged ions are not transmitted under the same conditions as large, lowly charged stripped oligomers on the modified Q-Exactive. To detect them, we changed minimal conditions to facilitate their transmission (see Methods) and acquired a sister mass spectrum for each heteromer tandem MS selection. Applying the changes and recording data at sufficient signal intensity could be achieved in less than one minute, and yielded two charge series at low m/z from which accurate ratios could be determined (Figure **6.8b**). We then split the deconvolved tandem MS data into single- and double-stripped assignments and added one or two subunit masses to each, respectively, assuming that the ratio of the subunits reflected the likelihood of each dissociation event (Figure **6.8c**).

This yielded a best approximation of the portion of the solution ensemble captured in the tandem MS experiment. Similar to the homomeric distributions, oligomers retain a preference for sub-dimers, reflected in the prevalence of even numbers of total subunits (Figure **6.8c**). Within each stoichiometry, no combination of αB-crystallin and Hsp27 is excluded, with binomial distributions seemingly dependent on the initial subunit molar ratio (Figure **6.8d**). The distribution visualized on a grid (Figure **6.8e**) confirms that the mode of αB-crystallin·Hsp27 assembly

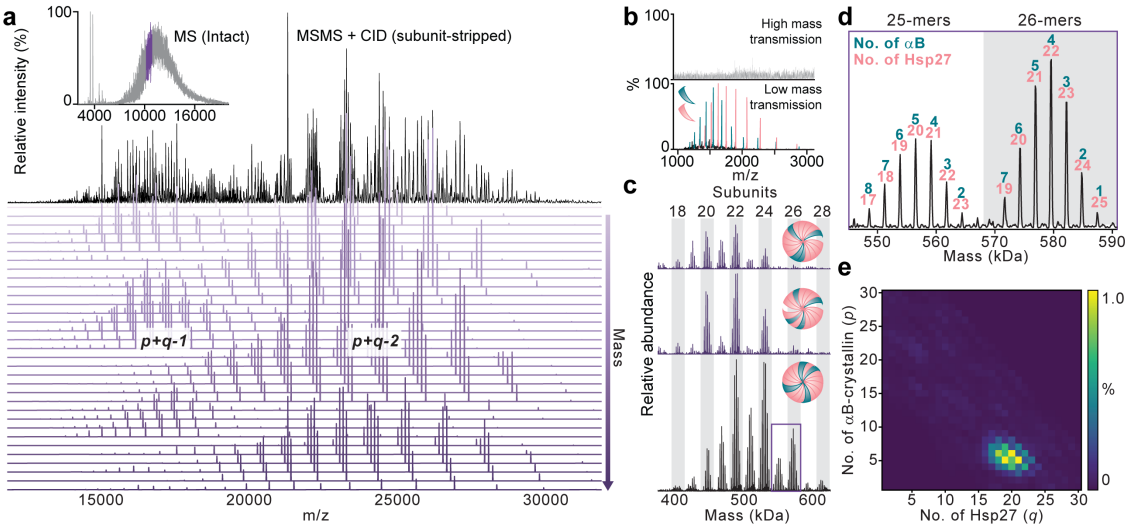


Figure 6.8. Tandem MS of heteromers enables determination of relative solution abundances of specific stoichiometries within a defined m/z window. a. Native tandem MS of a mixture of 3 to 1 Hsp27·αB crystallin excluding all ions in the quadrupole except those with charge double their subunit number. Inset, intact MS with transmitted ions in purple; black, MSMS + collisional dissociation; expanded purple, most abundant charge series identified within the CID data. A pattern emerges of alternating predominantly single- (*p+q-1*) and double- (*p+q-2*) stripped species. **b.** Low m/z region from the spectrum in **a** and its sister MS with parameters adjusted to transmit dissociated subunits at low m/z. This is used to derive the dissociated subunit ratio. **c.** Mass distributions from single- and double-stripped oligomer signal in **a** before mass correction (purple) and the collective distribution after correction using the subunit ratio (black). **d.** Detail view of the boxed region in **c** showing the compositions of heteromers with 25 and 26 subunits. **e.** Grid visualization of the subset heteromer distribution.

most closely resembles our stochastic model (Figure **6.1c**), with a superimposed preference for paired subunits.

Now that we had achieved characterization of a subset of the solution population, we wished to expand the approach to encompass broader ranges for p and q. We therefore investigated the possibility of combining multiple assignments derived from adjacent tandem MS selections. The region investigated in Figure **6.8** was divided into 5 selection windows and CID applied to each, resulting in 5 assignable mass spectra (Figure **6.9a-b**). Dissociation product ratios were measured for each and used to derive 5 mass-corrected distributions (Figure **6.9c**). Most stoichiometries were detected in multiple selection windows, as expected based on the multiplicity of intact charge states, which enhances confidence in the accuracy of the assignments. Summing these generated an overall distribution for the region that is extremely similar to that obtained from a single selection window (Figure **6.9d**), retaining the

centroid and dimer-biased substructure.

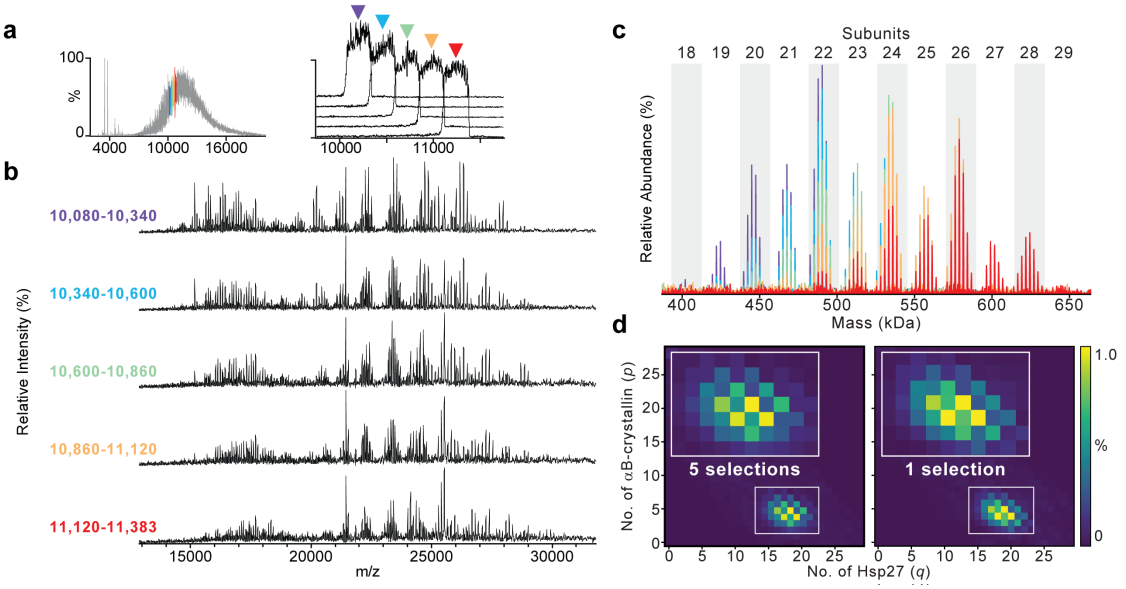


Figure 6.9. A heteromeric distribution can be reconstructed from the sum of its parts. Five native tandem MS acquisitions of a mixture of 3 to 1 Hsp27·αB-crystallin without **a** and with **b** CID. **c.** Corrected mass distributions derived from each of the selection windows. **d.** Heteromer distributions generated as the sum of the five assignments in **c** or from a single broad selection window.

Having established the reliability of pooling segmented data, we expanded the approach to obtain more comprehensive distributions. CID data were collected in 500 m/z wide successive increments across intact oligomer signal, until signal to noise deteriorated. Assignable data were combined as in Figure **6.9**. The resulting distributions are shown for αB-crystallin·Hsp27 co-assemblies at three subunit molar ratios, revealing a highly heterogeneous mode of co-assembly (Figure **6.10a**). The average mass is maintained in the hundreds of kDa, and the availability of subunits determines heteromeric composition. Collapsing the intensities along each axis reveals no preference for each type of subunit to occupy oligomers of any particular size or composition. (Note that, since reliable relative intensities were inaccessible, grids do not display free Hsp27 substoichiometries, which are present up to a tetramer.)

Under the conditions used here, we were unable to dissociate and measure all of the ions in the original assembly (Figure **6.10a**). Ions with mass greater than ≈ 700 kDa did not completely convert to charge-stripped species even at the maximal

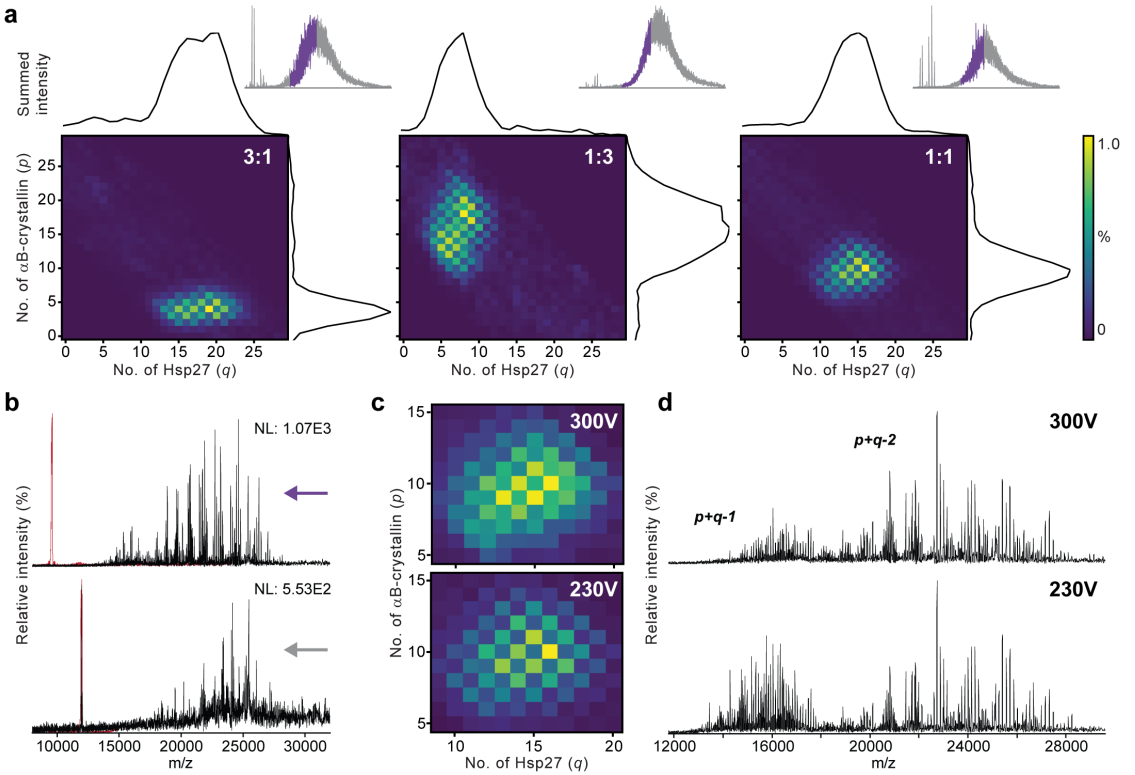


Figure 6.10. Snapshots of co-assembled αB-crystallin·Hsp27 heteromers, and factors affecting the results. a. The proteins populate a broad range of stoichiometries at varying ratios (≈ 3 to 1, 1 to 3, and 1 to 1 Hsp27 to αB-crystallin), with specific compositions determined by the availability of subunits. Summed intensities along each axis reveal that subunits do not organize preferentially. To the top right of each, the corresponding intact assembly is purple where tandem MS data underlie the distributions in the grids. Gray regions of intact MS are not accounted for here. **b.** Tandem MS of a 1 to 1 assembly, selecting 100 m/z wide segments centered on 9,500 m/z (top) and 12,000 m/z (bottom), before CID (red) and after (black). Larger ions are not fully dissociated, and the resultant data is of insufficient quality for deconvolution. NL = normalized level, a measure of signal intensity. **c.** Co-assemblies calculated from the same sample using HCD potentials of 300V (maximum, top) and 230V. Despite subunit correction, relative even/odd abundances differ. **d.** Example tandem MS underlying **c** from selections at 10,000 m/z. Peaks enabling confident assignments are more widely dispersed with less activation.

activation available (Figure **6.10b**). This is attributed to the use of nitrogen in the HCD cell: because N_2 molecules are relatively light, the conversion of kinetic energy to internal energy is insufficient to dissociate subunits from ions above a size threshold. In addition, despite the modifications facilitating high-mass transmission, tandem MS at high m/z also worsened signal to noise (Figure **6.10b**), which did not improve with increased HCD pressure. Despite the exclusion of the largest complexes, no variability in the way the proteins co-assemble was observed across the 200-700 kDa range, and so it is extremely unlikely that they would organize differently at higher masses. Thus, the distributions here faithfully capture key

characteristics of co-assembly. Heavier collision gases such as Ar, Xe, or SF_6 would be expected to impart enough energy to dissociate ions above 700 kDa, facilitating measurement of larger stoichiometries and overcoming the mass limitation in the present work.

Separating ions in the mass spectrometer as opposed to in solution is advantageous in that error within a distribution cannot arise from imprecise preparation of multiple samples or from variability in instrument performance. A possible source of error is the extent of dissociation. Ideally, the applied post-hoc correction should remove this error. In practice, however, the amount of single- and double-stripped signal used to derive assignments does affect the final distribution. At approximately equimolar subunits, a stronger dimer-paired preference is observed at 230V compared to 300V activation (Figure **6.10c**). More dissociation events occur at 300V, removing signal from the single-stripped region by shifting it into the double-stripped region (Figure **6.10d**). The less activated spectra therefore contain more peaks, and so the distribution reconstructed from this dataset is likely to better reflect the species in solution. Further evidence in favour of the even-weighted distribution can be found in the dissociation patterns, whereby odd stoichiometries are predominantly assigned in the single-stripped region of the data, and even in the double-stripped (Figure **6.8a**). Hence, HCD energy should be tuned for maximal data dispersion along m/z.

These results describe the behaviour of Hsp27·αB-crystallin assemblies at equilibrium. To gain insight into heteromer kinetics, we next performed time-resolved experiments.

6.3.5 Monitoring kinetics of co-assembly

In order to monitor the co-assembly process, proteins were mixed in a 1 to 1 molar ratio and incubated at 37°C, and aliquots flash-frozen at various time intervals. Rather than collect enough data to derive broad distributions at each time point, the duration of which would certainly lead to re-equilibration in the needle, we focused only on species restricted to an 800 m/z transmission window centered on m/z 10,371 (the peak position for all oligomers $\alpha B_p Hsp27_q^{2(p+q)+}$ where p = q). Mass-corrected distributions within this window at selected times show the formation and disappearance of specific heteromers as the system reaches equilibrium exchange of subunits (Figure **6.11a**).

A previous study examined the kinetics of Hsp27·αB-crystallin co-assembly by native MS. Because resolution was lower, only the appearance of a broad peak diagnostic of heteromers was monitored over time (Aquilina et al., 2013). This yielded an ensemble rate of co-assembly, showing that it is a first-order process and is relatively fast ($k = 7.1 \times 10^{-2}$ min^{-1} at 37°C) compared to other sHsp exchange rates. Here, we extract more information by tracking the formation of specific complexes and stoichiometries, shown for a range of possible 28-mers and 30-mers (Figure **6.11b-c**). More highly imbalanced stoichiometries (e.g., $\alpha B_2 Hsp27_{26}$) are populated briefly and then recede as the distribution approaches a set of intermixed species closer to equimolar. The observation of all possible intermediate stoichiometries confirms that the basic unit of exchange is the monomer, with monomer dissociation the rate-limiting step. Although the ACD·ACD and ACD·C interactions are relatively low-affinity (Table 6.1), these must coincide with any intra-subunit NTD breakage in order to free a monomer, creating the longer timescale of fully equilibrated subunit exchange. This is consistent with previously proposed mechanisms (Bova et al., 2000; Basha et al., 2012), and with the absence of free heterodimers (Figure **6.6c**).

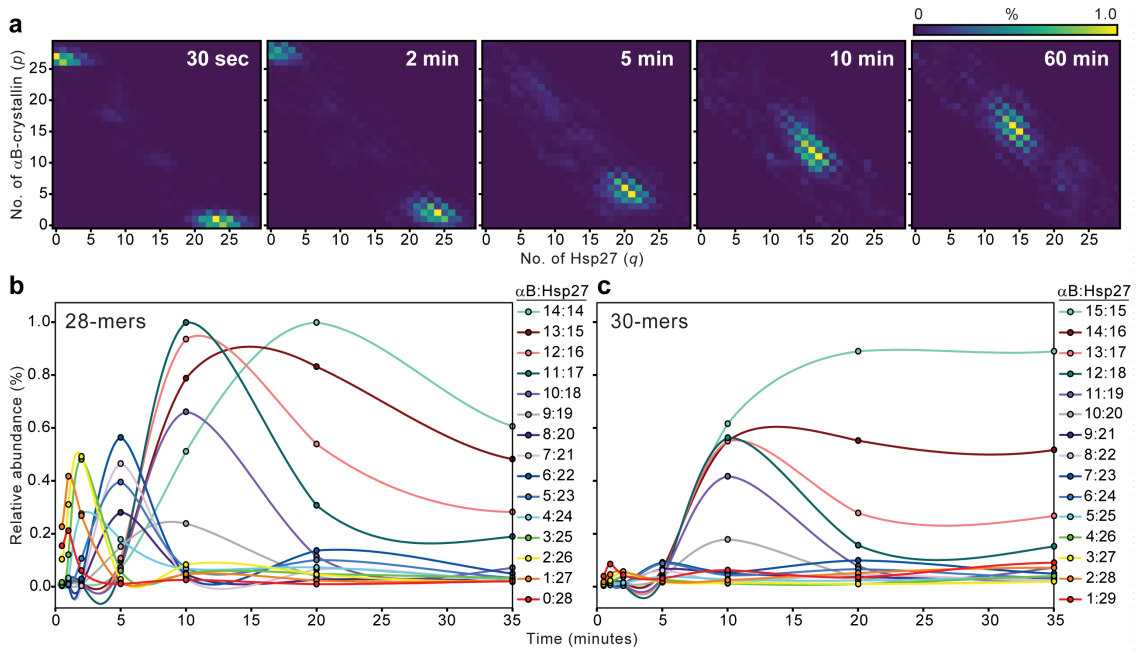


Figure 6.11. Real-time monitoring of αB-crystallin·Hsp27 co-assembly. a. CID-corrected distributions of the same 800 m/z width tandem MS selection of 1 to 1 αB-crystallin·Hsp27, incubated at 37°C for the designated times. **b.** Relative abundances within each time point of various 28-mer permutations. All possible stoichiometries between 0/28 and 14/14 are observed. **c.** Relative abundances within each time point of 30-mer permutations. Early 30-mers are presumed to be excluded from the tandem MS window.

Heteromers with 30 subunits appear only later in the time series (Figure **6.11c**). This is likely due to initial hetero-30-mers (αB_1Hsp27_{29}, αB_2Hsp27_{28}, etc.) having intact m/z outside the boundaries of the tandem MS window. Thus, because the kinetic experiment requires selectivity among the vast heterogeneity of the system, it should be interpreted such that all species of interest are observable throughout. An additional caveat for this approach lies in the apparent suppression of some oligomer populations. For example, the distribution at 5 minutes is weighted toward Hsp27 despite the equimolar pool of both subunits in the sample (Figure **6.11a**). This could be an artefact of data processing, or it could arise from transmission effects, where the instrument conditions employed ultimately favour one population over the other. These limitations should be appropriately accounted for, and the latter will likely be refined in future iterations of the experiment; but they do not obscure the most biologically relevant conclusions drawn from these data, namely, the mechanism and time scale of exchange.

6.4 Discussion

This chapter has described a method for characterizing the compositions of highly heterogeneous and dynamic protein assemblies. We find that αB-crystallin and Hsp27 co-assemble in a manner very similar to their polydisperse and dimer-biased self-assembly, creating an order of magnitude more mass-distinct heteromers. The stoichiometries and relative abundances of over 120 of these are available from a single sample using our approach, which represents the most polydisperse protein assemblies quantified by any method to date.

We examined the rate of co-assembly, which has been linked to sHsp activity, putatively because some chaperone functions require regions inaccessible in oligomers to access targets (Skouri-Panet et al., 2012; Stengel et al., 2010). The rate was found to rely on dissociation of monomers, on a timescale comparable to what has been previously reported for the most polydisperse human sHsps (Datskevich et al., 2012; Aquilina et al., 2013). Rates could serve to maintain subunits in oligomeric states under cellular conditions where promiscuous target-binding interfaces are not needed. The ability of the two most abundant human sHsps to exchange subunits freely would expand the plasticity of stress response, with more permutations allowing the cell to maintain more chaperone-ready units in a holding state for a given sHsp expression level, until their release is triggered.

The results highlight the importance of accounting for heteromerization with regard to αB-crystallin and Hsp27 in experimental biology. Our findings suggest that common approaches toward elucidating functions, such as gene knock-outs and knock-ins, will have ripple effects, changing the intracellular populations of not just one protein but also of the complexes it forms, and consequently of free subtetrameric Hsp27. Such ripple effects may be significant, particularly if a certain

population is responsible for the function under scrutiny.

Towards probing function, having visualized co-assembly of the unmodified proteins under basal-like conditions, we can next examine effects on heteromer composition and kinetics of changes linked to chaperone activity *in vivo*. These include, for example, innate changes to the proteins such as post-translational modifications (Geum et al., 2002) and sequence variants (Simon et al., 2013); as well as changes to their environment such as redox imbalance (Bodi et al., 2017) and pH shifts (Golenhofen et al., 2002; Kotter et al., 2014). It may also be feasible to interrogate client-binding at the stoichiometric level, shedding light on the molecular underpinnings of how each protein maintains distinct clients (Arrigo, 2013). This could address questions which have long eluded the field regarding which sHsp configurations are 'active' for various functions.

We anticipate that the approach can readily be applied to other sHsp systems, such as αB·αA-crystallin, whose heteromers comprise up to 40% of all protein in the eye lens (Horwitz et al., 1999); or Hsp22 with any other musculoskeletally expressed sHsp (Sun et al., 2004; Fontaine et al., 2005). Given the data's dependence on mass ratios, one could pre-empt such experiments by considering how possible complexes would arise in m/z space and, if useful, neutrally engineering the masses of recombinant proteins to produce the richest information. Since no human sHsps are more polydisperse than αB-crystallin and Hsp27, expanding the combinatorial space, such as three-subunit assemblies, may also be achievable. Ultimately, it is clear that intra-family associations comprise a significant portion of the interactions sHsps make. They should be investigated commensurate with this understanding, in synchronization with, rather than as an afterthought to, client and substrate activities.

In this chapter, I have demonstrated the utility of the most advanced native

mass spectrometry platform available to disentangle a level of heterogeneity previously intractable in structural biology. These experiments represent a crucial advancement toward understanding the link between co-assembly and chaperone function.

Acknowledgments

I am grateful to Michael Marty for working with me to implement several new tools for data processing and analysis; to Joseph Gault for sharing his expertise on the Orbitrap platform and for reviewing the chapter; to Charlie Silver for the substantial progress he made establishing the feasibility of this work during his Masters in the group; and to Stephen Weeks for providing the plasmid and protocol for expression of SUMO-Hsp27.

6.5 Methods

Protein expression and purification

αB_{ACD}, $Hsp27_{ACD}$, full-length αB-crystallin, and full-length Hsp27 were expressed and purified as described previously (Hochberg et al., 2014) and as described in Chapters 2 and 4 herein. Mutation C137S was introduced into Hsp27 using a QuikChange site-directed mutagenesis kit (Agilent) and this variant was used for all heteromer experiments.

Peptides (αB_{Ctp}, $Hsp27_{Ctp}$, $\alpha B_{Ctp\text{-}ctrl}$, and $Hsp27_{Ctp\text{-}ctrl}$) were purchased from Biomatik at 99+% purity. Lyophilized peptides were resuspended in ddH_2O to a stock concentration of 1 mM, flash-frozen, and stored at -20°C until use. Peptides were diluted in ammonium acetate prior to mixing for MS experiments.

Native mass spectrometry: ACDs and Ctps

All MS of simplified protomer systems was performed using gold-plated capillaries prepared in-house on a Synapt G2 mass spectrometer (Waters) modified for the transmission of intact noncovalent protein complexes (Bush et al., 2010) with parameters as follows: capillary 1.5kV; sample cone 40V; extractor cone 3V; backing pressure 3.0-3.1 mbar; trap gas (argon) 3 mL min^{-1}; trap cell voltage 10V; transfer cell voltage 8V. Ion mobility mode was enabled with IM cell gas flow 22 mL min^{-1}; wave height 5.5V; wave velocity 300 m s^{-1}. A minimum of three technical repeats were collected for each experiment, all in the presence of acetonitrile vapour in order to promote charge reduction and maintenance of noncovalent contacts (Hopper et al., 2012). All proteins and peptides were mixed in 200 mM ammonium acetate pH 6.9 immediately prior to data collection. Where $Hsp27_{ACD}$ was present, DTT was included at a 10-fold molar excess and full reduction was confirmed by CID.

Data processing and analysis: ACDs and Ctps

For ACD·ACD mixtures, ratios were approximated for mixing based on protein concentrations measured by UV absorbance at 280 nm; but ratios input into the binomial equation were determined by the monomer ratio in deconvolved spectra collected concurrently where all dimers were collisionally dissociated (trap cell voltage 115V). Quantitation of homo- and heterodimers was based on relative peak intensities of the 7^+ dimer charge state following 2×2 smoothing in MassLynx software (Waters), assuming similar ionization efficiencies for all species. Quantitation of monomeric and dimeric species for peptide pH controls was done by extracting each in DriftScope and then comparing the summations of all monomer and all dimer peak intensities in MassLynx.

For ACD·Ctp mixtures, ACD concentrations were held constant at 5 μM and peptide concentrations were varied from 5 to 160 μM. Populations of free and peptide-bound monomers for construction of comparable binding curves were determined by deconvolution of raw spectra with the m/z range restricted to include only 5^+ and 6^+ monomer charge states and the upper bound of the mass set to 11.3 kDa. Deconvolutions and dissociation constant fitting were carried out using UniDec software (Marty et al., 2015).

Native MS of polydisperse oligomers on the Q-Exactive platform

Recombinant αB-crystallin and Hsp27 were stored in PBS at -80°C and buffer exchanged into 200 mM ammonium acetate pH 6.9 using BioRad biospin columns prior to MS. Each was analyzed alone at a monomeric concentration of 15 μM. To generate fully co-assembled populations, proteins were mixed at ratios of 1:1, 1:3, and 3:1 to final total concentrations of 60 μM and incubated at 37°C for 90 minutes. These were diluted by a factor of three prior to MS acquisition. For kinetic

analysis, proteins were mixed 1:1 to a final concentration of 10 μM each, aliquoted, and incubated in a water bath at 37°C. Aliquots were flash-frozen at 0, 0.5, 1, 2, 5, 10, 20, 35, 60, and 90 minutes. The error introduced by additional subunit exchange occurring in the dead time of the experiment was assumed to be negligible, since proteins were thawed on ice and exchange is very slow at low temperatures. To minimize error arising from exchange during data collection, once a needle was introduced to the instrument source, data were collected within ≈ 3 minutes or the sample was discarded.

Data were collected using gold-plated capillaries prepared in-house on a modified Orbitrap QExactive Plus mass spectrometer optimized for transmission of high-mass species (ThermoFisher Scientific) (Fort et al., 2017). Capillary voltage was 1.4kV in positive ion mode with source temperature 170°C and S-lens RF 200%. UHV pressure (nitrogen) was kept at 1.6-1.7 $\times$ 10^{-9} mbar (this is pumped into the HCD cell and is termed 'HCD pressure' in the text, but is read as UHV pressure on the instrument user interface, because the gauge is located in the subsequent vacuum stage). In-source fragmentation voltage was -200V for heteromers and Hsp27, and -180V for homomeric αB-crystallin. Ion transfer optics were as follows: injection flatapole 10V, inter-flatapole lens 8V, bent flatapole 6V, transfer multipole 4V, C-trap entrance lens 3V. The RF MP2 and MP3 voltages were overridden to remain constant at maximum value (800+V). Nitrogen was used in the high-energy collision (HCD) cell. HCD energy was 0V for intact oligomer spectra and ranged from 200V-300V for subunit-stripped spectra, as described in the text. Resolution was 17,500 at m/z = 200 for a transient time of 64 ms, and the noise threshold was set to 3. To improve signal quality, transients were typically combined in groupings of 15-30 microscans. Tandem MS spectra with CID were collected either across the intact oligomer distribution in sequential selection windows 500 m/z wide (for distribution

analysis) or encompassing a subset of oligomers (for kinetic studies) as described in the text.

Concomitantly with each subunit-stripped oligomer spectrum, a new spectrum was recorded after lowering the UHV pressure to 6.3×10^{-10} mbar and changing the pulser mode from 0 to 100. These adjustments facilitated transmission and detection of highly charged monomers.

Data processing and analysis: polydisperse oligomers

Heteromer data were calibrated using homomeric spectra collected on the same day (typical drift was within ± 3 m/z) and deconvolved using UniDec software. Data were input with no smoothing, subtraction, or binning, and allowing nonlinear m/z sampling. For subunit-stripped oligomers, we used an m/z range of 9,000-32,000 and charge range 10^{+}-50^{+}. Mass sampling and peak FWHM were adjusted to ensure close fitting of the data, and charge scaling was enabled. Data quality could at this stage be rapidly assessed by using the Oligomer and Mass Tools function to assign heteromers, and manually ensuring that assignments and charge series were comprehensive and logical. The Native Charge/Mass Tools function was then used to extract single- and double-subunit stripped regions (with Gaussian distributions and a z-width of 3). To deconvolve dissociated subunits from sister mass spectra, the m/z and charge ranges in UniDec were lowered to 1,000-3,200 and 5^{+}-25^{+}, and intensity ratios in the zero charge mass spectrum were recorded. A custom Python script was written to import the UniDec files output from Native Charge/Mass Tools and, given arguments of the two protein masses and their fractional dissociation populations, to correct for each dissociation event and sum the resulting intensities into a single distribution. These distributions were combined and visualized using UniDec's Data Collector Utility feature.

For kinetic analysis, each mass spectrum was deconvolved and corrected in the same manner. Intensities for stoichiometries of interest were extracted from grids and normalized to the most abundant species within each time-point.

References

The Big Book on Small Heat Shock Proteins, volume 8 of *Heat Shock Proteins*. Springer, 2015.

J. A. Aquilina, J. L. Benesch, O. A. Bateman, C. Slingsby, and C. V. Robinson. Polydispersity of a mammalian chaperone: mass spectrometry reveals the population of oligomers in alphab-crystallin. *Proc Natl Acad Sci U S A*, 100(19):10611–6, 2003.

J. A. Aquilina, S. Shrestha, A. M. Morris, and H. Ecroyd. Structural and functional aspects of hetero-oligomers formed by the small heat shock proteins alphab-crystallin and hsp27. *J Biol Chem*, 288(19):13602–9, 2013.

A. P. Arrigo. Human small heat shock proteins: protein interactomes of homo- and hetero-oligomeric complexes: an update. *FEBS Lett*, 587(13):1959–69, 2013.

A. J. Baldwin, G. R. Hilton, H. Lioe, C. Bagneris, J. L. Benesch, and L. E. Kay. Quaternary dynamics of alphab-crystallin as a direct consequence of localised tertiary fluctuations in the c-terminus. *J Mol Biol*, 413(2):310–20, 2011.

E. Basha, H. O'Neill, and E. Vierling. Small heat shock proteins and alpha-crystallins: dynamic proteins with flexible functions. *Trends Biochem Sci*, 37(3):106–17, 2012.

J. L. Benesch, B. T. Ruotolo, D. A. Simmons, and C. V. Robinson. Protein complexes in the gas phase: technology for structural genomics and proteomics. *Chem Rev*, 107(8):3544–67, 2007.

B. Bodi, E. P. Toth, L. Nagy, A. Toth, L. Martha, A. Kovacs, G. Balla, T. Kovacs, and Z. Papp. Titin isoforms are increasingly protected against oxidative modifications in developing rat cardiomyocytes. *Free Radic Biol Med*, 113:224–235, 2017.

M. P. Bova, H. S. McHaourab, Y. Han, and B. K. Fung. Subunit exchange of small heat shock proteins. analysis of oligomer formation of alphaa-crystallin and hsp27 by fluorescence resonance energy transfer and site-directed truncations. *J Biol Chem*, 275(2):1035–42, 2000.

M. F. Bush, Z. Hall, K. Giles, J. Hoyes, C. V. Robinson, and B. T. Ruotolo. Collision cross sections of proteins and their complexes: a calibration framework and database for gas-phase structural biology. *Anal Chem*, 82(22):9557–65, 2010.

P. N. Datskevich, E. V. Mymrikov, and N. B. Gusev. Utilization of fluorescent chimeras for investigation of heterooligomeric complexes formed by human small heat shock proteins. *Biochimie*, 94(8):1794–804, 2012.

S. P. Delbecq, S. Jehle, and R. Klevit. Binding determinants of the small heat shock protein, alphab-crystallin: recognition of the 'ixi' motif. *EMBO J*, 31(24):4587–94, 2012.

J. den Engelsman, S. Boros, P. Y. Dankers, B. Kamps, W. T. Vree Egberts, C. S. Bode, L. A. Lane, J. A. Aquilina, J. L. Benesch, C. V. Robinson, W. W. de Jong, and W. C. Boelens. The small heat-shock proteins hspb2 and hspb3 form well-defined heterooligomers in a unique 3 to 1 subunit ratio. *J Mol Biol*, 393(5):1022–32, 2009.

J. M. Fontaine, X. Sun, R. Benndorf, and M. J. Welsh. Interactions of hsp22 (hspb8) with hsp20, alphab-crystallin, and hspb3. *Biochem Biophys Res Commun*, 337(3):1006–11, 2005.

K. L. Fort, M. van de Waterbeemd, D. Boll, M. Reinhardt-Szyba, M. E. Belov, E. Sasaki, R. Zschoche, D. Hilvert, A. A. Makarov, and A. J. R. Heck. Expanding the structural analysis capabilities on an orbitrap-based mass spectrometer for large macromolecular complexes. *Analyst*, 143(1):100–105, 2017.

D. Geum, G. H. Son, and K. Kim. Phosphorylation-dependent cellular localization and thermoprotective role of heat shock protein 25 in hippocampal progenitor cells. *J Biol Chem*, 277(22): 19913–21, 2002.

N. Golenhofen, A. Arbeiter, R. Koob, and D. Drenckhahn. Ischemia-induced association of the stress protein alpha b-crystallin with i-band portion of cardiac titin. *J Mol Cell Cardiol*, 34(3): 309–19, 2002.

M. Heirbaut, F. Lermyte, E. M. Martin, S. Beelen, F. Sobott, S. V. Strelkov, and S. D. Weeks. Specific sequences in the n-terminal domain of human small heat-shock protein hspb6 dictate preferential hetero-oligomerization with the orthologue hspb1. *J Biol Chem*, 292(24):9944–9957, 2017.

G. R. Hilton, G. K. Hochberg, A. Laganowsky, S. I. McGinnigle, A. J. Baldwin, and J. L. Benesch. C-terminal interactions mediate the quaternary dynamics of alphab-crystallin. *Philos Trans R Soc Lond B Biol Sci*, 368(1617):20110405, 2013.

G. K. Hochberg and J. L. Benesch. Dynamical structure of alphab-crystallin. *Prog Biophys Mol Biol*, 115(1):11–20, 2014.

G. K. Hochberg, H. Ecroyd, C. Liu, D. Cox, D. Cascio, M. R. Sawaya, M. P. Collier, J. Stroud, J. A. Carver, A. J. Baldwin, C. V. Robinson, D. S. Eisenberg, J. L. Benesch, and A. Laganowsky. The structured core domain of alphab-crystallin can prevent amyloid fibrillation and associated toxicity. *Proc Natl Acad Sci U S A*, 111(16):E1562–70, 2014.

G. K. A. Hochberg, D. A. Shepherd, E. G. Marklund, I. Santhanagoplan, M. T. Degiacomi, A. Laganowsky, T. M. Allison, E. Basha, M. T. Marty, M. R. Galpin, W. B. Struwe, A. J. Baldwin, E. Vierling, and J. L. P. Benesch. Structural principles that enable oligomeric small heat-shock protein paralogs to evolve distinct functions. *Science*, 359(6378):930–935, 2018.

J. T. Hopper, K. Sokratous, and N. J. Oldham. Charge state and adduct reduction in electrospray ionization-mass spectrometry using solvent vapor exposure. *Anal Biochem*, 421(2):788–90, 2012.

J. Horwitz, M. P. Bova, L. L. Ding, D. A. Haley, and P. L. Stewart. Lens alpha-crystallin: function and structure. *Eye (Lond)*, 13 (Pt 3b):403–8, 1999.

Q. Hu, R. J. Noll, H. Li, A. Makarov, M. Hardman, and R. Graham Cooks. The orbitrap: a new mass spectrometer. *J Mass Spectrom*, 40(4):430–43, 2005.

B. Jovcevski, M. A. Kelly, A. P. Rote, T. Berg, H. Y. Gastall, J. L. Benesch, J. A. Aquilina, and H. Ecroyd. Phosphomimics destabilize hsp27 oligomeric assemblies and enhance chaperone activity. *Chem Biol*, 22(2):186–95, 2015.

S. Kotter, A. Unger, N. Hamdani, P. Lang, M. Vorgerd, L. Nagel-Steger, and W. A. Linke. Human myocytes are protected from titin aggregation-induced stiffening by small heat shock proteins. *J Cell Biol*, 204(2):187–202, 2014.

M. T. Marty, A. J. Baldwin, E. G. Marklund, G. K. Hochberg, J. L. Benesch, and C. V. Robinson. Bayesian deconvolution of mass and ion mobility spectra: from binary interactions to polydisperse ensembles. *Anal Chem*, 87(8):4370–6, 2015.

E. V. Mymrikov, A. S. Seit-Nebi, and N. B. Gusev. Heterooligomeric complexes of human small heat shock proteins. *Cell Stress Chaperones*, 17(2):157–69, 2012.

S. Simon, V. Dimitrova, B. Gibert, S. Virot, N. Mounier, M. Nivon, C. Kretz-Remy, V. Corset, P. Mehlen, and A. P. Arrigo. Analysis of the dominant effects mediated by wild type or r120g mutant of alphab-crystallin (hspb5) towards hsp27 (hspb1). *PLoS One*, 8(8):e70545, 2013.

F. Skouri-Panet, M. Michiel, C. Ferard, E. Duprat, and S. Finet. Structural and functional specificity of small heat shock protein hspb1 and hspb4, two cellular partners of hspb5: role of the in vitro hetero-complex formation in chaperone activity. *Biochimie*, 94(4):975–84, 2012.

F. Stengel, A. J. Baldwin, A. J. Painter, N. Jaya, E. Basha, L. E. Kay, E. Vierling, C. V. Robinson, and J. L. Benesch. Quaternary dynamics and plasticity underlie small heat shock protein chaperone function. *Proc Natl Acad Sci U S A*, 107(5):2007–12, 2010.

Y. Sugiyama, A. Suzuki, M. Kishikawa, R. Akutsu, T. Hirose, M. M. Waye, S. K. Tsui, S. Yoshida, and S. Ohno. Muscle develops a specific form of small heat shock protein complex composed of mkbp/hspb2 and hspb3 during myogenic differentiation. *J Biol Chem*, 275(2):1095–104, 2000.

X. Sun, J. M. Fontaine, J. S. Rest, E. A. Shelden, M. J. Welsh, and R. Benndorf. Interaction of human hsp22 (hspb8) with other small heat shock proteins. *J Biol Chem*, 279(4):2394–402, 2004.

M. van de Waterbeemd, K. L. Fort, D. Boll, M. Reinhardt-Szyba, A. Routh, A. Makarov, and A. J. Heck. High-fidelity mass analysis unveils heterogeneity in intact ribosomal particles. *Nat Methods*, 14(3):283–286, 2017.

M. J. Vos, B. Kanon, and H. H. Kampinga. Hspb7 is a sc35 speckle resident small heat shock protein. *Biochim Biophys Acta*, 1793(8):1343–53, 2009.

Concluding remarks

Summary of findings

In this thesis, I have described the biophysical and structural characterization of several interactions made by sHsps *in vivo*. Altogether, these insights add to the literature regarding specialist, rather than generalist, functions of sHsps.

In Chapter 2, I showed that a cardiac-specific domain of the elastic muscle protein titin is a target of αB-crystallin; and in Chapter 4, confirmed another biomechanical muscle protein, filamin C, as a target of Hsp27. Each of these were recognized by the sHsp while in their native, folded states, placing them as clients of the chaperones rather than substrates. The binding sites within the sHsps were narrowed to the peptide level and found to reside within conformationally heterogeneous regions of the C- and N-termini, respectively. Both regions are involved in modulating the assembly of sHsp oligomers, bolstering the prevailing view that quaternary dynamics and function are tightly linked.

The interaction between titin and αB-crystallin was found to be significantly weakened by the R157H cardiomyopathy-causative variant. Scaling-up to the tissue level, these results were reflected in experiments on mouse heart muscle fibers: the chaperone stiffened fibers across the physiological length range, and was less effective

when mutated to R157H. We also discovered a naturally occurring protein alteration that regulated the Hsp27-filamin C interaction in the form of phosphorylation. Previous studies had established that phosphorylation of Hsp27 disrupts oligomers, and that it occurs in muscle under mechanical stress. We report phosphorylation and up-regulation of Hsp27 in the hearts of a mouse model of heart failure, alongside an interaction with filamin C. Importantly, our findings point to a force-dependent mode of strengthened binding upon Hsp27 phosphorylation. A self-contained study on filamin C, described in Chapter 3, bolstered this conclusion by providing experimental evidence to support the use of gas-phase unfolding as a method to examine functionally relevant unfolding trends in biomechanical proteins.

In Chapter 5, we examined cvHsp, which previous studies had suggested does not function as a generalist chaperone. Indeed, it displayed markedly different quaternary structure to the other sHsps explored in this thesis, with much less propensity for oligomerization and polydispersity; and its curious redox-dependent behaviour hinted at different tertiary structure as well. Our newly established rheological and MS-based assays show promise for gaining further insight into cvHsp specialist functions in muscle, and in particular its relation to mechanosensitivity, with clients filamin and actin of interest.

The final results chapter pushed the boundaries of the degree of heterogeneity that can be unraveled by native MS. We tackled the highly polydisperse αB-crystallin·Hsp27 co-assembled oligomer population, and were able to assign well over 100 stoichiometries within single samples and watch how individual species formed over time. Due to the heterogeneity involved, details of sHsp co-assembly have to date remained largely enigmatic, despite being among the most common interactions these proteins make. Now, we are equipped with a powerful approach to chip away at this component of their function.

A framework for categorizing sHsp function

Based on these results, and in the context of the broader literature on the processes involving sHsps, I conceptualize their function in a framework that encompasses a multitude of roles from physiological to pathological conditions. This landscape can be subdivided coarsely into four quadrants (Figure **7.1**). Under minimal stress, when most proteins in the cell can be presumed to populate their native states, sHsps are primarily engaged in specialist client-binding (lower left). Also in the specialist descriptor, I include self- and co-assembly, since these interactions are both native-state and precise (lower right). With mounting stress, the proteome becomes increasingly destabilized. Some sHsps then adopt generalist roles, sequestering misfolded substrates in contained phase-separated regions (upper right) or forming soluble complexes with them in order to prevent cascades to amorphous aggregates or amyloid fibrils in canonical holdase fashion (upper left).

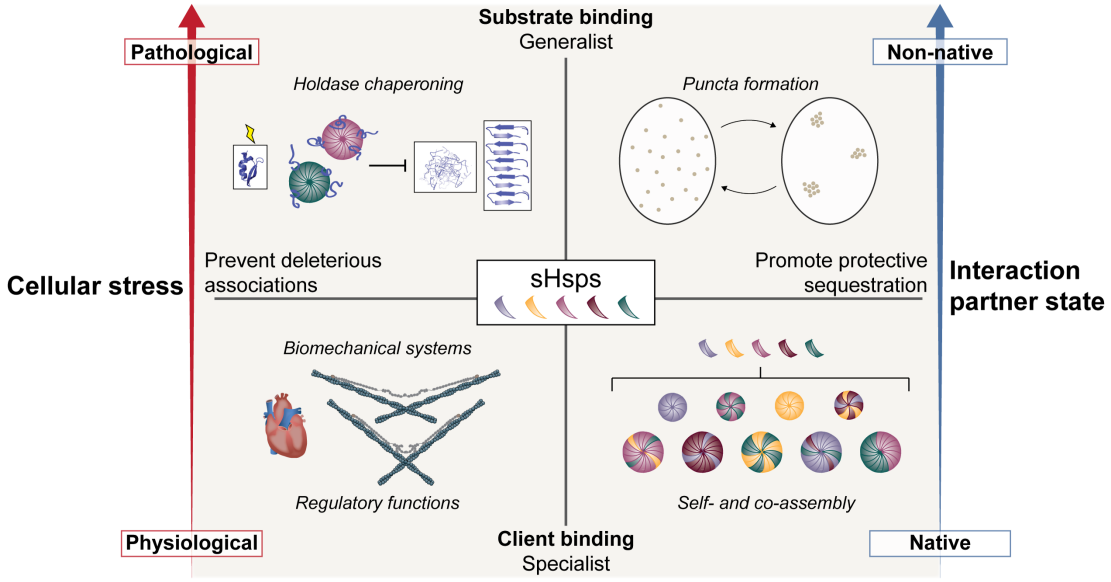


Figure 7.1. The sHsp functional landscape.

Thus, the left and right division arises between functions that serve to prevent interactions that should not occur (left) and ones that facilitate interactions that are protective (right; for example, oligomerization can shield promiscuous interfaces

when they are not needed). Certain sHsps cover more of this landscape than others, and biochemical changes, to the environment or in the form of protein modification, can shift their focus between quadrants.

In particular, this thesis has furthered our understanding of native partner sHsp interactions, which have received little attention compared to roles fitting the generalist paradigm. I place biomechanical systems in the preventative-client quadrant, and note that the term 'native' as it applies to these systems must account for the routine structural distortions induced by physiological force, which may bridge a biophysical gap between misfolding substrates and more rigid clients. Two specific examples of biomechanical sHsp-client systems were explored here, both in connection to heart failure. This work and previous reports, as well as sHsp abundance in muscle and implications in musculoskeletal pathologies, strongly hint at the existence of other clients that may fit into this piece of an expanded sHsp paradigm.